SUPERCONDUCTING MICROWAVE RESONATORS FOR COSMOLOGY AND ASTROPHYSICS WITH CCAT

A Dissertation

Presented to the Faculty of the Graduate School

of Cornell University

in Partial Fulfillment of the Requirements for the Degree of

Doctor of Philosophy

by

Cody J. Duell

August 2024

SUPERCONDUCTING MICROWAVE RESONATORS FOR COSMOLOGY AND ASTROPHYSICS WITH CCAT

Cody J. Duell, Ph.D.
Cornell University 2024

Across the millimeter and submillimeter sky, we see relic radiation giving evidence that the early universe went through a hot, dense phase out of which all modern structures (stars, galaxies, galaxy clusters, etc.) eventually coalesced. Precision measurements of this light, the cosmic microwave background, serve as a foundation to our modern understanding of the universe and present us with a means to probe physics at a wide range of scales. Higher precision measurements will further inform our models of the universe and provide constraints on beyond-standard-model physics, such as dark energy, inflation, and the existence of additional light relativistic particles in the early universe.

Attaining these higher constraints with upcoming ground-based observatories such as the Fred Young Submillimeter Telescope and the Simons Observatory will require unprecedented numbers of superconducting detectors operating at nearly the fundamental limits of sensitivity. One such detector technology is the kinetic inductance detector (KID), a superconducting resonator that allows for natural multiplexing and photon-limited performance. Prime-Cam, one of two primary survey instruments for the CCAT collaboration's six-meter Fred Young Submillimeter Telescope, will ultimately deploy more than 100,000 KIDs across seven independent instrument modules.

In this thesis, we present an overview of some of the author's contributions to the field of experimental cosmology as a member of the Atacama Cosmology Telescope, Simons Observatory, and CCAT collaborations. In particular, we describe the development, design, and test of many key elements of the detectors and readout for the 280 GHz and 350 GHz instrument modules for CCAT's Prime-Cam receiver. We provide a comparative analysis of aluminum and titanium-nitride-based KIDs, the two most common KID materials at millimeter and submillimeter wavelengths, both of which are being used in Prime-Cam. We then describe the cryogenic readout system for the 280 GHz instrument module, including a demonstration of photon-noise limited performance with prototype detectors. Next, we detail the cryogenic focal planes and detector array modules for the 280 GHz instrument module and provide status updates on the three completed arrays. We conclude with a discussion of several interesting science cases that these technologies may enable when deployed.

BIOGRAPHICAL SKETCH

Cody Duell was born and raised in Norwich, NY. In 2010, he graduated from Seton Hall University, receiving a Bachelor of Arts with Honors in Philosophy and a minor in Classical Civilizations. In 2011, Cody was married to Hope Spithaler, who he met in his first days attending Seton Hall. In 2017, he completed a Bachelor of Science with Honors from the City College of New York (CCNY) with a concentration in Physics and a minor in Mathematics. During his time at CCNY, he conducted research in computational biophysics under Prof. Marilyn Gunner, using Monte Carlo methods to explore changes in local charge states as proteins bind or lose ions.

In the late summer of 2017, Cody joined the Department of Physics at Cornell University as a graduate student, and in spring of 2018 he joined the research group of Michael Niemack where his first project was to take the group's first measurements of kinetic inductance detectors. During his time in the Niemack lab, he has been involved in several collaborations, including the Atacama Cosmology Telescope, the Simons Observatory, and CCAT. His primary research has been in the development of superconducting detectors and readout technologies for the upcoming SO and CCAT instruments. Additionally, he has worked with data from the Atacama Cosmology Telescope in searches for time-domain signals including magnetars and fast radio bursts.

Cody and Hope welcomed their son, Arlo, in March of 2021 and their daughter, Iris, in December of 2023. After completing his graduate studies, Cody will be remaining at Cornell to contribute towards the deployment of CCAT's first light instrumentation.

To Mom and Dad

for bringing me up.

To Arlo and Iris

for lighting up my sky.

To Hope

for more than I have words to say.

ACKNOWLEDGEMENTS

In a thesis about KIDs, it feels appropriate to say that it took a village. There are so many people who inspired and encouraged me on my journey that I am certain to fall short in trying to acknowledge all of them. Nonetheless, I will try to do so here.

First, I would like to thank my advisor, Mike Niemack. Upon arriving at Cornell, I didn't plan to study experimental cosmology and had only very naive conceptions of what that would even entail, but through a few casual conversations you won me over, and I couldn't be happier that you did. Thank you for your enthusiasm. Thank you for your abundant patience. Thank you for being a positive example of how to balance family with academic pursuits. Most of all, thank you for continually guiding, supporting, and pushing me in my work.

Next, I want to say thank you to Jim Cordes and Liam McAllister for providing valuable feedback, advice, and encouragement while serving on my committee over the past several years.

I was fortunate to be a part of an amazing research group. To those who preceded me as graduate students - Brian, Pato, Jason, Eve, and Nick - thank you for showing me the ropes, mentoring me, and your friendship. I'll always associate closing up the DR with dollar beers and popcorn. To the current graduate students - Zach, Ben, Lawrence, Rodrigo, Alicia, and Ema - thank you for sharing the load and supporting me however was needed. To Steve Choi and Yaqiong Li: thank you for sharing your incredible levels of expertise and for your mentorship. To Sam Walker: thank you for your infectious enthusiasm and encouragement. Lastly, a massive thank you to the many undergraduates I've worked with over the years, including Noah, Pedro, Haruki, Colin, Jesse, Kshama, Erik, Mahiro, and many more.

Beyond our group, Cornell has been an amazing place to do research, and there are so many individuals whose knowledge and kindness I have benefited from. Thank you to Gordon Stacey, Terry Herter, Thomas Nikola, Nick Battaglia, Abby Crites, Amit Vishwas, Steve Parshley, and George Gull for several years of collaboration on CCAT and other topics. Thank you to Shami Chatterjee for your advice and guidance in my time domain studies (though it didn't quite make it to this thesis). Thank you to Paul Corlies for teaching me almost everything I know about our lab's FTS.

The technical work here would not have been possible without my many external collaborators. A massive thank you is owed to the folks at NIST, particularly Hannes Hubmayr, Jiansong Gao, Jay Austermann, Jordan Wheeler, and Mike Vissers. You made my many visits to Boulder some of the highlights of my graduate experience and taught me a tremendous amount. Thank you to the many colleagues and friends that I met as a part of ACT, SO, and CCAT, including Phil Mauskopf, Chris Groppi, Adrian Sinclair, Sam Gordon, Yilun Guan, Fernando Zago, Arthur Kosowsky, Heather McCarrick, Suzanne Staggs, Lyman Page, Mark Devlin, Brad Dober, Sarah-Marie Bruno, Erin Healy, Yuhan Wang, Max Silva-Fever, Adam Hincks, Sigurd Naess, Jesse Treu, Emily Biermann, Shawn Henderson, Stefania Amodeo, and many more.

Away from the lab, there have been so many friendly faces who have helped to make my time at Cornell a joy. Thank you to Kacey Acquilano, Craig Wiggers, Debra Hatfield, Casey Neville, and many others from the Physics Department for making it such a welcoming place when I arrived and throughout my time. To my many friends through Cornell - Naomi, Michelle, Divya, Tres, Kevin, Margaret, Shaun, Mari, Derek, Dante, Eamonn, Sam, and many, many others - I cannot thank you enough for keeping me sane and entertained. I am especially thankful for Ofri and Laura and for Mike and Mike.

To my friends in Ithaca, including Katie, Andrew, Eva, Dylan, Jenn, Brad, Christine, Amelia, David, Diana, Sarah, and Morgan: thank you. To my friends from the outside world: Kyle, Jay, Cadell, John, Marc, Lucie, Eric, Sara, Ross, Sabina, Tim, Michele, Linda, Drew, Jordan, Nick, Dylan, Jenny, Greg, Shanna, Christian, and many, many more: thank you. To my old friend, Scott: thank you and I miss you. Thank you to my mentors at City College of New York, Prof. Gunner and Prof. Nair, as well as to my friends and colleagues there. Thank you to my mentors at Seton Hall University, particularly Prof. Lake and Prof. Stark.

Finally, I would like to thank my family. I have so many aunts, uncles, and cousins who have been such a constant blessing to have in my life that I don't even dare trying to list them all here. A special thanks to Scott, Shirley, Emma, and Josh for being such a massive help from even before we moved to Ithaca.

To my sister, Lacey: thank you for inspiring me from day one and still going strong. To the rest of the Williams family: I love you and thank you. To my grandma: I wish you could have seen me here, but thank you for 35 years of love. To my father-in-law, Marty: thank you for all your support in ways both large and small. To my cat, Yama: thanks for the snuggles. I already fed you. You're not getting more. To Mom and Dad: thank you for laying my foundation and providing endless love and support. I can never thank you enough for making all of this possible.

To my 3-year-old, Arlo and my 4-month-old, Iris: thank you for being patient when Daddy has to work and for bringing me joy in the most routine and unexpected moments. You make all of this worthwhile.

Lastly, to my wife, Hope: I can not begin to express how thankful I am for

you. Thank you for your patience through these seven eventful years. In full sincerity, I wouldn't be half of the man I am without your love and support. I would marry you again eight days a week. I love you and thank you.

TABLE OF CONTENTS

LIST OF TABLES

LIST OF FIGURES

CHAPTER 1

INTRODUCTION

Cosmology is one of the only areas of modern physics that sensitively depends on calculations from both general relativity and particle physics. It is a triumph of modern science that these theories governing such distinct domains – the incomprehensibly large and the inconceivably minute – yield sensible predictions that have been verified to great accuracy. This convergence of domains makes the field of cosmology and the extreme environment of the early universe uniquely insightful as a testing ground for new physics. By using the universe as our test system, we have the opportunity to study physics that is often inaccessible by any other means.

At the same time, we *are* restricted in observational cosmology and astrophysics to observing from afar the physics in which we are interested and comparing those observations with predictions. Much to the author's initial disappointment, being an experimentalist in cosmology does not consist of creating new universes and perturbing the laws of physics or the thermal history.[1] Much of the challenge in the fields of modern cosmology and astronomy is finding (or building) the right "eyes" with which to view the universe and suss out the finer details. The role of the instrument is to capture the true signal and to observe the sky as accurately and precisely as possible. The confounding effects of trying to observe in the middle of a galaxy at our current point in the history of the universe (and through an atmosphere in the case of ground-based telescopes) means decomposing the sky into many combined signals in the analysis, but through this decomposition we can probe both the extremes of the early uni-

[1] Yet.

verse, and the intervening ages that sit between the emission of that light and its detection.

This dissertation describes the development, design, and test of many key elements of the detectors and readout for the 280 GHz and 350 GHz instrument modules for CCAT's Prime-Cam receiver. In this introduction, I provide some scientific background to motivate the driving goals of the project, buoyed by examples from work that I contributed to with the Atacama Cosmology Telescope (ACT). Chapter 2 describes the underlying physics behind superconducting resonators and, more specifically, microwave kinetic inductance detectors (MKIDs or KIDs), which serve as the driving detector technology for Prime-Cam. Chapter 3 provides a detailed comparison of the two types of MKIDs intended for deployment with Prime-Cam's 280 GHz instrument module. Chapter 4 serves as a description of the cryogenic readout system specific to the 280 GHz and 350 GHz instrument modules, including a demonstration of photon-noise limited performance in the laboratory with prototype detectors and readout system in preparation for observations in Chile. Chapter 5 describes many of the key aspects of cryogenic focal planes and detector array modules for the 280 GHz module. Finally, Chapter 6 serves as a conclusion and a look forward to what work remains prior to first light.

1.1 Cosmology & The Expanding, Evolving Universe

It is a remarkable fact that when we look out into the universe we are looking back in time and the further away we look, the further back we see. In the early part of the 20th century, as astronomers developed ways to measure cosmological distances, several (most famously, Edwin Hubble) came to the somewhat

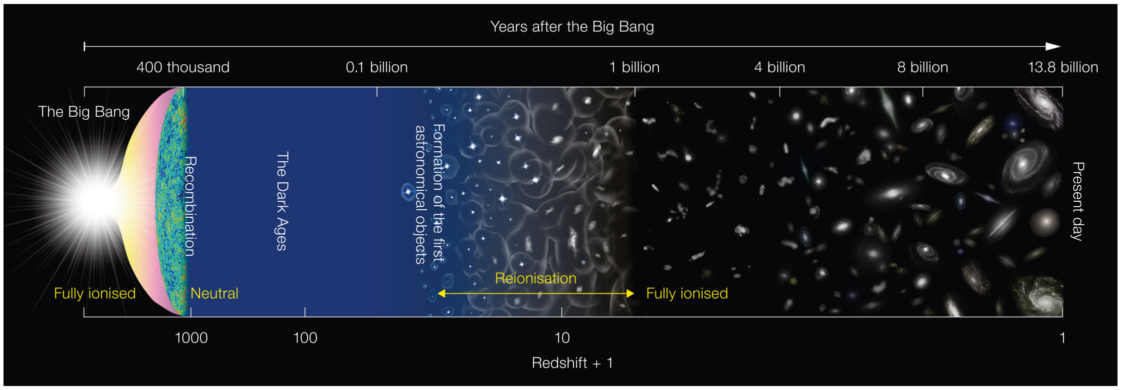

Figure 1.1: A schematic diagram depicting the history of the universe as understood through our current models. Following a hot dense early phase that lasted a few hundred thousand years, the universe transitions into a neutral phase and light is able to freely stream in the form of the cosmic microwave background. This neutral gas then condenses gravitationally over the course of several hundred million years to form more familiar structures, including the first stars (whose radiation eventually causes the "re-ionization" of the free gas), galaxies, and galaxy clusters. Image credit: NAOJ.

shocking realization that many objects in the sky were *much* further away than expected and that these distant objects were seemingly all moving away from us [57, 98, 99]. Moreover, how fast they were moving away was correlated with how far away they were [58]. These objects, the first non-Milky Way galaxies, and the correlation between distance and recession speed (which would later become known as Hubble's law or the Hubble-Lemaître law) were the first building blocks of observational cosmology. Rather than a static, immovable heavens, the universe is expanding. Eventually, this expansion was understood in the context of the "Big Bang" picture of cosmology.

In the framework of general relativity, expansion is a relatively generic result of assuming that the universe is isotropic and homogeneous on some large scale. In other words, the universe looks the same in all directions (isotropic) and locations (homogeneous) when viewed on large scales [35, 109]. The Big-

Bang model states that the universe was once extremely hot and dense, and over time it expanded and cooled to its present state. The assumption of a previous hot, dense epoch was formulated by George Gamow and his collaborators who were successful in using it to explain the abundance of light elements, particularly hydrogen and helium, that we see in the universe [6, 7, 40]. The idea was beautifully confirmed in 1964 with the measurement of the cosmic microwave background (CMB), a leftover radiation from the hot plasma redshifted to a few Kelvin in the present day [83].

Since these early formulations, the theory has expanded greatly to encompass additional observations, most significantly the stringent initial conditions imposed by the CMB's uniformity [90, 109], the convergent discovery of dark matter across various observations [13, 88, 91, 111], and the similar emergence of dark energy [84, 89, 112]. Today Big-Bang cosmology has been refined to the modern framework of a universe dominated by dark energy and gravitationally-shaped by cold dark matter with initial conditions set by a period of inflation. This modern paradigm is generally referred to as the standard model of cosmology or ΛCDM cosmology - where Λ refers to a cosmological constant, the simplest form of dark energy, and "CDM" refers to cold dark matter. ΛCDM has been phenomenally successful in explaining or predicting a wide variety observations, including the aforementioned light element abundances, the distribution of matter throughout the universe, and the existence and detailed properties of the CMB.

A general history of the universe according to the standard model of cosmology is depicted in Figure 1.1 while a detailed treatment can be found in [35] and [109]. Following a period of inflationary expansion, the early universe was an extreme environment reaching energies many, many orders of magnitude higher than those seen at even the most powerful colliders. As expansion-driven cooling occurred, various processes began to fall out of thermal equilibrium or freeze-out. Neutrinos decoupled from the plasma at around one second, protons fused into light nuclei (deuterium, tritium, helium, etc.) until about three minutes, and, presumably at some early time period, dark matter fell out thermal equilibrium with both regular matter and photons and began the slow process of gravitational collapse. Following the end of light element fusion, also referred to as big-bang nucleosynthesis, the plasma continued to evolve and cool down as a tightly coupled gas of electrons, baryons, and photons. After approximately 380,000 years, the universe had cooled sufficiently for electrons and protons to combine into neutral hydrogen atoms (a period somewhat confusingly referred to as ”recombination”) allowing photons to freely stream and baryons to collapse into dark matter potential wells. With the decoupling of matter and radiation at this point, there is a ”dark” period of several hundred million years. Eventually, the first hydrogen-rich stars turned on and began to re-ionize the remaining medium during an extended period referred to as the epoch of reionization. From this point, roughly one billion years following the big bang, we are in a universe much closer to what we know today with recognizable galaxies and stars, and an extremely thin, ionized intergalactic medium.

1.2 The Cosmic Microwave Background

The cosmic microwave background serves as one of the key pillars of modern cosmology and provides us with a rich dataset for probing physics at all scales. We can use it to peer back throughout cosmic time to the earliest acces-

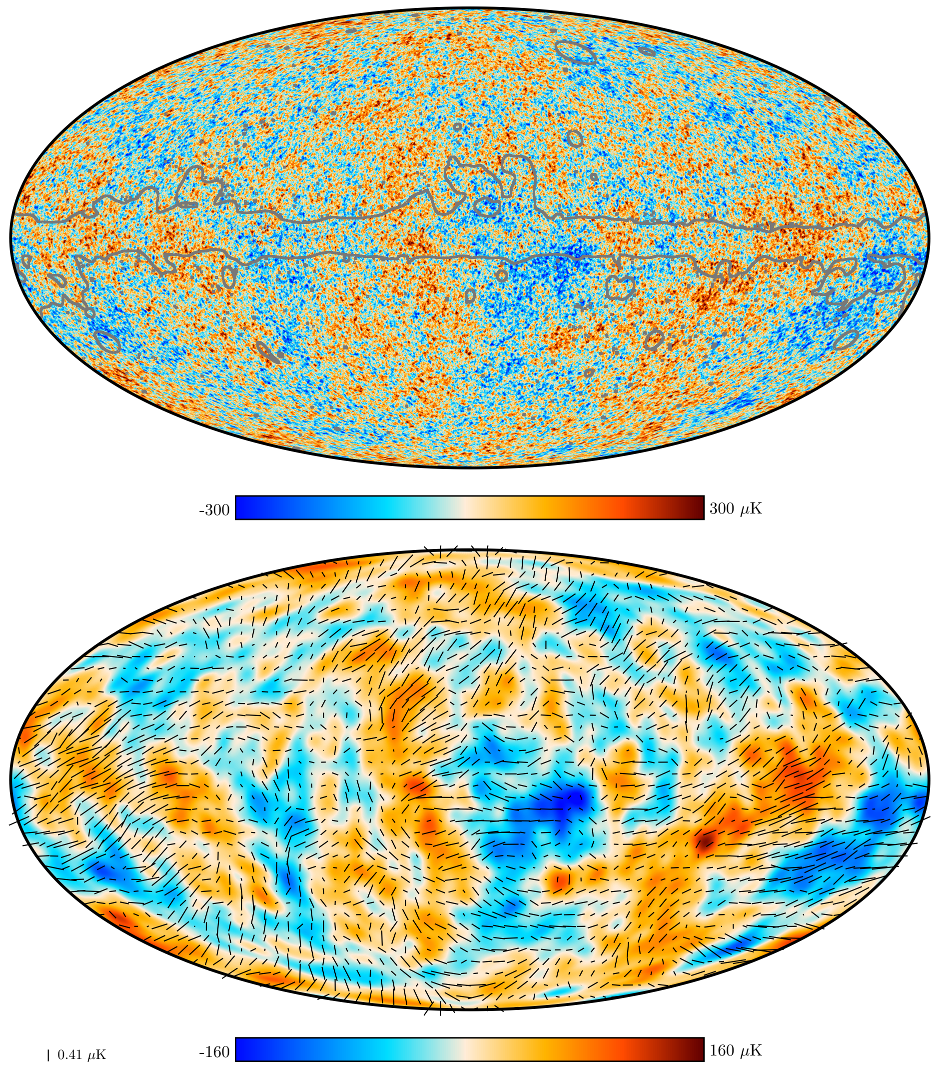

Figure 1.2: Full sky maps of the CMB temperature (top) and polarization (bottom) anisotropies from the Planck collaboration. Foreground emission from the galactic plane has been removed and the brightest foreground regions are outlined in gray in the temperature map. The temperature map displays the variation about the mean temperature with the solar dipole removed. Polarization anisotropies are conveyed by the orientation and length of the black bars, representing the electric field, atop a reduced resolution temperature map for visual reference. Figures from [4].

sible moments in the history of universe. While very nearly a perfect, isotropic blackbody, the richness of the CMB comes from the minute fluctuations, or anisotropies, of temperature and polarization. After recombination around $z \approx 1090$[2], photons freely stream from the surface of last scattering to be dutifully measured by telescopes in Chile, picking up small distortions along the way. Those fluctuations that were imprinted by the primordial plasma are referred to as primary anisotropies. They show us oscillations or sound waves in the baryons and electrons about small perturbations in the uncoupled dark matter distribution during recombination. Those distortions from interacting with matter along the way are referred to as secondary anisotropies, and carry additional information about the evolution of the universe. As light propagates through the gravitational landscape, there will be a redshift from the time-varying gravitational potential it sees (the integrated Sachs-Wolfe effect), and it will undergo gravitational lensing. There will also be scattering by ionized gas in both the relatively homogeneous intergalactic medium and gravitationally-collapsed objects such as galaxy clusters (the Sunyaev-Zel'dovich or SZ effect).

Figure 1.2 shows measurements of the CMB anisotropies by the Planck collaboration with the mean temperature of 2.726 K [37] subtracted away, as well as the solar dipole, which is the Doppler shift introduced by the motion of the solar system with respect to the CMB rest frame [85]. By characterizing the statistical distribution across the sky, we can get a much deeper probe into the physics of ΛCDM cosmology than just the measurements at any one point on the sky. The angular power spectrum describes the angular size of the fluctuations by

[2]Given the expansion history of the universe, the redshift of the wavelength, λ, from the rest value is often used as a shorthand for describing how far away something is in both space and time. The standard notation comes from the ratio of the observed wavelength, λ_{obs}, to the wavelength in our reference frame, λ_0, $\frac{\lambda_{obs}}{\lambda_0} = (1 + z)$, wherein the present day corresponds to $z = 0$.

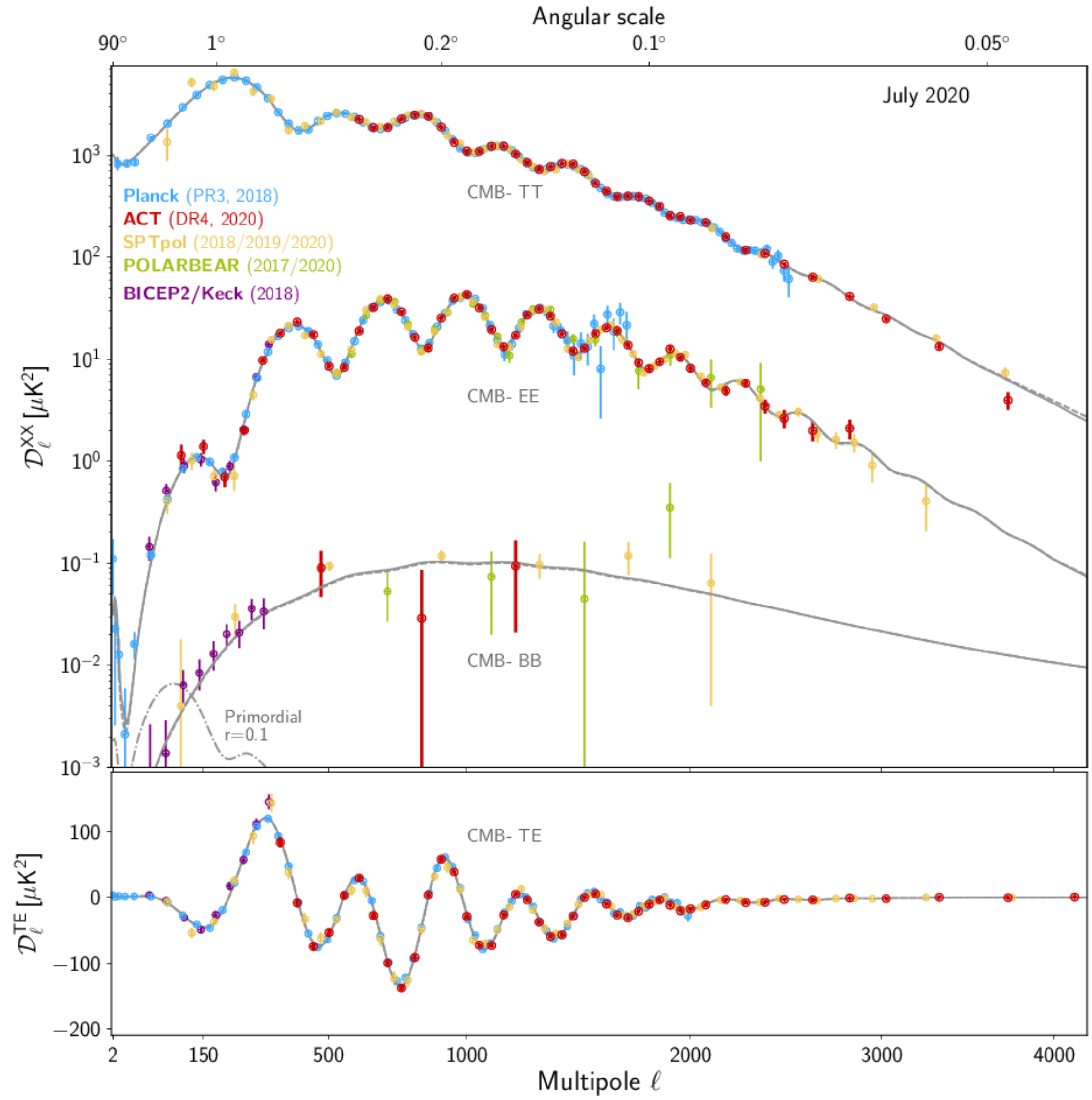

Figure 1.3: Recent power spectra measurements in temperature and polarization based on measurements from a variety of experiments. The models shown, which are nearly indistinguishable, are from Planck (dashed), and ACT plus WMAP (solid). The B-mode signature due to primordial inflation with tensor-to-scalar ratio of r=0.1 is shown as a dot-dashed line. The lower plot shows the temperature and E-mode cross-correlation spectra. Figure from [19].

decomposing the sky into spherical harmonics and taking the correlations in temperature or polarization as a function of multipole moment, l. Figure 1.3, taken from [19], shows several recent measurements of the angular power spectra for temperature and E- and B-mode polarization, as well as the temperature and E-mode cross-correlation spectra in the lower plot. The structure of these curves can be seen quite clearly and is perhaps the strongest confirmation of ΛCDM. The locations and relative heights of each of the peaks informs us about the total energy density, the baryonic and cold dark matter densities, the nature of the initial inflationary density perturbations, and the optical depth at reionization. All of this data is well-described by a parametrization of ΛCDM with just six parameters, shown in Figure 1.3 in solid and dashed lines. These represent the current forefront of the field based on work I contributed to as part of the ACT collaboration. At the same time, there is also more to be learned from these spectra. As we move to ever-higher multipoles, ever-better noise performance (particularly in polarization), and additional frequency bands, we can begin to further distinguish between models with additional parameters.

1.3 The Local & Evolving Universe

The story described in the previous section is, of course, incomplete. Besides the CMB, we see objects in the local universe across a wide range of angular scales. Stars appear as point sources, while nearby galaxies or more distant galaxy clusters appear as extended objects of relatively small angular size. Dust within our galaxy emits at slightly higher temperatures, dominating the large angular scale power at far-infrared frequencies. When studying the CMB power spectrum, the light from these sources can be considered contaminating foregrounds. They add or remove power from different angular scales by either adding their own emission or by absorbing and blocking the CMB photons. The most heinous example of this is the impact of galactic dust on the polarization spectra. A detection of low-l power in the B-mode spectra would be a unique signature of inflationary gravitational waves, yet even models with relatively strong signals in this B-mode spectra are swamped by the B-mode emission from nearby dust. At the same time, you could say that one person's foregrounds are another person's science case, and there are marvelous synergies for doing additional science while observing the CMB.

As an example of these synergies, we can consider galactic and time domain science. Observing the CMB requires observing large areas of the sky with a high cadence. This is very different from the observing strategies for targeting specific astronomical objects, as we are motivated by a desire to increase the overall statistics of our sky sample when measuring the power spectrum. For example, while observing as part of the ACT collaboration, we covered nearly half of the total sky and we might expect to return to the same patch of sky on a cadence of roughly two weeks. Within these observations then, there is a wealth of data for studying our local galaxy, as well as seeking out transient events or time domain signals.

One of the most wide open areas for study in the microwave regime is the frequency and nature of transient phenomena. Some of the most exciting observations at other frequencies have come from transient phenomena such as supernovae, fast radio bursts, active galactic nuclei, and gamma ray bursts. Additionally, time domain signals from periodic objects such as pulsars and Cepheid variables are both inherently interesting as astronomical objects and

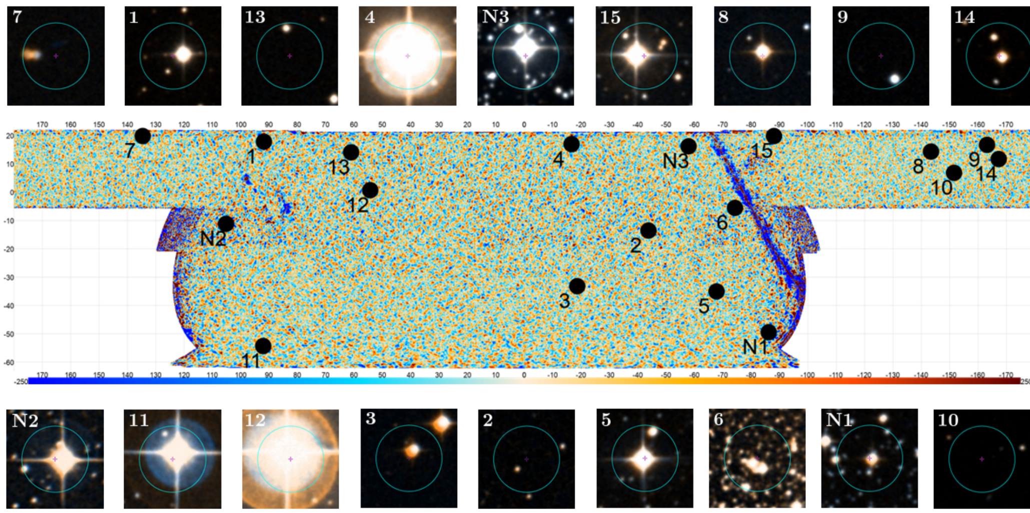

Figure 1.4: Transient events found from a systematic, map-based search of data from 2017 to 2019 with the Atacama Cosmology Telescope (ACT). Most of these events were spatially coincident with bright stars. Figure from [65].

important for their use in probing other aspects of the universe. At this time, there have only been a handful of blind searches in the microwave sky for transients [51, 65, 113]. Figure 1.4 shows the results of one of those searches using a subset of ACT data that had already been processed into 3-day maps as part of a targeted search for Planet 9 [73]. Given the varying noise levels and cadences over any given 3-day period, this strategy was only able to uncover a small fraction of transients within the data and will be improved in a forthcoming publication that uses single-observation depth maps.

On the other end of the spectrum, we can consider the large amount of foreground data that can be associated with the galactic plane. In CMB map-making, it is important to either remove galactic foreground emissions based on a model, or to mask those regions with strong emissions. The effects of this can be seen in Figure 1.4 as part of the galactic plane appears as an extended cold streak. At the same time, we can use this data to study dust and other

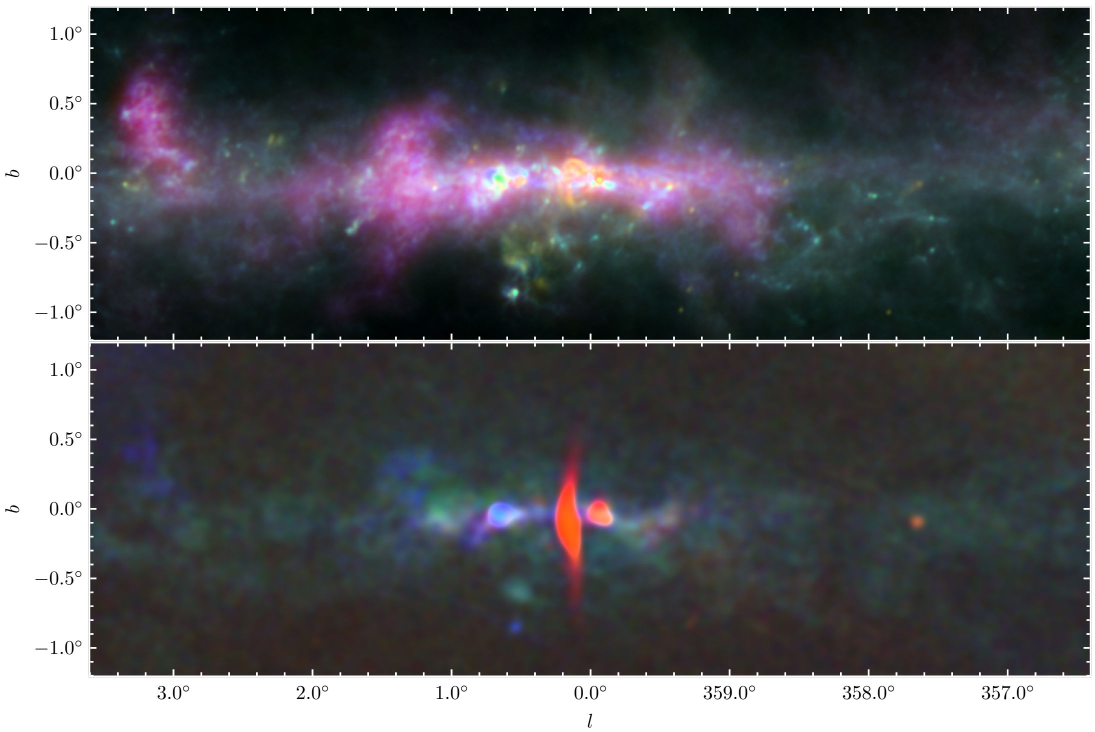

Figure 1.5: Composite maps of the Galactic center region made using data from ACT coadded with Planck data. Total intensity is shown on the top panel, while polarization intensity is shown on the bottom panel with the colors in each representing the 90 GHz (red), 150 GHz (green), and 220 GHz (blue) bands. Figure from [49].

millimeter emission within our galaxy. Figure 1.5 shows multi-frequency maps of the galactic center region made using ACT data coadded with Planck data in total intensity and polarization intensity. This combination of multi-band coverage and polarization sensitivity enabled us to probe the magnetic field structure and spatially varying emission mechanisms within the galactic center [49].

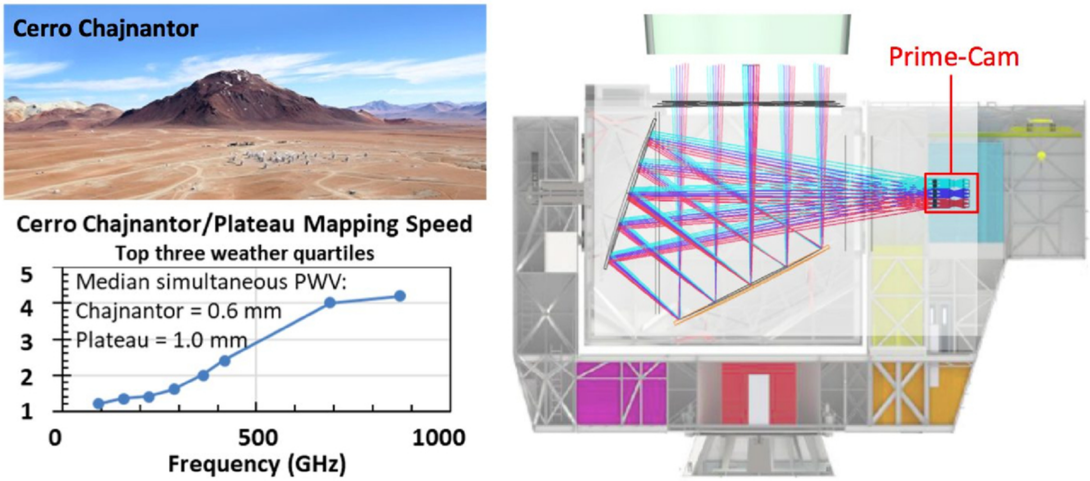

Figure 1.6: (Upper left) A view of Cerro Chajnantor, the site for FYST. (Lower left) The expected improvement in mapping speed as a function of frequency when compared to the nearby ALMA plateau. (Right) A cross-section of FYST with optics focused into the receiver cabin. Figure from [106].

1.4 CCAT & The Fred Young Submillimeter Telescope

The Fred Young Submillimeter Telescope (FYST[3]) is a six-meter aperture telescope being built by the CCAT collaboration[4] near the summit of Cerro Chajnantor in the Atacama Desert of northern Chile [21, 82]. At an elevation of 5600 meters, FYST will employ a modified off-axis, crossed-Dragone design [76], which offers a wide field-of-view and high throughput to take advantage of the exceptional atmospheric conditions. Figure 1.6 shows the site and optical designs for FYST, along with a plot of the anticipated improvement in mapping speed in comparison to the nearby ALMA plateau. Planned broadband, polarimetric surveys at five different frequency bands (220, 280, 350, 410, and 850 GHz) along with simultaneous spectroscopic surveys (with $R \sim 100$ from 210 to 420 GHz)

[3]Pronounced like "feast."

[4]CCAT is an international consortium including researchers from the USA, Canada, Germany, and Chile.

will take advantage of FYST's combination of wide field-of-view, a low emissivity telescope, and extraordinary atmospheric conditions [21]. FYST is scheduled to begin making observations in 2025.

1.4.1 Prime-Cam

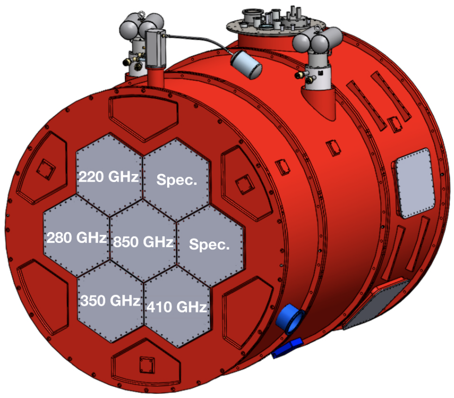

Figure 1.7: (Left) A model of the Prime-Cam cryostat with a potential instrument module configuration from [17]. (Left) Mod-cam, the first light receiver and module testbed, shown in lab from [107].

With FYST's unparalleled survey capabilities in the submillimeter, CCAT will target a diverse set of science goals in cosmology and far-infrared astronomy [21]. These include:

- Investigating the formation, growth, and large-scale structure of the first star-forming galaxies through spectroscopic intensity mapping of the redshifted [CII] line;
- Improving constraints on primordial gravitational waves and new particle species obtainable from observations of the cosmic microwave background (CMB) by characterizing signal-limiting foreground dust polarization across multiple wavelengths;

- Probing fundamental physics such as dark energy and the sum of the neutrino masses through the Sunyaev-Zel'dovich (SZ) effect;
- Revealing the effects of active galactic nuclei-star formation feedback in clusters by measuring the SZ signal for more than 1000 galaxy clusters;
- Tracing the history of dusty star formation by combining photometric measurements from CCAT-prime surveys with those made at optical and near-infrared wavelengths;
- Expanding our understanding of the variable millimeter and submillimeter sky across a wide range of time-scales through a combination of wide-area and focused surveys with high cadence.

Much of the first-generation science goals will be tackled by Prime-Cam[5] (shown in Figure 1.7), an instrument that has been previously detailed in [106]. Prime-Cam is a 1.8-m diameter cryostat that will host up to seven independent instrument modules spanning 220–850 GHz, each with a $\sim$1.3 degree field-of-view, allowing for the completion of simultaneous broadband and spectroscopic surveys [17].

1.4.2 280 GHz Instrument Module & Mod-Cam

As Prime-Cam will not be ready at first light, the first of the Prime-Cam instrument modules, the 280 GHz module, will be tested and deployed within Mod-Cam, a single module testbed for telescope commissioning and development of future modules. The 280 GHz instrument module will be used for both

[5] Additionally, a two-color heterodyne array receiver, CHAI (the CCAT-prime Heterodyne Array Instrument) will occupy 25% of FYST's observing time over the first five years of operation.

wide-field and small-field surveys and is populated with three independent, feedhorn-coupled detector arrays with a shared optical path. By capitalizing on advances in the fabrication of large format arrays of background-limited polarimeters [9, 12, 59], this first module will deploy ∼10,000 detectors on three hexagonally-tiled 15 cm wafers and will lay the foundation for the eventual 100,000+ detectors that will be deployed on Prime-Cam. Details of Mod-Cam and the 280 GHz instrument module can be found in [107].

1.5 Superconducting Detectors

When observing in the millimeter and sub-millimeter with a ground-based telescope such as FYST or ACT, detector technology has reached a point of maturity where the most significant gains can only be made by adding more detectors to our focal plane. Photon noise-limited performance has been achieved with superconducting transition edge sensors (TESes) [54, 56], however the readout requirements for these detectors is sufficiently complex as to be the limiting factor in total detector count [53, 55]. These complexities also create a significant cost and technology barrier for their use by smaller teams or instruments, though they have the benefit of being a proven technology with relatively mature understanding of on-sky performance.

In comparison, microwave kinetic inductance detectors (MKIDs or KIDs) similarly take advantage of the exquisite sensitivity that superconductivity allows, while also being naturally multiplexed in such a way as to significantly reduce complexity in both cold readout and fabrication. Because of this promise, all currently planned instrument modules for Prime-Cam will utilize MKIDs.

At the same time, MKIDs are substantially less mature in terms of deployment and our understanding of on-sky performance. While Prime-Cam's 280 GHz instrument module will not serve as the first on-sky demonstration of MKIDs [1, 71, 114], it will be the first deployment in a wide-field survey instrument and will be at an exceptional site, providing a critical demonstration of their sensitivity and performance in such a context. With all this in mind, the remainder of this thesis provides significant background and detail on the 280 GHz Instrument Module detectors and readout, much of which is also applicable to the 350 GHz Instrument Module and the rest of the Prime-Cam instrument.

CHAPTER 2

MICROWAVE KINETIC INDUCTANCE DETECTORS

Microwave Kinetic Inductance Detectors (MKIDs or KIDs) are a type of superconducting microwave resonator that detects light of a given frequency by coupling incident radiation to an absorbing inductive element. By taking advantage of the small gap energies associated with the superconducting transition and tuning the material and geometry of the detector to a desired use case, MKIDs can offer wide frequency coverage and dynamic range. In this chapter, we provide a brief overview of the key concepts behind MKIDs, including points from the theory of superconductivity and microwave network analysis. The treatment here is intended to provide all the information needed for modeling and fitting the responsivity and noise performance of an MKID both intrinsically and within a noisy environment, as well as understanding the underlying assumptions and where these models may fail. More specifically, we introduce the concepts needed to understand the Mattis-Bardeen equations for complex conductivity in the forms they are used to connect measurable resonator parameters to underlying concepts like gap energy, Δ, and quasiparticle number density, n_{qp} which vary as a function of bath temperature and incident power [41]. We start with some background information on complex conductivity followed by a description of the relevant concepts from superconductivity as they arise from the theory of Bardeen-Cooper-Schreiffer (BCS theory). Then we discuss the ideas from microwave resonators that are necessary to connect these concepts to MKIDs. Finally, we relate the equations from superconductivity to the responsivity and noise performance of MKIDs in response to the various pair-breaking mechanisms. For a more detailed discussion of the underlying physics of MKIDs, the author recommends [42]. For a more thorough treatment of the concepts from microwave network analysis, see [87].

2.1 Conductors & Complex Conductivity

Before discussing superconductors, it is useful to consider the case of a normal conductor in the Drude model and how kinetic inductance normally appears in the conductivity. In this model, the movement of electrons (or other charge carriers) through a lattice in response to an applied alternating electric field, $\vec{E}(\omega)$, gives rise to a local form of Ohm's Law [8]. This take the form

$$\vec{J}(\omega) = \sigma(\omega)\vec{E}(\omega), \tag{2.1}$$

where $\vec{J}(\omega)$ is the current density, ω is the angular frequency (related to the frequency, f, by $\omega = 2\pi f$), and $\sigma(\omega)$ is the conductivity. In the Drude model, $\sigma(\omega)$, is a complex function that captures the competition between free motion of the electrons and scattering events within the material, taking the form

$$\sigma(\omega) = \frac{\sigma_{dc}}{1 + j\omega\tau} = \sigma_1 - j\sigma_2\ . \tag{2.2}$$

In this equation, σ_{dc}, is the DC conductivity (e.g. when $\omega = 0$), τ is the mean scattering time, and j is defined by $j^2 = -1$.

Generally, we describe the real component of the conductivity, σ_1, as the resistive part and the imaginary component of the conductivity, σ_2, as the inductive part, because they respectively give rise to a energy dissipation and a phase lag between the current and the applied field. Moreover, the inductive component is referred to as the kinetic inductance, because it is an inductive term that arises purely from the inertia of the charge carriers. This is energy that gets stored in the motion of the charge carriers (i.e. kinetic energy). Alternatively, it may be useful to think of this as a phase delay that is caused by the finite time it takes to accelerate a massive particle.

When viewing Equation 2.1, it is easy to see why kinetic inductance is generally negligible and $\sigma_1 \gg \sigma_2$ for normal metals at room temperature. In this case, electron scattering times are extremely short, on the order of 10^{-14} s, and $\omega\tau \ll 1$ even for frequencies up to 10 GHz or more. Considering things in terms of energy, electrons in a normal metal are scattered too rapidly to effectively store energy in their motion. This makes for a material that is almost purely resistive. If we instead consider a case where the mean scattering time increases such that $\omega\tau \gg 1$, we have a material where $\sigma_2 \gg \sigma_1$ and the conductivity can be thought of as almost purely inductive. This is the case of the superconductor, which we consider in the following section.

2.2 Superconductivity

Superconductivity is sufficiently rich in both phenomenology and theory that it can be a daunting subject for the experimentalist whose primary interest is in using the detectors rather than studying the materials. In this section, we provide some rough context for the concepts and equations that pertain to MKIDs without delving into the microscopic BCS theory that would be required to derive them. For those interested in a more detailed understanding of the underlying theory, [104] is an excellent resource for general knowledge, while the previously mentioned [42] is a thorough treatment of how these equations arise from the microscopic theory.

2.2.1 Basic Phenomenology: Cooper Pairs & Quasiparticles

The defining traits of superconductors are the surprising absence of DC resistivity below a critical temperature, T_c, accompanied by the expulsion or exclusion of all static magnetic fields, otherwise known as the Meissner effect[1]. This can be understood in the context of BCS theory as arising from the pairing of conduction electrons with opposite spin and momentum into bosonic Cooper pairs that condense into the ground state around the Fermi level with zero net spin and momentum[2] [14]. In this paired state, Cooper pairs are then protected from scattering by an energy gap, 2Δ, which tends towards $2\Delta_0 = 3.528 k_B T_c$, with k_B being the Boltzmann constant[3], as the temperature T goes to 0. How is this possible?

The key is the attraction that arises between negatively-charged conduction electrons through perturbations in the positively-charged ion lattice, i.e. phonons. This phonon-mediated attraction between electrons is in opposition to their mutual repulsion through the Coulomb force and allows for the possibility of bound states. A simplified picture is that passing electrons create short-

[1]While the loss of DC resistance is perhaps more surprising, it's worth noting that the Meissner effect is the indicator that something beyond classical electrodynamics is occurring. The expulsion of existing magnetic fields is distinctly different from the expected behavior of a classical conductor with zero resistance, which would "freeze in" any existing magnetic flux.

[2]Two comments on the momentum states of conduction electrons versus Cooper pairs. There are two questions that quickly arise upon learning about the pairing of opposite momentum states. First, if the electrons have opposite momentum, how do they stay paired/do they break and reform with other partner electrons? Second, if the Cooper pair has zero net momentum, how do we get non-zero current? The answer to the first question is that they do stay paired, but it no longer makes sense to talk about the individual electrons, as they are now part of a new object, the Cooper pair. In essence, the electrons are continually scattering between the various available momentum states by exchange of virtual phonons, but always remaining in the ground state with zero net momentum. The answer to the second is that they need to have zero net canonical momentum, $\vec{p}$, which is $(m\vec{v} + e\vec{A}/c)$, where m is the mass, $\vec{v}$ is the velocity, e is the charge, $\vec{A}$ is the electromagnetic vector potential, and c is the speed of light. In the case of an applied field, where $|\vec{A}| > 0$, this implies non-zero $\vec{v}$.

[3]While I will try to be relatively consistent with writing k_B for the Boltzmann constant, there are also many equations where the subscript is dropped for convenience and I will just use k.

lived regions of positive charge by attracting nearby ions, which are slower to relax due to their much higher mass. These regions of positive charge attract nearby electrons. At higher temperatures, the thermal motions of lattice ions wash away any coherence to the perturbations of a single electron long before they can add up to overcome the repulsion. Below the critical temperature, T_c, the coherence length of these effects grows to overcome the repulsive interaction and create an energy gap or band gap.

If we think about this in the context of states available to electrons in the material, the positive interaction through phonon scattering takes single electron states around the Fermi energy and allows them to combine into paired states that have lower total energy. This effectively pushes those states around the Fermi energy and piles them up on both sides of the Fermi energy. The total gap in available states is 2Δ and is the cumulative effect of all the possible ways that a Cooper pair can scatter while remaining in the ground state. A consequence of this is that any unpaired electrons occupying available momentum states reduces the gap. The equation in the BCS theory that determines whether Δ exists and how large it is takes the form of a consistency equation, which can be used to numerically solve for $\Delta(T)$:

$$\frac{1}{N_0 V_{BCS}} = \int_0^{\hbar\omega_c} \frac{1 - 2f\{(E^2 + \Delta^2(T))^{\frac{1}{2}}\}}{(E^2 + \Delta^2(T))^{\frac{1}{2}}} \, dE \; . \tag{2.3}$$

The left side of this equation includes N_0, which is the single spin density of states at the Fermi energy, and V_{BCS}, (generally just called V) which is a potential energy that governs the interaction strength of electron-phonon scattering. On the right side, we are integrating over E, which is the single particle energy relative to the Fermi energy, from 0 (the Fermi level) to some cutoff value, $\hbar\omega_c$, where ω_c is the cutoff frequency[4]. The f seen in the numerator is the distribution

[4]This is usually taken to be on order of the maximum energy available to phonons (as limited

function, which in thermal equilibrium should be the Fermi-Dirac distribution. This would make the numerator $tanh\frac{1}{2}\beta(E^2+\Delta^2)^{\frac{1}{2}}$, where $\beta=(k_BT)^{-1}$. By solving this equation in the limits of $T=0$ and $T=T_c$, where the gap is Δ_0 and 0, respectively, we arrive at the previously mentioned result[5]

$$\Delta_0 = 1.76 k_B T_c\,. \tag{2.4}$$

The variation in the gap energy as a function of temperature is shown in Figure 2.1 for aluminum, taking $T_c = 1.2\ K$ and using a Debye temperature of 450 K. One important thing to notice about this plot is that even up to $0.5\ T_c$, the deviation in Δ from the maximum value at Δ_0 is still less than 5%. Considering the detectors for Prime-Cam generally operate around $0.1\ T_c$, this is the basis for later approximations where we assume the gap to be roughly constant at Δ_0, the value when $T=0$.

The superconducting state is suitably delicate that it can be broken not just by adding thermal energy, but also by surpassing a critical applied magnetic field, H_c, or by driving a strong enough current, I_c. There is a bit of nuance to the behavior of a superconductor in an applied magnetic field, as we further distinguish between type I superconductors, in which the superconducting state is extinguished above H_c, and type II superconductors, in which some magnetic penetration begins above a lower critical field, H_{c1}, and continuously increases up to a higher critical field, H_{c2} [104]. As one might expect, in type II super-

by the interatomic spacing), which is the Debye energy (frequently expressed in terms of the Debye frequency, ω_D, or the Debye temperature, Θ_D or T_D), however the actual value is not particularly sensitive to the cutoff so long as $\hbar\omega_c \gg \Delta_0$. This is particularly useful, since there is much contradiction in the available literature as to what the Debye energy of a particular material actually is in the low temperature limit.

[5]One thing to note is that there are approximations being taken in this calculation that can push the gap away from the canonically quoted value of $2\Delta_0 = 3.52 k_B T_c$. Real-world measurements of the gap energy have generally shown $2\Delta_0/k_BT_c$ to be between 3 and 4.5, so this result has been rightly seen as a great success of BCS theory, but the numerical precision should not be overstated.

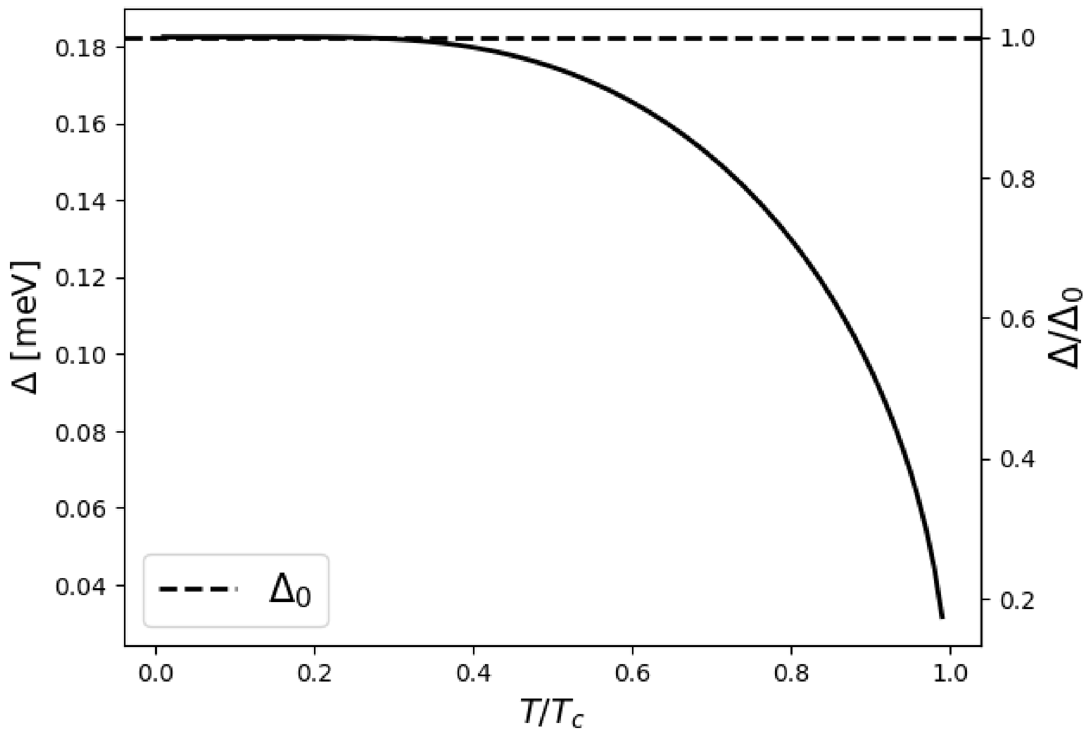

Figure 2.1: The gap energy Δ as a function of normalized or reduced temperature (T/T_c) for aluminum, using $T_c = 1.2\ K$. The behavior of the gap (without accounting for external pair-breaking) is the same for any standard BCS superconductors, and can be scaled by Δ_0, as shown on the right-side axis.

conductors, the superconducting state is continuously diminished between H_{c1} and H_{c2} and fully extinguished above H_{c2}. This intermediate state magnetic flux penetration occurs in quantized flux tubes, called vortices, within which the material is in a quasi-normal state. As is shown in section 2.2.3, this is all somewhat complicated in the case of thin films.

2.2.2 Quasiparticle Generation & Recombination

While Cooper pairs enable the qualitatively unique aspects of superconductors, at finite temperature there also exists a population of unpaired conduction electrons generated by excitations out of the Cooper pair state called quasiparticles[6]. These quasiparticles give rise to some amount of loss in response to AC fields, as well as non-zero surface resistance. Within MKIDs, the three mechanisms for generating quasiparticles include thermal excitation, pair-breaking photon absorption at frequencies, ω, where $\hbar\omega \geq 2\Delta$, and microwave photon absorption from the readout system where $\hbar\omega < 2\Delta$.

The total quasiparticle density can be calculated using the equation

$$n_{qp} = 4\int_{\Delta}^{\infty} N_s(E,\Delta)f(E)dE \tag{2.5}$$

where $f(E)$ is the distribution function (which may deviate non-negligibly from Fermi-Dirac) and N_s is the modified BCS quasiparticle density of states:

$$N_s(E,\Delta) = \frac{N_0 E}{\sqrt{E^2 - \Delta^2}} \; . \tag{2.6}$$

We also have a factor of 4 in Equation 2.5 from counting both electron and hole excitations.

In all cases, this integral is dominated by quasiparticles with energies near the gap (generally for MKIDs, this means within a factor of a few times $\hbar\omega$, where ω is the microwave readout frequency). Taking the limit of $T = T_c$ with $f(E)$ as the standard Fermi-Dirac distribution function, we can calculate the total number of available quasiparticles per unit volume to be

$$n_{qp} = 2N_0 k_B T_c \ln 2 \; . \tag{2.7}$$

[6]A quick note on the term quasiparticle in this context for the curious or pedantic. You may be familiar with the concept of a quasiparticle from the standard free electron theory of solids, where the interactions between the cation lattice and conduction electrons can be captured by replacing the mass of the electron, m_e, with an effective mass, μ_e, but the same charge as the electron [8]. This is slightly different from that case, in that excitations are not just about the electrons having a modified mass, but also being in linear combinations with positively-charged holes in the Fermi sea [104]. The holes states are important for conductivity and dissipation in particular, because their opening allows for unpaired electrons below the Fermi energy to also participate in conduction. You may also see these referred to as Bogoliubov quasiparticles (or even in some places as Bogoliubons). Fortunately, none of these details are important for our purposes.

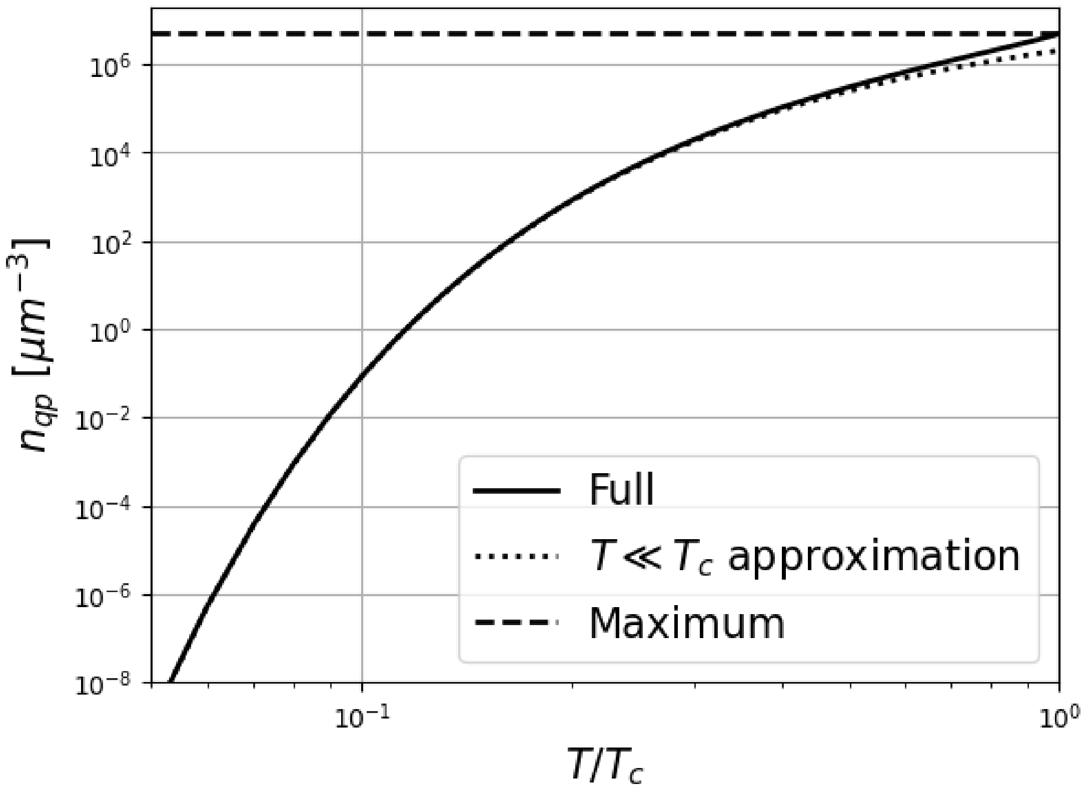

Figure 2.2: The quasiparticle density, n_{qp}, as it varies with the reduced temperature for aluminum (using $N_0 = 1.72\text{x}10^{10}\ eV^{-1}\mu m^{-3}$) calculated using Equation 2.5. The dotted line shows the low-temperature approximation from Equation 2.8 and the dashed line shows maximum attainable quasiparticle density at T_c.

If we consider only thermal quasiparticles at low temperatures ($< 0.2\,T_c$), we can approximate Equation 2.5 with the expression

$$n_{qp}(T) = 2N_0\sqrt{2\pi k_B T \Delta_0}e^{-\Delta_0/k_B T}\ . \tag{2.8}$$

One occasionally important thing to consider, as has been discussed elsewhere [60] is that Equation 2.8 systematically underestimates n_{qp}, which can be important to account for if using thermal response to calibrate for optical response. The quasiparticle density as a function of T/T_c is shown in Figure 2.2.

If we now consider the case of incident photons with $\hbar\omega \geq 2\Delta$, we generate quasiparticles at a rate that depends on the total power absorbed (P_{abs}), the volume of the absorbing region (V), the ratio of the photon energy to the gap energy, and the quantum efficiency of pair-breaking (η_{ph}). Expressed as a time derivative, this is:

$$\frac{dn_{qp}}{dt} = \frac{\eta_{ph} P_{abs}}{V\Delta} \,. \tag{2.9}$$

Here, the total power absorbed, P_{abs}, is after any optical efficiencies, polarization selection, and detector coupling efficiencies have been accounted for, in other words, how much power is making it into the detector volume. The quantum efficiency, η_{ph}, describes how much of the energy actually goes into pair-breaking. This has been discussed in detail by in [52] in the context of calculating expected efficiencies across a wide range of values for $\hbar\omega/\Delta$. For the detectors and photon energies used in the 280 GHz and 350 GHz instrument modules, this efficiency is expected to be roughly $0.4 - 0.6$. Importantly, some of the excess energy goes into driving the quasiparticles into a nonequilibrium distribution, which has been measured experimentally [30]. This impacts n_{qp} through $f(E)$ in the full integral, and leads to increased dissipation.

A similar story of quasiparticle "heating" can be applied to microwave photon absorption from readout tones. In that case, the additional energy injected into the quasiparticle population can, after multiple absorptions, reach energies of more than twice the gap ($> 4\Delta$). Upon decaying back down towards the gap energy, these can release phonons with enough energy to break a Cooper pair. At the same time, interactions between the microwave probe tones and the quasiparticle-phonon system can, in certain cases, lead to quasiparticle "cooling" by increasing the quasiparticle recombination rate. This has been measured and discussed in [29] and has been observed to cause counter-intuitive behavior in our aluminum 280 GHz witness pixels, as discussed in Chapter 3. For the purposes of this chapter, we ignore this method of quasiparticle generation, as it is significantly subdominant to the effect of optical pair-breaking photons.

Turning our attention back to Equation 2.9, in order to turn this into an excess quasiparticle population, we need an estimate of the quasiparticle lifetime, τ_{qp}, but this is complicated by the interplay between the pair-breaking rate, the gap energy, and existing quasiparticle density. One empirically successful description of this lifetime, given in [119], is

$$\tau_{qp} = \frac{\tau_{max}}{1 + n_{qp}/n^*} \tag{2.10}$$

where n^* is the crossover density, which is generally observed to be $\sim 100\ \mu m^{-3}$ [119] for many materials. The maximum observed quasiparticle lifetime, τ_{max}, is measured to be be between $100 - 1000\ \mu s$ for many relevant materials. While the underlying physics limiting τ_{max} is not well understood, the general decrease in τ_{qp} with increasing n_{qp} can be understood as arising from the increased availability of both hole states and potential partners for pairing and seems to be somewhat broadly applicable even away from thermal equilibrium.

If we take this implied recombination rate and use it in the context of the full generation-recombination equation (which is just assuming a steady state, i.e. that the the recombination rate matches the combined thermal and pair-breaking generation rates), we can derive a more complete expression for total n_{qp} [94, 119]:

$$n_{qp}(T, \Gamma) = \sqrt{(n_{th}(T)^2 + n^*)^2 + 2\Gamma\tau_{max}n^*/V} - n^* \ . \tag{2.11}$$

Here $n_{th}(T)$ is accounting for thermally-generated quasiparticles (i.e. evaluating Equation 2.5 using the Fermi-Dirac distribution and with the gap shifted from its thermal value to account for additional pair-breaking), while $\Gamma(P_{abs}, P_{read})$ is

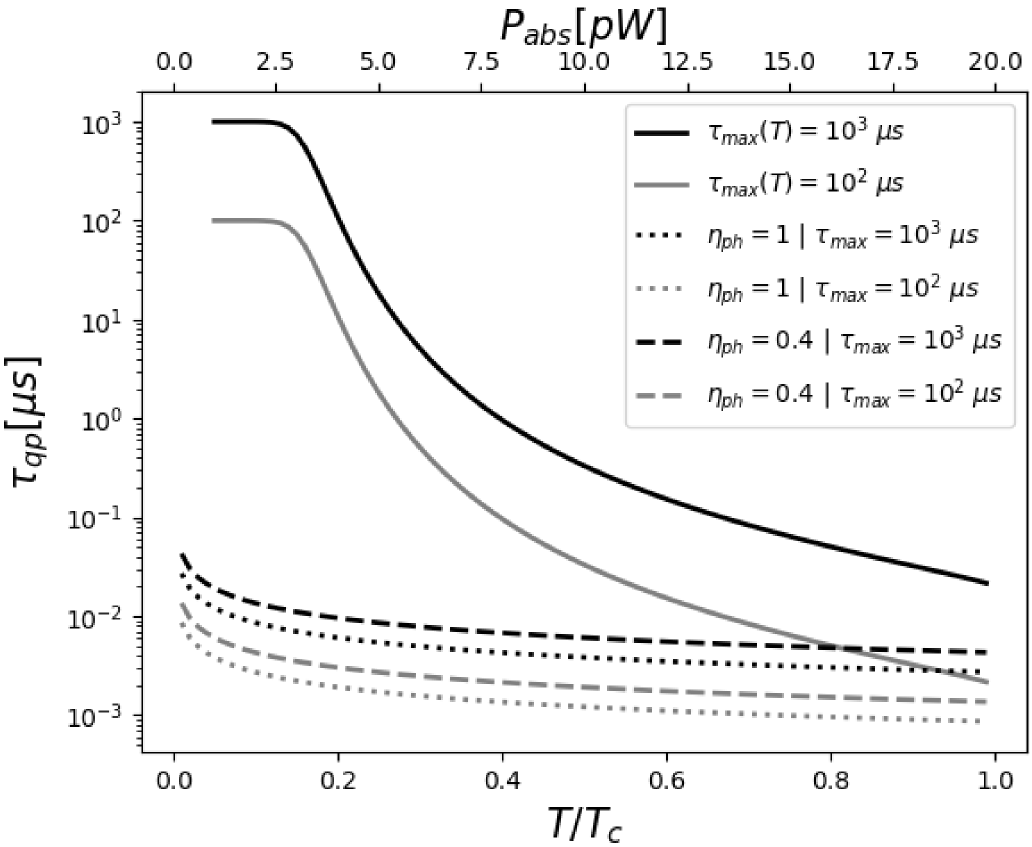

Figure 2.3: Quasiparticle lifetimes for two common values of τ_{max}, using $n^* = 100\ \mu m^{-3}$. Solid lines correspond to thermally-sourced quasiparticles in aluminum (using $N_0 = 1.72\text{x}10^{10}\ eV^{-1}\mu m^{-3}$ and $T_c = 1.2$ K and calculated from Equation 2.10), while dotted (dashed) lines correspond to absorbed photon loading from 0-20 pW (calculated using Equation 2.12 with $\eta_{ph} = 1\ (0.6)$, $T = 100$ mK, and a total absorber volume of $\sim\ 100\ \mu m^3$). Increasing the volume dilutes the optical quasiparticles, leading to an increase in τ_{qp}, which is a similar effect to decreasing η_{ph}.

the combined generation rate from optical photon absorption and microwave readout photon absorption. If we take the reasonable limit for MKID operation where n_{qp} is dominated by optically-generated quasiparticles (i.e. $n_{th} \ll n_{qp}$ and $\hbar\omega \ll \Delta$, where ω is the readout frequency), then Equation 2.10 approximates to

$$\tau_{qp} = \frac{\tau_{max}}{\sqrt{1 + 2\Gamma(P_{abs})\tau_{max}/N^*}}, \tag{2.12}$$

where $N^*/V = n^*$. Figure 2.3 shows the implied τ_{qp} for multiple values of τ_{max}

in the case of only thermally-generated quasiparticles, as well as under optical loading conditions similar to what might be expected for the 280 GHz instrument module. One important takeaway is that operating in the pair-breaking dominated regime tends to keep quasiparticle lifetimes several orders of magnitude lower than they would be otherwise.

2.2.3 Penetration Depth & Thin Films

Before discussing the complex conductivity of a thin film, it is important to specify what we mean when we take the thin film limit. In brief, a thin film is one whose thickness, d, is much less than either the penetration depth, λ, or the coherence length, ξ_0[7], which can be thought of as the sphere of influence or effective size of Cooper pairs. This means that the magnetic field fully penetrates the film and the current density throughout is roughly constant. These conditions also add up to being able to take the local (or dirty) limit rather than needing to apply the full nonlocal version of the theory. Essentially, the mean free path, l of an electron is dominated by surface scattering and much smaller than it would be in a bulk sample. This also has the interesting effect that a type I superconductor behaves as a type II superconductor in the context of a thin film[8].

The penetration depth, λ, is the distance over which a magnetic field is exponentially screened. This must occur at some scale, so as to be consistent with Maxwell's equations, and was predicted as a product of the London equations,

[7] The coherence length, ξ_0, can be estimated as $\xi_0 = \hbar v_F / \pi \Delta_0$, where v_F is the Fermi velocity.

[8] This is because the parameter that sets the type behavior of a superconductor is $\kappa = \lambda/\xi$, which is the ratio of the penetration depth (λ) to the coherence length (ξ). For $\kappa > 1/\sqrt{2}$, we have a type II superconductor. This applies for thin films as both λ and ξ are limited by the thickness of the film.

a quite successful early phenomenological model for superconducting electrodynamics that preceded the development of BCS theory. In the London theory, we have the following equation [104]

$$\lambda_L = \sqrt{\frac{mc^2}{4\pi n_s e^2}} \geq \lambda_L(0) = \sqrt{\frac{mc^2}{4\pi n e^2}} \tag{2.13}$$

where n_s is the number density of electrons in the superconducting state, n is the total number density of conduction electrons, and e and m are the charge and the mass of the electron respectively. In this way, $\lambda_L(0)$ (or λ_{L0}) serves as the lower bound on the penetration depth at $T = 0$, when all available electrons are expected to be in the superconducting state. Moreover, through the dependence on n_s, λ_L has a temperature dependence that diverges as T approaches T_c. For many real materials, λ_{L0} is predicted to be in the range of 20 nm, though nonlocal electrodynamics tend to drive λ to values of 500 nm. In fact, in the local limit (which is formally when $l \ll \lambda_{L0}$ or $\xi_0 \ll \lambda_{L0}$), the penetration depth λ_{local} can be written as $\lambda_{local} \approx 105$ nm x $\sqrt{\rho_n[\mu\Omega cm]/T_c[K]}$ [119], where ρ_n is the normal-state resistivity. This is enhanced even further for thin films, where the effective penetration depth, λ_{eff}, varies inversely as the square of the film thickness or roughly λ_{local}^2/d [42]. For the types of detectors being used for Prime-Cam, the film thickness, d, is approximately $20\ nm$, which, as calculated for Al thin films in [42], yields $\lambda_{eff} \approx 1000$ nm.

2.2.4 Complex Conductivity: Mattis-Bardeen Theory

Now that we have a sense of how these two populations of quasiparticles and Cooper pairs arise, we can discuss how they contribute to the complex conductivity of the superconducting thin film following the analysis from [42]. It is helpful to approach this system in what is referred to as the two-fluid model of conductivity, which assumes the conductivity can be thought of as a sum of the response of normal (quasiparticle, n_{qp}) and superconducting (Cooper pair, n_s) components [46]. When applying an AC electromagnetic field, the normal component, which is to say the unpaired electrons under the guise of quasiparticles, predominantly acts in a dissipative or resistive manner as penetrating fields drive their motion and turns some fraction of the input energy to heat. At the same time, the superconducting electrons act in an almost purely reactive or inductive capacity, storing energy and introducing a lag in the phase. This leads to the expression

$$\sigma(\omega) = \sigma_1 - j\sigma_2 = \frac{n_{qp}e^2\tau}{m} - j\frac{n_s e^2}{\omega m} \tag{2.14}$$

where $\omega = 2\pi f$ is the angular frequency of the electric field.

By applying the BCS theory to a superconductor in an AC field, Mattis and Bardeen yielded equations relating the normal state conductivity, σ_n, to the two components of the complex conductivity in the thin film, local limit of a superconductor at temperature T. These take the following forms:

$$\begin{aligned}\frac{\sigma_1}{\sigma_n} =& \frac{2}{\hbar\omega}\int_{\Delta}^{\infty} \frac{[f(E) - f(E+\hbar\omega)](E^2 + \Delta^2 + \hbar\omega E)}{\sqrt{(E^2 - \Delta^2)[(E+\hbar\omega)^2 - \Delta^2]}} dE \\ &+ \frac{1}{\hbar\omega}\int_{min(\Delta-\hbar\omega,-\Delta)}^{-\Delta} \frac{[1 - 2f(E+\hbar\omega)](E^2 + \Delta^2 + \hbar\omega E)}{\sqrt{(E^2 - \Delta^2)[(E+\hbar\omega)^2 - \Delta^2]}} dE\end{aligned} \tag{2.15}$$

$$\frac{\sigma_2}{\sigma_n} = \frac{1}{\hbar\omega}\int_{max(-\Delta,\Delta-\hbar\omega)}^{\Delta} \frac{[1 - 2f(E+\hbar\omega)](E^2 + \Delta^2 + \hbar\omega E)}{\sqrt{(\Delta^2 - E^2)[(E+\hbar\omega)^2 - \Delta^2]}} dE \tag{2.16}$$

where f once again corresponds to the distribution function[9]. When $\hbar\omega < \Delta$, as

[9]We are also quietly assuming in this version of the equations that we have the equilibrium density of states, though this is not necessarily always the case as discussed in [27, 67, 119].

is the case for microwave readout frequencies, the second term in σ_1 can be discarded, but it is included here for completeness, since it does become significant for incident photons of higher frequencies. In thermal equilibrium, these are straightforward to calculate uisng the Fermi-Dirac distribution, but in the presence of external pair-breaking (i.e. from an incident flux of photons), we must account for that additional term in our distribution function. This is generally done by adding an effective chemical potential, μ^*, as described in [41] based on the treatment of Owens and Scalopino [79].

In this formalism, the Fermi-Dirac distribution is modified to

$$f(E, \mu^*, T) = \frac{1}{1 + e^{\frac{E-\mu^*}{k_B T}}} \,. \tag{2.17}$$

Accounting for this, we can gather each of the necessary equations for n_{qp}, Δ, σ_1, and σ_2 (2.5, 2.3, 2.15, and 2.16, respectively) and insert $f(E, \mu^*, T)$ as our distribution function. This leaves us with four equations and four variables (T, μ^*, n_{qp}, and Δ), as well as four parameters[10] (N_0, T_c, ω, and σ_n). Now, as we are interested in finding what happens to these terms when changing either temperature or optical power, we make a few additional assumptions and look to a few cases that are relevant.

First, we make the assumptions that we are well below the transition, which is to say $kT \ll \Delta$, and that we are probing our superconductor at a frequency well below that required for pair-breaking ($\hbar\omega \ll \Delta$). Both of these are most certainly the case for MKIDs in operation. The third assumption we make is that $e^{-\frac{E-\mu^*}{k_B T}} \ll 1$. This is a bit less obvious, but can be easily verified by even rough estimates of n_{qp} with millimeter to submillimeter photons. Under these

[10]These are the parameters for the thin film response only, though you may also consider other parameters such as the resonator volume or detector efficiency. I'm not including them here as these are not fundamental to determining the interplay between these equations.

assumptions, the previous equations simplify to the following.

$$n_{qp}(T) = 2N_0\sqrt{2\pi k_B T\Delta}e^{-\frac{\Delta-\mu^*}{k_B T}} \tag{2.18}$$

$$\frac{\Delta}{\Delta_0} = 1 - \sqrt{\frac{2\pi k_B T}{\Delta}}e^{-\frac{\Delta-\mu^*}{k_B T}} = 1 - \frac{n_{qp}}{2N_0\Delta} \tag{2.19}$$

$$\frac{\sigma_1}{\sigma_n} = \frac{4\Delta}{\hbar\omega}e^{-\frac{\Delta-\mu^*}{k_B T}} sinh(\xi)K_0(\xi) \tag{2.20}$$

$$\frac{\sigma_2}{\sigma_n} = \frac{\pi\Delta}{\hbar\omega}[1 - 2e^{-\frac{\Delta-\mu^*}{k_B T}} e^{-\xi} I_0(\xi)] \tag{2.21}$$

Here, $\xi = \frac{\hbar\omega}{2k_B T}$, and K_n and I_n are the nth order modified Bessel functions of the first and second kind respectively. Now we can further consider two relevant cases and the resulting shift in σ.

Thermal Response of Complex Conductivity

Let us take the above equations and allow T to vary independently, while fixing $\mu^* = 0$. In this case, to first order we wind up with the following system of equations:

$$n_{qp}(T) = 2N_0\sqrt{2\pi k_B T\Delta_0}e^{-\frac{\Delta}{k_B T}} \tag{2.22}$$

$$\frac{\sigma_1(T)}{\sigma_n} = \frac{4\Delta_0}{\hbar\omega}e^{-\frac{\Delta_0}{k_B T}} sinh(\xi)K_0(\xi) \tag{2.23}$$

$$\frac{\sigma_2(T)}{\sigma_n} = \frac{\pi\Delta_0}{\hbar\omega}\left[1 - \sqrt{\frac{2\pi k_B T}{\Delta_0}}e^{-\frac{\Delta_0}{k_B T}} - 2e^{-\frac{\Delta_0}{k_B T}} e^{-\xi} I_0(\xi)\right] . \tag{2.24}$$

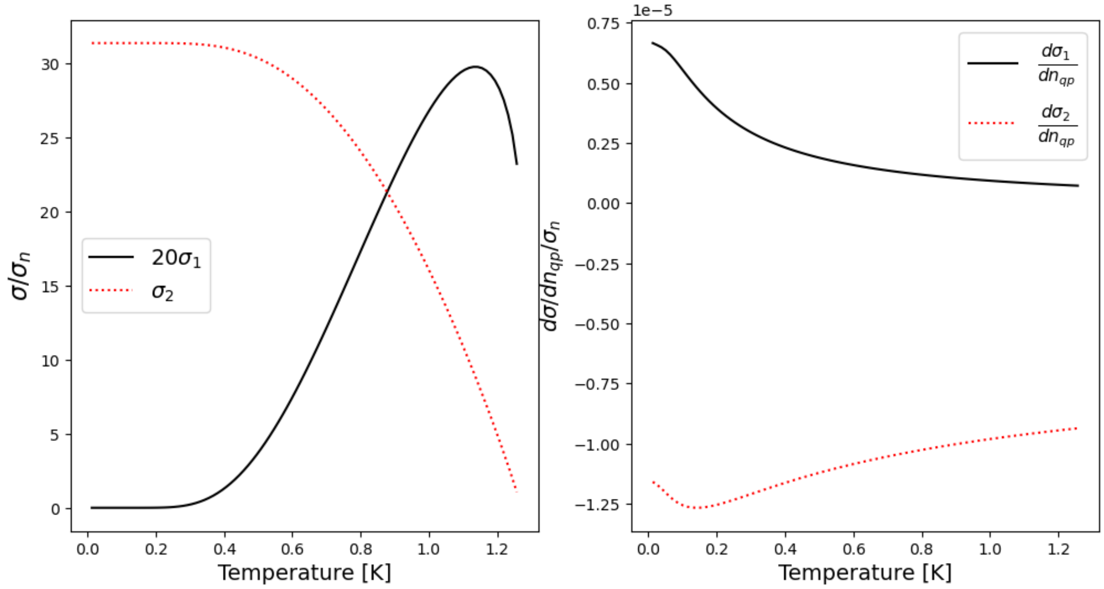

Figure 2.4: (Left) Real and imaginary components of complex conductivity (normalized by σ_n) as a function of bath temperature for aluminum with T_c = 1.28 K. The real component is multiplied by a factor of 20 to make it visible on the same scale. (Right) The change in the complex conductivity in response to a change in quasiparticle number density as a function of bath temperature (once again normalized by σ_n. Both figures are inspired by [42].

Furthermore, the change in conductivity as a result of the shifting quasiparticle density is approximately

$$\frac{d\sigma_1}{dn_{qp}} = \sigma_n \frac{1}{N_0 \hbar \omega} \sqrt{\frac{2\Delta_0}{\pi k_B T}} sinh(\xi) K_0(\xi) \left[\frac{\frac{\Delta_0}{k_B T} - \xi \frac{cosh\xi}{sinh\xi} + \xi \frac{K_1(\xi)}{K_0(\xi)}}{\frac{\Delta_0}{k_B T} + \frac{1}{2}} \right] \tag{2.25}$$

$$\frac{d\sigma_2}{dn_{qp}} = \sigma_n \frac{-\pi}{2N_0 \hbar \omega} \left[1 + \sqrt{\frac{2\Delta_0}{\pi k_B T}} e^{-\xi} I_0(\xi) \frac{\frac{\Delta_0}{k_B T} + \xi - \xi \frac{I_1(\xi)}{I_0(\xi)}}{\frac{\Delta_0}{k_B T} + \frac{1}{2}} \right] . \tag{2.26}$$

Figure 2.4 shows σ_1, σ_2, $\frac{d\sigma_1}{dn_{qp}}$ and $\frac{d\sigma_2}{dn_{qp}}$ as a function of bath temperature from equations 2.23, 2.24, 2.25, and 2.26.

Excess Pair-Breaking Response of Complex Conductivity

Now shifting to the situation where we are only interested in the response from excess pair-breaking, we choose n_{qp} as an independent variable, along with T and use this to eliminate the explicit dependence on μ^*. This leads to equations of the following form:

$$\frac{\sigma_1(n_{qp},T)}{\sigma_n} = \frac{2\Delta_0}{\hbar\omega}\frac{n_{qp}}{N_0\sqrt{2\pi k_B T\Delta_0}}sinh(\xi)K_0(\xi) \tag{2.27}$$

$$\frac{\sigma_2(n_{qp},T)}{\sigma_n} = \frac{\pi\Delta_0}{\hbar\omega}\left[1 - \frac{n_{qp}}{2N_0\Delta_0}\left(1 + \sqrt{\frac{2\Delta_0}{\pi k_B T}}e^{-\xi}I_0(\xi)\right)\right] . \tag{2.28}$$

Once again we can look at the derivative terms, and we find something that looks quite similar to the previous result:

$$\frac{d\sigma_1}{dn_{qp}} = \sigma_n\frac{1}{N_0\hbar\omega}\sqrt{\frac{2\Delta_0}{\pi k_B T}}sinh(\xi)K_0(\xi) \tag{2.29}$$

$$\frac{d\sigma_2}{dn_{qp}} = \sigma_n\frac{-\pi}{2N_0\hbar\omega}\left[1 + \sqrt{\frac{2\Delta_0}{\pi k_B T}}e^{-\xi}I_0(\xi)\right] . \tag{2.30}$$

This is nearly the same response in the complex conductivity as seen in the thermal response, save for some additional terms that can be calculated to be quite close to unity for the cases that we consider here. As discussed in [41] and demonstrated in [60], this can be seen as a demonstration of the equivalent response in MKIDs to both thermal and optically-generated quasiparticles. Now, we can move away from the pure theory side of things and get a bit closer to discussing the operating principles behind MKIDs.

2.3 Microwave Resonators & S-Parameters

At this point, it is worth stepping aside from the realm of superconductivity and providing some context for why we are focusing on the complex impedance. The short-ish answer is because it is directly measurable in the form of the surface impedance, Z_s, which is measured near resonance by making the superconducting film into a LC resonator and coupling it to a microwave feedline. In this section, we discuss how and what we can actually measure about the resonators in preparation for the following discussion of MKID parameters, responsivity, and noise.

2.3.1 Preliminaries: Microwave Networks & S-parameters

When we want to measure a circuit, we commonly take a look at the scattering parameters or S-parameters. The S-parameters describe the behavior of a circuit based on its response to inputs at the two ends. The one that we are most interested in is S_{21}, which is defined as

$$S_{21} = \frac{V_2}{V_1} \tag{2.31}$$

where V_i corresponds to the voltage measured on the ith port. And more generally:

$$S_{ij} = \frac{V_i}{V_j}$$

A generic description of the two-port S-parameters defines them as such:

- S_{11} is the reflection on the input port.
- S_{12} is the reverse voltage gain (i.e. the gain from an output port signal seen on the input port).

- S_{21} is the forward voltage gain (i.e. the gain from an input port signal seen on the output port).
- S_{22} is the reflection on the output port.

These are measuring quadrature signals, meaning that they contain both amplitude and phase information, and, as such, we employ phasor notation where necessary. Thus a voltage signal, $V(t)$, can be written as

$$V(t) = Re\left[|V(t)|e^{j\omega t}\right] \tag{2.32}$$

where ω is the frequency of the measurement tone. For microwave networks, it is most useful to describe the propagation of signals and the chaining of elements in terms of S-parameters and impedances. Each element transmits, reflects, or dissipates some parts of the incident signal in accordance with its relative impedance. Of particular relevance for us is the case of a signal propagating past a shunt impedance (essentially a coupled circuit element that can draw power away from primary network path in a system-dependant manner). This can be worked out to be:

$$S_{21} = 1 - \frac{1}{1 + 2Z_r/Z_0} \tag{2.33}$$

where Z_0 is the characteristic impedance of the microwave feedline (typically 50 Ω) and Z_r is the shunt impedance. If we take a resonator and couple it to our feedline capacitively, then we have our example of a shunt impedance.

2.3.2 Resonant Circuits & Quality Factors

Resonators have three basic parameters that you can observe from a frequency sweep: the resonant frequency f_0, the total quality factor Q, and the dip depth,

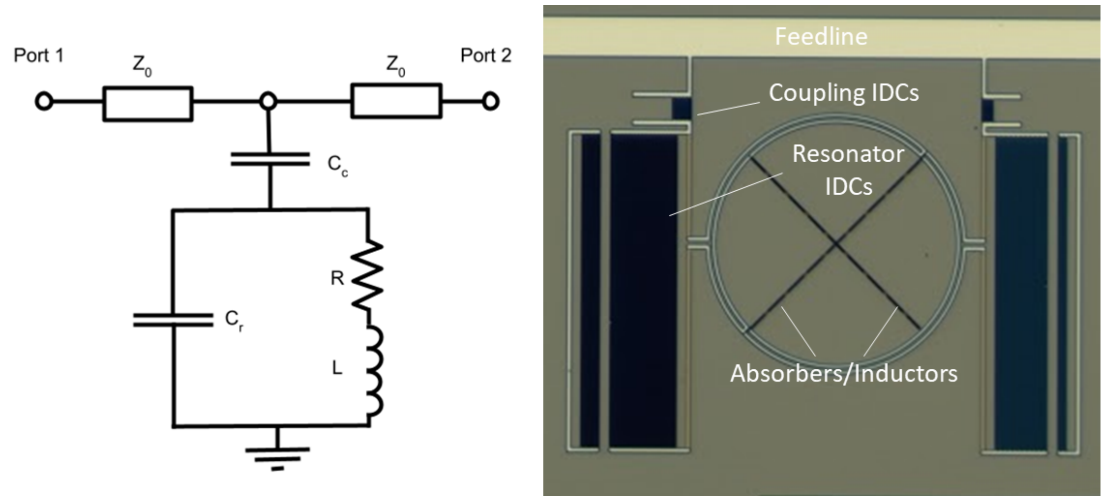

Figure 2.5: (Left) A circuit diagram of a single capacitively-coupled resonator with inductance L, resistance R, capacitance C_r, coupling capacitance C_c, and line impedance Z_0. (Right) A polarization-sensitive kinetic inductance detector pixel, containing two equivalent resonators.

D, which is related to the ratio of the coupling quality factor, Q_c (which we'll define shortly), to the total quality factor as

$$D = 20\log_{10}(1 - \frac{Q}{Q_c}) \, . \tag{2.34}$$

Additionally there are several parameters that come from the readout circuit and the previously-mentioned coupling quality factor (which may be complex and written as either Q_c or Q_e) that quantifies how the resonator is coupled to the circuit.

Thinking about the resonant parameters more concretely, f_0 is the frequency at which energy transfer from the circuit to the resonator is most effective and impedance is at a minimum. Given a known circuit, as in Figure 2.5, this is given by

$$\omega_0 = 2\pi f_0 = \frac{1}{\sqrt{LC}} = \frac{1}{\sqrt{L(C_r + C_c)}} \, . \tag{2.35}$$

The quality factor, Q, describes the ratio of energy stored to energy dissipated over the course of a cycle, as well as describing the resonator width in frequency space:

$$Q = \frac{f_0}{\Delta f} \tag{2.36}$$

where Δf is the resonator bandwidth (a particularly useful term when we look at the frequency domain transfer function of a resonator). For a coupled resonator, we break up the total resonator Q into the internal quality factor Q_i and coupling quality factor, Q_c, or, more generally, the external quality factor, Q_e, with values being added much like parallel resistances:

$$\frac{1}{Q} = \frac{1}{Q_i} + \frac{1}{Q_c} = \frac{1}{Q_i} + Re\left(\frac{1}{Q_e}\right) . \tag{2.37}$$

Since the Qs are inversely proportional to the loss, we can intuitively make sense of this inverse addition by realizing that we are essentially adding the loss terms together with a shared total energy. The internal quality factor can be described by that element's impedance, Z_L,

$$Q_i = \frac{Im\{Z_L\}}{Re\{Z_L\}} = \frac{\omega_0 L_{total}}{R_{eff}} \tag{2.38}$$

with the final term here being specific to a capacitively-coupled resonator with total inductance L_{total} and effective resistance R_{eff} [67]. Lastly, the coupling quality factor, Q_c, in the capacitively-coupled case can be described as follows

$$Q_c = \frac{2(C_r + C_c)}{\omega_0 C_c^2 Z_0} \tag{2.39}$$

with C_r being the resonator capacitance and C_c being the coupling capacitance [67].

The external and coupling quality factors are not precisely equal, but in the case of a well-behaved circuit, they are generally nearly identical. The difference is that, while Q_c is only describing energy lost to the coupling circuit, Q_e

also includes any other energy dissipated externally to the resonator itself and any added phase response, including through impedance mismatches. As such, Q_e is a complex quantity, while using Q_c alone requires an additional asymmetry parameter to account for additional phase rotations due to impedance mismatches [61].

When we take an S_{21} trace near resonance, the equation that we are effectively measuring as a function of frequency $\omega = \omega_0(1+x)$ is [36, 67]

$$\begin{aligned} S_{21} &= 1 - \frac{1+j\epsilon}{1+j\epsilon\frac{Q}{Q_c}}\frac{Q}{Q_c}\left[\frac{1}{1+2jQx/(1+j\epsilon\frac{Q}{Q_c})}\right] \\ &\approx 1 - \frac{Q}{Q_c}\frac{1}{1+2jQx} \end{aligned} \tag{2.40}$$

where ϵ is an asymmetry parameter. When accounting for the environmental factors, one needs to fit for something of the form

$$S_{21} = A(\omega)e^{j\theta(\omega)}\left(1 - \frac{Q}{Q_e}\frac{1}{1+2jQx}\right) \tag{2.41}$$

where $A(\omega)e^{j\theta(\omega)}$ is a frequency-dependent complex normalization. Depending on how widely you are sweeping and how well matched your readout network is, you may be able to account for the environment with a constant complex normalization term, but more generally you want something with additional parameters such as [87]

$$A(\omega)e^{j\theta(\omega)} = \sqrt{A + B\delta f}\, e^{-i(2\pi\delta f\tau + \theta_0)} \tag{2.42}$$

where A, B, τ, and θ_0 are fit parameters and δf is a way of capturing the frequency-dependence from some convenient offset (usually the starting frequency or the resonant frequency). Figure 2.6 shows a simulated resonator both before and after accounting for a cable term such as the above. For a more detailed derivation of some of these expressions in the context of capacitively coupled resonators, good resources are Appendix A of [77] as well as [61].

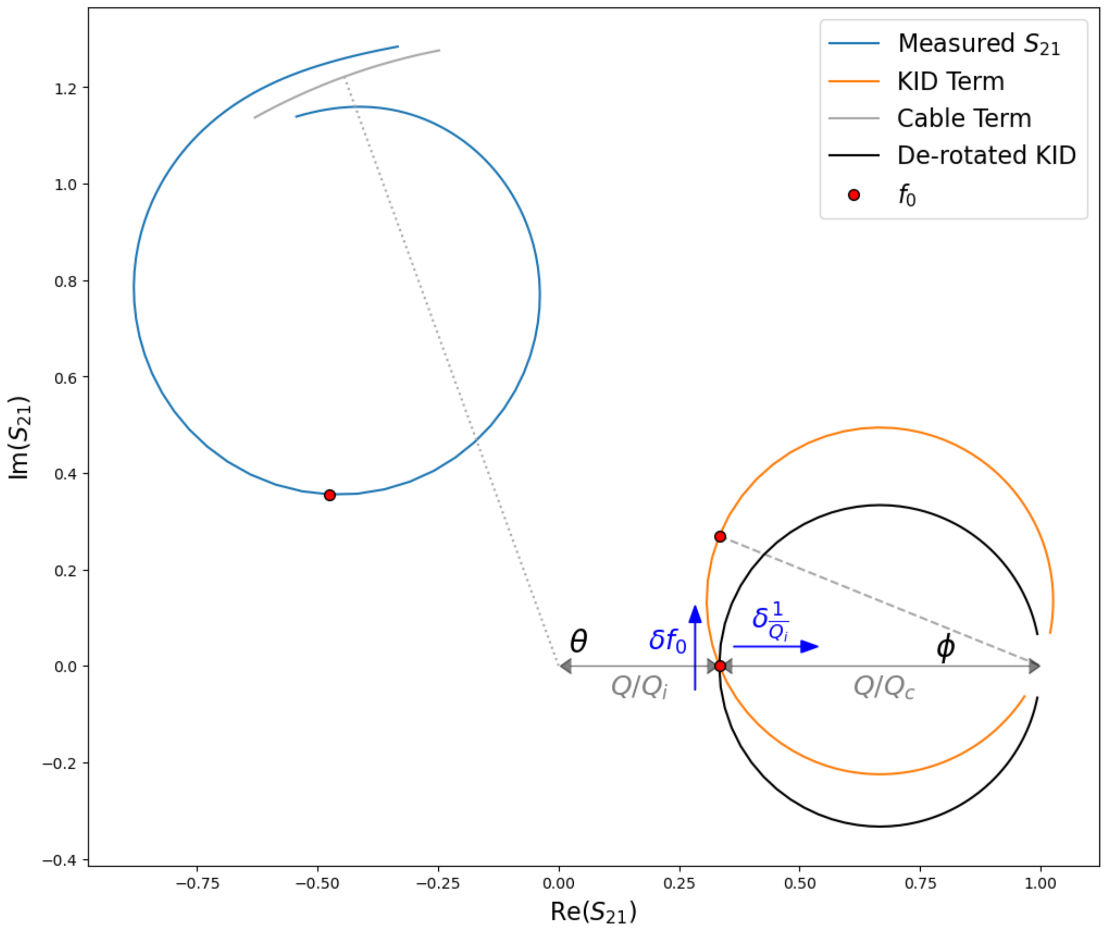

Figure 2.6: The complex transmission for a resonator with cable delays and complex normalization (shown in blue) distorts and rotates the resonance circle. By fitting the full complex data, you can separate out the cable and resonance terms (shown in gray and orange, respectively). The angle, θ, is set by an overall normalization, and the skew between the two sides of the resonance circle is generated by the frequency dependence of the cable delay. The pure resonance circle is anchored to the point (1,0), rotated at an angle, ϕ, that is determined by the mismatch with the coupling impedance, and rescaled by a factor of secϕ. When the impedance mismatch is accounted for, the resonance circle diameter is Q_r/Q_c. The directions marked as δf_0 and $\delta\frac{1}{Q_i}$, correspond to the directional shift from decreasing f_0 or Q_i, respectively.

2.4 Principles of Kinetic Inductance Detectors

Now that the preliminaries are out of the way, we can combine them to see how changes in the complex conductivity from either bath temperature variations or external photon-loading translate into shifting resonator parameters.

2.4.1 Surface Impedance of MKIDs

From the equation for complex conductivity, σ, with the reasonable assumption that $\sigma_2 \gg \sigma_1$, the surface impedance[11] for a superconducting thin film[12] of thickness, t, can be calculated as [42]

$$Z_s = \frac{1}{\sigma t} = \frac{1}{(\sigma_1 - j\sigma_2)t} \approx \frac{\sigma_1}{\sigma_2^2 t} + \frac{j}{\sigma_2 t} \,. \tag{2.44}$$

This is related to the sheet resistance, R_s, and sheet kinetic inductance, $L_{k,s}$, (or sheet reactance, X_s) in the standard manner:

$$Z_s = R_s + j\omega L_{k,s} = R_s + jX_s \tag{2.45}$$

which can be used along with the geometric inductance, L_g, to arrive at expressions for f_0 and Q_i.

[11] The surface impedance, Z_s, which has units of $\Omega/\square$, is related to the impedance, Z, by the equation $Z = Z_s(l/w)$, where l is the length and w is the width.

[12] This expression for the surface impedance is particular to a thin film in the local limit. In the thick film and extreme anomalous limits, the form of Z_s changes, but the main impact on these expressions is to add an additional factor to the differential relationship between Z_s and σ, which can be propagated to later expressions as appropriate. More generally, the expression that we will care about is [42]

$$\frac{\delta Z_s}{Z_s} = \gamma \frac{\delta \sigma}{\sigma} \tag{2.43}$$

where $\gamma = -1$ in the thin film local limit, $\gamma = -1/2$ in the thick film local limit, $\gamma = -1/3$ in the extreme anomalous limit.

2.4.2 Responsivity

Using the above and including the geometric inductance term, L_g, we can plug these expressions into the equations for f_0 and Q_i and see how perturbations in σ result in perturbations in the resonator parameters. The resonant frequency is given by[13]

$$\omega_0 = \frac{1}{\sqrt{(L_g + L_k)C}} = \frac{1}{\sqrt{(L_k/\alpha)C}} \tag{2.46}$$

where $\alpha = \frac{L_k}{L_g+L_k}$ is the kinetic inductance fraction, which is the proportion of the inductance attributable to the kinetic inductance, L_k, of the film itself. A change in L_k propagates to ω_0 as

$$\frac{d\omega_0}{dL_k} = -\frac{1}{2}\frac{\omega_0}{L_g + L_k} = -\frac{\alpha}{2}\frac{L_k}{\omega_0}\,. \tag{2.47}$$

Since α does not change appreciably with a small shift in the conductivity, we can see the effects best by rearranging this to look at a fractional shift in the resonant frequency, $x \equiv \frac{\omega_0(T)-\omega_0(T_0)}{\omega_0(T_0)}$:

$$\delta x = \frac{\delta\omega_0}{\omega_0} = -\frac{\alpha}{2}\frac{\delta L_k}{L_k} = \frac{\alpha}{2}\frac{\delta\sigma_2}{\sigma_2}\,. \tag{2.48}$$

For the internal quality factor, it is easier to work with reciprocals, i.e. the internal loss, meaning that we have

$$Q_i^{-1} = \frac{Re\{Z_s\}}{Im\{Z_s\}} = \frac{R}{\omega L} = \alpha\frac{\sigma_1}{\sigma_2}\,. \tag{2.49}$$

Since the fractional shift in σ_2 is much smaller than the the shift in σ_1, the fractional shift in ωL is also much smaller than the the shift in R (less than a percent

[13]Note that we are using L_k here rather than $L_{k,s}$ as above. This is just the surface kinetic inductance multiplied by a geometric factor, which is the total number of squares there are in the active area added end to end. It is important to note that the sides of the squares are always set by the width of the trace.

for L_k alone until $T \gtrsim T_c/3$). With this in mind, we can safely ignore the effects of variation on that term and focus on the shift in σ_1 and R from increasing quasiparticle density. The change in the internal loss can then be expressed as:

$$\delta Q_i^{-1} = \frac{\delta R}{\omega L} = \alpha \frac{\delta R}{\omega L_k} = \alpha \frac{\delta \sigma_1}{\sigma_2} \; . \tag{2.50}$$

Using the fact that $\sigma_2 \approx \pi \Delta_0 \sigma_n / \hbar\omega$[14] at the temperatures we are interested in and $|\sigma_2| \gg |\sigma_1|$, along with the equations from from section 2.2.4, we can arrive at the following relationship between $\delta\sigma$ and δn_{qp}[15]:

$$\frac{\delta \sigma}{|\sigma|} = \frac{S_1(\omega,T) + iS_2(\omega,T)}{2N_0\Delta_0} \delta n_{qp} \tag{2.51}$$

where $S_1(\omega, T)$ and $S_2(\omega, T)$ are

$$S_1(\omega,T) \approx \frac{2}{\pi}\sqrt{\frac{2\Delta_0}{\pi k_B T}} sinh(\xi) K_0(\xi) \tag{2.52}$$

$$S_2(\omega,T) \approx 1 + \sqrt{\frac{2\Delta_0}{\pi k_B T}} e^{-\xi} I_0(\xi) \tag{2.53}$$

This can then be directly translated into the following expressions for δx and δQ_i^{-1} in terms of changes in the quasiparticle density:

$$\delta Q_i^{-1} = \frac{\alpha S_1(\omega,T)}{2N_0\Delta_0} \delta n_{qp} \tag{2.54}$$

[14] We note that this low temperature approximation of σ_2 also gives us a convenient estimate for $L_{k,s} = \frac{\hbar R_s}{\pi \Delta_0}$

[15] This is under the assumption that perturbations maintain an equilibrium quasiparticle distribution function, $f(E)$, which is not always the case [30].

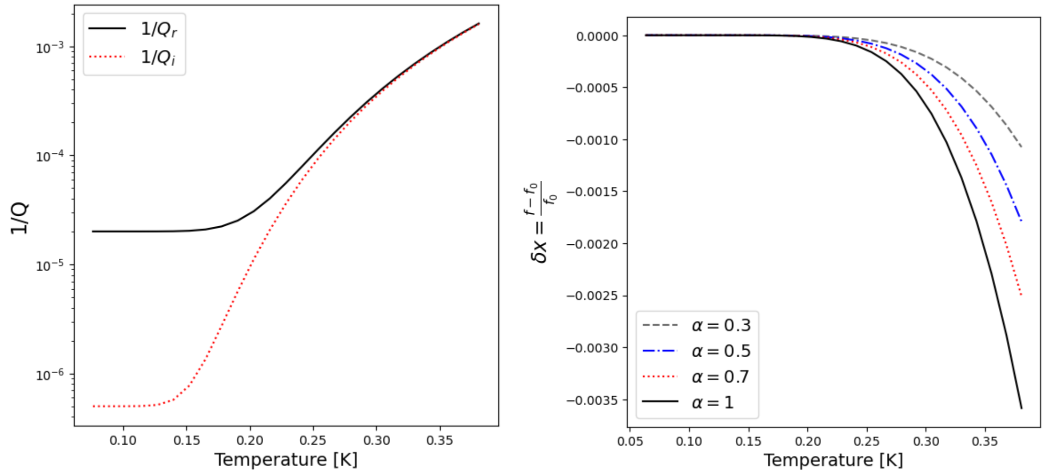

Figure 2.7: Calculated shifts in resonance frequency and quality factor with changing bath temperature, using the same parameters as given in Figure 2.4. The internal quality factor is assumed to be limited by other forms of loss to 2x10^6 and the coupling quality factor is 50,000. Fractional frequency shift is plotted for various kinetic inductance fractions.

$$\delta x = -\frac{\alpha S_2(\omega, T)}{4N_0\Delta_0}\delta n_{qp} \,. \tag{2.55}$$

Examples of these shifts are plotted in Figure 2.7 for a variety of kinetic inductance fractions and parameters relevant to CCAT detectors.

We can also define the ratio

$$\beta = \frac{S_2}{S_1} = \frac{\delta\sigma_2}{\delta\sigma_1} = -2\frac{\delta x}{\delta Q_i^{-1}} \tag{2.56}$$

which tells us the relative strength of these two responses, and is useful for predicting the direction of a shift in the resonance circle due to a perturbation in the quasiparticle density. Since the response is nearly the same for thermally-generated quasiparticles as it is for optically-generated quasiparticles, we should expect the value of β in terms of the ratio of δx and δQ_i^{-1} to be roughly the same in both cases. For the detectors that are discussed in the next chapter, the predicted range of values for β is approximately 4–10 when operating at a bath temperature of 100 mK. This tells us the response is predominantly in the imaginary direction, shifting the phase of the resonance circle. Depending on whether we are heavily Q_i-dominated (under-coupled) or more closely matched to Q_c, this relative response will be even further skewed towards the phase direction. (In the Q_c-dominated regime, the δQ_i^{-1} response becomes negligible.)

Ultimately, the above is only describing the shift in resonance and loss due to the quasiparticle system, meaning that additional contributions to the total behavior such as radiative or two-level system (TLS) loss should be accounted for when predicting the behavior of the combined shift in the resonant frequency, x_{total}, or the overall internal quality factor, $Q_{i,total}$. We can use a similar derivation as for δQ_i^{-1} and δx to arrive at the following expressions for the predicted contributions that arise from the the Mattis-Bardeen equations, which we call $Q_{i,MB}^{-1}$ and x_{MB}:

$$Q_{i,MB}^{-1}(\omega, T, n_{qp}) = \frac{\alpha S_1(\omega, T)}{2N_0\Delta_0} n_{qp} \tag{2.57}$$

$$x_{MB}(\omega, T, n_{qp}) = -\frac{\alpha S_2(\omega, T)}{4N_0\Delta_0} n_{qp} \, . \tag{2.58}$$

These can then be added to any other internal loss (such as TLS loss, $Q_{i,TLS}$ or radiative loss, $Q_{i,rad}$) or frequency shift mechanisms (such as shifts due to TLS functions, x_{TLS}, or random scatter from stray magnetic fields, $x_{scatter}$) to arrive at $Q_{i,total}$ or δx_{total}:

$$\frac{1}{Q_{i,total}} = \frac{1}{Q_{i,MB}} + \frac{1}{Q_{i,TLS}} + \frac{1}{Q_{i,rad}} + ... \tag{2.59}$$

$$x_{total} = x_{MB} + x_{TLS} + x_{scatter} + ... \tag{2.60}$$

A more complete derivation of the above can be found in [42] and [77].

Response to Thermal Load

First considering the response of a KID to a change in the bath temperature, we can use the expressions

$$\frac{dx}{dT} = \frac{dx}{dn_{qp}} \frac{dn_{qp}}{dT} \tag{2.61}$$

and

$$\frac{dQ_i^{-1}}{dT} = \frac{dQ_i^{-1}}{dn_{qp}} \frac{dn_{qp}}{dT} \tag{2.62}$$

and the low-temperature approximation for $\frac{dn_{qp}}{dT}$:

$$\frac{dn_{qp}}{dT} \approx \frac{n_{qp}}{T} \left(\frac{1}{2} + \frac{\Delta_0}{k_B T} \right) \approx 2N_0 \sqrt{2\pi k_B T \Delta_0} e^{-\Delta_0/k_B T} \frac{1}{T} \left(\frac{1}{2} + \frac{\Delta_0}{k_B T} \right) \tag{2.63}$$

Combining these with Equation 2.54 and Equation 2.55, we get the following expressions for the temperature responsivity of the resonance frequency and internal quality factors:

$$\frac{dx}{dT} = -\frac{\alpha e^{-\Delta_0/k_B T}}{2T} \sqrt{\frac{2\pi k_B T}{\Delta_0}} \left(\frac{1}{2} + \frac{\Delta_0}{k_B T} \right) S_2(\omega, T) \tag{2.64}$$

$$\frac{dQ_i^{-1}}{dT} = \frac{\alpha e^{-\Delta_0/k_B T}}{T}\sqrt{\frac{2\pi k_B T}{\Delta_0}}\left(\frac{1}{2}+\frac{\Delta_0}{k_B T}\right) S_1(\omega, T)\ . \tag{2.65}$$

These expressions can then be used to fit for the material parameters, principally the gap, Δ_0, and the kinetic inductance fraction, α.

Response to Optical Loading

Now let us consider the response to an optical load, P_{abs}. Naturally, with the detection mechanism for MKIDs being through the photon-induced pair-breaking and production of quasiparticles, we need to clarify the relationship between n_{qp} and P_{abs}. The general expressions for the responsivity in both resonator parameters looks like

$$R_x = \frac{dx}{dP_{abs}} = \frac{dx}{dn_{qp}}\frac{dn_{qp}}{dP_{abs}} \tag{2.66}$$

$$R_{Q_i^{-1}} = \frac{dQ_i^{-1}}{dP_{abs}} = \frac{dQ_i^{-1}}{dn_{qp}}\frac{dn_{qp}}{dP_{abs}}\ . \tag{2.67}$$

Thus our problem boils down to finding some analytic expression for n_{qp} in terms of P_{abs}. We start by looking at a simplified version of the rate equations for quasiparticle generation and recombination through various mechanisms, and then look at a few different possible cases. A more complete discussion of this and the following can be found in [94] and [67].

In general, we have

$$\frac{dn_{qp}}{dt} = \Gamma_{opt} + \Gamma_{therm} + \Gamma_{read} - \Gamma_{rec} \tag{2.68}$$

where Γ_{opt}, Γ_{therm}, and Γ_{read} are the quasiparticle generation rates from optical photons, thermal excitations, and readout tone photons, and Γ_{rec} is the quasiparticle recombination rate. This is simplified from the full set of equations that can be found in [16] and [47]. As in the previous discussion about quasiparticle lifetimes, we make the further simplification that we can ignore Γ_{read} here. In a steady state, we know that

$$\frac{dn_{qp}}{dt} = 0 \tag{2.69}$$

and therefore

$$\Gamma_{opt} + \Gamma_{therm} = \Gamma_{rec}\ . \tag{2.70}$$

We can now plug in the expressions for each component

$$\frac{\eta_{ph} P_{abs}}{\Delta_0 V} + \gamma N_0^2 8\pi k_B T \Delta_0 e^{-2\Delta_0/k_B T} = \frac{n_{qp}}{\tau_{qp}} \tag{2.71}$$

where η_{ph} represents the pair-breaking efficiency for the absorbed photons, V represents the absorber volume, and $\gamma = 1/(n_{qp}\tau_{qp})$ is a constant that relates the quasiparticle density and lifetime. Now with this in mind we consider two general cases.

1. The quasiparticle population is dominated by optically-generated pair-breaking ($\Gamma_{opt} \gg \Gamma_{therm}$).
2. The quasiparticle population is dominated by thermal quasiparticles or another background source of quasiparticles, or, more generally, the recombination time is independent of P_{abs}.

This first case has been observed in aluminum MKIDs [38, 68], while the second case has been seen in TiN MKIDs [59].

In the first case, Equation 2.71 can be simplified to

$$\frac{\eta_{ph} P_{abs}}{\Delta_0 V} = \gamma n_{qp}^2 \tag{2.72}$$

and the steady-state population of quasiparticles is $n_{qp} = \sqrt{\frac{\eta_{ph} P_{abs}}{\gamma \Delta_0 V}}$. From this, we can see that a DC perturbation in P_{abs} leads to

$$\frac{dn_{qp}}{dP_{abs}} = \frac{1}{2}\sqrt{\frac{\eta_{ph}}{\gamma P_{abs} \Delta_0 V}} \tag{2.73}$$

and a more general perturbation by a signal at fixed frequency, ω, looks like

$$\frac{dn_{qp}}{dP_{abs}} = \frac{1}{2}\sqrt{\frac{\eta_{ph}}{\gamma P_{abs} \Delta_0 V}} \frac{1}{1 + i\omega\tau_{qp}/2} \,. \tag{2.74}$$

Combining this with the expressions from Equation 2.54 and Equation 2.55 yields the following:

$$R_{Q_i^{-1}} = \frac{dQ_i^{-1}}{dP_{abs}} = \frac{\alpha S_1(\omega, T)}{4 N_0 \Delta_0} \sqrt{\frac{\eta_{ph}}{\gamma P_{abs} \Delta_0 V}} \frac{1}{1 + i\omega\tau_{qp}/2} \tag{2.75}$$

$$R_x = \frac{dx}{dP_{abs}} = \frac{1}{f_0} \frac{df_0}{dP_{abs}} = -\frac{\alpha S_2(\omega, T)}{8 N_0 \Delta_0} \sqrt{\frac{\eta_{ph}}{\gamma P_{abs} \Delta_0 V}} \frac{1}{1 + i\omega\tau_{qp}/2} \,. \tag{2.76}$$

The most relevant behavior here is the inverse square root dependence on the absorbed optical power and the volume of the absorber region.

In the second case, where τ_{qp} is independent of P_{abs}, we can decouple the thermal generation and recombination terms from Γ_{opt} and rewrite the generation-recombination equation as

$$\frac{dn_{qp}}{dt} \approx \frac{\eta_{ph} P_{abs}}{\Delta_0 V} + \Gamma_{therm} - \frac{n_{qp}}{\tau_{eff}} \tag{2.77}$$

where Γ_{therm} and τ_{eff} are constants that depend only on the bath temperature. In this scenario, propagating a small signal perturbation in P_{abs} leads to

$$\frac{dn_{qp}}{dP_{abs}} \approx \frac{\eta_{ph}\tau_{eff}}{\Delta_0 V}\frac{1}{1+i\omega\tau_{eff}} \,. \tag{2.78}$$

Now for the responsivities, we have

$$\frac{dQ_i^{-1}}{dP_{abs}} = \frac{\alpha S_1(\omega,T)}{2N_0\Delta_0}\frac{\eta_{ph}\tau_{eff}}{\Delta_0 V}\frac{1}{1+i\omega\tau_{eff}} \tag{2.79}$$

$$\frac{dx}{dP_{abs}} = -\frac{\alpha S_2(\omega,T)}{4N_0\Delta_0}\frac{\eta_{ph}\tau_{eff}}{\Delta_0 V}\frac{1}{1+i\omega\tau_{eff}} \tag{2.80}$$

Now we see a constant response with changes to P_{abs}, along with an increased sensitivity to the absorber volume.

In the intermediate case where both optically- and thermally-generated quasiparticles are relevant, the equations become

$$n_{qp} = \sqrt{\frac{\Gamma_0 + \eta_{ph}P_{abs}/\Delta_0 V}{\gamma}} \tag{2.81}$$

$$\frac{dn_{qp}}{dP_{abs}} = \sqrt{\frac{\eta_{ph}}{\gamma\Delta_0 V}}\frac{1}{\sqrt{P_0 + P_{abs}}} \tag{2.82}$$

where P_0 represents an effective "dark" loading power with generation rate Γ_0 that limits the quasiparticle lifetime at low optical loading levels. This model captures a wide variety of possible contributors to this "dark" loading, and displays a transition from a roughly constant response (as in case 2) to an inverse square root-dependence (as in case 1). This intermediate model is most relevant to the aluminum MKIDs that are discussed in the next chapter.

2.4.3 Nonlinearity & Bifurcation

While microwave probe tone power is ideally a negligible contributor to the detector response, it must be accounted for when optimizing detector performance, as there are ways which the microwave tone can impact the resonator parameters and line shape. The principle effect of the probe tone comes through the nonlinear kinetic inductance, which is a current-dependent contribution to the kinetic inductance of the form

$$L_k \approx L_{k,0}(1 + \frac{I^2}{I_*^2}) \tag{2.83}$$

where $L_{k,0}$ is the kinetic inductance value at low current values, I is the current, and I_* is the critical current where pair-breaking begins to set in. Since this is an effect on the Cooper pairs, rather than the quasiparticles, the result of this is predominantly a reactive shift in the resonance frequency at higher current densities, which takes the form

$$\delta x = -\frac{1}{2}\frac{\delta L}{L} = \frac{\alpha}{2}\frac{I^2}{I_*^2}\,. \tag{2.84}$$

As shown in [100], the current is connected to the tone power through the expressions of the resonator energy in terms of both inductance, L, and proportion of the readout power, P_r that is dissipated:

$$E_r = \frac{1}{2}LI^2 = \frac{2Q_r^2}{Q_c}\frac{1}{1+4Q_r^2x^2}\frac{P_r}{\omega_r}\,. \tag{2.85}$$

Relating this back to our expression for δx, we can write this shift in terms of the resonator energy, E_r, and a critical energy, E_*,

$$\delta x = -\frac{E_r}{E_*} \tag{2.86}$$

where $E_* = LI_*^2/\alpha$ is on the order of the inductor condensation energy, $E_{cond} = N_0\Delta_0^2 V/2$ (where V is the volume [67]. If we now plug the expression for E_r into the equation for δx, we wind up with a cubic equation for the distorted x:

$$x = x_0 + \frac{2Q_r^2}{Q_c}\frac{1}{1+4Q_r^2x^2}\frac{P_r}{\omega_r E_*}\,. \tag{2.87}$$

Since it is slightly easier to work with, we multiply x by Q_r so that our cubic equation is for the variable $y = Q_r x$, which is the distance to the resonator measured in resonator line widths. We further simplify everything by introducing the nonlinearity parameter, $a \equiv \frac{2Q_r^3}{Q_c}\frac{P_r}{\omega_r E_*}$. This gives us an expression that takes the form

$$y = y_0 + \frac{a}{1+4y^2} \tag{2.88}$$

which can be solved and inverted to yield new resonator states with shifted ω_r. These appear as a distortion in the resonator shape from a purely linear resonator, where ω_r moves as the tone approaches $y_0 = 0$. Some of this can be seen in Figure 2.8.

Finally, we note that an interesting thing happens with Equation 2.88 at roughly $a \geq 0.77$. Beyond this point, which corresponds to a particular power level, this equation goes from having a single real solution at all values of y_0 to having a growing region with three real solutions, two of which are stable. This point is referred to as bifurcation, as the resonator can now switch between multiple states. This has the added effect that the resonator shape is affected by the direction of the sweeping probe tone. When increasing frequency, the

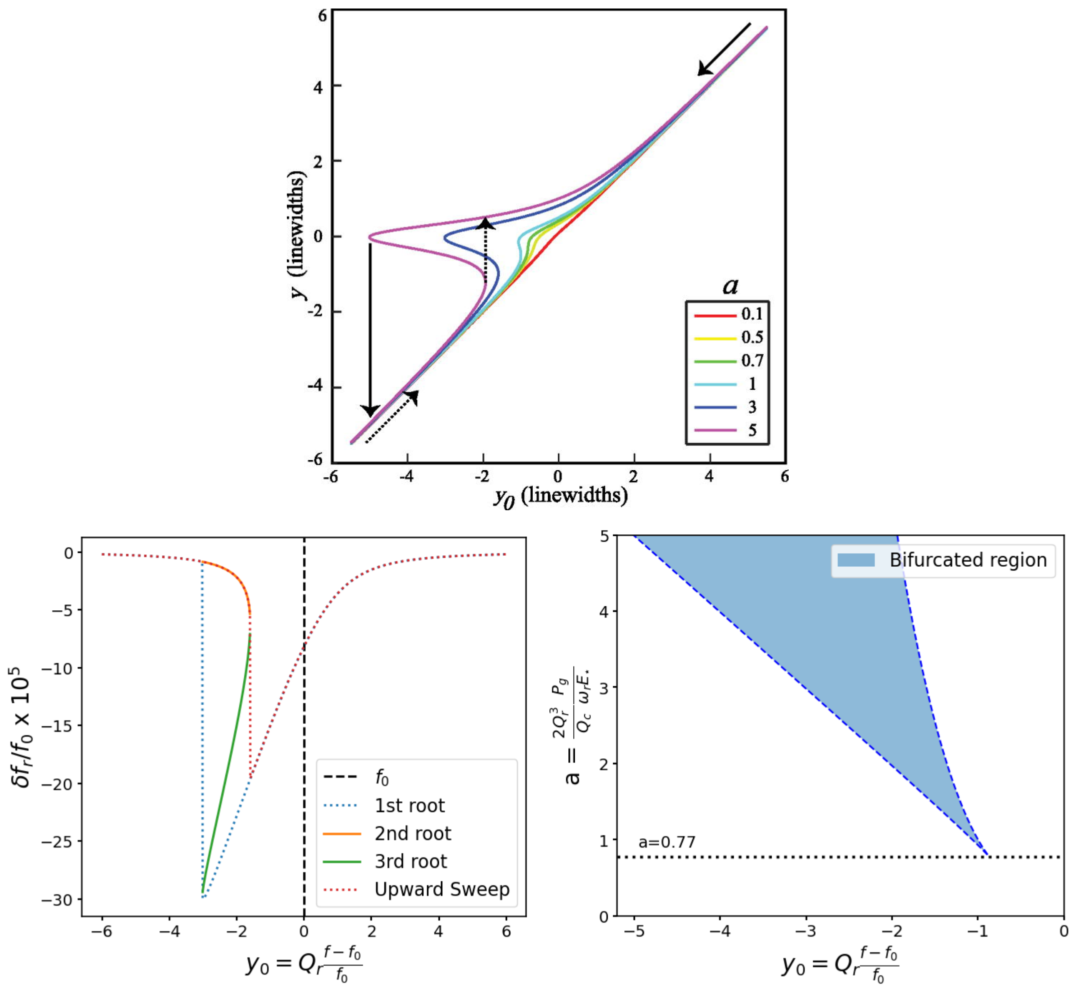

Figure 2.8: (Top) Plot taken from [100] of measured distance from resonance (in linewidths) due to nonlinear kinetic inductance versus the unloaded distance (i.e. the x-axis is a constant sweep in frequency) for a variety of values for the nonlinearity parameter, a. Anything other than a straight line with unity slope implies that the resonant frequency, f_r, is changing as greater tone power makes it into the resonator. For $a \gtrsim 0.77$ the distorted y includes a region where a single frequency corresponds to multiple possible resonant frequencies, referred to as bifurcation. Arrows indicate possible paths that might be measured when sweeping an S_{21} trace. (Lower left) A more detailed look at the possible solutions for f_r that become available while sweeping in frequency for $a = 3$. (Lower right) The region of frequency space (in line widths) where bifurcated states become available as a function of a, a proxy for tone power. In this region, we would expect to see additional noise as the resonator switches between available states.

snap between stable states occurs at a higher frequency than when probed with decreasing frequency. This is shown in Figure 2.8. Because of the potential for switching noise between states in the bifurcated regime, it is generally preferable to stay several dB below the bifurcation point in tone power.

In addition to the nonlinear kinetic inductance, there are further nonlinearities that impact the detector resonant frequency and quality factor. These include the absorption and re-emission of microwave photons by two-level systems at the interface between the dielectric and the superconductor [43, 81], as well as the redistribution of quasiparticles into nonequilibrium states from tone-power pumping [29]. These will not be discussed here, but some of their effects are explored in greater detail in the next chapter.

2.5 Sensitivity & Noise

Having described the principles behind KIDs, we can now move on to the most critical piece: the response and sensitivity to incident optical power. To understand this sensitivity, we need to briefly discuss the noise hierarchy and the various components that have some impact on our observed time streams. Following the path of light entering our telescope depositing energy into our detectors, being read out, and stored as digital time-ordered data for later reconstruction, there are noise contributions and spectral responses and distortions that are picked up at each step of the way. It can be useful to work backwards from the true signal of interest so that we can call out these various noise components, ignoring errors in mapmaking that can be introduced from miscalibration, as well as any differentiation between photons from background/foreground loading and true signal photons.

Beginning with the optical signal, there is Poissonian photon noise. Within the superconductor, there is generation-recombination (GR) noise caused by the discrete nature of quasiparticles being generated (both optically and thermally) and recombining. Taking a step further to consider the resonator as a whole, there is a spectral response caused by the resonator ring-down, but much more relevant is the noise due to two-level systems (TLS) in the dielectric of the capacitors. Within the overall readout circuit, there is general readout noise that is thermal in nature, as well as amplifier noise. Finally, the digitization of the signal comes with some amount of noise from the analog-to-digital converters. Of these, we will touch a bit further on the contributions of GR noise, TLS noise, and photon noise, while saving the readout and amplifier noise for Chapter 4.

2.5.1 Background

Describing the spectral behavior of noise sources requires use of the one-sided power spectral density, $S_{qq}(f)$, which is the Fourier transform of the autocorrelation function. This is defined as

$$S_{qq}(f) = \lim_{T \to \infty} \frac{1}{T} |\tilde{q}(f)|^2 \tag{2.89}$$

where $\tilde{q}(f)$ is the Fourier transform of $q(t)$, which is a placeholder for whatever our function of interest is. The sensitivity is generally reported in terms of noise equivalent power (NEP), which has units of $W/\sqrt{Hz}$. This is the amount of power that could be measured with a signal-to-noise of one after 0.5 seconds of integration (or equivalently, in 1 Hz of bandwidth). From the units, we might infer, correctly, that the NEP is proportional to the square root of the power spectral density.

A practical measurement of this for MKIDs involves converting the complex time stream, $S_{21}(t)$ (or more accurately, $\delta S_{21}(t)$), into $\delta P_{abs}(t)$ by way of our responsivity (which we will denote here as R_q), taking the square root of the power spectral density from that processed time stream, and adding corrections to account for the relevant time constants. Written out explicitly this looks like:

$$NEP_q^{KID}(f) = \sqrt{S_{qq}(f)}\left(\frac{dq}{dP}\right)^{-1}\sqrt{1+(2\pi f\tau_{res})^2}\sqrt{1+(2\pi f\tau_{qp})^2} \tag{2.90}$$

where τ_{res} and τ_{qp} are the time constants due to the resonator ringdown and quasiparticle lifetimes respectively.

Note that, depending on how we are reading out the resonator, q might refer to the amplitude ($|S_{21}(t)|$) or the phase ($\theta(t) = \arctan\left[\mathfrak{Im}(S_{21}(t))/\mathfrak{Re}(S_{21}(t))\right]$) of the resonator, which correspond in a relatively straightforward way to the δQ_i^{-1} and δf_0, respectively. Details of this correspondence are described in [119], but can also be worked out through Equation 2.41 with the cable/environment terms removed[16]. In the case of Prime-Cam, we are using phase-based readout. So long as we are predominantly interested in measuring at sampling frequencies such that $2\pi f\tau_{res} \ll 1$ and $2\pi f\tau_{qp} \ll 1$, this simplifies to

$$NEP_x^{KID}(f) = \sqrt{S_{xx}(f)}\left(\frac{dx}{dP_{abs}}\right)^{-1} \tag{2.91}$$

The measured result is inclusive of the NEP contributions from each element of the signal chain described above. When estimating or comparing NEP to our

[16]To clarify further, this correction (removing what I've called the environmental factors) needs to be done on the raw data in order to properly have a correspondence of δQ_i^{-1} with amplitude and δf_0 with phase. In general, which is to say without accounting for cable parameters and impedance mismatches, this relationship can be arbitrarily distorted.

expectations, we can use the expressions for individual components (NEP_i) and sum them in quadrature as

$$NEP^2 = \sum_{\text{all terms}} NEP_i^2 \,. \tag{2.92}$$

One final comment before moving on is about the notation. Since we will only be dealing with the autocorrelation moving forward unless otherwise noted, we will switch the notation for the power spectral density from $S_{qq}(f)$ here to the simpler $S_q(f)$.

2.5.2 Time Constants

As mentioned above, there are a variety of different time scales that must be taken into consideration when optimizing the performance of your KIDs or estimating the noise. During operation, individual resonators are monitored with a single probe tone that is sampled at regular intervals depending on the telescope scanning speed and desired data rate. For CCAT's 280 GHz arrays, this sample rate is ~ 500 Hz. Additionally, there are two intrinsic time constants that are set by the KID itself. These are the resonator ring down time and quasiparticle lifetime.

The resonator ring down time, τ_{res}, arises when considering the time domain transfer function of a resonator that is being probed at a frequency of f by a perturbation at frequency ν [119]:

$$\zeta(\nu, f) = \frac{1 - S_{21}(f+\nu)}{1 - S_{21}(f)} \,. \tag{2.93}$$

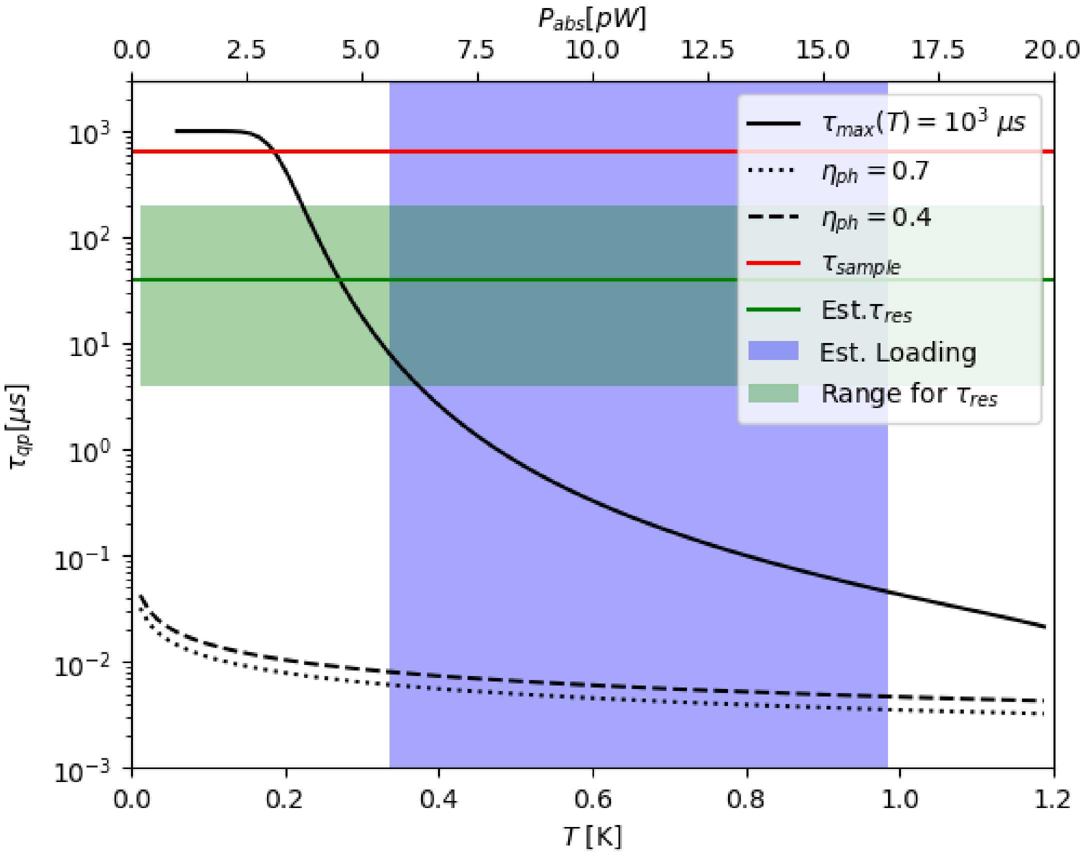

Figure 2.9: The range of different time scales relevant for KID performance in Prime-Cam's 280 GHz module. The solid black line is the quasiparticle lifetime, τ_{qp}, as a function of temperature (shown on the lower x-axis) for a purely thermal QP population with τ_{max} of 1 ms. While attainable in dark conditions for Al, this should be seen as an extreme limiting case of τ_{qp}. The dashed and dotted lines are τ_{qp} with $\eta_{ph} = 0.4$ and $\eta_{ph} = 0.7$, respectively, and the same τ_{max}, assuming the N_{qp} is dominated by optical loading (shown plotted on the upper x-axis). The green region shows the range of loading conditions expected at the site. The blue region is a conservative range of possible resonator time constants, τ_{res}, during operation (with Qs from 2,000 to 30,000 and f_rs from 300 MHz to 1 GHz). Finally, the solid red line shows a sampling time constant of $\tau_{sample} = 640\ \mu$s for time-ordered data. As can be seen, even with relatively unrealistic assumptions, τ_{res} is nearly an order of magnitude faster than the sample rate, and, well-below the expected optical loading, τ_{qp} is several orders of magnitude faster.

When on resonance, this looks like

$$\zeta(\nu, f) = \frac{1}{1 + 2iQ_r \frac{\nu}{f_0}} \tag{2.94}$$

which is just a low-pass filter with a cut off frequency set by $f_{cut} = 1/\tau_{res} = f_0/2Q_r$. This means that a high Q resonator fundamentally rings down at a slower rate than a lower Q resonator, an important consideration when balancing sampling rates with high multiplexing numbers. The more tightly packed your resonators are in readout bandwidth, the less overhead you will have before needing to account for the resonator ringdown.

As we've already described some of the important aspects of quasiparticle lifetimes, we won't dwell on that here, except to mention that it should be much faster than the sample rate so as not to reduce the time domain response to incident signals. Figure 2.9 shows a variety of time constants that are relevant for the operation of Prime-Cam's 280 GHz resonators. The important take away is that the resonator ringdown time and quasiparticle lifetimes that are expected are much faster than the intended sample rate.

2.5.3 Photon Noise

The ultimate goal for our detector is to attain "photon-limited" sensitivity, meaning that the dominant source of noise is the intrinsic shot noise from random photon arrival times. The noise that is intrinsic to the source looks like [28, 119]

$$NEP^2_{photon} = 2P_{abs}\hbar\omega(1 + n_o) \tag{2.95}$$

where P_{abs} is the total power actually absorbed by the detector, ω is the photon frequency, and $n_o = (e^{\hbar\omega/k_BT} - 1)^{-1}$ is the photon occupancy number. For the frequencies and source temperatures generally under consideration with Prime-Cam, $\hbar\omega \gg k_B T$ and n_0 can be ignored, however when relevant it adds a term that goes as P_{abs}^2 to NEP_{photon}^2.

2.5.4 Generation-Recombination Noise

Within the superconductor, the dynamic balance of pair-breaking, due to optical absorption and thermal fluctuations, and random recombination through scattering leads to discrete statistical fluctuations in the charge carrier densities of both Cooper pairs and quasiparticles. This generation-recombination noise, as it is called, can be estimated by looking at the overall fluctuations in the total population of quasiparticles as done in [119] or [27]. In general, the power spectral density due to generation-recombination noise is spectrally white except for a high frequency cutoff set by the quasiparticle lifetime [27]:

$$S_{GR}(f) = \frac{4N_{qp}\tau_{qp}}{1 + (2\pi f \tau_{qp})^2} \tag{2.96}$$

where N_{qp} is total quasiparticle number and τ_{qp} is the quasiparticle lifetime discussed in section 2.2.2. While generation noise due to optical power is accounted for in the photon noise above, there is also thermal generation noise and recombination noise. A full consideration of the thermal generation noise and recombination noise yields the following expression for the NEP attributable to generation-recombination [119]:

$$\begin{aligned} NEP_{GR}^2 &= \frac{4\Gamma_{th}\Delta_0^2}{\eta_{ph}^2} + \frac{2N_{qp}\Delta_0^2}{\eta_{ph}^2}(\tau_{max}^{-1} + \tau_{qp}^{-1}) \\ &= \left[2N_{qp,th}(\tau_{max}^{-1} + \tau_{th}^{-1}) + 2N_{qp}(\tau_{max}^{-1} + \tau_{qp}^{-1})\right]\frac{\Delta_0^2}{\eta_{ph}^2}\,. \end{aligned} \tag{2.97}$$

Here Γ_{th} is the thermal quasiparticle generation rate, $N_{qp,th}$ is the thermal population of quasiparticles, and τ_{th} is the estimated thermal quasiparticle lifetime. The factor of $(\Delta_0/\eta_{ph})^2$ arises from the conversion factor $(dN_{qp}/dP_{abs})^{-2}$. If we make the assumption that our quasiparticle population is dominated by optically-generated photons such that the thermal generation term is negligible, then we can combine this expression with the photon noise to get a single formula for fully photon-limited NEP:

$$NEP_{GR+photon} = \sqrt{2P_{abs}\left(\hbar\omega(1+n_o) + \frac{\Delta_0}{\eta_{ph}}\right)}. \tag{2.98}$$

2.5.5 TLS Noise

Finally, we consider the noise due to two-level systems (TLS). Early on in the development of KIDs, it was shown that there is excessive loss and noise in the frequency direction that is well-modeled by the presence of a random, uniform distribution of TLS within the amorphous dielectric surface layers [44, 45]. By tunneling between two states, these TLS can absorb microwave photons from the probe tone and increase loss. In addition, the random tunneling causes fluctuations of the dielectric constant that lead to similar fluctuations in the measured resonant frequency. A detailed treatment of these fluctuations leads to the following expressions for the fractional shift in the resonant frequency (δx_{TLS}) and the change in the internal resonator loss ($\delta Q^{-1}_{i,TLS}$) [42]:

$$\delta x_{TLS} = \frac{F_{TLS}\delta_0}{\pi}\left[Re\left(\Psi\left(\frac{1}{2} - \frac{\hbar\omega}{2\pi i k_B T}\right)\right) - \log\frac{\hbar\omega}{2\pi k_B T}\right] \tag{2.99}$$

$$\delta Q^{-1}_{i,TLS} = F_{TLS}\delta_0 \left(\frac{\tanh(\frac{\hbar\omega}{2k_B T})}{1 + |P_r/P_{sat}|} \right)^{1/2} \tag{2.100}$$

where F_{TLS} is the filling fraction for what portion of the resonator volume is host to TLS, P_r/P_{sat} is the ratio of the tone power (P_r) to some saturation power (P_{sat}), Ψ is the complex digamma function, and δ_0 is a the dielectric loss tangent. It is worth noting that these expressions show the different ways to minimize the impacts of TLS effects: by moving to higher tone powers, higher bath temperature, or lower probe tone frequency. In all cases, the reduction can be understood as the TLSs being saturated to the point where emission of radiation balances out absorption.

With this semi-empirical model for the various contributions to TLS noise, this is one component that is traditionally designed around beforehand and measured after-the-fact. In general, this component has a frequency dependence that goes as

$$S_x^{TLS}(f) \propto f^{-1/2} T_{bath}^{-\beta} P_r^{-1/2} \tag{2.101}$$

with T_{bath} being the bath temperature and β being between 1.2 and 2 [44, 63].

2.5.6 Total NEP

Looking back at the full expression for frequency-based readout and adding in the readout noise for completeness, we can predict the following [119]:

$$
\begin{aligned}
NEP^2_{freq} = 2P_{abs}h\nu(1+n_o) + \frac{4\Gamma_{th}\Delta_0^2}{\eta_{ph}^2} + \frac{2N_{qp}\Delta_0^2}{\eta_{ph}^2}(\tau_{max}^{-1}+\tau_{qp}^{-1}) \\
+ \frac{4\eta_a\chi_{qp}\Delta_0}{\eta_{ph}^2}P_a + \frac{8N_{qp}^2\Delta_0^2}{\beta^2\eta_{ph}^2\chi_c^2\chi_{qp}^2\tau_{qp}^2}\frac{k_BT_a}{P_a} \\
+ \frac{8N_{qp}^2\Delta_0^2Q_i^2}{\beta^2\eta_{ph}^2\chi_{qp}^2\tau_{qp}^2}S_{freq}^{TLS}\,.
\end{aligned}
\tag{2.102}
$$

The first three terms are the photon, thermal generation, and recombination noise, followed by the tone-power generation noise (which is hopefully negligible), amplifier noise, and lastly TLS noise. η_a is the tone power quasiparticle generation efficiency, P_a is the absorbed readout tone power, χ_{qp} is the fraction of internal loss due to quasiparticles, β is the ratio of the frequency response to the dissipation response from Equation 2.56, χ_c is the coupling efficiency factor ($4Q_cQ_i/(Q_c+Q_i)^2$), and T_a is the noise temperature of the amplifier.

CHAPTER 3

COMPARISONS OF TIN & AL KINETIC INDUCTANCE DETECTORS

Superconducting detectors have become the state of the art for measuring faint astronomical signals at millimeter and submillimeter wavelengths. Kinetic inductance detectors (KIDs), a type of superconducting resonator [26], have become an increasingly popular choice in recent years due to their sensitivity and ease of multiplexing. KIDs allow for high detector counts and photon-limited sensitivity, while also being simpler to read out than comparably-sensitive transition edge sensors. At the same time, the technology is new enough that there remain significant questions about their noise performance and optimization for the field, one of the most basic of which is the choice of material for the detector. For photon-limited operation of KIDs at millimeter and submillimeter wavelengths, KIDs have typically been designed for bath temperatures of 100–300 mK with an inductor transition temperature, T_c, of 0.5–1.5 K [1, 12, 33, 110]. At the same time, the material must also be robust to fabrication at wafer-scales and repeated cryogenic cycling.

Given these constraints, two of the most popular materials for KIDs in these bands are aluminum (Al) and titanium-nitride (TiN), both of which have shown photon-limited noise performance [59, 68] and have been fabricated at array scales. The primary difference between these materials is that TiN is a "disordered" superconductor, meaning that it has much higher resistivity above T_c than Al, which has several implications, including higher kinetic inductance per square and easier impedance matching for photon absorption. Imaging experiments that have fielded Al KIDs include NIKA [71], NIKA2 [1], OLIMPO [80], and MUSCAT [15], while TiN detectors have seen use for MAKO [101], BLAST-

TNG [33], TolTEC [114], and, at slightly higher frequencies, ARCONS [69].

CCAT's 280 GHz instrument module for Prime-Cam provides an opportunity to test these two materials side-by-side in a near 1:1 setting. It will include ~10,000 kinetic inductance detectors (KIDs) across three arrays. The first KID array was fabricated out of tri-layer titanium-nitride/titanium/titanium-nitride (referred to here as TiN/Ti/TiN or TiN), while the other two arrays were entirely out of aluminum (Al). All three arrays were fabricated on 550-micron silicon-on-insulator wafers by the Quantum Sensors Group at the National Institute for Standards and Technology (NIST) in Boulder, CO.

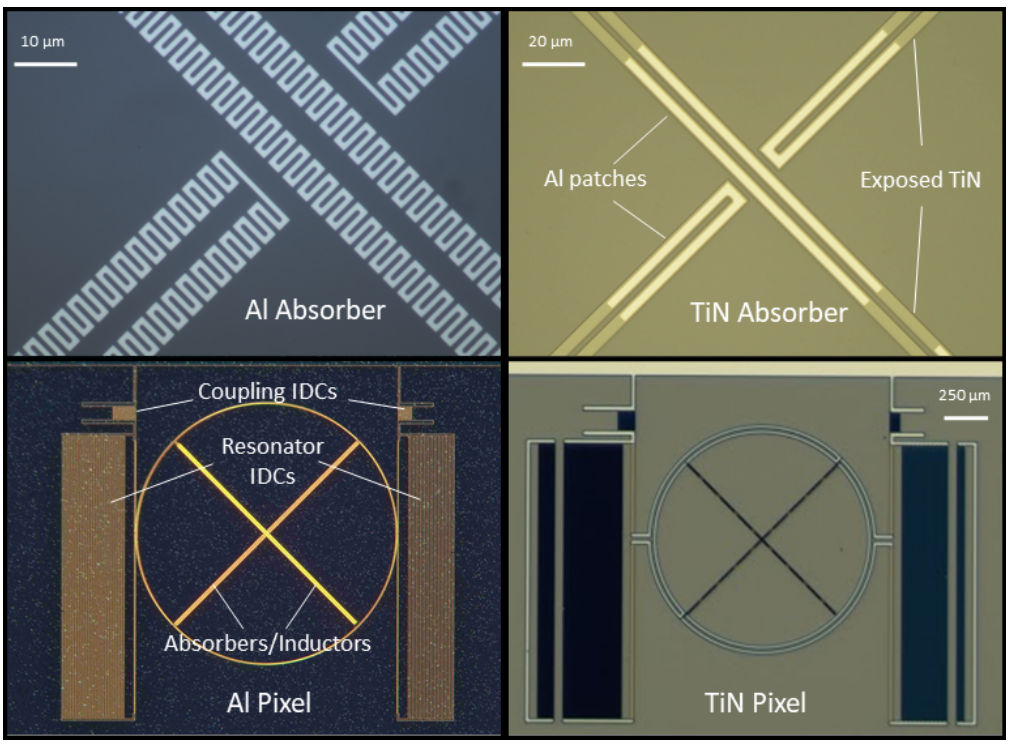

Figure 3.1: TiN pixel design (bottom right) showing two polarization-sensitive detectors. (Bottom left) Al pixel design shown at a similar scale. Close-ups of the respective absorbers are shown on the top, displaying both the meandered Al absorber and the TiN absorbers with Al patches.

3.1 Designs for 280 GHz TiN and Al Pixels

Two types of KID pixels have been developed for the 280 GHz instrument module. As described above, one of these uses TiN and the other uses Al. Both pixel types are lumped element polarimeters evolved from previous NIST designs. A single pixel contains two detectors with front-side illuminated, orthogonal antennas that are impedance-matched to the feedhorn-coupled waveguide. The primary components include a polarization-sensitive antenna that serves as both the inductor and a direct absorber, an interdigitated capacitor (IDC) for coupling to the readout line, and an IDC to set the total capacitance. On the backside, the wafer is deep-etched down to the 80-μm device layer and deposited with an aluminum ground plane, making a quarter-wavelength reflective backshort to improve the optical coupling. Sample devices are shown in Figure 3.1.

The Al devices are passivated with a layer of amorphous silicon and have a $T_c \sim 1.4$ K and sheet resistance of $R_s \sim 1\ \Omega/\square$ (Ohms per square). The TiN/Ti/TiN trilayer devices have a $T_c \sim 1.1$ K, and $R_s \sim 90\ \Omega/\square$. Due to Al having much lower normal resistance, the Al inductor is meandered with finer traces ($\sim$1 μm vs. $\sim$4 μm linewidth) (as shown in Figure 3.1) to better match the waveguide impedance. To tune the desired absorber volume while balancing responsivity and coupling efficiency, 100-nm thick patches of Al are placed above the TiN multilayer absorber to act as a short without significantly affecting the impedance as done in the TolTEC designs [12]. Finally, the Al detectors have slightly larger capacitor geometries. Additional details can be found in [11, 12, 18].

3.2 Data and Testing Methods

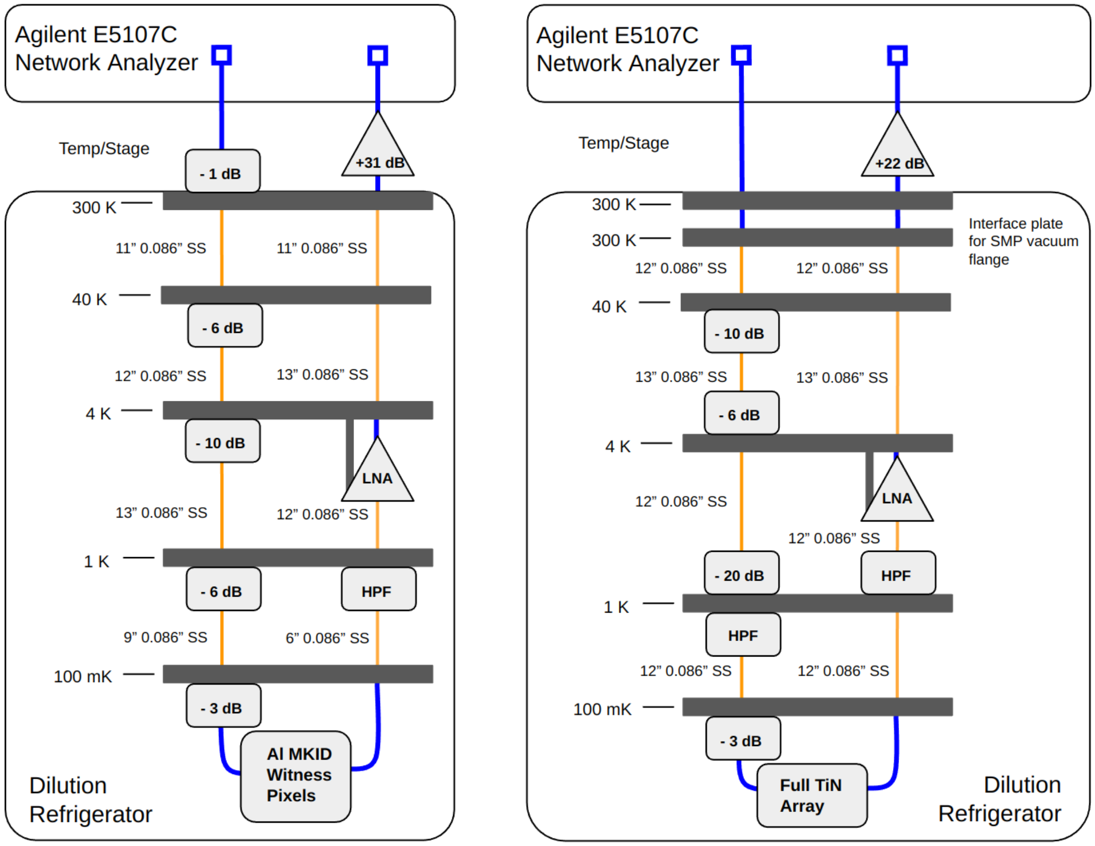

Figure 3.2: Block diagrams of the cryogenic RF chains for data presented here. (Left) The set-up for data acquired at Cornell in a Bluefors SD-250 using Al "witness" pixels fabricated simultaneously with the first full array. The total attenuation (including cable loss) on the input side was roughly 34 dB $\pm$ 1 dB. (Right) is the set-up for data acquired in a Bluefors LD-400 using the fully assembled TiN array. The total input attenuation here (again including cable loss) was roughly 47 dB $\pm$ 1 dB. The low noise amplifiers at 4 K provided roughly 28 dB of gain in both cases.

Lab testing of individual pixels and full arrays is ongoing at NIST and Cornell (see Chapters 4 and 5). While the full range of testing at NIST and Cornell has informed the discussion presented, all data shown here has been acquired using the testbeds described/shown in Figure 3.2-3.6. For the Al-detectors, three "witness" pixels that were fabricated on the same wafer as the first com-

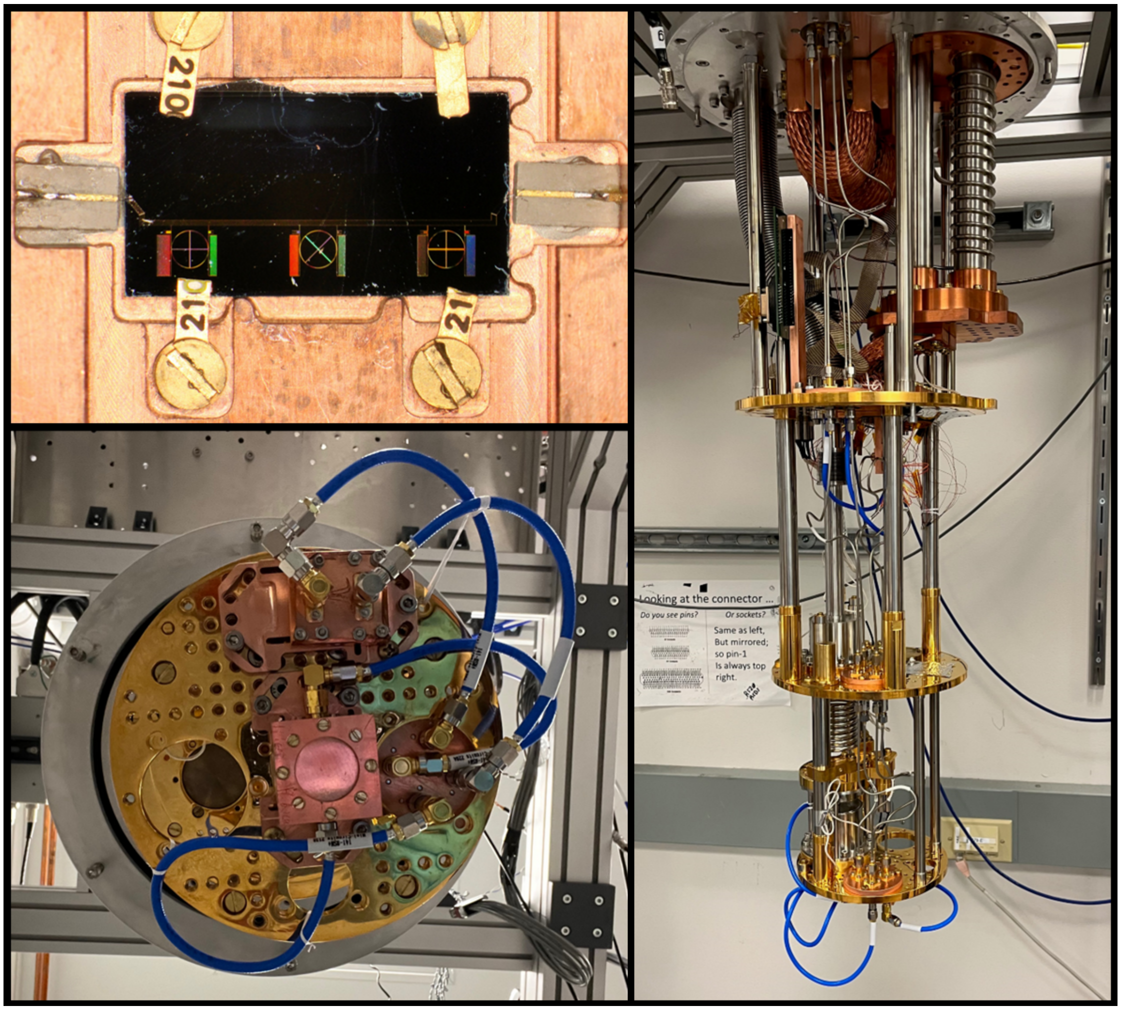

Figure 3.3: Measurement instrumentation for Al ”witness” pixels. (Top left) Three-pixel Al ”witness” chip measured with feedhorn block and filters removed. Five of the six detectors shown were used for testing, while one of the polarization directions in the central pixel was shorted to ground. (Bottom left) The centrally-located witness pixel box (shown with filters installed) as mounted in the Bluefors SD-250 for use with a cryogenic black-body load. (Right) The cryogenic readout chain diagrammed in Figure 3.2 from 40 K down to 100 mK.

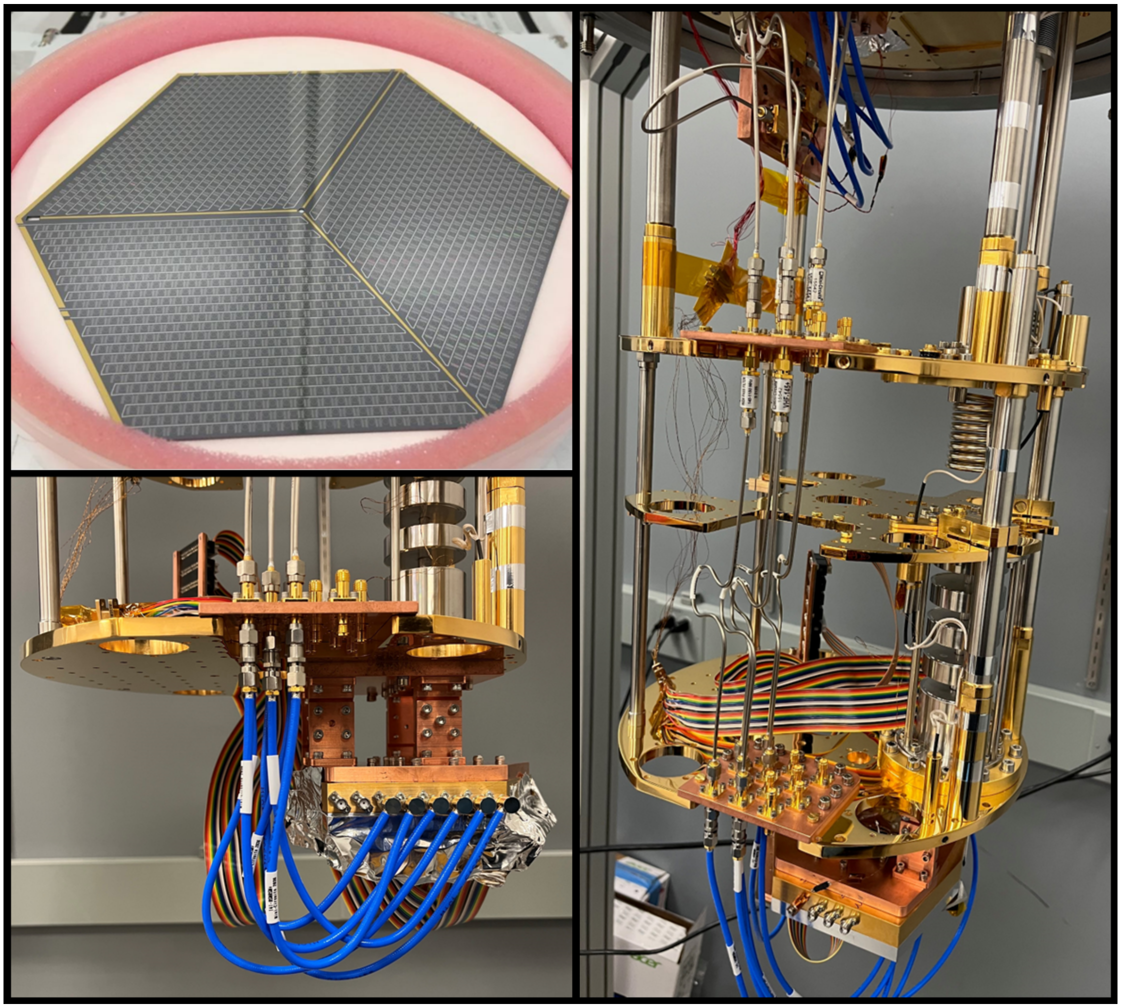

Figure 3.4: Measurement instrumentation for TiN detectors. (Top left) Full TiN array measured prior to installation in the focal plane array package. (Bottom left) Side-view of the fully-assembled focal plane array package mounted in a Bluefors LD-400 for array mapping with an LED-board. (Right) Wider view of the cryogenic readout chain diagrammed in Figure 3.2 from 4 K down to 100 mK.

pleted array were placed in a box with conical metal feedhorns, which was then mounted on the 100 mK stage of a Bluefors SD-250. This set-up allows for measurement with a cryogenic black-body source or with an external window that allows for optical access at a range of base temperatures down to ~ 58 mK when fully-closed or ~ 80 mK with windows in place. All data has been acquired with either an Agilent E5107C Network Analyzer or a Xilinx ZCU111 radio frequency system-on-a-chip (RFSoC) while using the cryogenic black-body or with the feedhorns taped over.

The TiN-detectors have primarily been measured using the completed first full array in a Bluefors LD-400. The primary focus of the testing has been on mapping the array with LEDs for post-fabrication editing [66], meaning that the array has been mounted with several LED PCBs and the requisite wiring on the front of the feedhorns. With this restriction, the bath temperature was limited to $\gtrsim 155$ mK during the bath temperature sweeps, which is higher than the expected operating temperature of 100 mK. All of the TiN data presented here has been acquired with the network analyzer.

3.2.1 Al Detector Overview

An extensive amount of data has been acquired with the Al "witness" pixels under a variety of bath temperature, optical loading, and tone power conditions. A sample trace from all five KIDs can be seen in Figure 3.5. All five resonators are between 500 MHz and 901 MHz. Measured coupling quality factors (Q_c) are in the range of 18,000 to 36,000, and under designed loading conditions, the total Qs ought to be the range of 8,000 to 20,000 with a few caveats. As is discussed further in sections 3.3 and 3.4, tone power optimization has a significant impact on both the measurable resonator parameters and the observed shape of the resonance circle, particularly at tone powers that are most relevant for operation. Since these effects on the line shape are not easily modeled, they significantly skew any resonator fits to systematically underestimate quality factors and rotate the impedance mismatch angle described in 2.3. Figure 3.6 shows

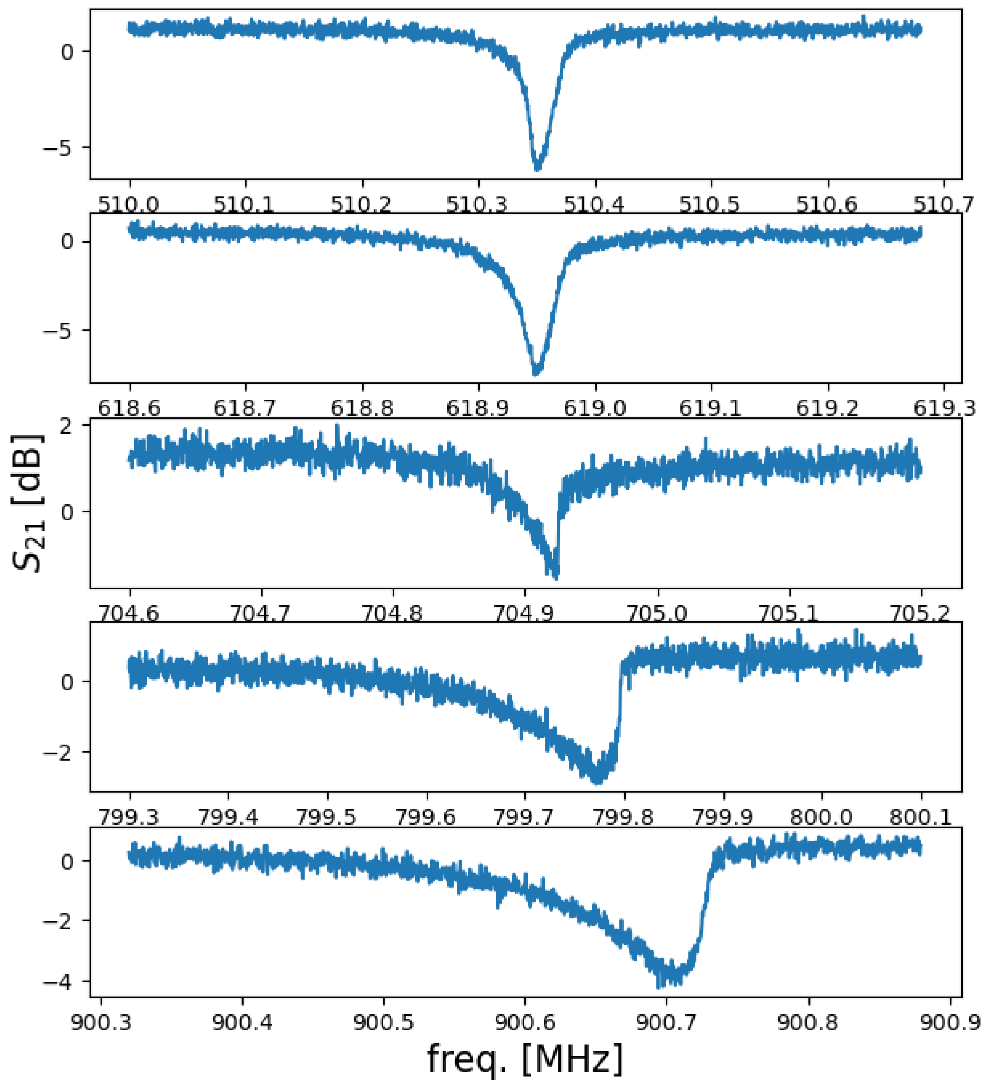

htbp

Figure 3.5: All five Al detectors from the witness pixel chip described above shown at 100 mK bath temperature under a 13 K blackbody load and with a VNA tone power of -44 dBm which is $\sim$ 1-2 dB below bifurcation for the top three resonators and $\sim$ 3-5 dB below bifurcation for the lower two detectors.

how going from low powers to higher powers pushes the KID from deeply in the Q_i-dominated regime ($Q/Q_c < 0.5$) through critical coupling ($Q/Q_c = 0.5$) to the Q_c-dominated regime ($Q/Q_c > 0.5$).

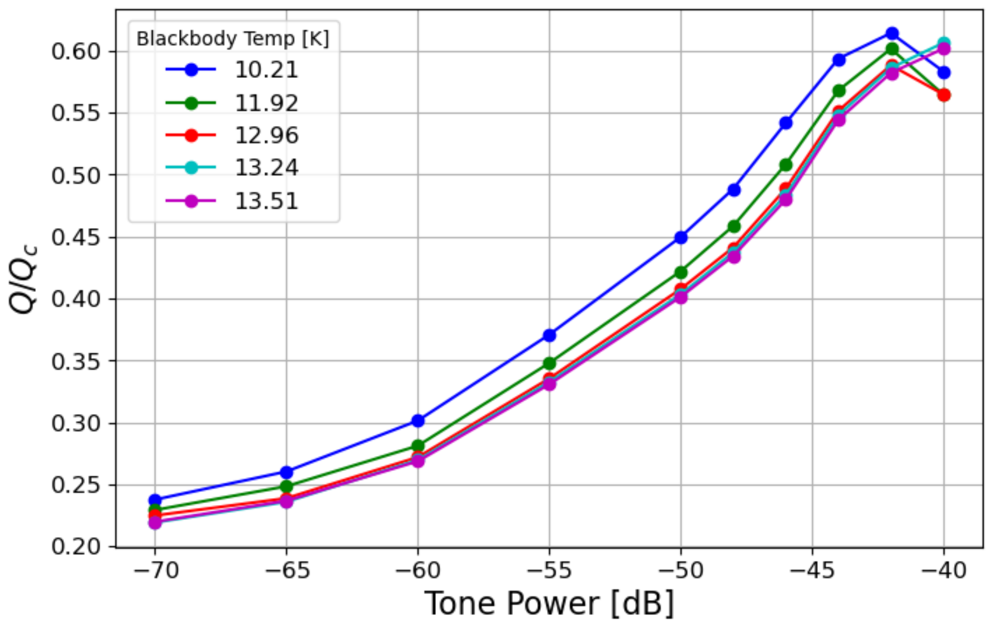

Figure 3.6: The ratio of the Q/Q_c as a function of raw probe tone power in dBm (not accounting for additional losses). Different colors correspond to cryogenic black-body temperatures and fits at the highest tone powers are somewhat unreliable. The noteworthy aspect here for tone-power optimization is that at each load temperature the changing tone power drives the resonator from being Q_i-dominated ($Q/Q_c < 0.5$) to Q_c-dominated ($Q/Q_c > 0.5$). Resonator noise is higher when operating in the Q_i-dominated regime.

Figure 3.7 shows the the resonator response to changing bath temperatures based on well-fit data, which is, by necessity, 15-20 dB below the optimal operating powers of the resonators. This "under-driving" of the resonators shows most significantly in the plots of the internal resonator loss, Q_i^{-1} (also sometimes written as tanδ_i), which is much larger and much less consistent between KIDS than it would be under optimal tone powers. Figure 3.8 shows more clearly the impact of "under-driving" the resonators, with color showing the power dissi-

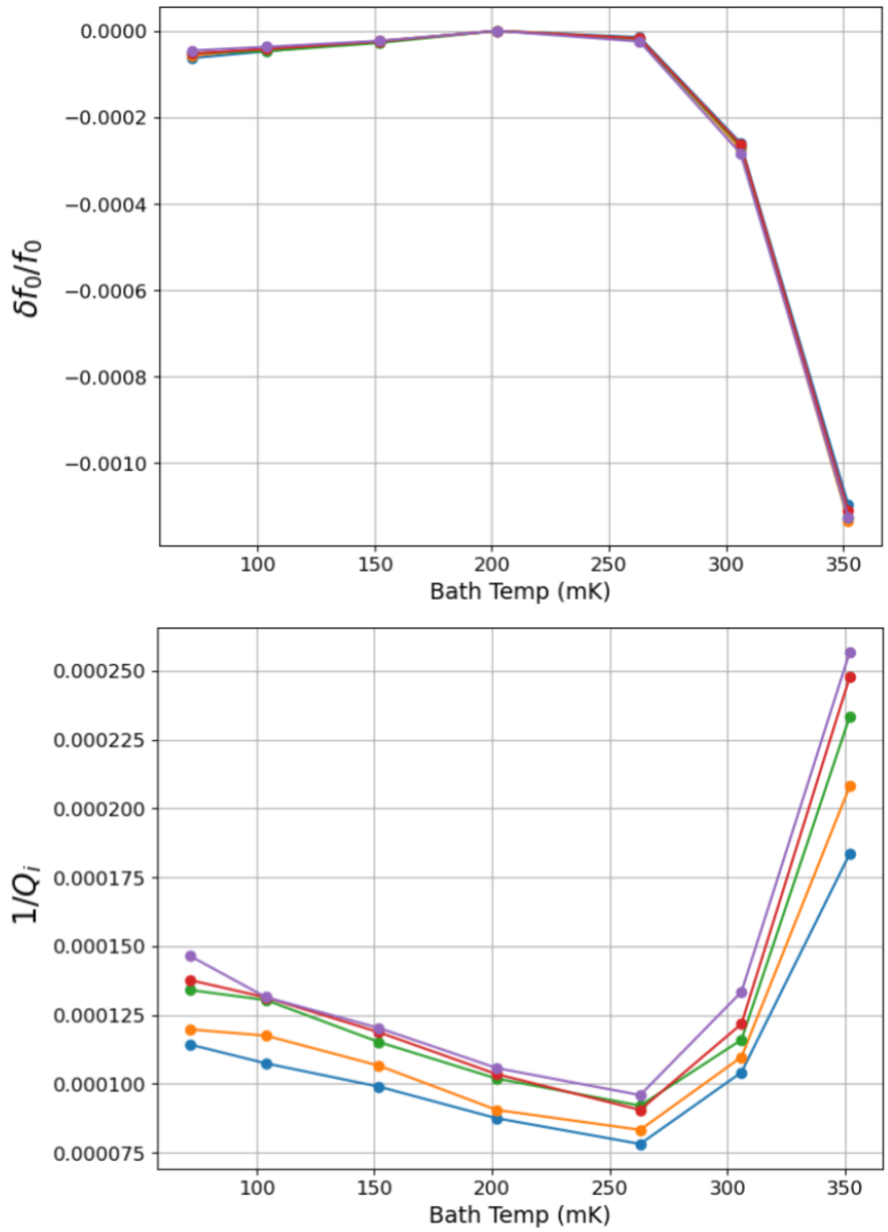

Figure 3.7: (Top) Fractional frequency shift vs. bath temperature based on fitted data from five Al detectors under a 3 K blackbody load and ~ 15 dB below bifurcation for ease of fitting. (Bottom) Internal loss (Q_i^{-1}) vs. bath temperature for the same fits. While both parameters are sensitive to tone power, the quality factors are much more-so, causing the relatively wide spread between these detectors in comparison to TiN fits.

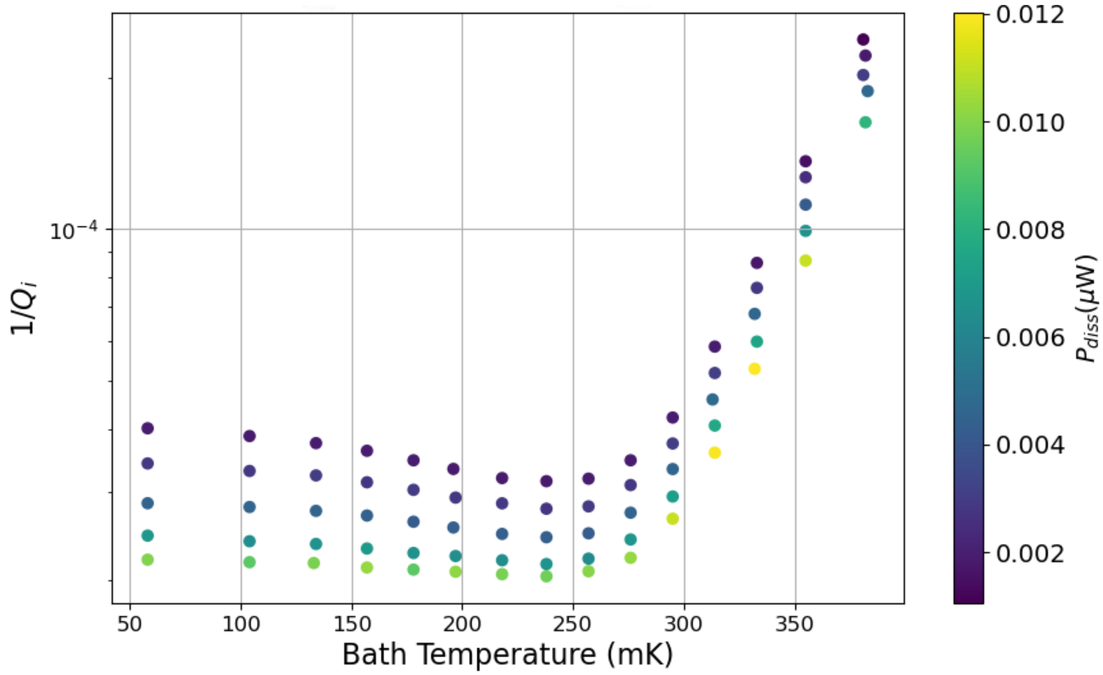

Figure 3.8: Internal loss over total resonator internal energy (Q_i^{-1}) for an Al resonator as a function of bath temperature on the x-axis and colored by internal power dissipated demonstrating sensitivity to power. The dissipated power is estimated using the total attenuation, probe tone power, and the S_{21} maximum dip depth. This sensitivity is what complicates the resonator fitting and tone-power optimization.

pated by the resonator, a proxy for tone power. In the most extreme cases, Q_i is varying by a factor of a few from low tone power to bifurcation.

3.2.2 TiN Detector Overview

The testing for the TiN array has been both more extensive and less controlled, given the constraints of the set-up for LED-mapping. Figure 3.9 shows an S_{21} sweep in dB for the band of resonators from network 5 used for more extensive testing with specific resonators used being starred. This narrow range was selected at random for purely practical reasons to reduce testing time given the

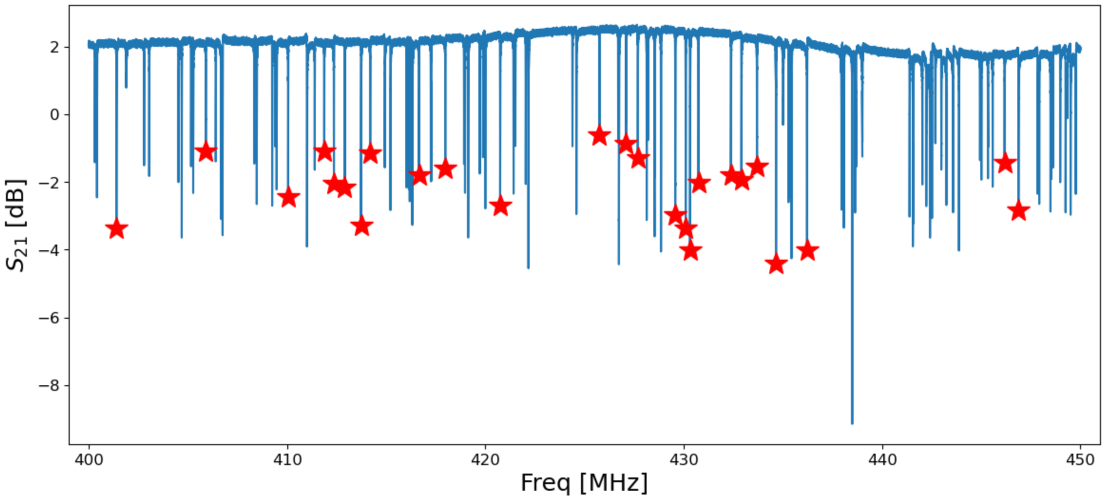

Figure 3.9: The narrow band used for bath temperature sweeps with the specific resonators starred. The sub-band data shown was acquired at 155 mK with estimated tone power of -94 dBm.

limited control over the detector environment in comparison to the Al KIDs. All of the starred resonators were well-fit across the full range of bath temperatures and powers. Measured coupling quality factors (Q_c) are in the range of 45,000 to 130,000, and under designed loading conditions, the total Qs are expected to be in the range of 5,000 to 10,000. This tends to put the resonators firmly in the undercoupled or Q_i-dominated regime, as can be seen in Figure 3.10. Even in the best conditions, which should be well-under the loading conditions expected on-site, very few of the resonators have a ratio of $Q/Q_c > 0.5$. Figure 3.11 shows the the resonator response to changing bath temperatures for a single resonator selected at random. These detectors show monotonic behavior that is not significantly influenced by tone power across the full range of bath temperatures observed. This can be contrasted with the Al KIDs seen in Figure 3.7 that show distinct extrema in both plots.

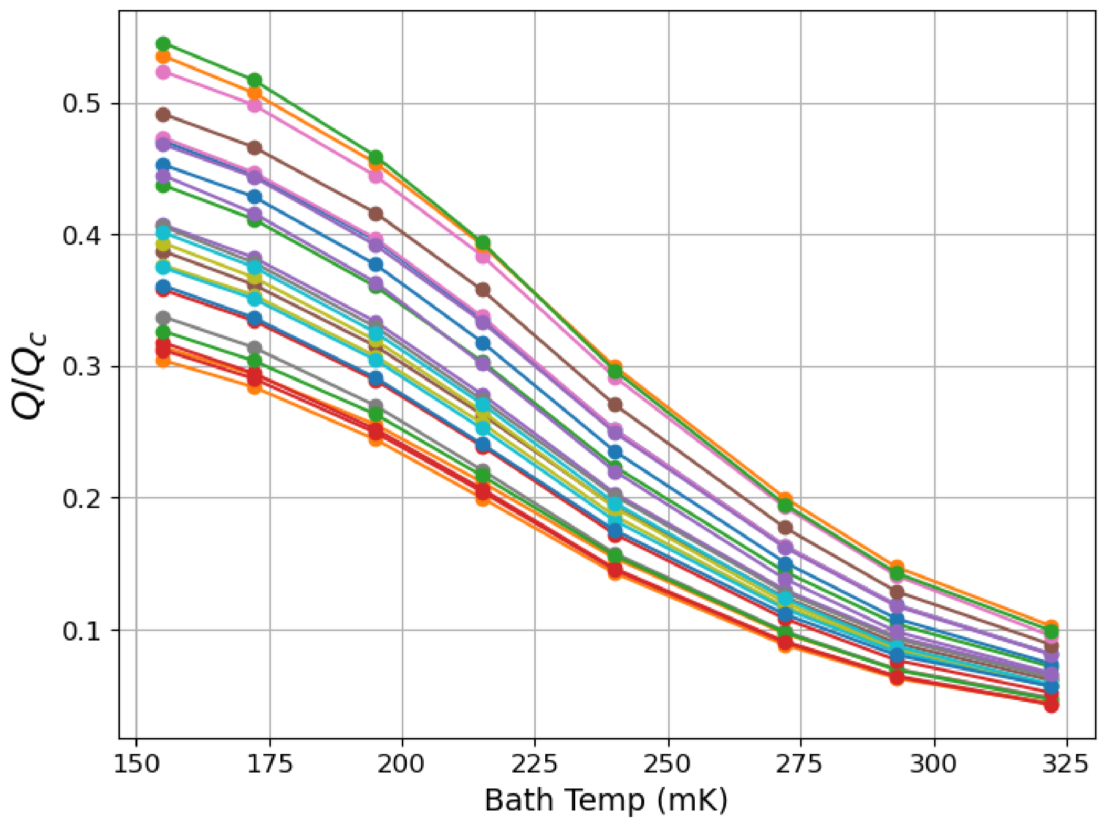

Figure 3.10: Plots of the ratios Q/Q_c (which is closely related to the dip depth) for all 25 TiN detectors as a function of bath temperature. We can clearly see that most of the resonators remain in the under-coupled, Q_i-dominated regime even at low-temperatures.

3.3 Preliminary Discussion

As stated at the start of section 3.2, lab testing of individual witness pixels and full arrays is ongoing at NIST and Cornell. With further detector editing planned prior to deployment, we can only make preliminary statements based on current detector performance. At this time, both detector designs are still planned for deployment. Yields for both types of arrays are expected to be 95% or better following LED mapping and post-fabrication editing [66], which is currently in progress for all three arrays. Measured quality factors, responsivity,

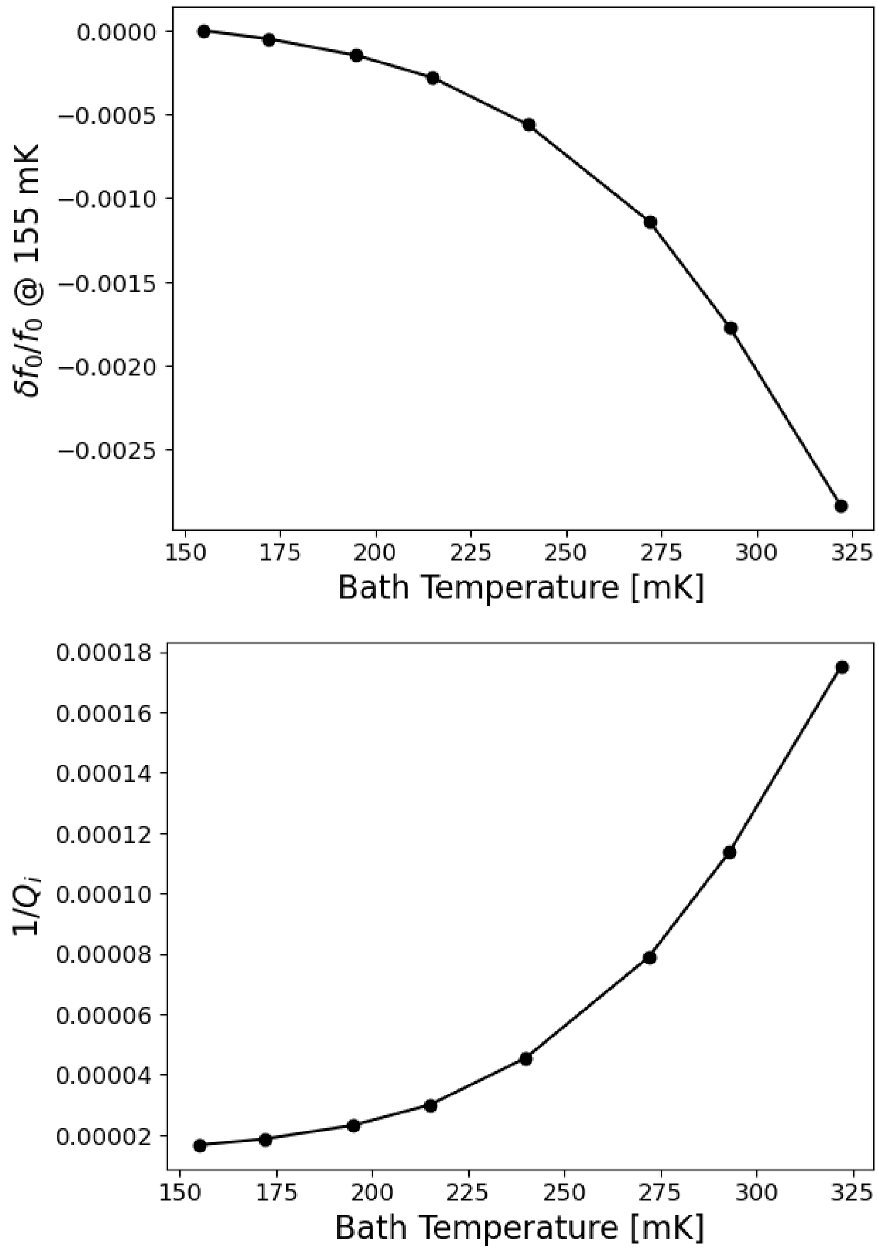

Figure 3.11: (Top) Fractional frequency shift vs. bath temperature for one of the TiN resonators. This resonator was chosen at random, since all of the resonators showed near identical response (as can be seen in Figure 5.14). (Bottom) Internal loss (inverse Q_i) as a function of bath temperature for the same resonator.

and noise have met expectations [21]. It is worth noting that, when optimally driven, the Al detectors have slightly higher internal quality factors under load (significantly higher when dark). While both detectors are expected to return science-grade data, there are several differences in performance that can be expected to impact operation or final map-making.

The noise profile of the two materials is distinct, particularly at low frequencies, which is one of the features that motivated a shift towards Al detectors. The Al detectors have been measured to have exceptionally low 1/f noise [11], whereas the TiN have a higher photon-activated noise contribution at low frequencies. This is particularly relevant for wide-field surveys and reconstructing large angular scales, as for science cases involving the cosmic microwave background.

Additionally, the different optical response curves of the materials has been well documented [38, 59]. While TiN KIDs show an unexpectedly linear response to optical illumination, Al detectors have a square-root dependence. This means detector tuning requirements during observations may differ between arrays.

One final point of discussion is the tone power sensitivity and nonlinearity, as touched on briefly in the preceding section, and with greater depth in the following section. Optimizing tone power is an integral part of achieving the highest signal-to-noise for KIDs in the field. It is generally preferable to read out KIDs at the highest tone powers attainable without reaching bifurcation, to both maximize signal-to-noise going into the first-stage amplifier and minimize TLS noise. On this count, it is useful that the Al detectors bifurcate at higher tone powers. However, as a result of the interplay between the nonlinear ki-

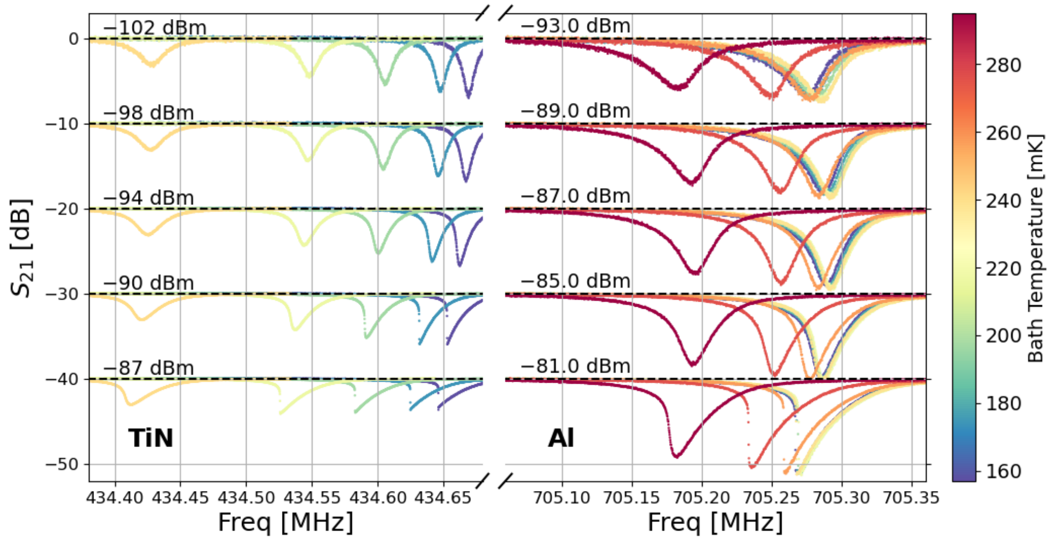

Figure 3.12: Typical response to changing tone power and bath temperature for TiN (left) and Al (right) with a 10 dB offset between powers for readability. The response of TiN is well fit accounting for nonlinear kinetic inductance [100], leading to a monotonic frequency shift with both tone power and temperature, while total Q decreases with increasing temperature and remains constant with tone power. In contrast, the Al resonant frequency increases between -93 dBm and -87 dBm, before decreasing at higher powers up to bifurcation, while the Q continually increases with tone power. Similarly, the Q and frequency increase with bath temperature up to $\sim$220 mK at all powers. Tone power is estimated at the detector and should be accurate within 3 dB.

netic inductance [100] and nonequilibrium quasiparticle dynamics [29], the Al detectors show more complicated interactions between tone power linearity, optical loading, and the observed resonator parameters, requiring careful tuning. Some of this is seen in Figure 3.12, which shows the non-monotonic relationship between tone-power and measured resonant frequency and Q. This also significantly distorts the resonator line shape, making it difficult to fit for these parameters. This sensitivity to tone power will very likely necessitate either frequent tuning as observing conditions vary, or resonator tone-tracking, which is planned for implementation after deployment [97]. How this will impact observing efficiency and on-sky noise performance remains to be seen.

3.4 Detector Nonlinearity

Given the distinct behaviors described in the preceding section and observed in Figures 3.12, 3.7, and 3.11, it is worth spending a bit more time on the nonlinear resonator response to probe-tone power. When describing resonator behavior, either linear or nonlinear, we are describing a single-pole Lorentzian that is parameterized by a center frequency and a quality factor. For the particular case of a capacitively-coupled resonator, as we previously saw in Equation 2.40, the transmitted signal, S_{21}, takes the form

$$S_{21} = 1 - \frac{Q}{Q_c}\frac{1}{1+2jQ\frac{f-f_0}{f_0}} = 1 - \frac{Q}{Q_c}\frac{1}{1+2jQx}, \tag{3.1}$$

where Q is the total quality factor, Q_c is the coupling quality factor, f_0 is the center frequency, f is the frequency being probed, and $x \equiv \frac{f-f_0}{f_0}$. In the complex, or Argand, plane this traces out a circle of diameter Q/Q_c that is centered at $(1-\frac{Q}{2Q_c}, 0)$. Given the definitions of Q and S_{21}, we also saw in Equation 2.85 that we can write the resonator's internal energy, E_r, as

$$E_r = \frac{2Q^2}{Q_c}\frac{1}{1+4Q^2x^2}\frac{P_r}{2\pi f_0}, \tag{3.2}$$

where P_r is the readout tone power. Critically, the probe tone appears here through both the tone power (P_r) and the frequency (through $x = \frac{f-f_0}{f_0}$). In the case of a linear resonator, the parameters f_0 and Q are stationary and each point on the resonance circle can be mapped back to the same values. If instead there is some dependance of circuit parameters on the internal energy, then we can see non-linear behavior, where, the underlying parameters are changing along with the tone power or frequency. This can be driven by a number of different underlying physical processes and can give rise to a wide range of behaviors, many of which are described in [103]. In general, however, we can refer to nonlinearities as either reactive (where f_0 is changing), dissipative (where Q is changing), or both. Reactive nonlinearities shift the position (often just referred to as the phase) on the resonance circle, while dissipative nonlinearities change the diameter of the circle and the circle-phase relationship to f.

3.4.1 Types of Nonlinearities

In Section 2.4.3, we described nonlinear kinetic inductance, how it can impact the resonant frequency through the inductance, and how this can impact the resonator shape and cause the resonator state to bifurcate. This is a purely reactive nonlinearity, and, when viewed on the resonance circle at higher powers, appears as a lop-sided jump in phase with no change in diameter. The asymmetry is caused by f_0 shifting monotonically to lower frequencies as the resonator energy increases. As f approaches f_0 from below ($x < 0$), x^2 decreases and E_r rises, pulling f_0 down in frequency at an increasing rate until eventually we jump over the center frequency and x^2 begins to increase again. On high-side, where $x > 0$, the resonator relaxes back into it's higher frequency state as E_r decreases, following the probe tone and causing the phase to evolve more slowly than it would otherwise.

Another source of nonlinearity with a well-defined impact is loss to two-level systems (TLS) [43, 81], described in Section 2.5.5 in the context of noise. At very low temperatures and tone powers, TLS fluctuations increases the overall loss, decreasing the Q. Crucially, this effect is reduced at higher temperatures and powers, allowing for nonlinearity. As the power stored in the TLS increases, the Q likewise increase such that the circle diameter reaches a maximum on resonance. This can cause the resonance circle to take on an oblong shape, appearing squashed on the sides. This effect is generally quite small by design, as the total loss is the sum of several contributions, chiefly the coupling loss (loss to the readout line), the loss to the quasiparticle system, and the TLS loss. Detectors are designed to operate in regimes dominated by coupling loss or quasiparticle loss. While this effect is included for completeness, it is not particularly relevant for the discussion at hand.[1].

Finally, quasiparticle absorption of microwave photons has been shown to lead to strongly nonlinear behavior [29, 30]. By driving quasiparticles out of thermal equilibrium, sub-gap microwave photons push the system away from the expected Fermi-Dirac distribution, as well as explicitly altering the density of states. Both of these appear when calculating the AC conductivity from the Mattis-Bardeen equations, allowing for tone power to alter the conductivity in both reactive and dissipative manners. While calculating these effects is beyond the scope of this work[2], we briefly describe the two scenarios that can be observed, which correspond to an effective "heating" or "cooling" of the quasiparticle system. It should be noted that, while these scenarios are observed in [29] to occur at different temperature regimes, they are sufficiently complicated that either "heating" or "cooling" can occur at a wide range of temperatures. In the case of quasiparticle cooling, quasiparticles are excited by the probe tone

[1]The most definite evidence that the nonlinear behavior described here is not due to a TLS nonlinearity are the strongly correlated reactive and dissipative nonlinearities, the lack of suppression with increasing bath temperature, and the near-identical temperature scaling for resonators on both ends of the band [43, 44, 78].

[2]For more detailed discussion of this approach, refer to [47, 52, 93, 102].

to recombine more rapidly than they would otherwise, causing both a reduction in loss (increase in Q) and kinetic inductance (increase in f_0). The increase in Q causes the diameter of the circle to increase as you approach resonance, while the increase in f_0 causes the probe frequency to approach resonance more slowly from below and more rapidly from above, leading to an asymmetry. In the case of quasiparticle heating, the excess energy in the quasiparticle system instead suppresses recombination, causing an increase in both loss and inductance in a manner similar to above-gap pair-breaking radiation. Decreasing the Q in this case squashes the resonance circle in the opposite manner to above, meaning that the diameter is at a minimum when on resonance. Decreasing the resonance frequency causes an effect similar to the nonlinear kinetic inductance, resulting in an asymmetry in the resonance circle of the same manner.

Since the kinetic inductance nonlinearity is monotonic and well-understood, we can account for it in a relatively straightforward manner when fitting a resonator. This is the case for the TiN KIDs. In cases where multiple observable nonlinearities arise from different, potentially opposing physical effects, this modeling becomes more difficult. For the Al KIDs these effects are severe enough to significantly alter the observed resonator profile and bias fits using either a standard linear model or a model incorporating nonlinear kinetic inductance. As such, it is useful to "unwrap" the resonance circle to show what nonlinearities most significantly impact the observed resonator shape.

3.4.2 Unwrapping the Resonance Circle

Beginning from a measurement of S_{21}, if we remove the factors that arise from the environment (i.e. the cables, amplifiers, etc.) and the impedance mismatch (the rotation angle of the external quality factor, Q_e), we can arrive back at the pure resonator expression[3]. Shifting our anchor point to the origin for convenience, we can rewrite this expression (which we call $\hat{s}_{res}$) in terms of the two parameters that ought to be linear:

$$\begin{aligned} \hat{s}_{res} = 1 - S_{21,res} &= \frac{Q}{|Q_e|} \frac{1}{1 + 2jQ\frac{\omega - \omega_0}{\omega_0}} \\ &= \frac{A(\omega)}{1 + 2jy(\omega)} \,. \end{aligned} \tag{3.3}$$

Here, $A = Q/|Q_e|$ is the diameter of the resonance circle (related to the dip depth) and $y = Q\frac{\omega-\omega_0}{\omega_0} = Qx$ is the distance from the center frequency as measured in line-widths. For a linear resonator, A will be constant and y will be linear in frequency with the slope set by the Q and the zero value set by $\omega_0 = 2\pi f_0$. With the environment and impedance mismatch accounted for, we can convert a position in the complex plane to an implied A and y, thus, we can use these to fit for Q, f_0, and $|Q_e|$. From Equation 3.3, we can calculate

$$y(\omega) = -\frac{1}{2}\frac{\mathfrak{Im}(\hat{s}_{res})}{\mathfrak{Re}(\hat{s}_{res})} \tag{3.4}$$

and

$$A(\omega) = \left[1 + \left(\frac{\mathfrak{Im}(\hat{s}_{res})}{\mathfrak{Re}(\hat{s}_{res})}\right)^2\right] \mathfrak{Re}(\hat{s}_{res}), \tag{3.5}$$

where $\mathfrak{Re}(\hat{s}_{res})$ and $\mathfrak{Im}(\hat{s}_{res})$ are the real and imaginary parts of $\hat{s}_{res}$, respectively. Using these expressions to identify trends in Q and f_0 does require a good estimation of and proper accounting for environmental effects. Additionally, the

[3]Figure 2.6 shows an example of the types of effects that need correcting to give our resonator the expected form.

appearance of $\mathfrak{Re}(\hat{s}_{res})$ in the denominator of both Equation 3.4.2 and Equation 3.4.2 means that the impacts of noise on calculated parameters becomes much larger for smaller resonance circles or farther away from resonance.

One final improvement to separating out reactive and dissipative nonlinearities in these plots is to plot $y_c = y/A = Q_c \frac{\omega-\omega_0}{\omega_0}$ rather than y, since Q_c generally does not change with tone power. We can think of this as now measuring the distance in terms of coupling line widths rather than resonator line widths. This is particularly useful in the presence of a dissipative nonlinearity when the resonator is more strongly Q_i-limited than in the data presented here, such as at higher bath temperatures or optical loading.

3.4.3 Nonlinearity Measurements

Turning our attention to the data, in Figures 3.13 and 3.14 we can see the standard kinetic inductance nonlinearity appearing in one of the TiN detectors. Figure 3.13 shows that the resonator remains on the same circle at all powers, though as we pass bifurcation there is a jump in phase. This is confirmed in Figure 3.14, where we have used the data from Figure 3.13 to calculate y and A for all points on the circle. We see a flat quality factor on the bottom, while the reactive nonlinearity in observable as a small distortion in y even well before bifurcation. This is reminiscent of the archetypal plot from [100] reproduced in Figure 2.8.

Let us now turn our attention to similar data from one of the Al KIDs in Figures 3.15 and 3.16. Even before moving to the nonlinearity parameters, it is possible to see the distortions in the Argand plane that are signatures of both

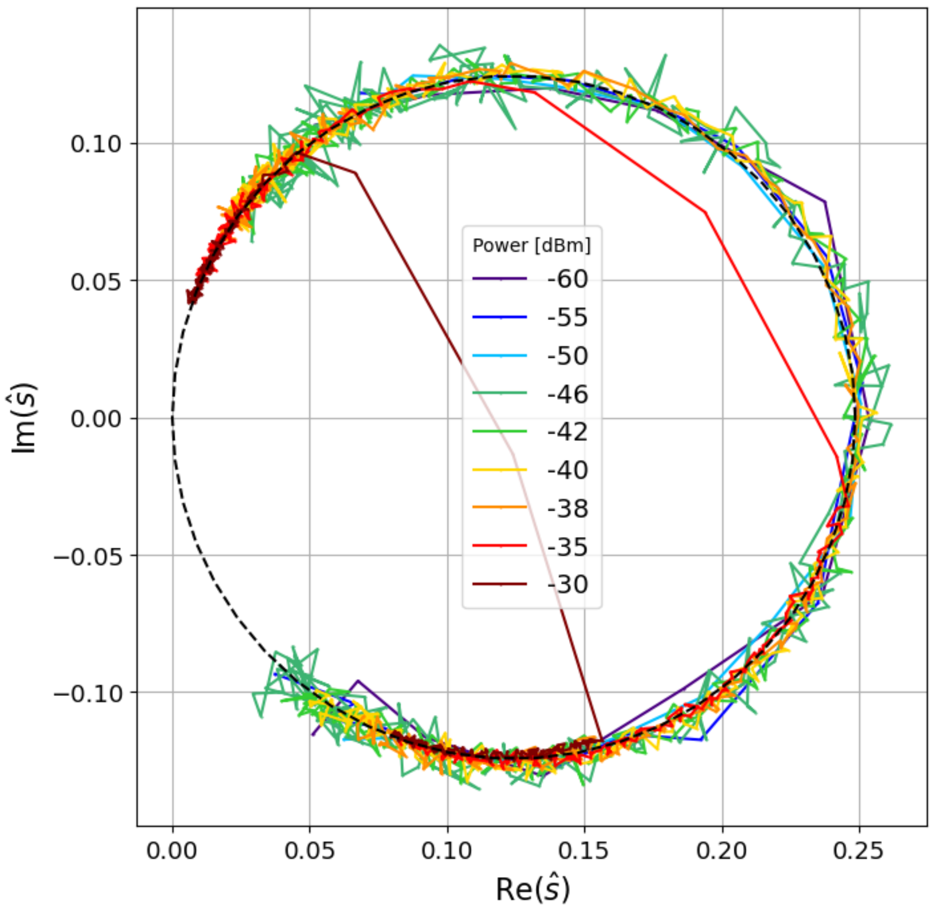

Figure 3.13: Transformed resonance circles as a function of raw tone power for a typical TiN detector. Note that for comparison with the Al-detectors in Figure 3.15, the total attenuation seen here is ∼13 dB higher and no averaging was used with this data, which is why the noise is significantly larger. The lowest tone powers are binned down to a lower frequency resolution, which is why the data gets less noisy at tone powers < 50 dBm. A fit resonance circle (dashed line) is shown for visual reference.

nonlinear kinetic inductance and quasiparticle "cooling." The resonance circle is expanding and pinching asymmetrically on the sides, while at the highest powers we see nonlinear kinetic inductance causing bifurcation.

Things become more clear in Figure 3.16, which shows A and y_c. In y_c it is clear that the coupling Q is not changing dramatically as the resonator is

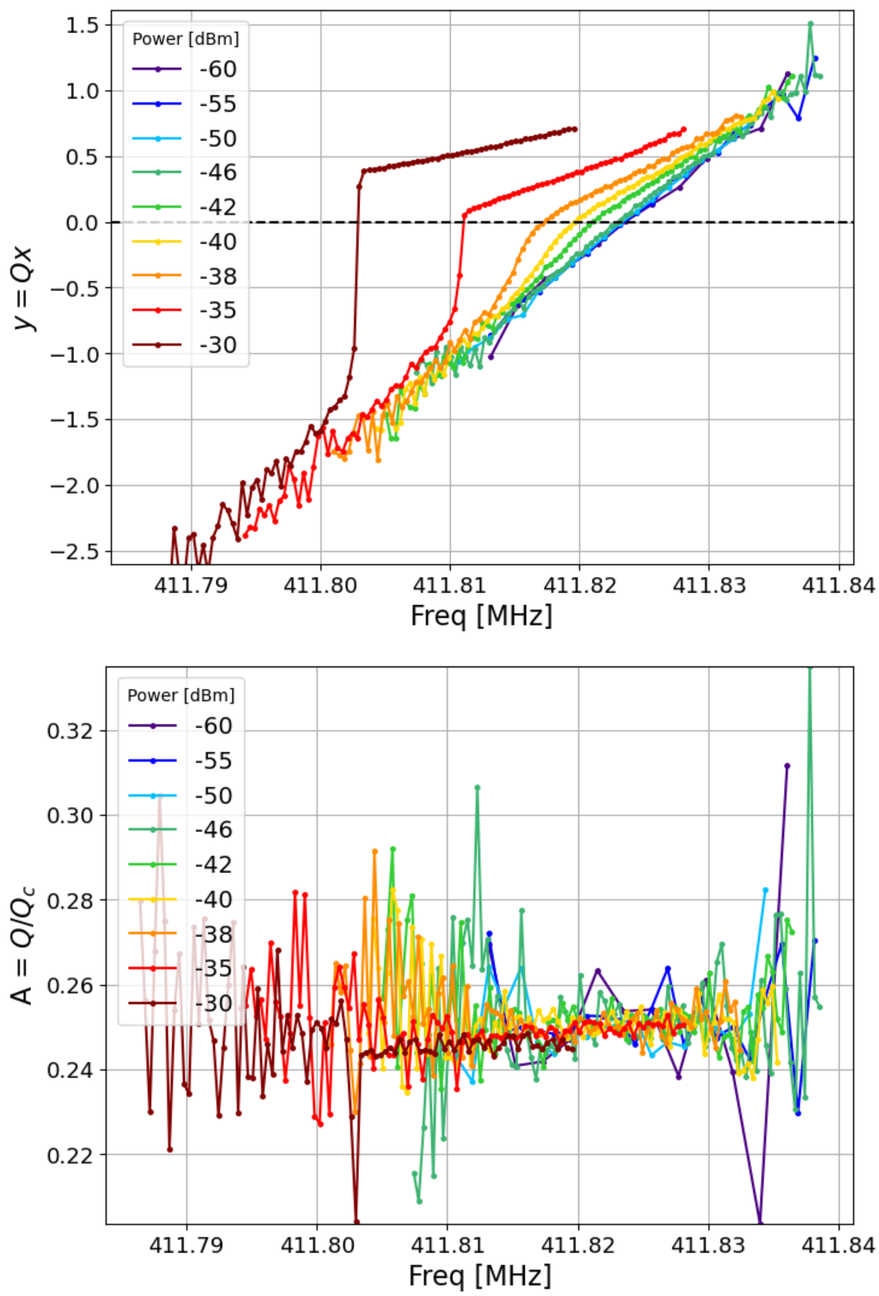

Figure 3.14: Resonance circles from 3.13 re-projected into the resonator parameters $A(\omega)$ and $y(\omega)$. As seen with the stability of the resonance circles in 3.13, the TiN detectors are well-modeled as having a purely reactive, monotonic non-linearity.

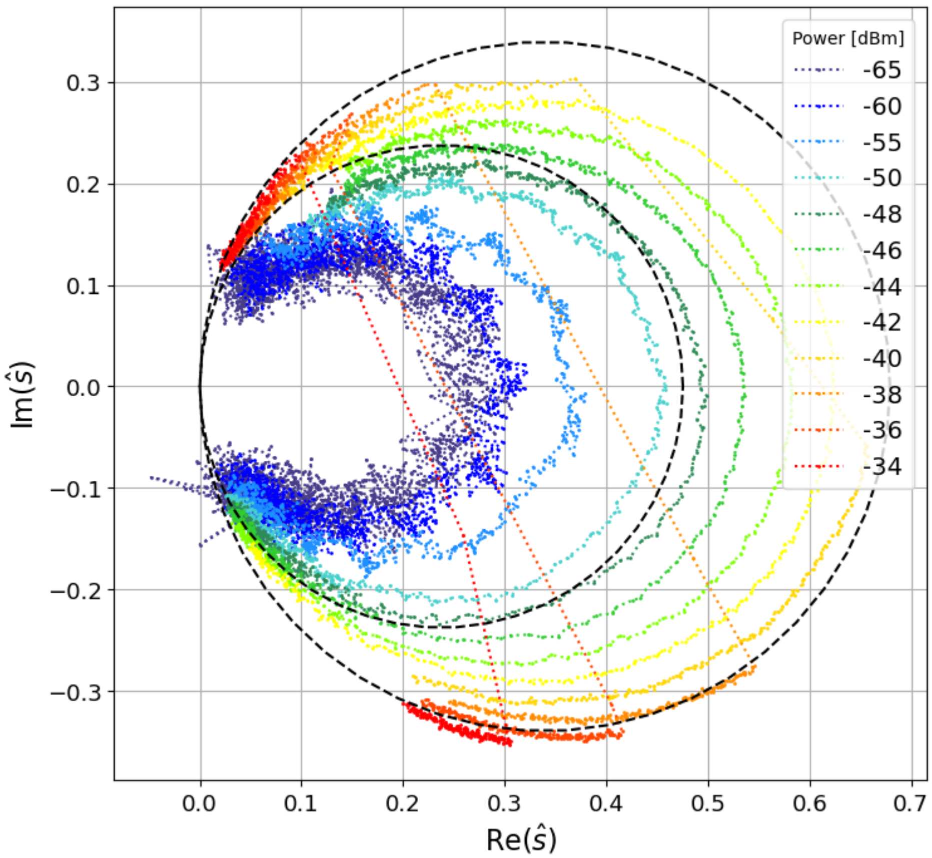

Figure 3.15: Transformed resonance circles as a function of raw tone power for a one of the Al detectors. We can immediately see the more complicated behavior than with the TiN detectors. The resonance circle is squashed into an asymmetric ”tear-drop” shape at higher powers and the diameter increases significantly with tone power. The dashed circles are included for visual reference.

being driven between two parallel states. At low powers, we observe a deformation that is similar to that seen from nonlinear kinetic inductance, except that this nonlinearity is occurring in the opposite direction. At higher powers, we observe the nonlinear kinetic inductance begin to flatten the response and eventually drive the resonant frequency back down in the opposite direction. This is corroborated by the plot of A, which shows the resonator beginning in a strongly Q_i-dominated regime and continually driven up into a strongly Q_c-dominated regime. We also see which way the resonance is being pushed by

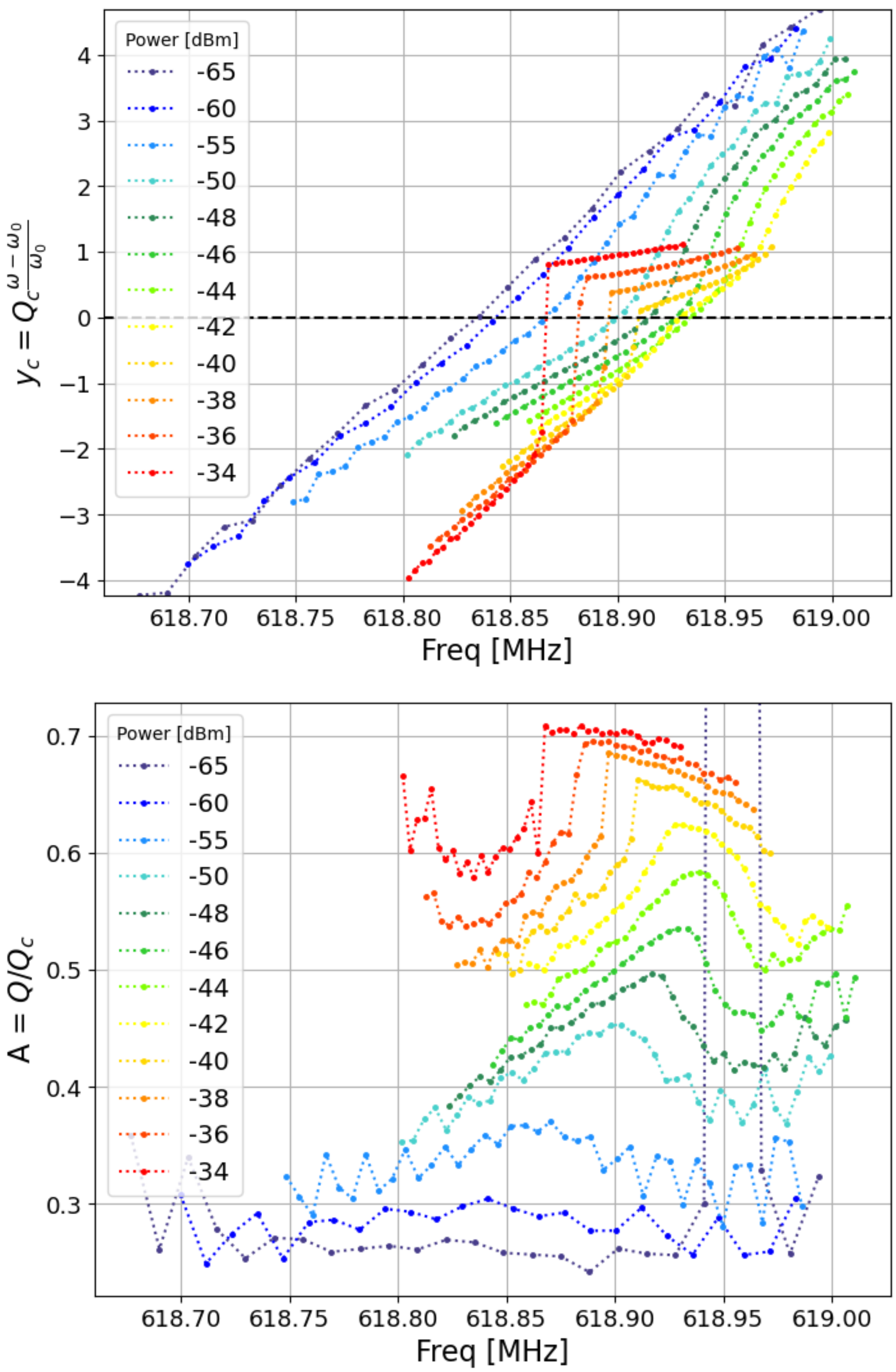

Figure 3.16: Plots of A and y_c from previous Al resonance circles with both reactive and dissipative nonlinearities. You can see a transition between nonlinear effects as the deformation in y_c changes directions with increasing power.

the asymmetry in A, where at lower powers there is a gradual increase in Q as we approach the center frequency, followed by a sharper drop off after passing it, as the resonator snaps back to its low power, low frequency state. At high powers however, the opposite occurs, the resonance is pulled down sharply and then follows the probe tone gradually as is typical of the kinetic inductance non-linearity.

CHAPTER 4

CRYOGENIC READOUT OF KIDS

Having previously considered the production and detection of astrophysical signals in kinetic inductance detectors, we now discuss the cryogenic readout design and how signals are recovered for processing outside of the receiver cryostat. In order to reach the combination of detector density, high total detector count, and low-noise while operating at 100 mK, the cryogenic readout must be carefully optimized with multiple, competing constraints. In a single 280 GHz or 350 GHz Instrument Module, we need to read out the signal of approximately 10,000 detectors at rates of $\sim$500 Hz, while maintaining low noise and a minimal thermal load. In addition, the design must be robust through multiple assemblies and for years-long operation on a telescope platform that is continually moving to scan all available regions of the sky. Finally, the readout needs to pass through multiple layers of shielding at various temperature stages without compromising those interfaces. In this chapter, we describe the cold readout for Prime-Cam's 280 GHz and 350 GHz Instrument Modules, as well as the various requirements and considerations that impacted the cryogenic readout designs, particularly noise performance, thermal loading, and mechanical/assembly constraints.

4.1 Readout Noise

The most critical role of the cold readout is ensuring that a probe signal can be sent to the detector arrays and measured without adding significant noise power or distortion to the data. In an ideal system, the readout noise will have a flat spectrum and can be characterized by an effective noise temperature, which is the temperature of a black body emitter that emits the observed level of noise power. Random thermal motion within the various components of the readout chain will produce white noise, referred to as Johnson-Nyquist noise, that scales with the physical temperature of the component and the bandwidth being measured. As the probe tone and signal propagate through the system, not only is it being modulated according to the scattering parameters, but it is also picking up this additive noise power due to the thermal fluctuations of charge carriers about the mean. We can work around this by arranging our network to substantially attenuate thermal noise from higher temperature stages on the input side and amplify the detector signal with a cryogenic low-noise amplifier at 4 K.

In an ideal scenario then, we would start with a probe tone of arbitrary power, attenuate it (along with the thermal noise) substantially at each successive temperature so that our thermal noise background at the detectors is $\sim$100 mK, connect these in a lossless manner to a low noise amplifier (LNA), and then amplify the signal once more arbitrarily high above the thermal background. However, practical limitations in the available tone power, the dynamic range of the amplifiers and analog-to-digital converters (ADCs), and the cost and thermal performance of various readout elements need to be balanced against the desired noise level when optimizing for real world performance.

In practice, this means that we need to match the tone power attenuation on the input to the ratio of the warmest and coldest stages (in our case 300 K to 100 mK requires roughly 35 dB of attenuation), as well as ensure the first stage cryogenic amplifier is suitably low noise to meet our needs. We can gain a better understanding of this and arrive at an estimate of the readout noise contributions from both the thermal fluctuations and the amplifier by following the noise through the signal chain a bit more formally.

4.1.1 Thermal Noise

It can be shown that the root mean square value of the thermal voltage fluctuations, V_n, will be [87]

$$V_n = \sqrt{\frac{4hfBR}{e^{hf/kT} - 1}}, \tag{4.1}$$

where B is bandwidth of the system, f is the center frequency of the bandwidth, R is the resistance of the system, and T is the physical temperature. In the Rayleigh-Jeans limit where $kT \gg hf$, this simplifies to

$$V_n = \sqrt{4kTBR} \tag{4.2}$$

from which we can also work out the power per unit bandwidth transferred to a matched load ($R = R_L$):

$$P = \frac{V_n^2}{4R} = kT\ . \tag{4.3}$$

In our system, all impedances are matched to $Z_0 = 50\ \Omega$.

Now let us can consider a network element with gain, G (or attenuation, $A = 1/G$), such as an attenuator. The noise temperature (T_N) for a passive, lossy two-port device with gain $G < 1$ is given by [87]

$$T_N = \frac{1-G}{G}T = (A-1)T \tag{4.4}$$

where T is the physical temperature of the component. The output from this element includes the input power and noise from the device itself multiplied by the gain. Accounting for this new noise power yields the following expression for the effective noise temperature at the output, T_{out}.

$$T_{out} = G(T_{in} + T_N) = \frac{T_{in}}{A} + \left(1 - \frac{1}{A}\right)T \tag{4.5}$$

Here, T_{in} is the input noise temperature, representing the power at the input of the device.

We can follow this process all the way through the chain to arrive at an effective noise temperature for the full input side of the system. If we have n total components with the i^{th} component having temperature T_i and attenuation A_i, the effective noise temperature of the system, T_{sys} will be

$$T_{sys} = \frac{T_{room}}{\prod_{i=1}^{n} A_i} + \sum_{i=1}^{n} \left(1 - \frac{1}{A_i}\right) \frac{T_i}{\prod_{j=i+1}^{n} A_j} \,. \tag{4.6}$$

This is referred to as the noise cascade equation. We can see that, for components where the attenuation is quite small, such that $A_i \approx 1$, the contributions to the effective noise temperature is negligible. This is particularly true for those components that are followed by a large amount of attenuation. Thus, we can get a very good estimate for the thermal noise on the input side of the system just by including the attenuators and any particularly lossy cables. This also provides good motivation for using extremely low loss superconducting cables between the detectors and the first stage amplification.

4.1.2 Amplifier Noise

After sending the probe tone through the array with high signal to noise, the primary goal is to boost that signal to such an extent that the remainder of the readout chain, which is necessarily at higher temperatures, does not add significantly to the noise. To that end, the first stage low noise amplifier (LNA) is perhaps the single most critical component in the cold readout chain. Unlike with passive devices such as attenuators, there is not a straightforward relationship between the noise temperature and the physical temperature and gain of the LNA. As such, the noise temperature of an amplifier generally needs to be measured and is one of the critical specifications provided by the manufacturer. In Prime-Cam's 280 GHz Instrument Module, the LNAs are expected to have noise temperatures of 2 K–4 K, while operating at a physical temperature of 4 K[1].

We have already seen one expression for the amplifier noise in terms of noise equivalent power (NEP) in chapter 2, but we arrive at it here from the perspective of noise temperature as described above. Thermal Johnson-Nyquist noise affects the LNA just as other components, including through thermal fluctuations in the bias voltage. The voltage power spectral density (PSD) of this thermal noise looks like

$$S_V^{amp} = 4kT_a Z_0 \tag{4.7}$$

where T_a is the noise temperature of the amplifier. More accurately, T_a should account for the effective temperature of the system up to the LNA with the amplifier noise temperature being the dominant term if designed correctly. In practice, the LNA noise temperature needs to be determined experimentally regardless of the specifications, and the input noise contributions can naturally be included in these measurements. In our system, the noise temperature seen at the input to the amplifier, T_{sys}, is generally designed to be around $T_a/10$, meaning that it adds $\sim 10\%$ to the overall readout noise (which is subdominant to the detector noise).

In order to compare the readout noise to the detector noise contributions from Section 2.5, we need to convert our voltage PSD, S_V, into a frequency PSD,

[1]Groppi Labs, Arizona State University, Tempe, AZ 85287 USA, www.thz.asu.edu

$S_{\delta f_0}$. This requires calibration through the scattering parameters using

$$S_{\delta f_0}^{amp} = S_V^{amp} \left(\frac{dV_{out}}{df_0} \right)^{-2} . \tag{4.8}$$

From the definition of S_{21} as the ratio of V_{out} to V_{in}, we can rewrite the calibration factor, $\frac{dV_{out}}{df_0}$, as

$$\frac{dV_{out}}{df_0} = V_{in} \frac{dS_{21}}{df_0} . \tag{4.9}$$

Using Equation 2.40 - with the assumption that we have already removed the cable calibration terms - we can write out $\frac{dS_{21}}{df_0}$ as

$$\frac{dS_{21}}{df_0} = -2j \frac{Q_r^2}{Q_c} \frac{f}{f_0^2} \frac{1}{(1 + 2jQ_r \frac{f-f_0}{f_0})^2} . \tag{4.10}$$

Assuming that we are near resonance such that $Q_r(f - f_0)/f_0 \ll 1$ and $f \approx f_0$, the final term goes to unity and one factor of f_0 cancels. We can then plug that expression into Equation 4.8:

$$\begin{aligned} S_{\delta f_0}^{amp} &= 4kT_a Z_0 \left(\frac{1}{V_{in}^2} \frac{Q_c^2 f_0^2}{4Q_r^4} \right) \\ &= \frac{kT_a}{P_r} \frac{Q_c^2 f_0^2}{Q_r^4} \end{aligned} \tag{4.11}$$

where $P_r = V_{in}^2/Z_0$ is the RF tone power at the input to the amplifier. In the case where we the total quality factor is limited by the coupling quality factor, this further simplifies to

$$S_{\delta f_0}^{amp} = \frac{kT_a}{P_r} \frac{f_0^2}{Q_r^2} , \tag{4.12}$$

however, as this is not always the case for Prime-Cam, we will not use this simplification.

With these expressions in hand, we can convert the frequency PSD to an NEP using Equation 2.91

$$NEP_{amp} = R_{freq}^{-1} \frac{Q_c f_0}{Q_r^2} \sqrt{\frac{kT_a}{P_r}} . \tag{4.13}$$

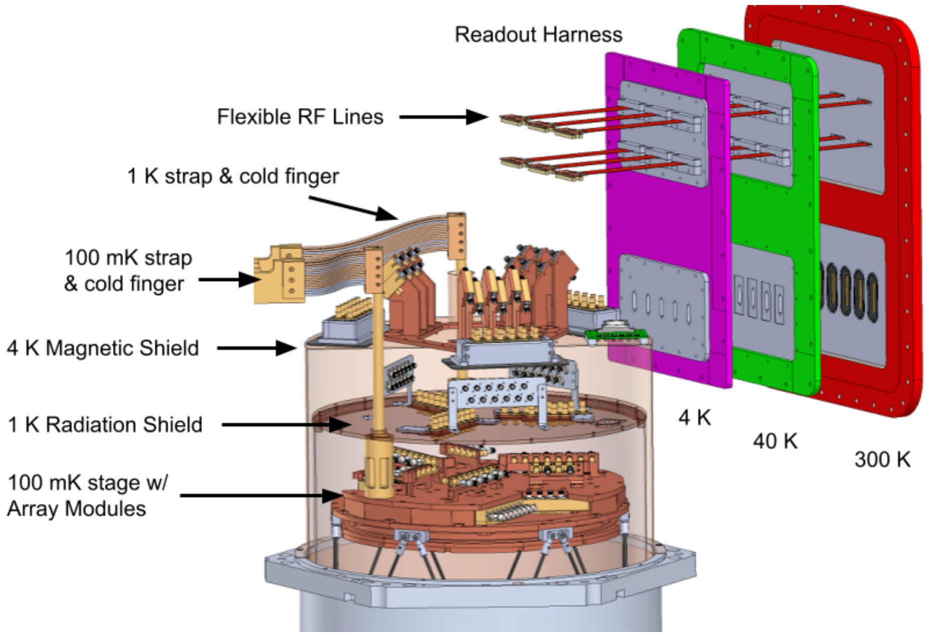

Figure 4.1: The entire cryogenic readout chain in Mod-Cam, including the instrument module (shown in cut-away view) and readout harness components. Each separate color in the readout harness represents a different temperature stage. The transition between the flexible stripline of the readout harness and coaxial cabling is not shown. As can be seen by comparison with later figures, this represents a slightly outdated design for several components, though the general layout has not changed. Figure reproduced from [107].

Finally, we can plug in our frequency responsivity, $\frac{df_0}{dP_{abs}}$, either measured or from Equation 2.76 or 2.80 to get an expression for the readout noise that is a bit more useful than that presented in Chapter 2 (found in Equation 2.102).

4.2 Instrument Module Readout Overview

When deployed on Prime-Cam, the 280 GHz and 350 GHz Instrument Modules will each contain roughly 10,000 detectors split across three arrays each with six networks (a total of 18 networks per module). Prior to the design of any individual module's readout (or even the final decision to employ KIDs), the design heritage from the Simons Observatory's Large Aperture Telescope Receiver (LATR) [117] and the choice for a modular layout of Prime-Cam set strict constraints on the overall mechanical and network layout, while also fixing the total cooling power available below 4 K and the available optical footprint.

Beyond these initial design constraints, Prime-Cam's higher frequency coverage in comparison to the SO LATR provides the opportunity for higher detector counts and a correspondingly higher number of readout networks. While the focal plane architecture and thermal loading per detector was significantly simplified by opting for kinetic inductance detectors rather than the transition edge sensors that the SO design was built around, the practical limitations of these detectors also reduce the optimal multiplexing factor from roughly 1,000 per line [92] to around 600 per line [97]. This results in a total of 18 networks for each polarimetric module at 280 GHz and 350 GHz.

In both Mod-Cam and Prime-Cam, the layout can be broken down naturally between the components mounted on or within the instrument modules (which includes components between 4 K and 100 mK), a shared readout harness spanning 300 K to 4 K, and an isothermal 4 K transition to connect the two. This network layout is shown schematically in Figure 4.2. Magnetic shielding is placed around each instrument module at 4 K, leaving a cylindrical volume behind each focal plane that is approximately 41 cm in diameter and 17.5 cm in depth for mounting all readout and associated mechanical components below 4 K. While the instrument modules are fully shared between both receivers, the readout harness and isothermal transitions are modified in Mod-Cam to accommodate its unique layout and purpose as a flexible testbed. The room temperature microwave frequency multiplexed readout system for Mod-Cam and

Prime-Cam is currently in development, and is designed to run on the Xilinx ZCU111 Radio Frequency System on a Chip (RFSoC) [97].

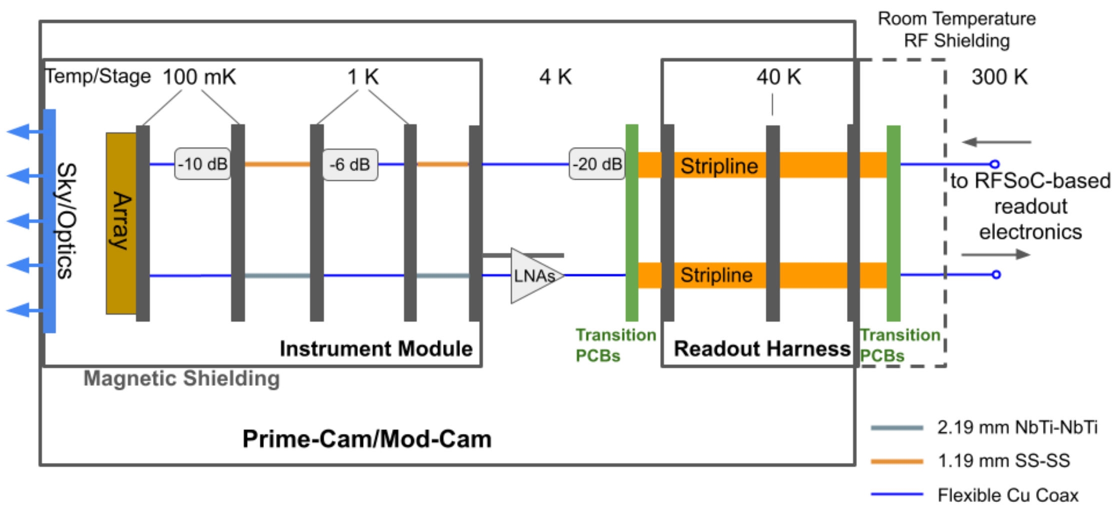

Figure 4.2: Network layout for the 280 GHz and 350 GHz instrument modules within both Prime-Cam and Mod-Cam, excluding the majority of the warm readout electronics. The cold readout is naturally separated into the instrument module and readout harness as shown here. Once outside of the receiver, the networks connect to an RFSoC-based readout system as described in [97], which also includes variable attenuators and additional room temperature amplification.

4.3 Network Summary

Taking a closer look at the network layout for the 280 GHz and 350 GHz instrument modules, Table 4.1 summarizes the primary components of the input chain and their contributions to the expected thermal noise seen at the LNA. As described in 4.1.1, the dominant contributions to the thermal noise are the attenuators at the 4 K, 1 K, and 100 mK stages. All semi-rigid coaxial cables and flexible stripline before the detector array are included, as these account for the majority of the remaining attenuation. Additionally, the superconducting cables between the output of the detectors and the input to the LNA are included to provide scale for loss and thermal noise added in that stage.

All of the NETs were calculated using Equation 4.6. Models for the semi-rigid coaxial cable thermal conductivity and temperature- and frequency-dependent attenuation were calculated using [20, 24, 74]. Estimates for the thermal conductivity and attenuation of the flexible stripline circuits were determined from [75, 108]. When calculating the NET contributions of the bridging components between temperature stages, the intermediate stage temperatures were estimated using these thermal models with the resulting numbers being 195 K for the connection from 290 K to 40 K, 29 K for the connection from 40 K to 4 K, 3.1 K for the connection from 4 K to 1 K, and 740 mK for the connection from 1 K to 100 mK.

For the semi-rigid coaxial cables, we are using 1.19 mm outer diameter stainless steel prior to the detectors and 2.19 mm outer diameter niobium-titanium cables between the array and the LNA [24]. The predominant considerations for the choice of materials were the attenuation and the passive thermal loading on the colder stages of the receiver. Prior to the detector array, stainless steel was chosen for use between temperature stages rather than copper-nickel cables due to the significant reduction in passive thermal loading. The expected thermal loading numbers are shown in Table 4.2[2] This will become increasingly important as we increase the number of instrument modules in Prime-Cam, but the design shown here remains well within the thermal budgets for a fully-populated Prime-Cam. A more thorough discussion of the considerations for

[2]Based on figures calculated with the code from https://github.com/ASU-Astronomical-Instrumentation/CryoChainCalc.

Table 4.1: A summary of all of the principal cryogenic readout components leading up to the first stage amplifier. The first column shows the temperature stage or stages that the component is connected to. The second column shows the expected loss in dB for the given component at 500 MHz (with 1 GHz shown in parentheses). The third column shows the expected contributions in mK to the NET at the input of the LNA using Equation 4.6. These estimates all assume just 0.5 dB of loss in the detector package, which is on the very low end of reasonable. The deeper the resonator dip, the lower these estimates become as the array further attenuates any thermal noise that precedes it. The key takeaways are that the attenuators and room temperature readout dominate the NET and the anticipated NET is well below that of the LNA. All additional components (including feedthroughs and hand-formable coaxial cables) are expected to contribute a few percent (or less) in total to the real NET. This is similar to or smaller than the uncertainties in the effective temperatures and attenuation values used.

Component	**Temperature [K]**	**Loss @ 0.5 (1) GHz [dB]**	**NET @ LNA [mK]**
Warm Readout	290	–	34
Stripline	290, 40, 4	1 (2)	5
4 K Attenuator	4	20 (20)	65
SS-SS to 1 K	4, 1	0.55 (0.75)	8
1 K Attenuator	1	6 (6)	57
SS-SS to 100 mK	1, 0.1	0.5 (0.7)	8
100 mK Attenuator	0.1	10 (10)	78
Detector Package	0.1	0.5–5	$\gtrsim$11
NbTi-NbTi to 1 K	0.1, 1	< 0.05 (< 0.05)	< 8
NbTi-NbTi to 4 K	1, 4	< 0.05 (< 0.05)	< 35
Estimated Total	–	**38 dB (39.5 dB)**	**$\sim$311 mK**

semi-rigid coaxial cable materials can be found in [62].

Looking past Table 4.1, the LNAs are expected to all have a gain of 28-32 dB in this frequency range. With a noise temperature of 2–4 K, this total gain moves the noise floor to between 6 and 13 dB above the room temperature noise. The remaining components in the cryogenic and warm readout are thus designed to keep the total loss below 3 dB until reaching the RFSoC enclosures, at which

Table 4.2: Expected thermal loading from readout components at each of the 4 K, 1 K, and 100 mK stages of the 280 GHz instrument module. The right column quotes the thermal loading for a total of 18.

Component	**Cold Temp. Stage** [K]	**Thermal Cond.** [μW cm/K]	**Cable Length** [cm]	**Cable Diameter** [mm]	**Thermal Loading** [μW]
LNAs	4	–	–	–	92,000
SS-SS to 1 K	1	8.4	16	1.19	28
SS-SS to 100 mK	0.1	1.0	14	1.19	1.2
NbTi-NbTi to 1 K	0.1	2.2	14	2.19	2.5
NbTi-NbTi to 4 K	1	13.1	8	2.19	88

point additional variable attenuators and amplifiers can be used to optimize the performance for the dynamic range of the analog-to-digital converters.

One important caveat to note about the proceeding discussion and Table 4.1 is that these are not accounting for any loss at the detector array itself, which is dependent on the dip-depth of the detectors and thus the particular loading conditions and responsivity. An additional caveat is that there still remains some significant uncertainties in the final operating temperatures of Prime-Cam's intermediate temperature stages due to the construction and characterization of the cryostat being not-yet-complete. This is the primary reason for presenting the NET contributions in this particular format, since it allows for relatively straight forward scaling once individual temperatures are determined more precisely. With these two caveats in mind, the data in Table 4.1 should be considered a rough estimate of an upper bound for the thermal readout noise. The fact that it is a factor of several below the amplifiers' noise temperatures tells us that we can quite confidently say that this noise will not impact our ability to reach photon-limited noise performance. Later on in this Chapter we describe some of the performance validation we have done to ensure this.

4.4 Module Mechanical Design Details

The readout design specific to the module is shown in Figure 4.3. The readout from the 100 mK arrays to 4 K relies on a combination of semi-rigid and hand-formable coaxial cables. The semi-rigid cables are stainless steel on the input side and niobium-titanium on the output side, while the hand-formable cables are copper. These copper cables are used at isothermal stretches to reduce complexity during installation. Attenuation is included at each stage on the input side to reach the desired tone power and noise temperature, and low-loss superconducting cables carry the output signal across between each of the temperature stages spanning from the array and first-stage amplification at 4 K. Coaxial cables running from the focal plane arrays are heat sunk at 1 K on the 1 K radiation shield, as well as at 4 K on the magnetic shield where all LNAs are located. After being routed through the magnetic shield, coaxial cables are surrounded by slotted A4K covers to complete the magnetic shielding. PCBs for breakout of LNA bias lines are also located at 4 K. To better understand the different mechanical aspects of this design and how they come together during the assembly process, we can consider this design starting at the detector level and working our way out of the module.

4.4.1 Interface to Arrays

Beginning with the 100 mK stage, the variations between the two different array module designs (see Chapter 5) necessarily require slightly different routing. Most notably, the TiN detector module has side-mounted SMA connectors, whereas the Al detector modules utilize rear-facing SMA connectors. To min-

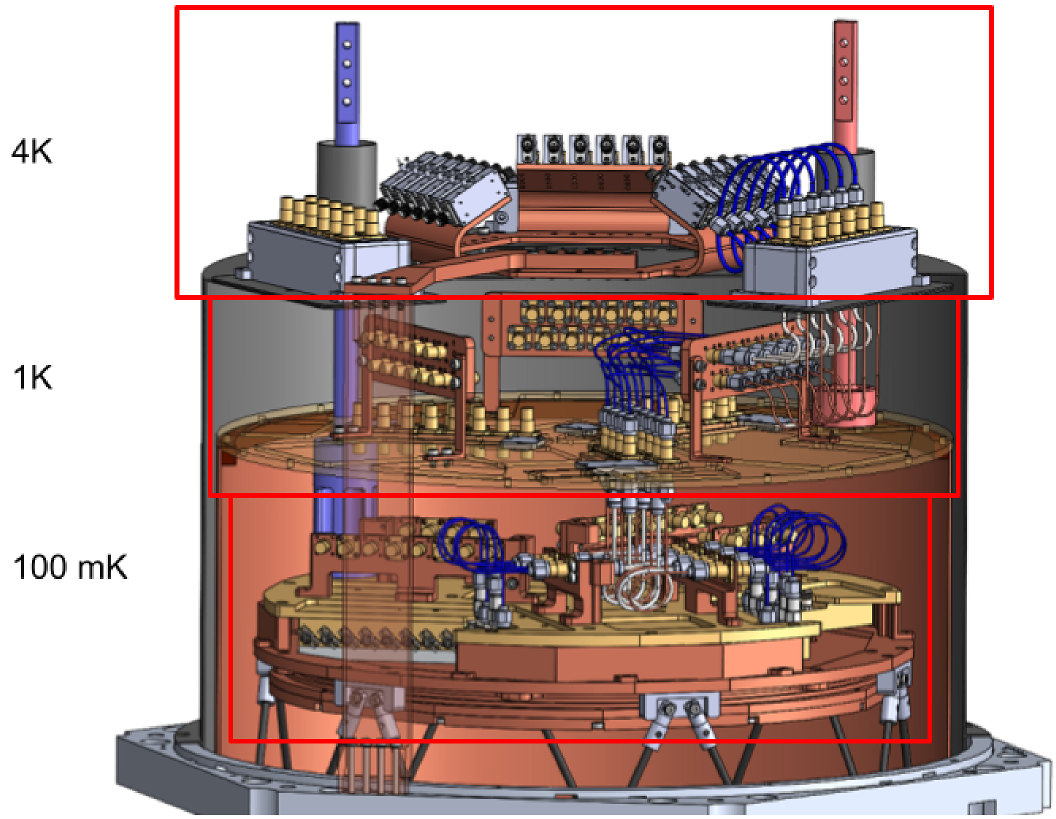

Figure 4.3: Cut-away overview of transitions from detector arrays to low noise amplifiers (LNAs) outside of the magnetic shielding at 4 K. The bottom of this image shows the 100 mK stage containing all detector arrays at the innermost layer of the module. The next level up includes a radiation shield with a blackened interior (shown as copper-colored here) and gold-plated lid at 1 K, for re-organizing the cable routing for 4 K and beyond. The top level and outermost section includes 18 LNAs at 4 K. Hand-formable copper cables are blue, superconducting NbTi cables are grey, and stainless steel cables are brown.

imize the complexity due to this, the routing directly to the arrays is handled by an isothermal stretch of hand-formable coaxial cables as pictured in Figure 4.4. This allows for identical cable routing for all of the semi-rigid coaxial cables between the two designs. It also allows for the use of right-angled SMA connectors for the TiN detectors and flexibility in the exact placement of the 100 mK attenuators. This is the only part of the design that has any differences across the three arrays.

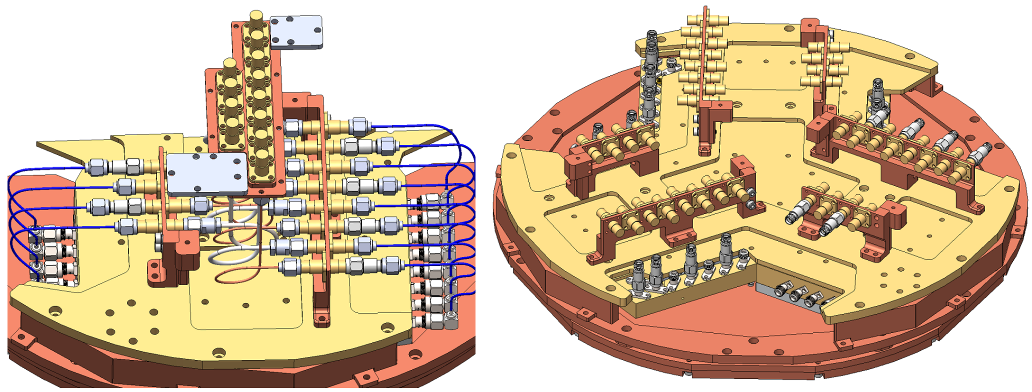

Figure 4.4: (Left) The 100 mK interface to the array shown as a close up for one of three arrays in Solidworks. The final interface uses hand-formable coaxial cables to allow for flexibility between the various connector positions and module designs. (Right) Everything from the 100 mK stage except for the coaxial cables.

4.4.2 Transition to 1 K

Making the transition up to the 1 K stage requires additional consideration for both the thermal loading and the practical assembly process. We use an assembly jig with removable installation posts to balance both of these aspects. The linkage between two stages of different temperature necessitates the use of semi-rigid coaxial cables with low thermal conductivity (as opposed to the copper conductors used for flexible, isothermal connections). On the input side where higher loss is acceptable (or even beneficial), we use stainless steel cables, whereas the output uses niobium-titanium, which is essentially loss-free at these temperatures. During assembly, the 1 K and 100 mK components are held together by two temporary posts, providing support for the semi-rigid cables. After the 1 K radiation shield lid is in place and the 1 K SMA feedthrough panels have been attached to it, these installation posts are removed from above and replaced with aluminum caps. An extended overlapping lip around the panel

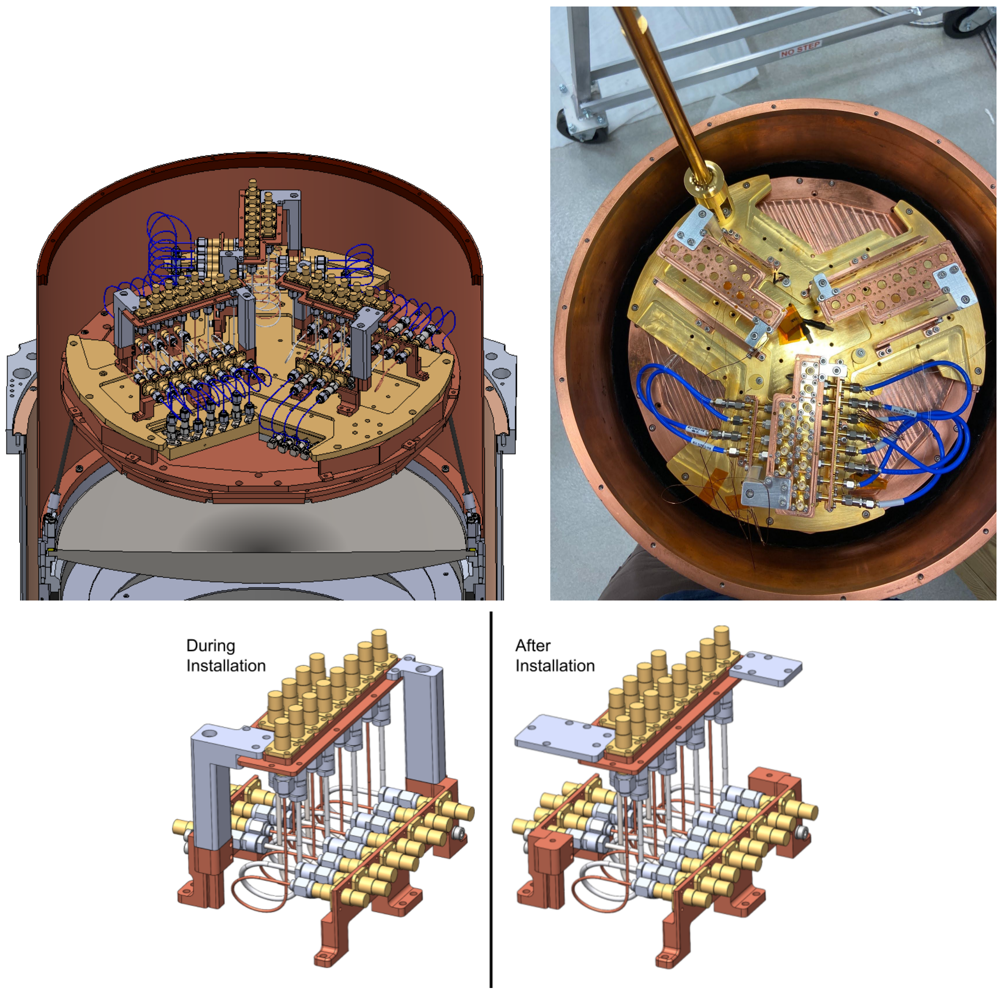

Figure 4.5: The 100 mK to 1 K transition prior to installation of the 1 K radiation shield lid shown in Solidworks (top left) and partially assembled with cables in loopback for a cryogenic test (top right). (Bottom) The assembly jig for installation of the 1 K radiation shield during installation with removable temporary posts in place, and afterwards with them removed.

edges is meant to mitigate any light leakage from the warmer stages down to the 100 mK stage. This is finished by a further layer of tape over the seams following installation.

4.4.3 Transition to 4 K

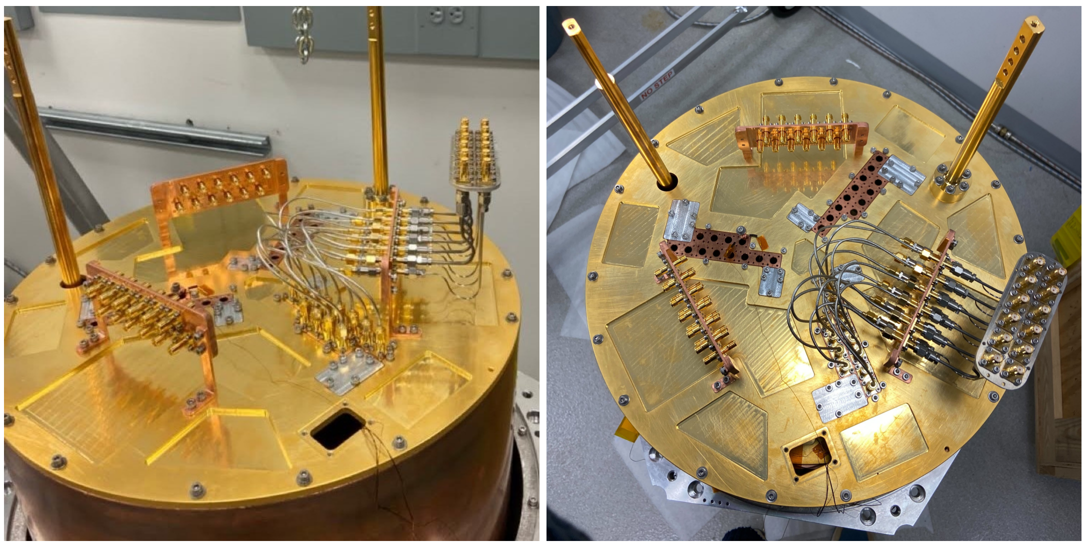

Figure 4.6: Cryogenic assembly test of the transition from 1 K to 4 K. As described below, intermediate interface is used to simplify cable routing with flexible cabling.

Transitioning up to the 4 K stage involves similar considerations to those for connecting the arrays up to the 1 K stage. Once again, the complexity is reduced by separating this out into a flexible isothermal stretch and a semi-rigid temperature transition. While making the transition up to the higher temperature stage and out of the magnetic shield, we are also re-organizing the cables from individual network pairs down at the detectors to groups of input lines and output lines (still keeping all three arrays separate). As seen in Figure 4.6, the messy transition is handled by flexible cable linking the 1 K feedhthrough panel of the installation jig to a simpler helper panel that mimics the eventual layout used in the 4 K magnetic shield feedthrough panel. From here, semi-rigid cable is once again used for transitioning to the higher temperature. Since the spacing is slightly less dense than the installation jig and the machining tolerances on the magnetic shield are considerably less precise, we do not use additional supports for the 4 K transition panel and instead rely on the rigidity of the cables to hold the panels in place during the installation of the magnetic shield. As a result, we need to be careful not to damage the cables during the installation process by bumping them or torquing them too heavily.

Rather than attempting to be light tight, the shielding consideration here is for stray magnetic fields. Once the larger magnetic shield has been installed with the readout feedthrough panels in place, the individual cables are surrounded by perpendicular slats to avoid having large gaps in shielding. The detailed assembly process for completing the magnetic shielding is shown in Figure5.4. At this point, we use supports to construct a small box around the feedthrough panels, some of which is shown in Figure 4.7 during a test assembly.

4.4.4 Rear of Module

After the installation of these 4 K transition boxes, the final aspect of the instrument module readout design is the installation of the 18 LNAs and their heatsink, which is given a strong thermal link down to the larger 4 K flange. For ease of cable routing, the LNAs are mounted at a slight upward angle that can be seen in Figure 4.8. As these are the dominant source of thermal load-

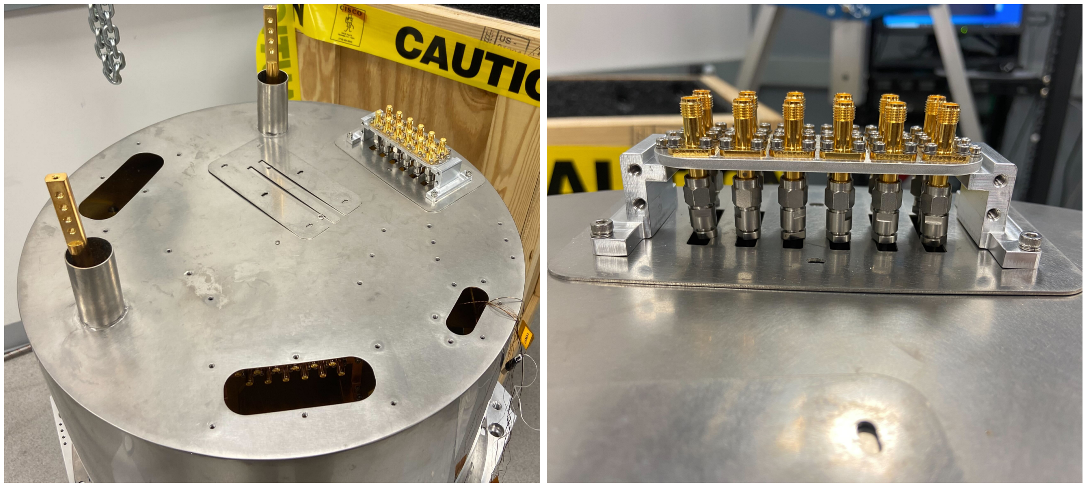

Figure 4.7: (Left) Wide view of the transition out of the magnetic shield during a cryogenic test assembly. (Right) Close-up view of the transition midway through the assembly of the box for supporting the feedthrough panel. During this particular test assembly, a spacing conflict between the semi-rigid cable connectors and the shielding slats was identified, which has since been resolved by adjusting the height of the box walls.

ing at low temperatures from the readout chain, the heatsink includes options for providing additional heat strap attachment points. DC wires for biasing the amplifiers are also broken out from larger cables through PCBs mounted on the rear of the module. From this arrangement of cables (the inputs arranged along the outside of the module and the outputs along the inside), the modules are connected to the readout harnesses through longer sections of flexible coaxial cable. The exact arrangement of the cables for this transition will differ between Mod-Cam and Prime-Cam, as well as by the position within Prime-Cam.

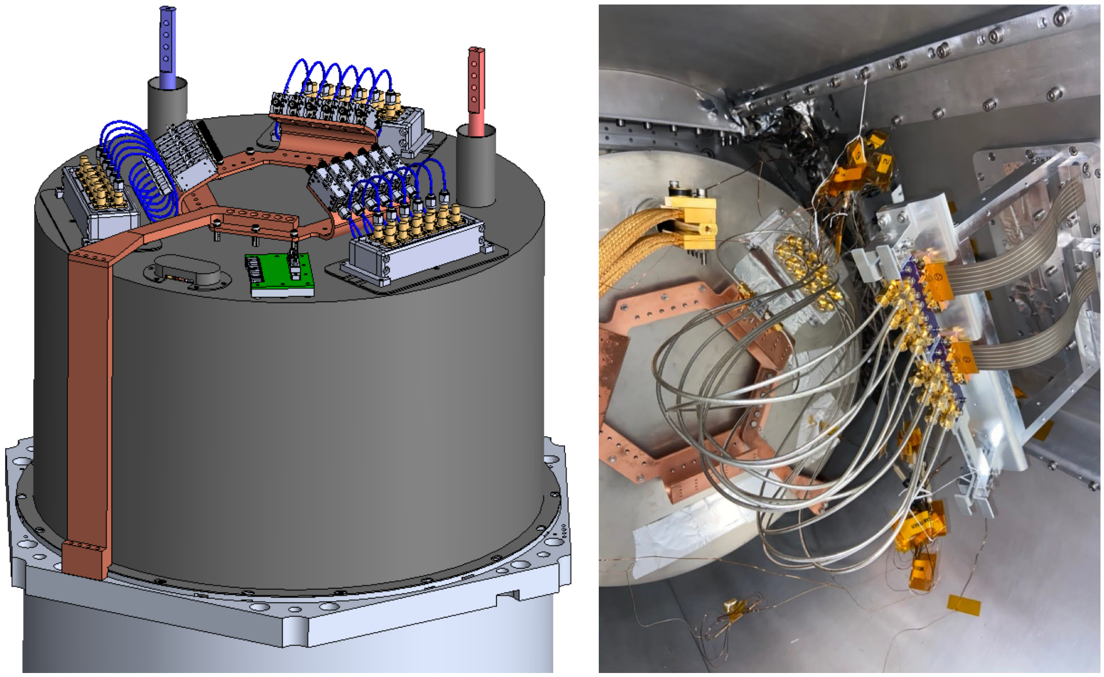

Figure 4.8: (Left) Rear of the 280 GHz instrument module as seen in Solidworks. (Right) A picture of the rear of the module and the transition to the readout harness during a cryogenic assembly test in Mod-Cam.

4.5 Readout Harness

From 4 K to 300 K, an RF stripline design based on those used for ALPACA [75, 108] runs roughly 18 inches of flexible radio frequency stripline through a readout harness with mechanical designs based on the Universal Readout Harness for the Simons Observatory [72, 92] (Figure 4.3). Each flexible board holds six RF feedlines with custom SMP connectors on both ends. These SMP connectors then mate to a transition board that switches all lines to SMA connectors. With six RF feedlines per stripline, a full detector array can be read out using just two striplines, each of which holds three of the six networks. The readout harness design shown, which is specific to Mod-Cam, sacrifices some efficiency in stripline density to allow for greater modularity when testing modules with alternative readout requirements or additional DC line requirements. Not shown in detail is coaxial cable routing required for transitioning between the readout harness and instrument module. This will require the most substantial modification between Mod-Cam and Prime-Cam.

4.6 Performance Validation

Significant work has been done to ensure that the described readout hardware will perform as expected during operation, both in terms of the noise performance and the mechanical robustness. While the full readout system has not yet been installed with detectors in Mod-Cam at the time of this writing, each of the individual components of the system has been demonstrated to perform as expected. We briefly describe some of the screening work that has been done towards this end and show some of the results.

While undergoing a full mechanical test of the 280 GHz instrument module within Mod-Cam, we were able to screen the mechanical performance of the cryogenic readout chain in its near entirety. Several pictures of this test assembly are shown throughout section 4.4. To allow for time domain reflectometry (TDR) measurements when cold, all attenuators were replaced with 0 dB equivalents and amplifiers were not included. In addition, to improve our understanding of the input and output sides of the readout chain separately, two of the networks were hooked up input-to-input and output-to-output. Figure 4.9 shows the transmission data for all six channels installed as measured at the output of the magnetic shield. These measurements were acquired at room temperature prior to the installation of the instrument module within Mod-Cam.

While taking a set of TDR measurements in this configuration, one of the hand-formable coaxial cables on the output-to-output chain was flagged for issues that would have normally caused its replacement at this step, but was left in place.

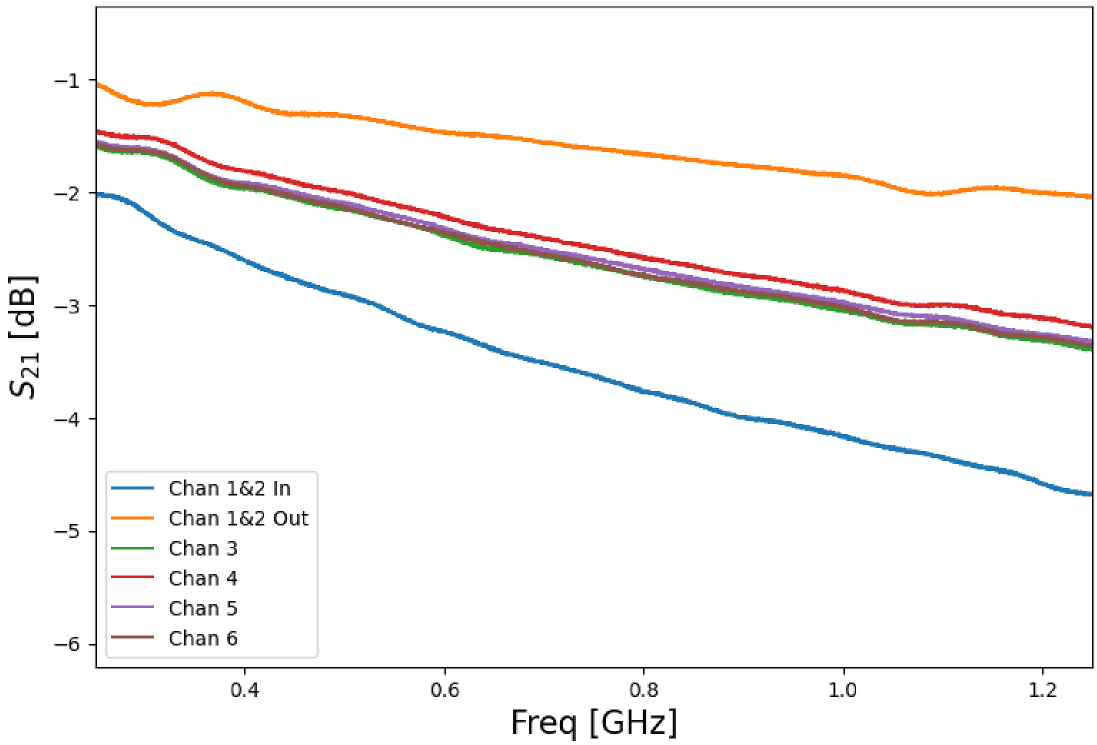

Figure 4.9: Transmission amplitude measurements acquired at room temperature for the instrument module only portion of the cold readout for performance validation prior to the module's installation in Mod-Cam for a full cryogenic test. All data was acquired with a vector network analyzer. For ease of troubleshooting when cold, all attenuators were replaced with 0 dB equivalents and the amplifiers were not included. Channels were hooked up in pass-through, with the exception of channels 1 and 2, which were hooked up input-to-input and output-to-output.

Following the installation of the instrument module, a pair of flexible striplines and interface PCBs were installed in the modular readout harness of Mod-Cam and tested warm similarly. These transmission results are shown in Figure 4.10 for six of the twelve lines. This particular set is shown because it successfully identified a problem (later confirmed to be a faulty PCB) through the resonance feature in channels 1 and 2. This particular issue could also be seen clearly in TDR and cross-talk measurements (shown on the inset to Figure 4.10) and demonstrated the success of these screening steps during the installation process. With these components flagged (but not replaced for this cooldown), we proceeded to cool down the entire module to its base temperature and retake these measurements with the fully assembled readout chains.

Cryogenic transmission measurements are shown in Figure 4.11. Channels 3 and 4 behaved precisely as expected, as did the channel 1 and 2 input-to-input chain, while the remaining 3 chains had transmission issues. The first and most straight-forward of these was the combined output chains that had previously been flagged for both a faulty coaxial cable and a faulty transition PCB. This chain developed a large resonance feature above 1 GHz that was almost certainly due to the transition PCB. Channel 5 had greatly reduced transmission, which was found to result from a failure in the transition from the readout harness to the instrument module, which was the only section not to have been screened prior to cool down. Similarly, channel 6 had reduced transmission with a variety of strong resonance features which resulted from a faulty component standing in for the 4 K amplifier, which is located between the two previously-screened sections of channel 6.

The final readout validation (prior to upcoming full tests with the completed module) has been the use of the warm readout electronics to demonstrate photon-limited performance levels in a cryostat with relatively larger NET than expected from the final components. Using the same set-up and detectors as described in Chapter 3 for Al pixel testing along with RFSoC-based readout

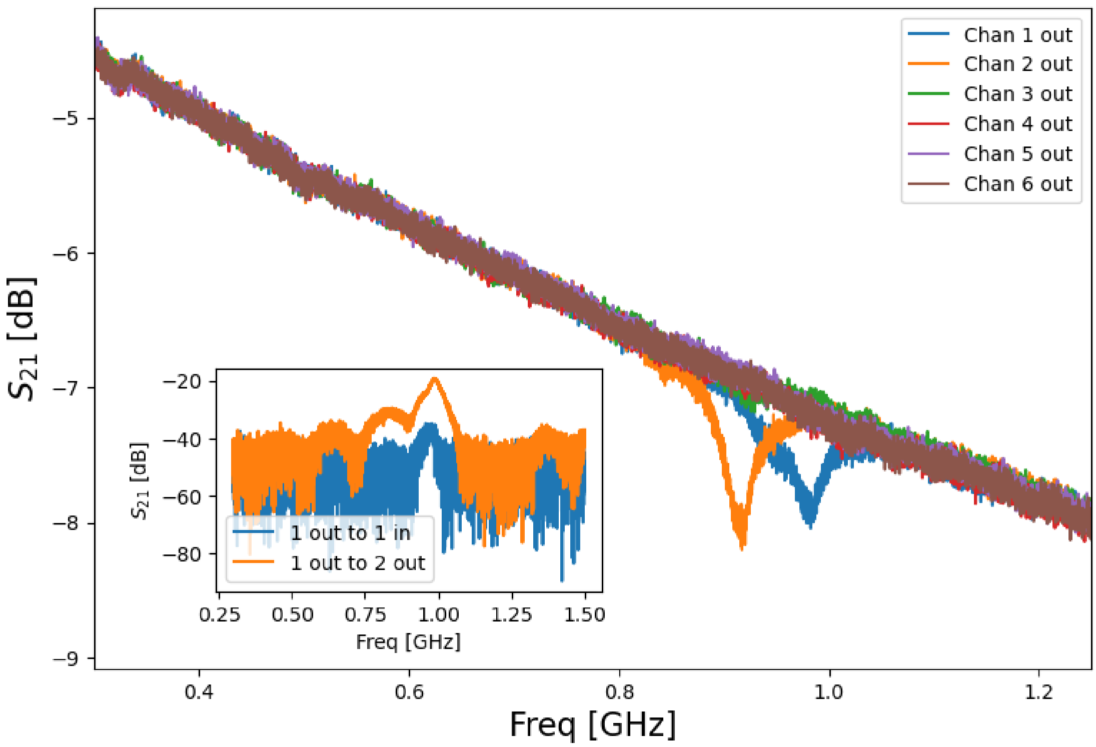

Figure 4.10: Example transmission amplitude measurements acquired at room temperature for the stripline and transition PCB portion of the cold readout following the stripline's installation in Mod-Cam for a full cryogenic test. As each stripline contains both input and output lines for half of an array, this is showing only the output lines across two striplines. While the inputs were fully consistent across all channels, a faulty transition PCB was identified and flagged for replacement during this particular screening. This could also be seen by looking at the cross-talk (shown in the inset) between channel 1 and 2 outputs and channel 1 input and output. All data was acquired with a vector network analyzer with averaging off and sweep time reduced to better observe transient behavior from loose connections which resulted in the elevated noise levels as compared to Figure 4.9.

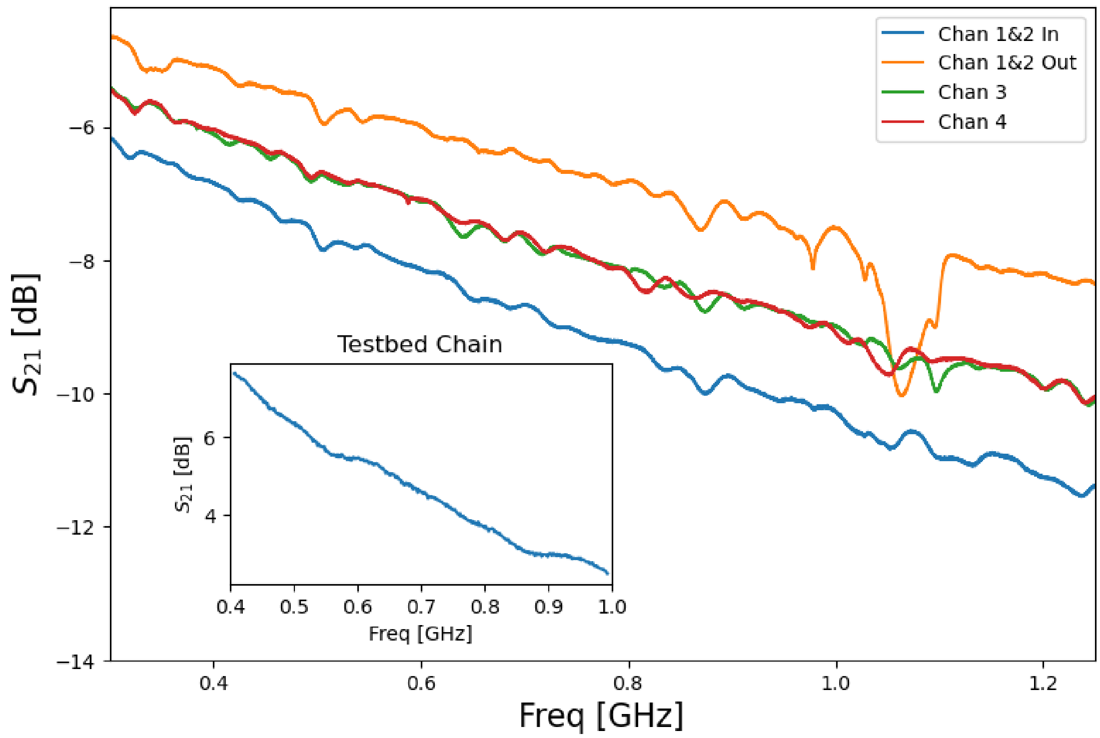

Figure 4.11: Full chain transmission amplitude measurements acquired at base-temperature in Mod-Cam for a full cryogenic test. As with Figure 4.9, all attenuators were replaced with 0 dB equivalents and amplifiers were not included. Channels 5 and 6 are excluded from this plot due to a flexible coax failure with channel 5 and a stand-in component failure for channel 6. The large resonance feature seen in the channel 1 and 2 outputs was found by time domain reflectometry to result from bad components that were flagged prior to cool down. All data was acquired with a vector network analyzer. For reference, the inset shows the readout chain used for noise measurements in Figure 4.12, which has an equivalent noise temperature that is a factor of five higher than the instrument module readout chains.

[97], Figure 4.12 shows measurements of the responsivity and noise equivalent power. The data were acquired using a cryogenic cold load as an optical source and tuned to be optimally biased. Figure 4.12 clearly demonstrates a substantial increase in noise with optical loading even while this system's readout noise is higher than what can be expected from the instrument modules. These results indicate that the readout design presented here is expected to be able to achieve photon-noise dominated performance on the telescope under realistic loading conditions.

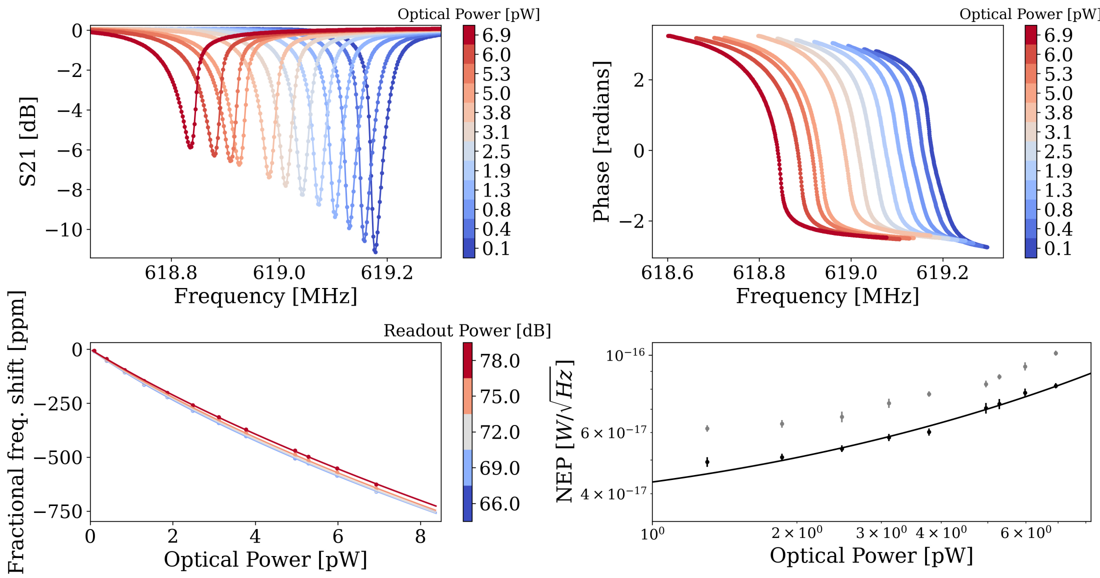

Figure 4.12: Responsivity and noise measurements for one of the 280 GHz aluminum witness detectors shown in Chapter 3 measured with an RFSoC. The top plots show the detector response in magnitude (left) and phase (right) under an increasing optical load from a cryogenic cold load. The bottom left shows the optical response as a function of optical load for a variety of probe tone powers. Note that the tone power includes an arbitrary absolute power offset, and should only be referenced for relative power. This is the relevant plot for converting voltage fluctuations to power fluctuations when processing noise data. The bottom right shows the noise equivalent power vs. optical power at an optimal tone power in black and 3 dB below in gray. The full noise model is shown plotted with the solid line, indicating that the detector is photon-noise dominated in the expected loading range of ~ 7 pW. Data and figures provided by Colin Murphy and Steve Choi.

CHAPTER 5

CCAT'S FIRST THREE KID ARRAYS

While the full deployment of Prime-Cam will support up to seven independent instrument modules with three detector arrays each, at first light and for commissioning the telescope we will deploy Mod-Cam's singular instrument module with three 280 GHz arrays. Additional detector arrays and instrument modules are under development for deployment alongside the 280 GHz module in Prime-Cam, including additional broadband modules centered at 350 GHz and 850 GHz [17, 106] and the EoR-Spec spectrometer module [22].

While the 350 GHz Instrument Module is planned to be uniform across its three arrays, the 280 GHz module includes two different detector and feedhorn array types. The first KID array utilizes a TiN/Ti/TiN tri-layer, while the other two arrays utilize a single layer of Al. All three arrays were fabricated on 550-micron silicon-on-insulator wafers by the Quantum Sensors Group at the National Institute for Standards and Technology (NIST) in Boulder, CO.

Each detector array is mounted at the instrument module's focal plane within an individual array package that serves several purposes, including aligning the detector wafer and feedhorns, coupling the array to RF readout lines, and thermally sinking everything to the 100 mK plate. This packaging is required to be robust through multiple assembly and disassembly cycles during testing and LED-mapping prior to deployment. The TiN array utilizes a gold-plated aluminum package and machined aluminum feedhorns, while the two Al arrays use gold-plated Si-platelet feedhorns with gold-plated copper packaging. These distinct feedhorn types require unique array package designs to meet the alignment and assembly requirements. Both feedhorns are based on

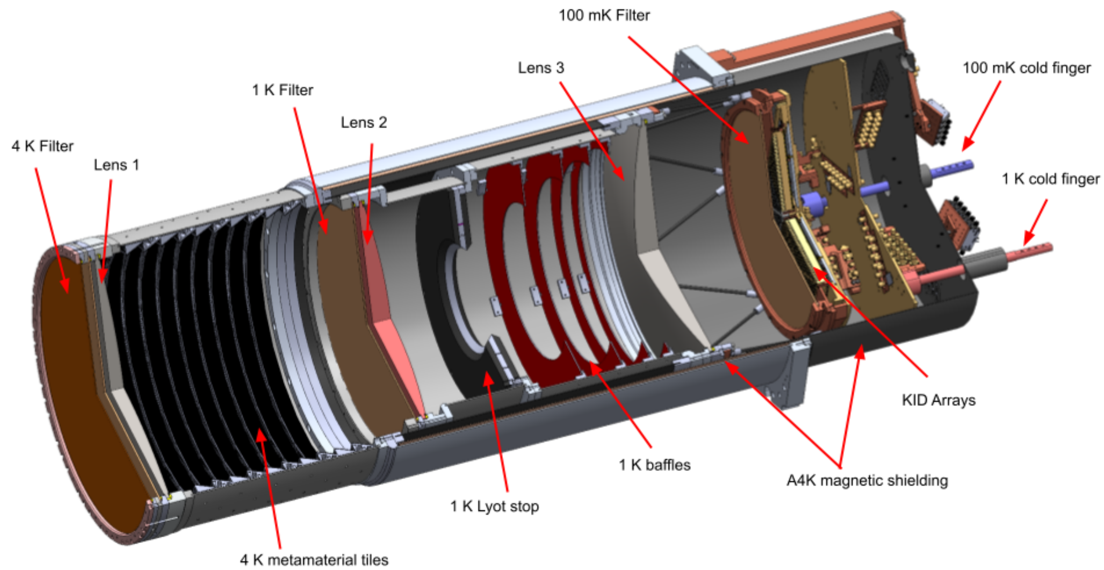

Figure 5.1: Cross-section view of the 280 GHz instrument module. Each of the three lens and filter positions can be seen, as well as additional features to reduce noise from stray light and magnetic fields. Figure based on Figure 5 of [107].

the same numerically-optimized spline profile used on TolTEC's 1.1 mm array [12, 95], and the differences in performance are expected to be minimal based on simulations and early measurements.

In this chapter, the focal plane packaging is described in detail for both styles of feedhorn and several milestones are described in the preparation of all three arrays for first light. We begin with an overview of the instrument module designs for context.

5.1 Instrument Module Overview

Just as there are many elements of shared design heritage between FYST and the Simon's Observatory's (SO) Large Aperture Telescope (LAT) and their respective cameras, Prime-Cam and the Large Aperture Telescope Receiver (LATR), the initial design for Prime-Cam's instrument modules was based on those of LATR Optics Tubes [117]. Many design elements were carried over with minor iteration, including thermal isolation, lens and filter placement, and cold finger designs. These can be seen in Figure 5.1, which shows a cutaway view of the 280 GHz instrument module with all optical and readout elements in-place. At the same time, the readout and thermal requirements at 100 mK for a focal plane based on transition edge sensors (TESes), as used by SO, is substantially different from those of an MKID-based focal plane. While the wiring is reduced in complexity for the Prime-Cam design in many ways, it also requires a roughly three-fold increase in the number of radio frequency lines dedicated to reading out detectors. Readout designs are discussed in greater detail in Chapter 4. A detailed description of the updated designs for the 280 GHz instrument module can be found in [107].

5.1.1 Temperature Stages & Optics

Each instrument module has an independent optical path with up to 36-cm diameter aperture optical elements, and includes 4 K, 1 K, and 100 mK stages. Light enters the module after passing through a 300 K ultra-high-molecular-weight polyethylene (UHMWPE) vacuum window and 40 K infrared-blocking filters [3]. It is then re-imaged onto the focal plane by three metamaterial, anti-reflection-coated silicon lenses [23, 25, 48] distributed between the 4 K and 1 K stages of the module. Out-of-band light is blocked by absorbing alumina filters [31], metal-mesh infrared-blocking filters [105], and low pass edge (LPE) filters [3], which also serve to define the high side of the pass-band. Further

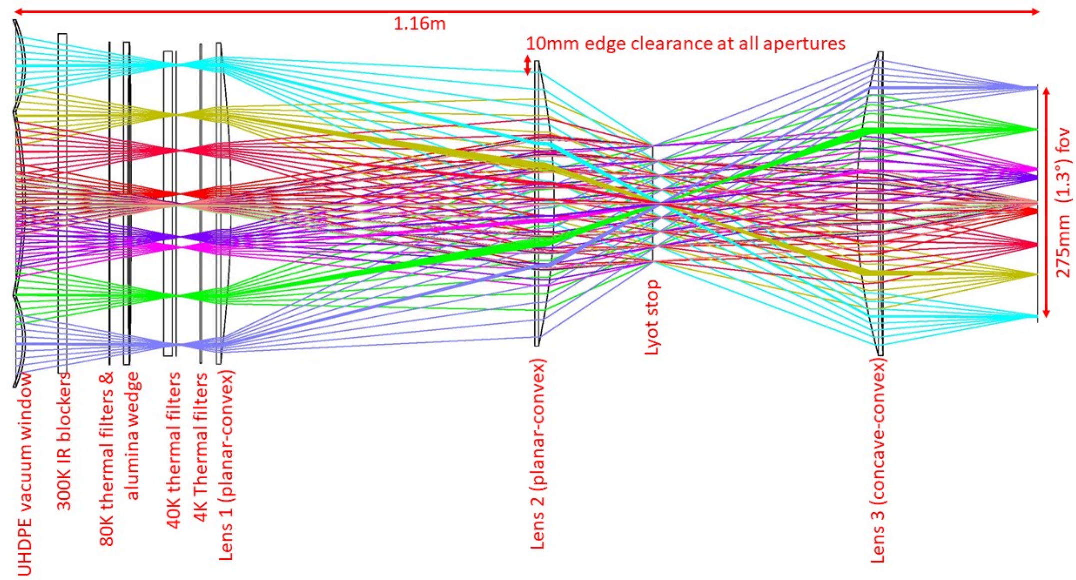

Figure 5.2: A ray trace of the cold optics design for a single Simons Observatory optics tube. This same overall cold optics design is shared for the 280 GHz instrument module. Figure reproduced from [31].

stray light mitigation is provided by the same injection molded, carbon-loaded plastic metamaterial tile coating design that was developed for the SO LATR modules [50, 115, 117]. Flat versions of these tiles are applied to the 1 K Lyot stop, while the 1 K ring baffles and shield are coated in Stycast 2850 FT with coarse and fine carbon powder. Figure 5.2 shows a ray-trace of the optical path through one of the Simons Observatory LATR optics tubes from [31].

5.1.2 Magnetic Shielding

Since kinetic inductance detectors are sensitive to stray magnetic fields (as shown in Figure 5.3), a magnetic shield is used as part of the 4 K stage to enclose the module from the mounting point for the low noise amplifiers to just beyond

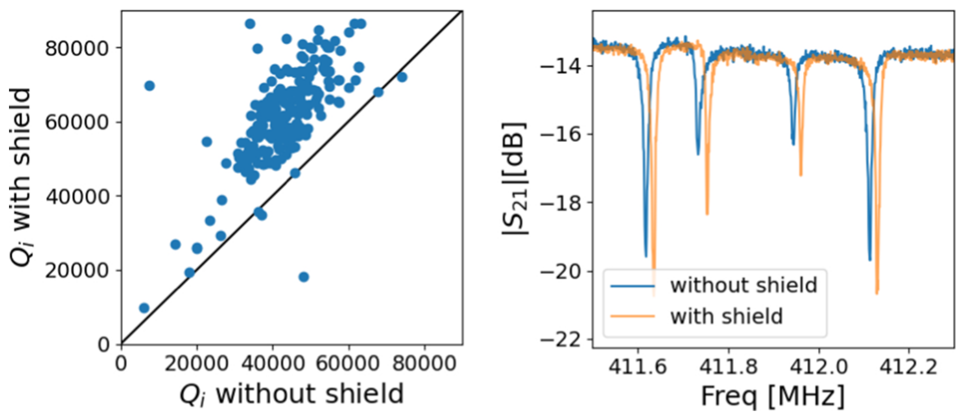

Figure 5.3: (Left) A comparison of the measured dark Q_i values both with and without a magnetic shield for one network on the 280 GHz TiN KID array. (Right) Close-up view of the transmission data for several resonators measured with and without the magnetic shield. Both of these plots demonstrate the clear increase in the internal loss as a result of stray magnetic fields. Figure reproduced from [18].

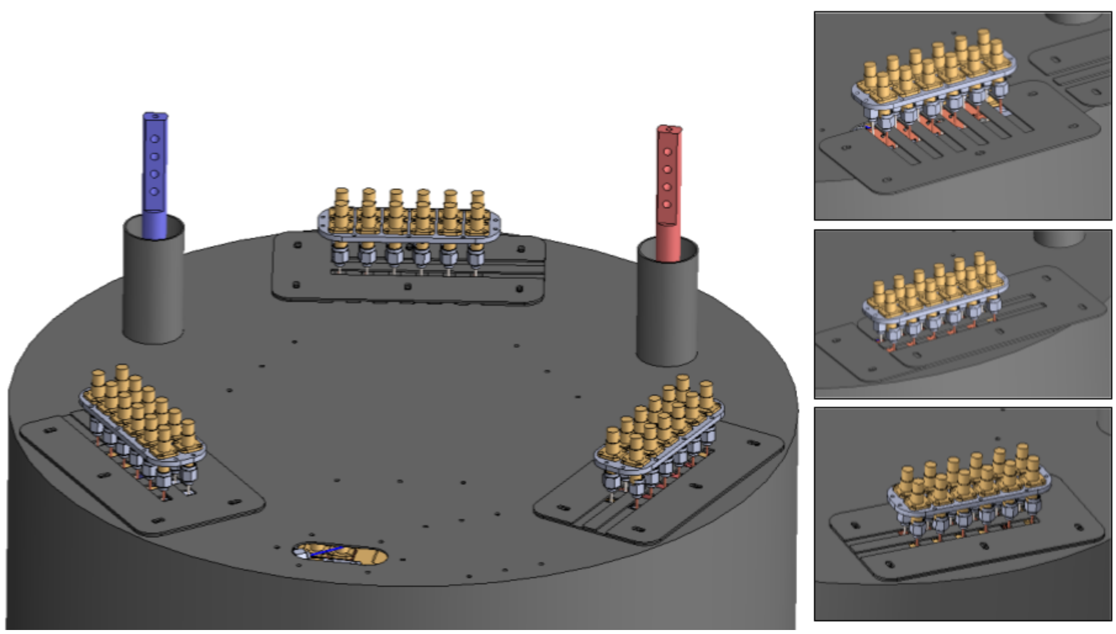

Figure 5.4: Rear view of the magnetic shield with readout components only partially assembled and installed for clarity. The inset images show the assembly process for the slotted covers which surround the semi-rigid coaxial cables.

the second lens. The A4K[1] magnetic shielding for the module was developed from the SO LATR design to accommodate the 280 GHz MKID readout design. In the SO design, extended ”chimney” designs surround the entrance points for both 1 K and 100 mK cold fingers and all readout lines to mitigate stray magnetic field leakage. Due to spatial constraints caused by the increased number of readout lines, the “chimney” design around the RF chains was replaced by a set of slotted covers that run perpendicular to one another and surround each individual coaxial cable. The extensions were kept around both cold fingers, but with a slight increase in the opening diameter to make assembly easier. Both of these features can be seen in Figure 5.4.

5.1.3 Focal Plane Layout

As previously mentioned, the 100 mK stage of 280 GHz instrument module is populated with three independent, hexagonally-tiled detector arrays with a shared optical path, totaling $\sim 10,000$ polarization-sensitive MKIDs. The layout of this stage can be seen in Figure 5.5. The three array modules are mounted directly to the 100 mK plate (referred to as the array plate in the figure) and are tiled symmetrically about the center of the module. The 100 mK cold finger attaches to this plate behind the initial all Al-machined array module featuring TiN detectors and Al-machined feedhorns. The peculiar shape of this plate is meant to allow access to SMA connectors while minimizing additional thermal mass and providing a large surface area for heatsinking the arrays. The final LPE filter is mounted just in front of the feedhorns and attached to a secondary interface ring. This interface ring is also the mounting point for the carbon-fiber

[1]Amuneal 4K material, (www.amuneal.com/)

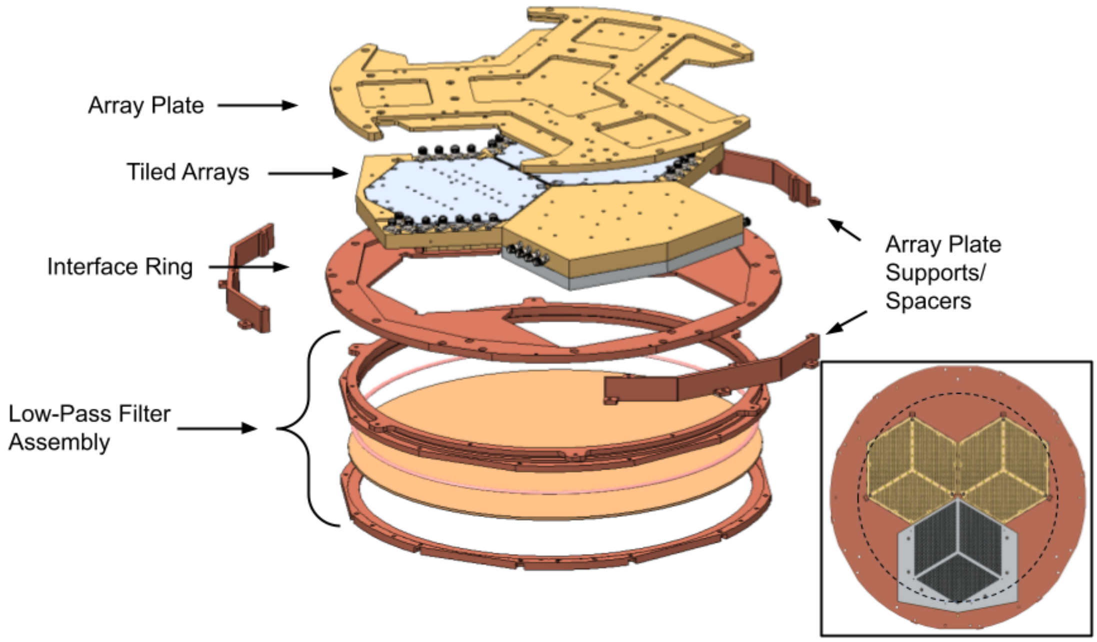

Figure 5.5: Layout of the 100 mK stage within the 280 GHz instrument module. Inset shows the hexagonal tiling of the three arrays as mounted. The dashed circle marks the optically illuminated region.

truss that rigidly supports the stage and provides thermal isolation from the 1 K stage of the instrument module. Details of this truss can be found in [107].

5.2 First CCAT KID Array

The first CCAT KID array contains 3,456 feedhorn-coupled, polarization-sensitive MKIDs fabricated from a TiN/Ti/TiN tri-layer on a hexagonal 550-μm thick, 15 cm diameter silicon-on-insulator wafer. It is optimized for observing a $\sim$60-GHz wide band centered at 280 GHz with background-limited sensitivity [17]. This array draws on the experience gained through developing detectors for the BLAST-TNG [32, 39] and TolTEC [9, 12] detector arrays. The resonators share the same design as the 280 GHz detectors designed for TolTEC, with ad-

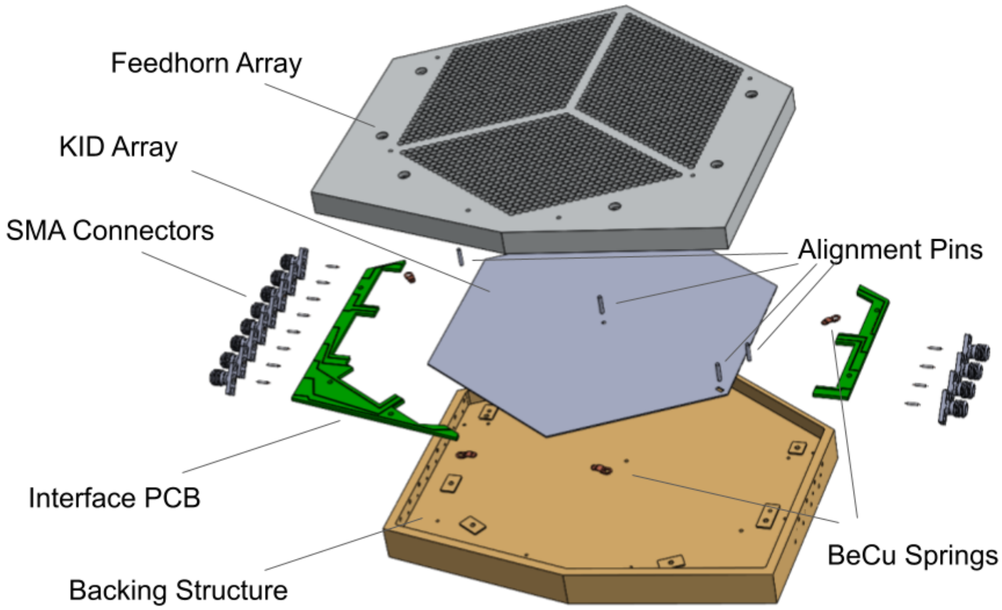

Figure 5.6: An exploded view of the Al-feedhorn focal plane assembly, including all alignment pins and readout hardware, but with screws and pogo pins removed.

justments in the absorber geometry to account for CCAT-prime's slightly lower atmospheric loading.

5.2.1 Design Considerations

The detector array is mounted within a focal plane assembly that also holds the aluminum-machined feedhorns. This mechanical assembly (shown in Figure 5.6) serves to set the alignment between the detectors and the feedhorns, couple the detectors with the RF lines for readout, and provide heatsinking to the dilution refrigerator so as to keep the entire assembly stable at the detectors' 100 mK operating temperature. As shown in the previous section, the hexagonal design allows for packing three arrays within a single instrument module, keeping all three as near as possible to the center of the instrument's focal plane. Designing and machining the mechanical components to meet the relatively strict alignment tolerances while minimizing risk of damaging the detector wafer during cooldowns provided several significant challenges.

Detector alignment is achieved by use of a pin-and-slot design, combining a tightly-fitted central pin with a radial slot and pin to allow for differential thermal contraction between the silicon wafer and the gold-plated aluminum backing structure. The aluminum-machined feedhorn array is aligned to the detector wafer by means of a separate pair of tight-fitting pins along the outer edge of the detector array. Particular care was paid to minimizing potential strain on the silicon wafer generated by thermal gradients between the aluminum backing structure and the feedhorn array during the cooling process. Hence, the choice was made to align the detectors and feedhorns to the backing structure through separate alignment pins. When cold, a 75 μm gap is achieved between the feedhorns' choke structures and the detector wafer across the 150 mm wafer by means of a set of raised mounting platforms along the outer edge of the detector wafer, which also serve as mounting points for the feedhorn array. These platforms, as well as the positions of the alignment pins, are shown in Figure 5.7. The gap between chokes and detector absorbers is critical for maintaining optical coupling efficiency and minimizing both cross-polarization and optical cross-talk between neighboring pixels. The gap is specifically designed to remain below $\lambda/10$ even with conservative machining tolerances. The rule of thumb using $\lambda/10$ is based on simulations similar to those seen in [70] and Chapter 6 of [34].

Pogo pins are placed along designated lanes that spread out radially from the center of the detector array to reduce microphonics, and slide along a gold

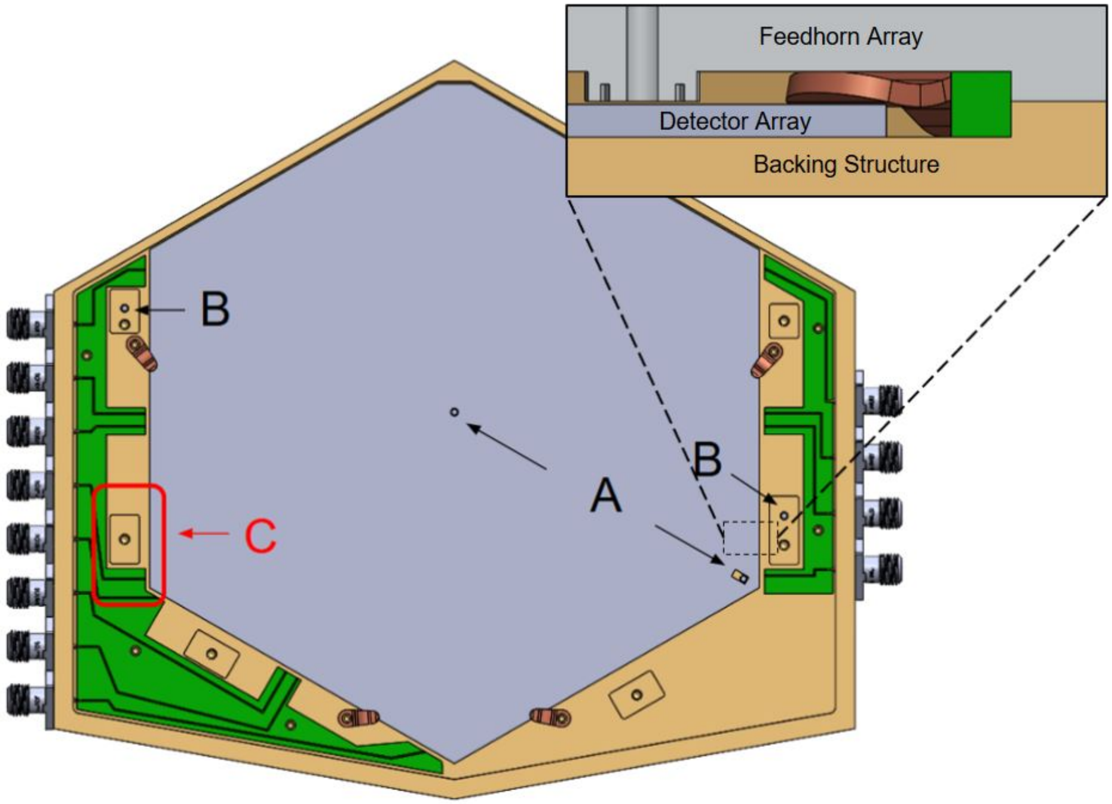

Figure 5.7: Several key features of the mechanical designs are labeled. (A) The pin-and-slot feature for detector alignment. (B) Separate pins for aligning the aluminum-machined feedhorn array on the aluminum base. (C) One of six raised platforms that help to set a $\sim$75 μm cold gap between the detector array and feedhorn array. and serve as mounting points for the feedhorn array. A close-up cross-sectional view of one of these is shown in the top right.

layer as the assembly cools. These lanes can be seen clearly in Figure 5.8. An additional layer of gold is placed along the edges of the detector array on four of the six sides allowing for gold wirebonds between the wafer's edge and the backing structure. This provides additional heat sinking for the array, while also improving the grounding beyond just surface contact with the backing structure.

The feedhorn array, including all choke structures, was machined at Arizona

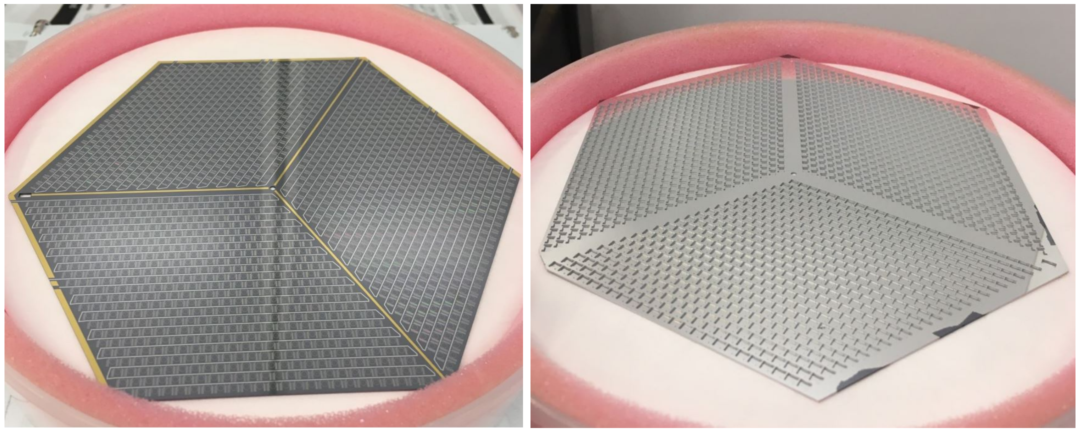

Figure 5.8: (Left) Top of the first completed 280 GHz KID array, which is approximately 13 cm wide. (Right) Bottom of the first light array with ground plane and etched quarter-wavelength backshorts.

State University out of 6061 aluminum based on a spline profile [12]. To reduce the potential for warping of the feedhorn array during thermal cycling due to built-up stress from machining, several rounds of thermal annealing were employed following an initial rough machining of the array. The annealing process involved rapidly moving the array between baths of liquid nitrogen ($\sim$77 K) and boiling water ($\sim$373 K) several times. This was intended to significantly reduce stress in the feedhorns, and thereby reduce the possibility of damaging the array during cooldowns or warm-up.

5.2.2 Assembly Concerns & Validation

With the strict requirements for optical alignment between the feedhorns and detectors while maintaining a $\sim$75 μm cold gap across the 15 cm wafer, the majority of the complexity for this array module was designing something that could achieve these tolerances reliably across many cooldowns and several assembly and disassembly cycles. Since the mounting methods for the feedhorn array are the critical elements for achieving these tolerances, the array is able to be placed and wirebonded on the array mount beforehand, with alignment pins and BeCu tabs installed prior to the feedhorns. The RF PCBs and SMA connnectors are installed prior to the placement of the array. As the BeCu tabs are machined out of sheet metal and hand-formed, they are the element with the lowest precision, making it especially important to position them properly prior to installing the feedhorns. One of the dummy wafers that was used for a mechanical test assembly prior to the real array became damaged as a result of a compounded error where: the BeCu tab was positioned slightly too far towards the middle of the array, the tab itself was formed to bend upward higher than designed, and it was machined out of a slightly thicker sheet metal than intended. One additional point of note was a failure in one of the SMA connecting pins after several cryogenic cycles. This was caused by a misalignment when installing the SMA connector such that the pin was pinched between the dielectric of the connector and the pin housing. The stress of multiple cycles eventually led to a break in this component, requiring a replacement.

Prior to actually installing the array within the final assembly, the components went through several steps of validation. Upon receipt of both the gold-plated backing structure and the machined feedhorn array, critical dimensions were verified both by hand and by microscope. Once satisfied that these components met our specifications, the entire array was assembled and cooled down multiple times, as mentioned above, with a mechanical wafer that was fabricated to the same dimensions as the final detector wafer, but without any device layers. To further verify that the system did not develop any touches between the wafer and the feedhorn array during the process of cooling down, a special shorting wafer was used that could be monitored electrically throughout the

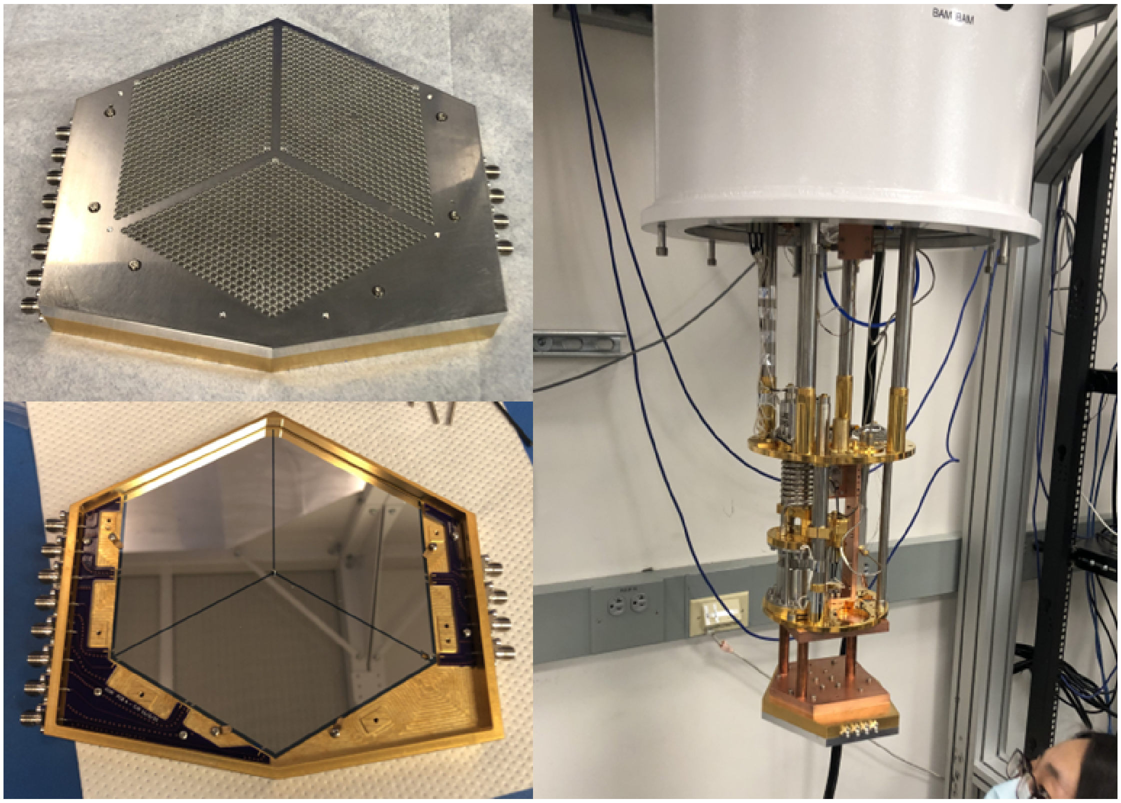

Figure 5.9: (Top left) Full array package with detector array assembled, prior to installation in Bluefors LD-400 for LED mapping. (Bottom left) Opened view of shorting wafer used for checking for cold touches. (Right) Bluefors SD-250 setup used for initial cryogenic assembly tests, with hand-formable coaxial cables removed.

cool down process. This shorting wafer, along with the cryogenic setup, and the completed final assembly is shown in 5.9. Once these tests were complete, the final detector array was installed in the assembly in order to map out pixel positions with an LED board for post-fabrication resonator editing.

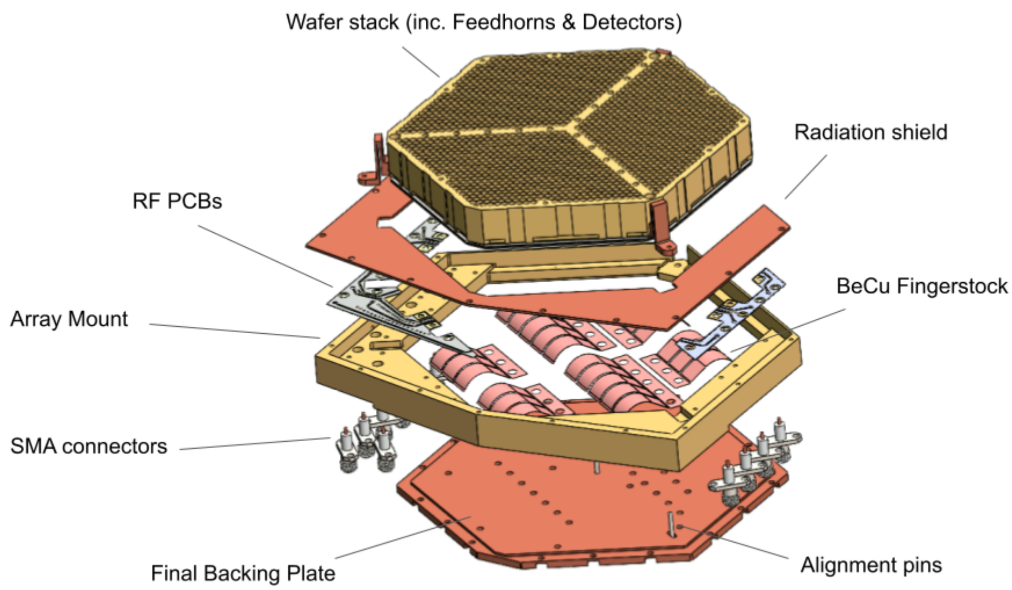

Figure 5.10: An exploded view of the Si-feedhorn focal plane assembly, including all alignment pins and readout hardware, but with screws removed.

5.3 Second & Third 280 GHz KID Arrays

Two additional arrays using Al KID designs have been fabricated, along with gold-plated Si-platelet feedhorn arrays. Each of these arrays has 3,448 total detectors (1,724 pixels), of which 3,414 are optically coupled. As with the aluminum-machined modules, the feedhorns are based on the numerically-optimized spline profile used on TolTEC's 1.1 mm array [12, 95]. This change from TiN to Al detectors was driven by dark testing results demonstrating reduced low frequency spectral noise and is discussed in Section 3.3. More details about the Al KIDs can also be found in [11]. The array packaging differs between both designs to accommodate the different alignment and heat-sinking requirements of the two feedhorn types, though overall pixel spacing and placement is the same. The overall package design (shown in Figure 5.10) shares many elements with the array packaging used by TolTEC as described in [10], but with several adjustments to allow for hexagonal packing.

5.3.1 Design Considerations

As with the Al-feedhorn design, the primary requirement for this design is being able to cool down the detectors safely in such a way that they are aligned with the feedhorns, electrically and thermally grounded, and do not experience any excessive strain or force. With the machined feedhorns, the alignment with the detectors posed the greatest challenge, due to differential contraction between the coupled elements. In the all-silicon design used for the second and third detector arrays, this alignment is no longer a major issue. Instead the challenge is to assemble the module in such a way that the detectors are able to be wirebonded to both the backing structure for grounding and the RF PCBs for readout, and that nothing is straining or cracking any individual element in the wafer stack.

Both Al arrays use gold-plated copper packaging to house the all-silicon detector and feedhorn stack. The silicon stack, shown in figure 5.11, includes a protective backing wafer, detector array, feedhorn chokes, interface wafer, and gold-plated feedhorns, along with a set of flexible copper feet that absorb any residual strain during the cooldown. These copper feet are attached to the feedhorn array by non-magnetic titanium 2-56 screws and thin number 2 nylon flat washers, and are screwed into the copper array mount in pre-tensioned positions so that they have only minimal strain at 100 mK. The optical alignment for this stack is set while warm using alignment pins. As shown in Figure 5.12, this is verified visually under a microscope and maintained through cooling due to

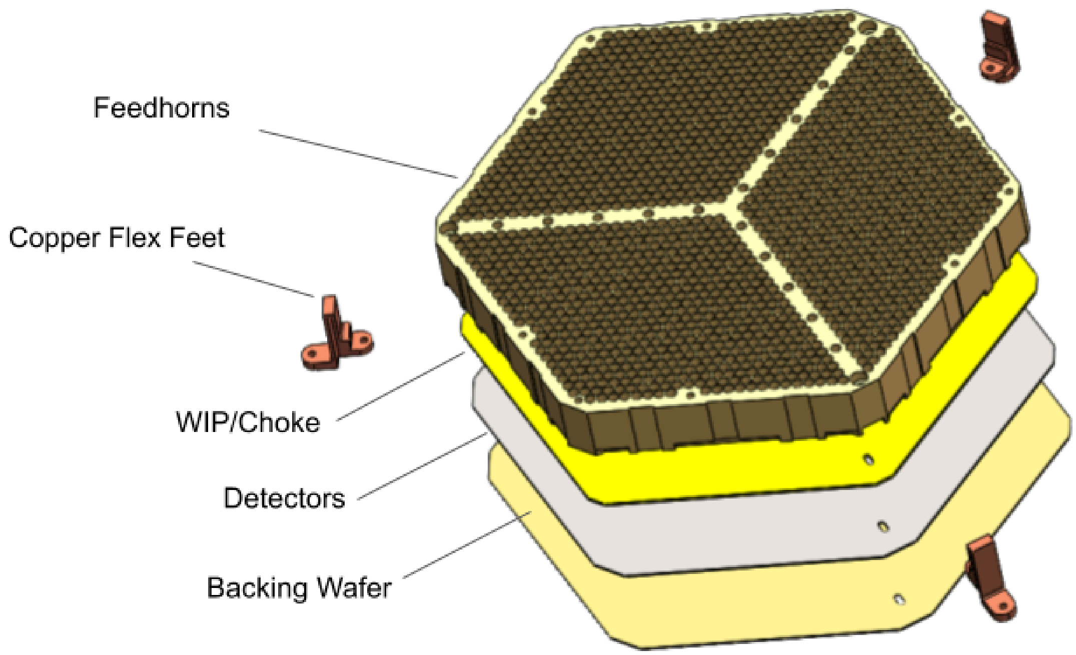

Figure 5.11: An exploded view of the feedhorn and wafer stack, including the backing wafer, detector array, and a combined layer for the waveguide interface plate (WIP) and spacer wafers.

the matched coefficients of thermal contraction. The waveguide gap is set by the interface plate. The feedhorn chokes are used to improve the optical coupling. The backing wafer protects the other wafers as they are held against the back of the silicon feedhorn array by flexible springs in the form of BeCu fingerstock.

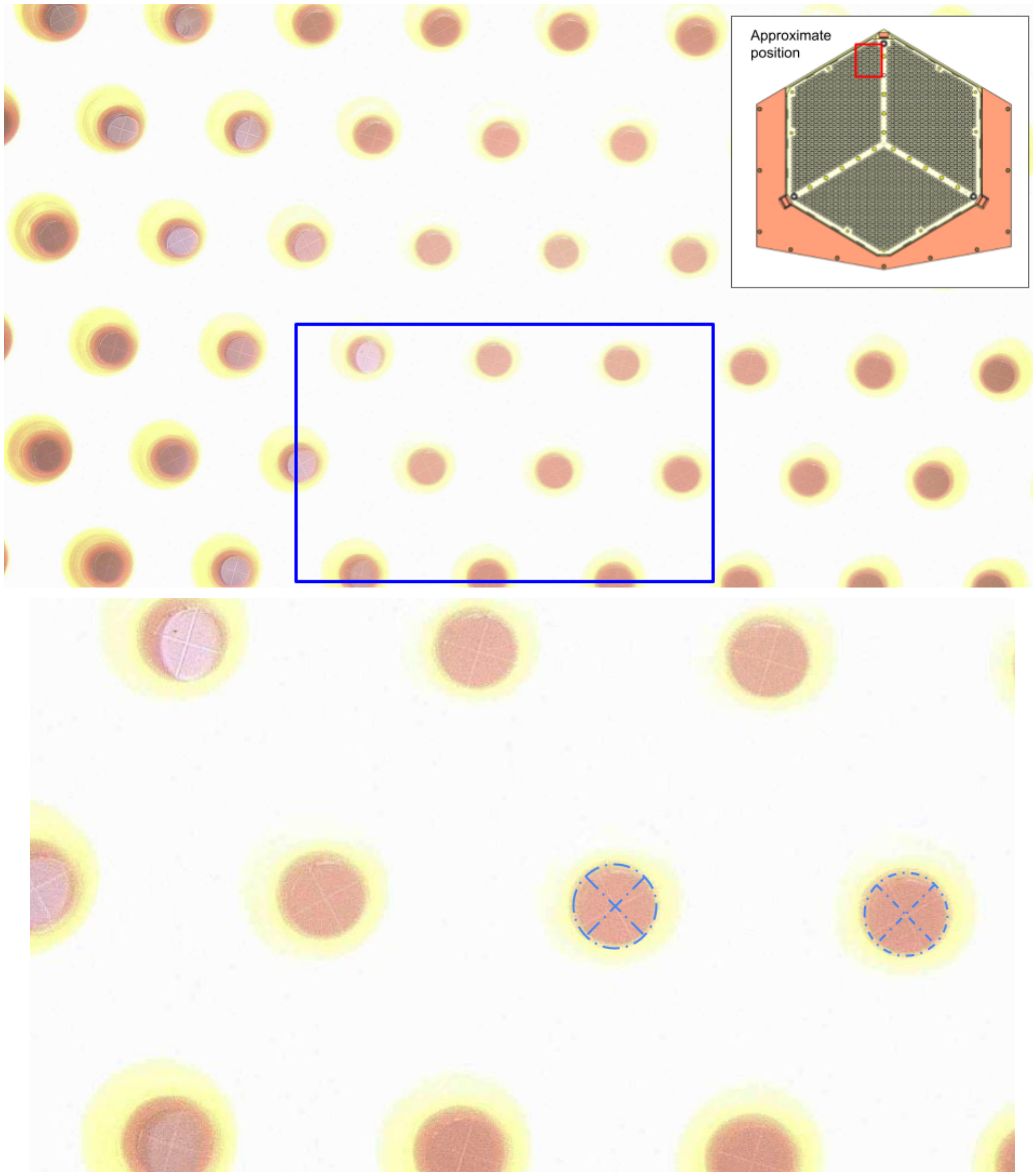

Figure 5.12: (Top) Example image used for verification of warm feedhorn alignment with detector absorbers with inset showing the approximate pixel position seen. Exact alignment is difficult to see due to the slight viewing angle in the microscope eye piece. (Bottom) Zoomed-in view of the blue rectangle with dot-dash crosses shown over two detector absorbers for visual reference.

5.3.2 Assembly Process

One of the primary difficulties with this assembly is maintaining the ability to access the top-side of the detector wafer for wirebonding, given that the final assembly has the detector array pressed tightly against the feedhorn stack from the underside. To accomplish this, the assembly process begins with the installation of a temporary bonding jig into the array mount, which fills the central region and temporarily holds two alignment pins. After placing the backing wafer, detector array, interface plate, and feedhorn chokes on the bonding jig, BeCu clips are used to hold down the wafer stack for wirebonding, beginning with gold wirebonds for heatsinking and grounding, and followed by aluminum wirebonds to the RF PCBs. With the top-side wirebonding complete, the BeCu clips are removed and the feedhorn array is lowered onto the detector wafer from above, then screwed in from the underside. The bonding jig is then removed, making use of an additional set of alignment pins to avoid applying torque to the detector stack. The final backing plate (with BeCu fingerstock in place) is then installed with careful tensioning to ensure the pressure increases roughly evenly across the array. At this point, the wirebonds are checked for continuity and the feedhorn-detector alignment is verified under a microscope, as shown in Figure 5.12.

5.4 Current Array Statuses

At the time of writing, all three of the 280 GHz arrays have been fabricated and are undergoing characterization at various stages. The TiN array has undergone extensive testing, and is nearly ready for post LED-mapping resonator editing.

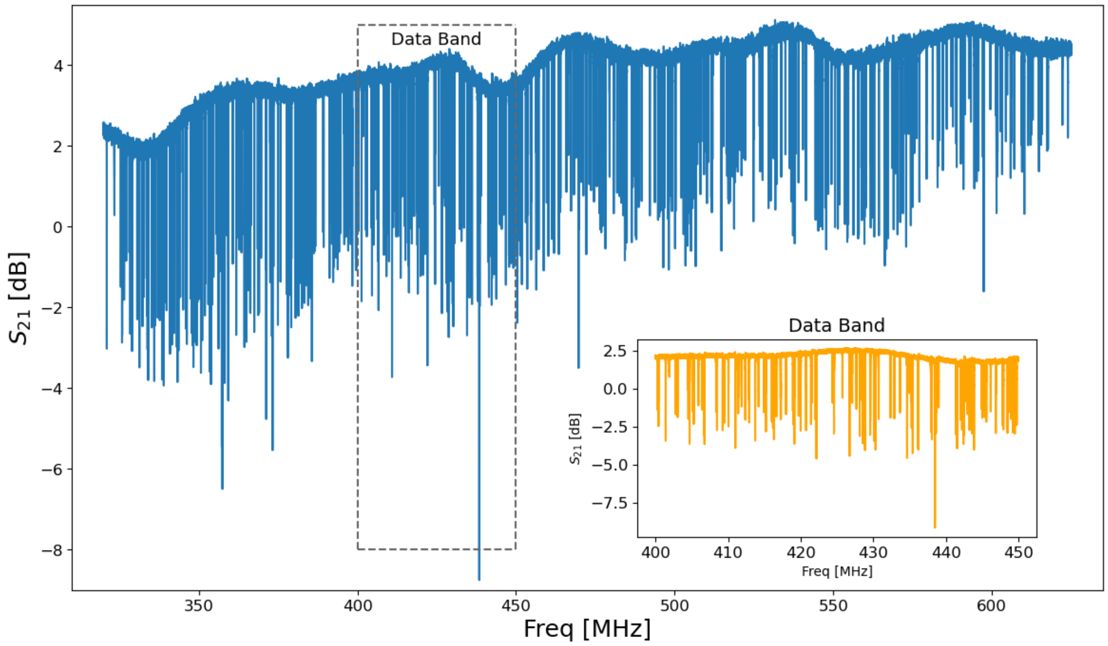

Figure 5.13: A full sweep of network 5 for the TiN array at a bath temperature of 145 mK and an estimated tone power of -96 dBm at the resonators. The inset region shows the band of detectors used for all bath temperature sweeps in Figure 5.14.

Figure 5.13 shows a full S_{21} sweep (in dB) of network 5 for the full TiN array at 145 mK, along with a close-up of a small band used for more extensive testing, previously described in 3.2. Within this narrow range, 25 detectors were selected for remaining fully within band and > 5 line-widths from nearby resonators in all sweeps up to the highest bath temperatures. These were well-fit across the full range of bath temperatures and powers. Figure 5.14 shows the resonator response to changing bath temperatures, with all 25 resonators overplotted. As is expected from the Mattis-Bardeen equations seen in 2.4.2, these detectors show monotonic behavior across the full range of bath temperatures that does not vary significantly with tone power. It should be noted that, during these bath temperature sweeps, the minimum bath temperature was limited to $\gtrsim 155$ mK, which is higher than the expected operating temperature of 100 mK.

Figure 5.15 shows a histogram of the total quality factors, internal quality factors, and coupling quality factors previously measured at ~ 105 mK on network 4 with the entire array closed up (dark) prior to LED-mapping. As with network 5, the bulk of the resonators had coupling quality factors (Q_c) in the range of 45,000 to 130,000. Based on measurements taken at NIST, the total Qs are expected to be in the range of 5,000 to 10,000 during operation under nominal optical loading conditions.

Of the two Al, arrays, both have completed LED-mapping at NIST, and the first has already completed its post-fabrication editing. The results of that, shown in Figure 5.16, were to effectively improve the total number of usable detectors (which is those detectors that are ≥ 5 line widths from their neighbors under expected loading conditions) by more than 30%. Trimming the resonance frequencies at this scale had not been done before with aluminum detectors, which are comparatively less robust than TiN detectors, making this demonstration a critical step in optimizing on-sky yield. While the overall yield improvement is encouraging, 85 (∼2.5% of the total) resonators were lost during the editing process, bringing the physical yield of identified resonators from 3230 to 3145. Similar or better results are anticipated for the second Al array, as well as the TiN array, which are both expected to be completed during the 2024 summer.

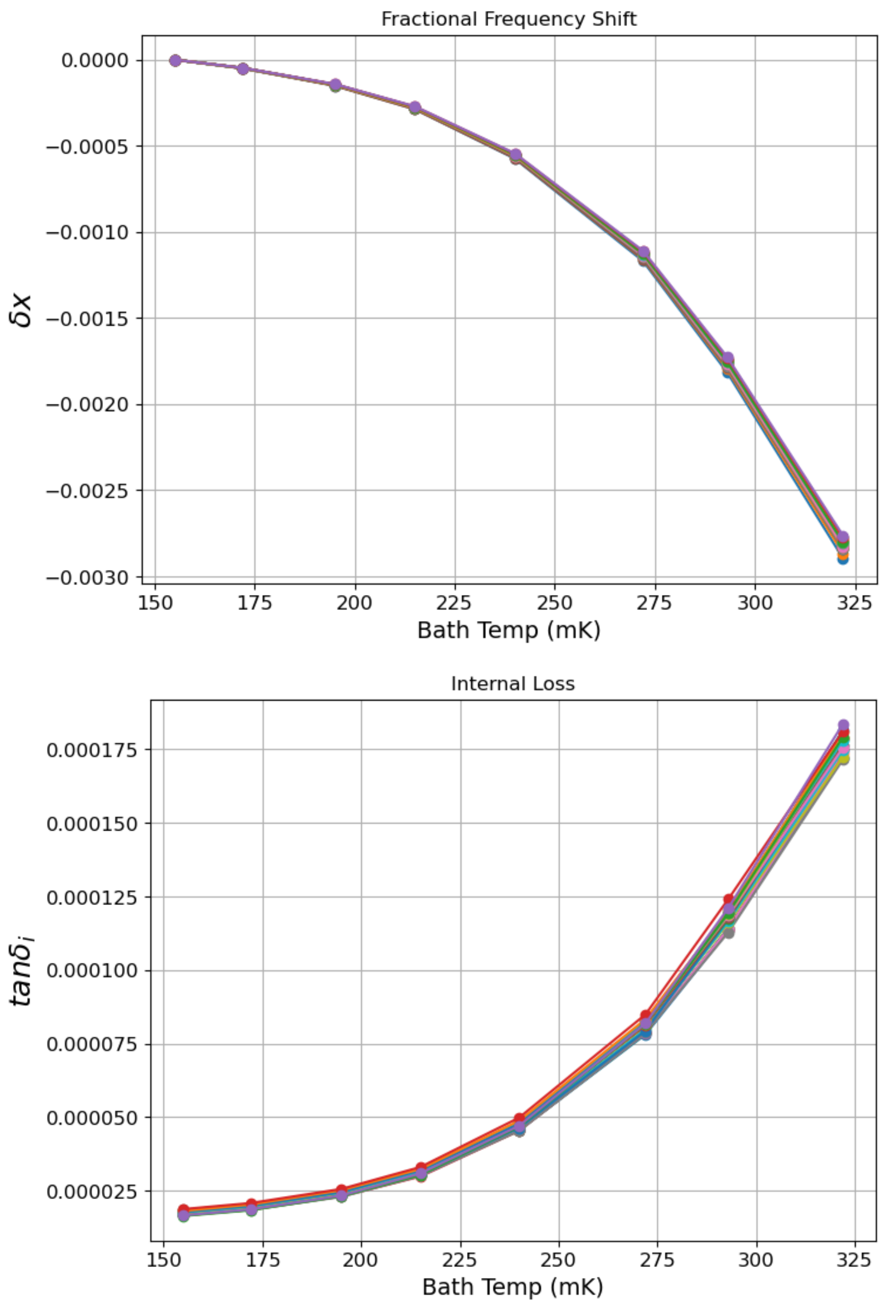

Figure 5.14: (Top) Fractional frequency shift vs. bath temperature based on fitted data from 25 TiN detectors. These were slightly less than half the resonators in a band from 400–450 MHz and were chosen because they remained fully within band up to the highest bath temperatures and were > 5 line-widths from any nearby resonators in all sweeps. (Bottom) Internal loss (inverse Q_i) as a function of bath temperature for the same resonator fits.

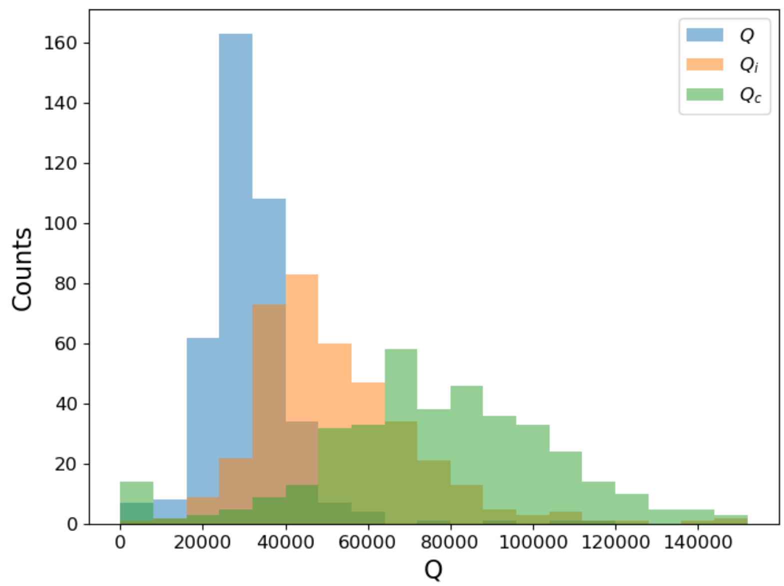

Figure 5.15: Example histogram of quality factors from a single representative network from the completed TiN array at a bath temperature of ~ 105 mK.

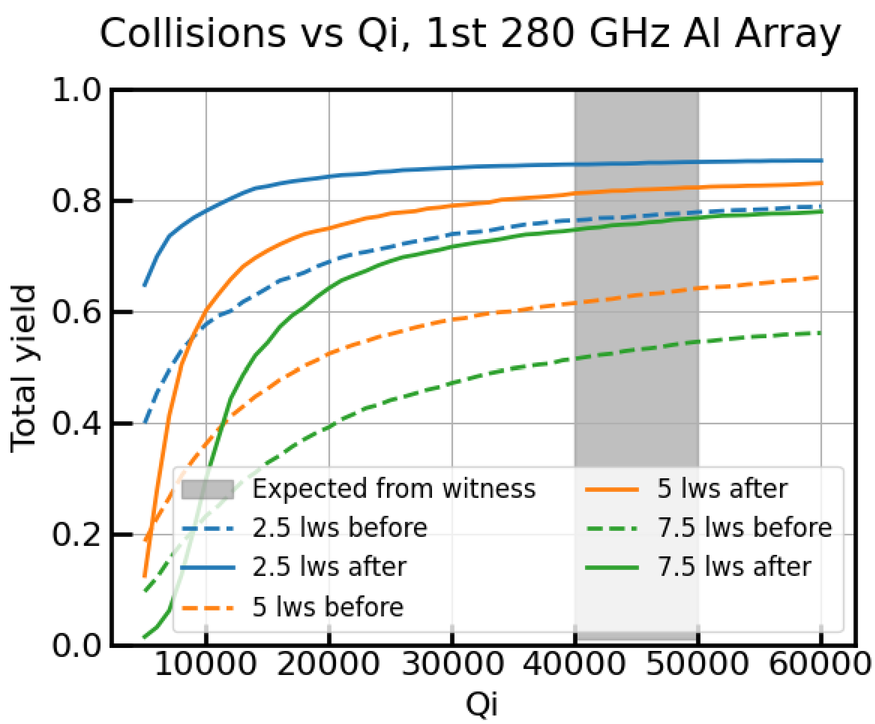

Figure 5.16: The expected number of usable resonators from the first aluminum KID array based on different cutoff criteria, with the expected range of internal quality factors during operation shown in gray. This is showing the fraction of resonators separated from their neighbors by greater than 2.5, 5, and 7.5 line-widths in blue, orange, and green respectively. The solid lines (after trimming) should be compared with the dashed lines (before trimming) to see the overall improvement. Figure produced by Jordan Wheeler.

CHAPTER 6

CONCLUSION

We conclude this dissertation with a brief discussion of some of the anticipated science from CCAT with FYST, highlighting a few interesting science cases (particularly as a complement to the Simons Observatory), as well as the work that remains to be done as we move towards first light.

6.1 Science with FYST

The CCAT collaboration brings together an international group of scientists focused on a wide range of astrophysical questions, from cosmology and large-scale structure to star formation and galactic science. This broad reach of science questions is enabled by the marriage of an exceptional site in Chile's Atacama with highly-sensitive, cutting-edge instrumentation. The 6-m aperture FYST, operating with Prime-Cam, will allow for large-scale mapping of the millimeter to submillimeter skies with wide frequency coverage (from 220 to 850 GHz across the planned polarization-sensitive modules). Each of the modules will sample its 1.3° diameter field-of-view to the diffraction-limit, populating the focal planes with an unprecedented number of feedhorn-coupled MKIDs. After five years of operation, the primary data products will be a 20,000 square-degree wide-field survey and a smaller deep-field spectroscopic survey, each with roughly 4,000 hours of integration time, as well as several shallower small field surveys. A detailed look at the science goals of these surveys is provided in [21], but we will just take a moment to discuss a few of the more exciting aspects from the perspective of a cosmologist.

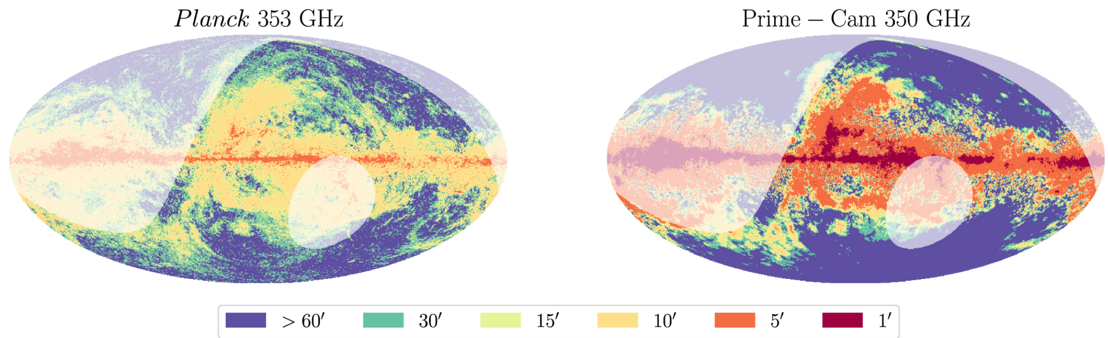

Figure 6.1: A comparison of the effective resolution for measurements of dust polarized intensity at signal-to-noise ratio > 3 for Planck at 353 GHz (left) and Prime-Cam at 350 GHz (right). Prime-Cam will offer a significant improvement in the fraction of the sky measured with high signal-to-noise at 5′ resolution or better, including significant portions of the galactic plane with a resolution of 1′. The white shaded region indicates the portion of the sky not observable by FYST. Figure from [21].

6.1.1 CMB Foregrounds

With the success of previous generations of CMB experiments, such as Planck and Advanced ACTPol, and the constraints currently placed on ΛCDM, modern cosmology has reached the point of using the CMB to probe new physics that is inaccessible at the moment in laboratory experiments. These include the study of inflation through the tensor-to-scalar ratio, r, and the existence of additional light particles or sources of radiation in the early universe through the parameter N_{eff}, which characterizes the effective number of relativistic species in the early universe. Evidence for either of these would appear in measurements of the CMB temperature and polarization anisotropies, with inflationary gravitational waves imprinting B-modes in polarization and additional light particles or radiation appearing in the high-l damping tail and the location of the various acoustic peaks.

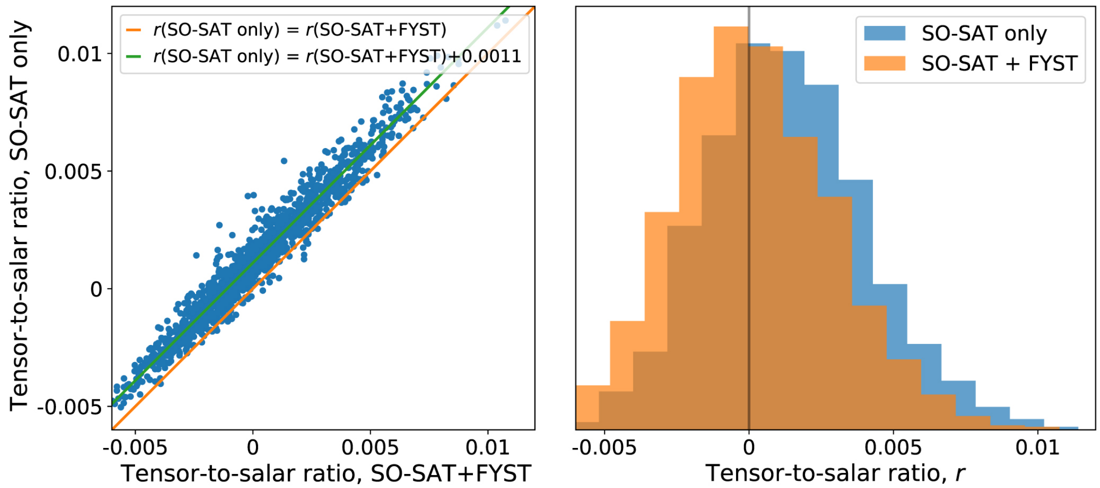

Figure 6.2: Left shows a scatter plot of the simulated best fit values for the tensor-to-scalar ratio, r, when measured with SO's Small Aperture Telescopes (SAT) only versus when combined with data from FYST. Right shows histograms of the same data. Both clearly display the possible systematic bias within the SO-only data set under common foreground modelling assumptions. As the simulations did not include a primordial B-mode signal, the "true" value would be $r = 0$. Figure from [21].

One of the fundamental limits on our measurement of these parameters, however, is our uncertainty on the emissions from galactic dust, particularly polarized emission. Based on observations from Planck [86], the polarized dust is well-described by a two-parameter modified black-body spectrum. The Simons Observatory is aiming to achieve an uncertainty in r of $\sigma(r) < 0.003$ and will be deploying a combination of several small aperture telescopes along with a large aperture telescope observing nearby to FYST across six frequency bands from 27 to 280 GHz. However, as seen in [2], uncertainty in the foreground emission parameters can cause a bias in r that is comparable to the overall statistical uncertainty. The additional high frequency coverage from Prime-Cam will provide the best constraints on polarized foreground emissions in the regions of the sky observed by SO. This can clearly be seen in Figure 6.1, showing the increased

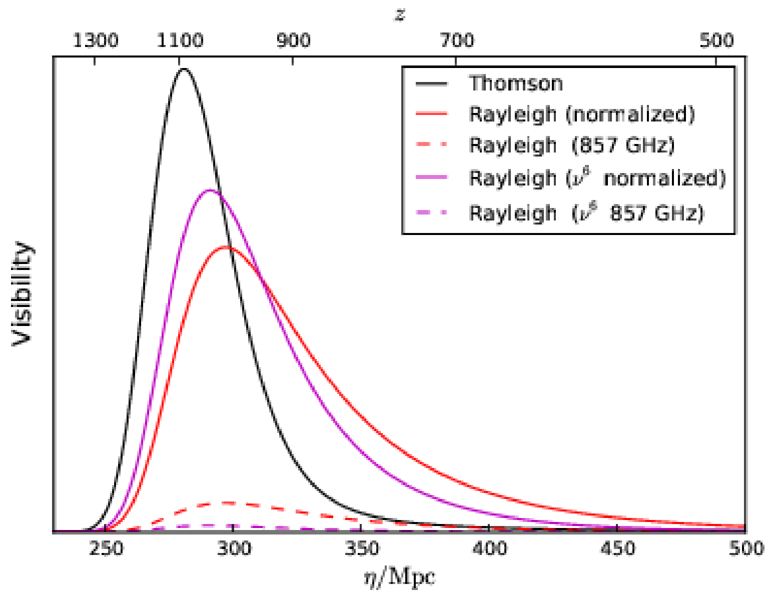

Figure 6.3: The normalized (solid) and relative (dashed) visibility functions for Rayleigh and Thomson scattering of photons showing the probability that a photon was last scattered at a particular conformal time, η, on the bottom axis, and redshift, z, on the top axis. Rayleigh terms scaling with frequency, ν, as ν^4 and ν^6 are shown separately with dashed lines showing the relative amplitude for 857 GHz. Figure from [64].

resolution in polarized dust intensity at high signal-to-noise from Prime-Cam's 350 GHz channel over Planck's 353 GHz channel. As forecasted in [21], this can significantly reduce the potential bias to $\sigma(r)$ and may reduce the need for SO to marginalize over the residual foreground, further improving constraints. This is shown in Figure 6.2. In this way, Prime-Cam's dust measurements may help to set the most stringent constraints on primordial gravitational waves.

6.1.2 Rayleigh Scattering of the CMB

Aside from aiding CMB measurements from SO, there remains a possibility for a unique CMB detection in the form of Rayleigh scattering from neutral hydrogen and helium around the time of recombination. While the early universe prior to the release of the CMB is dominated by Thomson scattering of photons off of free charged particles, as the number density of neutral species (initially helium and then predominantly hydrogen) begins to climb around and shortly after the time of recombination, Rayleigh scattering begins to have an impact. Since the density of neutral hydrogen and helium was anticorrelated with the density of free electrons, Rayleigh scattering has its largest effects at redshifts between roughly 1010 and 800. This is shown in Figure 6.3, which compares the evolving contributions of Thomson and Rayleigh scattering in the early universe as a function of both redshift and conformal time[1], η. This effect ought to be measurable by future observatories, including potentially FYST.

Since the cross-section for Rayleigh scattering has a strong frequency dependence in comparison to the roughly constant cross-section for Thomson scattering[2], it is expected to impart a distinct signature on the CMB that may be teased

[1]Conformal time is the total comoving distance that light could have traveled since $t = 0$, also referred to as the comoving horizon. This is the maximum separation beyond which two regions of space cannot be causally connected. The formal definition is

$$\eta \equiv \int_0^t \frac{dt'}{a(t')} \tag{6.1}$$

where $a(t)$ is the scale factor.

[2]For neutral hydrogen, the Rayleigh scattering cross-section goes as ν^4. The full expression is given by

$$\sigma_R(\nu) = \sigma_T \left[\left(\frac{\nu}{\nu_{eff}} \right)^4 + \frac{638}{243} \left(\frac{\nu}{\nu_{eff}} \right)^6 + \frac{1299667}{236196} \left(\frac{\nu}{\nu_{eff}} \right)^8 + ... \right] \tag{6.2}$$

where $\nu_{eff} \approx 3100$ THz and σ_T is the Thomson scattering cross-section [64].

out separately from the primary CMB anisotropies. The general effect is to increase the total baryon-photon coupling, adding a photon drag that delays last scattering and distorts the relationship between baryon and photon perturbations.

We can see some of the impact on the power spectra in Figure 6.4. On small scales, this leads to damping of both temperature and polarization anisotropies. At the same time, however, it also causes an increase in large-scale E-mode polarization by increasing the opacity and driving the source of the low-multipole polarization signal to a later time with an expected larger CMB quadrupole [5]. These contrasting shifts in the large and small-scale E-mode polarization mean that the B-mode signature from Rayleigh scattering is suppressed at large scales. This is because the B-mode polarization is produced by gravitationally-lensed E-modes across a range of scales, allowing the contributions to largely cancel [5]. Finally, the increased opacity at higher frequencies leads to a frequency-dependent shift in the surface of last scattering, increasing the sound horizon for higher frequencies [5, 116]. This can be seen as a slight shift in the peaks in Figure 6.4.

While these effects are sufficiently small (peaking at just the few percent level [116]), it is a part of the observed signal in both intensity and polarization. By taking advantage of the information in both primary and Rayleigh CMB anisotropy signals, measurements of the thermal and polarization autospectra and cross-spectra can significantly add to cosmological parameter constraints while uniquely probing the universe at the time of recombination. Since the Rayleigh-CMB sky contains a full additional set of modes from the early universe to probe, a detection would enable us to place tighter constraints on the

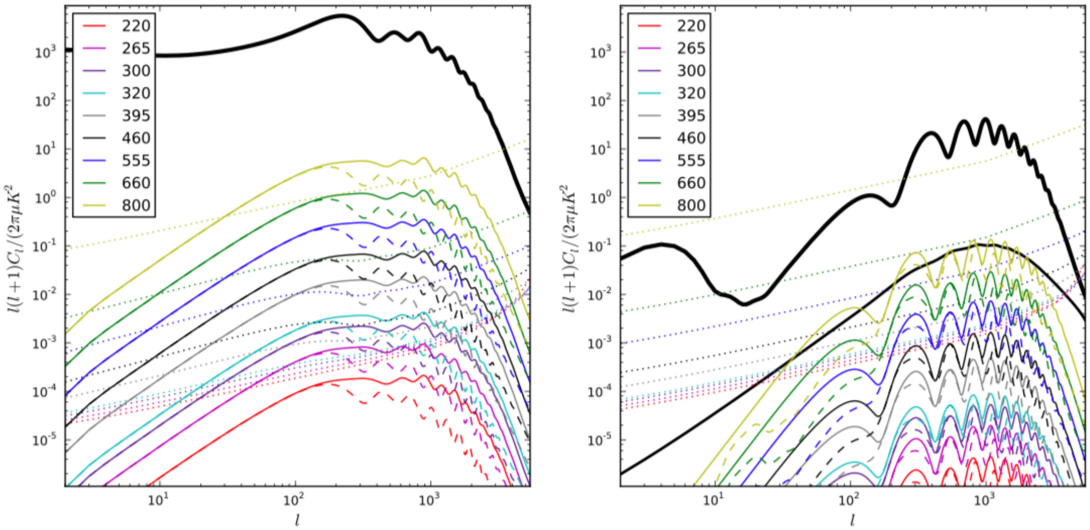

Figure 6.4: The Rayleigh autospectra at various frequencies (in GHz) in temperature (left) and E-polarization (right). Dashed lines show the uncorrelated component, while the solid black lines represent the primary power spectra. The lower, thinner black line on the right represents the primary B-polarization spectra. Dotted lines represent potential noise from the proposed PRISM instrument and can be ignored here. Figure from [64].

parameters of ΛCDM than ordinarily allowed by cosmic variance.

As sensitivity increases and methods for removing foregrounds improve, the signal from Rayleigh scattering is inching closer to detection. The first measurements will need to come through a cross-correlation with the primary CMB, and has likely been prevented to this point as a result of astrophysical foregrounds [21]. As described in [118], combining the frequency coverage and sensitivity of FYST with additional data sets from Planck and SO should deliver the best chances for a detection in the near-term future, though, as shown in Figure 6.5, the combination of foregrounds and sky noise are likely to keep a high signal-to-noise detection out of range. It seems increasingly likely that measuring the Rayleigh scattering signal well enough to improve cosmological constraints will require a space-based telescope.

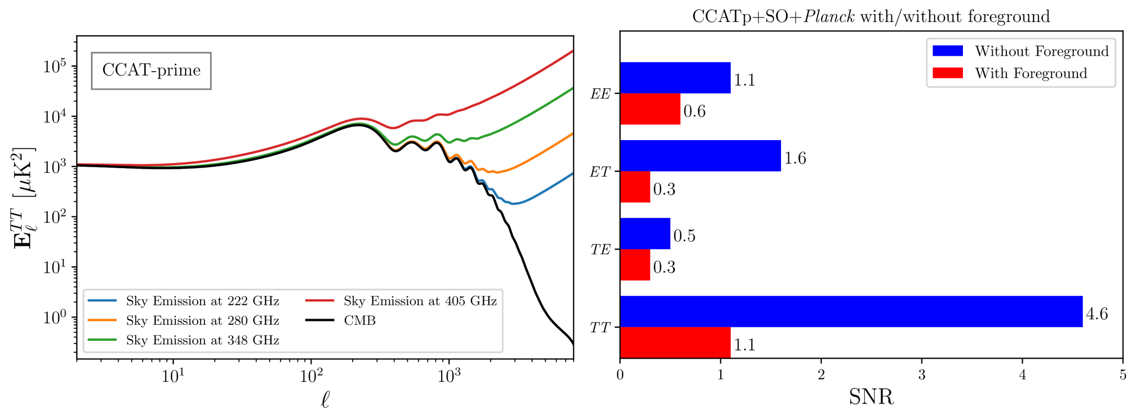

Figure 6.5: (Left) The predicted sky emission as a function of multipole for various frequency channels on Prime-Cam plotted with the CMB power spectrum. (Right) Forecasted signal-to-noise ratio with and without foregrounds for the CMB-Rayleigh scattering cross-spectrum using combined data from CCAT, SO, and Planck. Figures from [118].

6.2 Towards First Light

With much of the work already demonstrated and first light for FYST rapidly approaching, what remains to be done? The primary detector and readout technologies have been validated individually, but, prior to the complete module assembly, all three of the detector arrays must be in their complete and final state. This means the LED-mapping and trimming process must be completed to place each detector in its final position in frequency space. At the time of writing, this has been completed for one aluminum array, demonstrating a significant improvement in detector spacing to avoid collisions in operation. Both of the remaining 280 GHz arrays are currently undergoing position-to-frequency mapping by LEDs in preparation for editing in the near future at NIST. When completed, all three arrays will be installed within the full instrument module for demonstration and re-characterization within Mod-Cam.

Aside from the hardware, there is still work to be done for the readout software. As shown in [97] and [96], significant progress has been made in implementing readout strategies for Prime-Cam based on previous work on BLAST-TNG and TolTEC. Even so, there is still work to be done to improve the efficiency of detector tuning, monitoring, and converting between frequency and optical power. This is particularly the case for the aluminum detectors, given their more complicated nonlinear behavior.

6.3 Concluding Remarks

This dissertation describes many of the author's technical contributions to the development and demonstration of the detectors and readout for Prime-Cam's 280 GHz and 350 GHz instrument modules. This work was done in the context of the CCAT, ACT, and SO collaborations with the aim of advancing our fundamental understanding of cosmology and astrophysics. With the foundations laid in chapter 2, we presented comparative measurements and analysis of TiN and Al MKIDs in chapter 3. Both of these types of detector arrays are intended for deployment as part of the 280 GHz instrument module. In chapter 4, we described the design and validation of the cryogenic readout systems, with demonstrations of photon-noise limited performance in the laboratory. Chapter 5 similarly described the designs, fabrication, and validation of focal plane packages for two distinct feedhorn-coupled detector designs as well as some of the measurements being made as we move towards deployment. It is the author's hope that this work has paid a small but crucial role in helping to advance our understanding and exploration of the universe and our place in it.

BIBLIOGRAPHY

[1] R. Adam, A. Adane, P. a. R. Ade, P. André, A. Andrianasolo, H. Aussel, A. Beelen, A. Benoît, A. Bideaud, N. Billot, O. Bourrion, A. Bracco, M. Calvo, A. Catalano, G. Coiffard, B. Comis, M. De Petris, F.-X. Désert, S. Doyle, E. F. C. Driessen, R. Evans, J. Goupy, C. Kramer, G. Lagache, S. Leclercq, J.-P. Leggeri, J.-F. Lestrade, J. F. Macías-Pérez, P. Mauskopf, F. Mayet, A. Maury, A. Monfardini, S. Navarro, E. Pascale, L. Perotto, G. Pisano, N. Ponthieu, V. Revéret, A. Rigby, A. Ritacco, C. Romero, H. Roussel, F. Ruppin, K. Schuster, A. Sievers, S. Triqueneaux, C. Tucker, and R. Zylka. The NIKA2 large-field-of-view millimetre continuum camera for the 30 m IRAM telescope. *Astronomy & Astrophysics*, 609:A115, January 2018. Publisher: EDP Sciences.

[2] Peter Ade, James Aguirre, Zeeshan Ahmed, Simone Aiola, Aamir Ali, David Alonso, Marcelo A. Alvarez, Kam Arnold, Peter Ashton, Jason Austermann, Humna Awan, Carlo Baccigalupi, Taylor Baildon, Darcy Barron, Nick Battaglia, Richard Battye, Eric Baxter, Andrew Bazarko, James A. Beall, Rachel Bean, Dominic Beck, Shawn Beckman, Benjamin Beringue, Federico Bianchini, Steven Boada, David Boettger, J. Richard Bond, Julian Borrill, Michael L. Brown, Sarah Marie Bruno, Sean Bryan, Erminia Calabrese, Victoria Calafut, Paolo Calisse, Julien Carron, Anthony Challinor, Grace Chesmore, Yuji Chinone, Jens Chluba, Hsiao-Mei Sherry Cho, Steve Choi, Gabriele Coppi, Nicholas F. Cothard, Kevin Coughlin, Devin Crichton, Kevin D. Crowley, Kevin T. Crowley, Ari Cukierman, John M. D'Ewart, Rolando Dünner, Tijmen de Haan, Mark Devlin, Simon Dicker, Joy Didier, Matt Dobbs, Bradley Dober, Cody J. Duell, Shannon Duff, Adri Duivenvoorden, Jo Dunk-

ley, John Dusatko, Josquin Errard, Giulio Fabbian, Stephen Feeney, Simone Ferraro, Pedro Fluxà, Katherine Freese, Josef C. Frisch, Andrei Frolov, George Fuller, Brittany Fuzia, Nicholas Galitzki, Patricio A. Gallardo, Jose Tomas Galvez Ghersi, Jiansong Gao, Eric Gawiser, Martina Gerbino, Vera Gluscevic, Neil Goeckner-Wald, Joseph Golec, Sam Gordon, Megan Gralla, Daniel Green, Arpi Grigorian, John Groh, Chris Groppi, Yilun Guan, Jon E. Gudmundsson, Dongwon Han, Peter Hargrave, Masaya Hasegawa, Matthew Hasselfield, Makoto Hattori, Victor Haynes, Masashi Hazumi, Yizhou He, Erin Healy, Shawn W. Henderson, Carlos Hervias-Caimapo, Charles A. Hill, J. Colin Hill, Gene Hilton, Matt Hilton, Adam D. Hincks, Gary Hinshaw, Renée Hložek, Shirley Ho, Shuay-Pwu Patty Ho, Logan Howe, Zhiqi Huang, Johannes Hubmayr, Kevin Huffenberger, John P. Hughes, Anna Ijjas, Margaret Ikape, Kent Irwin, Andrew H. Jaffe, Bhuvnesh Jain, Oliver Jeong, Daisuke Kaneko, Ethan D. Karpel, Nobuhiko Katayama, Brian Keating, Sarah S. Kernasovskiy, Reijo Keskitalo, Theodore Kisner, Kenji Kiuchi, Jeff Klein, Kenda Knowles, Brian Koopman, Arthur Kosowsky, Nicoletta Krachmalnicoff, Stephen E. Kuenstner, Chao-Lin Kuo, Akito Kusaka, Jacob Lashner, Adrian Lee, Eunseong Lee, David Leon, Jason S. Y. Leung, Antony Lewis, Yaqiong Li, Zack Li, Michele Limon, Eric Linder, Carlos Lopez-Caraballo, Thibaut Louis, Lindsay Lowry, Marius Lungu, Mathew Madhavacheril, Daisy Mak, Felipe Maldonado, Hamdi Mani, Ben Mates, Frederick Matsuda, Loïc Maurin, Phil Mauskopf, Andrew May, Nialh McCallum, Chris McKenney, Jeff McMahon, P. Daniel Meerburg, Joel Meyers, Amber Miller, Mark Mirmelstein, Kavilan Moodley, Moritz Munchmeyer, Charles Munson, Sigurd Naess, Federico Nati, Martin Navaroli, Laura

Newburgh, Ho Nam Nguyen, Michael Niemack, Haruki Nishino, John Orlowski-Scherer, Lyman Page, Bruce Partridge, Julien Peloton, Francesca Perrotta, Lucio Piccirillo, Giampaolo Pisano, Davide Poletti, Roberto Puddu, Giuseppe Puglisi, Chris Raum, Christian L. Reichardt, Mathieu Remazeilles, Yoel Rephaeli, Dominik Riechers, Felipe Rojas, Anirban Roy, Sharon Sadeh, Yuki Sakurai, Maria Salatino, Mayuri Sathyanarayana Rao, Emmanuel Schaan, Marcel Schmittfull, Neelima Sehgal, Joseph Seibert, Uros Seljak, Blake Sherwin, Meir Shimon, Carlos Sierra, Jonathan Sievers, Precious Sikhosana, Maximiliano Silva-Feaver, Sara M. Simon, Adrian Sinclair, Praween Siritanasak, Kendrick Smith, Stephen R. Smith, David Spergel, Suzanne T. Staggs, George Stein, Jason R. Stevens, Radek Stompor, Aritoki Suzuki, Osamu Tajima, Satoru Takakura, Grant Teply, Daniel B. Thomas, Ben Thorne, Robert Thornton, Hy Trac, Calvin Tsai, Carole Tucker, Joel Ullom, Sunny Vagnozzi, Alexander van Engelen, Jeff Van Lanen, Daniel D. Van Winkle, Eve M. Vavagiakis, Clara Vergès, Michael Vissers, Kasey Wagoner, Samantha Walker, Jon Ward, Ben Westbrook, Nathan Whitehorn, Jason Williams, Joel Williams, Edward J. Wollack, Zhilei Xu, Byeonghee Yu, Cyndia Yu, Fernando Zago, Hezi Zhang, Ningfeng Zhu, and Simons Observatory Collaboration. The Simons Observatory: science goals and forecasts. *Journal of Cosmology and Astroparticle Physics*, 2019:056, February 2019. Publisher: IOP ADS Bibcode: 2019JCAP...02..056A.

[3] Peter A. R. Ade, Giampaolo Pisano, Carole Tucker, and Samuel Weaver. A review of metal mesh filters. In *Millimeter and Submillimeter Detectors and Instrumentation for Astronomy III*, volume 6275, pages 248–262. SPIE, June 2006.

[4] N. Aghanim, Y. Akrami, F. Arroja, M. Ashdown, J. Aumont, C. Baccigalupi, M. Ballardini, A. J. Banday, R. B. Barreiro, N. Bartolo, S. Basak, R. Battye, K. Benabed, J.-P. Bernard, M. Bersanelli, P. Bielewicz, J. J. Bock, J. R. Bond, J. Borrill, F. R. Bouchet, F. Boulanger, M. Bucher, C. Burigana, R. C. Butler, E. Calabrese, J.-F. Cardoso, J. Carron, B. Casaponsa, A. Challinor, H. C. Chiang, L. P. L. Colombo, C. Combet, D. Contreras, B. P. Crill, F. Cuttaia, P. de Bernardis, G. de Zotti, J. Delabrouille, J.-M. Delouis, F.-X. Désert, E. Di Valentino, C. Dickinson, J. M. Diego, S. Donzelli, O. Doré, M. Douspis, A. Ducout, X. Dupac, G. Efstathiou, F. Elsner, T. A. Enßlin, H. K. Eriksen, E. Falgarone, Y. Fantaye, J. Fergusson, R. Fernandez-Cobos, F. Finelli, F. Forastieri, M. Frailis, E. Franceschi, A. Frolov, S. Galeotta, S. Galli, K. Ganga, R. T. Génova-Santos, M. Gerbino, T. Ghosh, J. González-Nuevo, K. M. Górski, S. Gratton, A. Gruppuso, J. E. Gudmundsson, J. Hamann, W. Handley, F. K. Hansen, G. Helou, D. Herranz, S. R. Hildebrandt, E. Hivon, Z. Huang, A. H. Jaffe, W. C. Jones, A. Karakci, E. Keihänen, R. Keskitalo, K. Kiiveri, J. Kim, T. S. Kisner, L. Knox, N. Krachmalnicoff, M. Kunz, H. Kurki-Suonio, G. Lagache, J.-M. Lamarre, M. Langer, A. Lasenby, M. Lattanzi, C. R. Lawrence, M. Le Jeune, J. P. Leahy, J. Lesgourgues, F. Levrier, A. Lewis, M. Liguori, P. B. Lilje, M. Lilley, V. Lindholm, M. López-Caniego, P. M. Lubin, Y.-Z. Ma, J. F. Macías-Pérez, G. Maggio, D. Maino, N. Mandolesi, A. Mangilli, A. Marcos-Caballero, M. Maris, P. G. Martin, M. Martinelli, E. Martínez-González, S. Matarrese, N. Mauri, J. D. McEwen, P. D. Meerburg, P. R. Meinhold, A. Melchiorri, A. Mennella, M. Migliaccio, M. Millea, S. Mitra, M.-A. Miville-Deschênes, D. Molinari, A. Moneti, L. Montier, G. Morgante, A. Moss, S. Mottet, M. Münchmeyer, P. Natoli, H. U. Nørgaard-

Nielsen, C. A. Oxborrow, L. Pagano, D. Paoletti, B. Partridge, G. Patanchon, T. J. Pearson, M. Peel, H. V. Peiris, F. Perrotta, V. Pettorino, F. Piacentini, L. Polastri, G. Polenta, J.-L. Puget, J. P. Rachen, M. Reinecke, M. Remazeilles, C. Renault, A. Renzi, G. Rocha, C. Rosset, G. Roudier, J. A. Rubiño-Martín, B. Ruiz-Granados, L. Salvati, M. Sandri, M. Savelainen, D. Scott, E. P. S. Shellard, M. Shiraishi, C. Sirignano, G. Sirri, L. D. Spencer, R. Sunyaev, A.-S. Suur-Uski, J. A. Tauber, D. Tavagnacco, M. Tenti, L. Terenzi, L. Toffolatti, M. Tomasi, T. Trombetti, J. Valiviita, B. Van Tent, L. Vibert, P. Vielva, F. Villa, N. Vittorio, B. D. Wandelt, I. K. Wehus, M. White, S. D. M. White, A. Zacchei, and A. Zonca. Planck 2018 results - I. Overview and the cosmological legacy of Planck. *Astronomy & Astrophysics*, 641:A1, September 2020. Publisher: EDP Sciences.

[5] Elham Alipour, Kris Sigurdson, and Christopher M. Hirata. Effects of Rayleigh scattering on the CMB and cosmic structure. *Physical Review D*, 91(8):083520, April 2015. Publisher: American Physical Society.

[6] R. A. Alpher, H. Bethe, and G. Gamow. The Origin of Chemical Elements. *Physical Review*, 73(7):803–804, April 1948. Publisher: American Physical Society.

[7] Ralph A. Alpher and Robert C. Herman. On the Relative Abundance of the Elements. *Physical Review*, 74(12):1737–1742, December 1948. Publisher: American Physical Society.

[8] Neil W. Ashcroft and N. David Mermin. *Solid state physics*. Saunders college publ, Fort Worth Philadelphia San Diego [etc.], 1976.

[9] Jason Austermann, James Beall, Sean A. Bryan, Brad Dober, Jiansong Gao, Gene Hilton, Johannes Hubmayr, Philip Mauskopf, Christopher McKen-

ney, Sara M. Simon, Joel Ullom, Michael Vissers, and Grant W. Wilson. Large format arrays of kinetic inductance detectors for the TolTEC millimeter-wave imaging polarimeter (Conference Presentation). In *Millimeter, Submillimeter, and Far-Infrared Detectors and Instrumentation for Astronomy IX*, volume 10708, page 107080U. International Society for Optics and Photonics, July 2018.

[10] Jason E. Austermann, Yvonne Ban, James Beall, Marc Berthoud, Reid Contente, Natalie DeNigris, Bradley Dober, Jiansong Gao, Gene Hilton, Johannes Hubmayr, Steve Kuczarski, Dennis Lee, Emily Lunde, Zhiyuan Ma, Philip Mauskopf, Michael McCrackan, Christopher McKenney, Jeffrey McMahon, Giles Novak, Sophia Abi-Saad, Sara Simon, Kamal Souccar, Joel Ullom, Eric Van Camp, Jeff Van Lanen, Michael Vissers, and Grant Wilson. TolTEC focal plane arrays: design, characterization, and performance of kilopixel MKID focal planes. In *Millimeter, Submillimeter, and Far-Infrared Detectors and Instrumentation for Astronomy X*, volume 11453, page 114530A. SPIE, December 2020.

[11] Jason E. Austermann, James Beall, Jiansong Gao, Johannes Hubmayr, Joel Ullom, Michael Vissers, and Jordan Wheeler. Aluminum-based millimeter-wave kinetic inductance detectors on 150˜mm diameter substrates. In *Millimeter, Submillimeter, and Far-Infrared Detectors and Instrumentation for Astronomy XI*, volume PC12190, page PC121900X. SPIE, August 2022.

[12] J.E. Austermann, J.A. Beall, S.A. Bryan, B. Dober, J. Gao, G. Hilton, J. Hubmayr, P. Mauskopf, C.M. McKenney, S.M. Simon, J.N. Ullom, M.R. Vissers, and G.W. Wilson. Millimeter-Wave Polarimeters Using Kinetic Induc-

tance Detectors for TolTEC and Beyond. *Journal of low temperature physics*, 193(3-4):10.1007/s10909–018–1949–5, 2018.

[13] N. A. Bahcall, R. Cen, R. Davé, J. P. Ostriker, and Q. Yu. The Mass-to-Light Function: Antibias and Ω_m. *The Astrophysical Journal*, 541:1–9, September 2000. Publisher: IOP ADS Bibcode: 2000ApJ...541....1B.

[14] J. Bardeen, L. N. Cooper, and J. R. Schrieffer. Theory of Superconductivity. *Physical Review*, 108(5):1175–1204, December 1957. Publisher: American Physical Society.

[15] Thomas L. R. Brien, Peter A. R. Ade, Peter S. Barry, Edgar Castillo-Domìnguez, Daniel Ferrusca, Thomas Gascard, Victor Gómez, Peter C. Hargrave, Amber L. Hornsby, David Hughes, Enzo Pascale, Josie D. A. Parrianen, Abel Perez, Sam Rowe, Carole Tucker, Salvador Ventura González, and Simon M. Doyle. MUSCAT: the Mexico-UK Sub-Millimetre Camera for AsTronomy. In *Millimeter, Submillimeter, and Far-Infrared Detectors and Instrumentation for Astronomy IX*, volume 10708, pages 173–181. SPIE, July 2018.

[16] Jhy-Jiun Chang and D. J. Scalapino. Nonequilibrium superconductivity. *Journal of Low Temperature Physics*, 31(1):1–32, April 1978.

[17] S. K. Choi, J. Austermann, K. Basu, N. Battaglia, F. Bertoldi, D. T. Chung, N. F. Cothard, S. Duff, C. J. Duell, P. A. Gallardo, J. Gao, T. Herter, J. Hubmayr, M. D. Niemack, T. Nikola, D. Riechers, K. Rossi, G. J. Stacey, J. R. Stevens, E. M. Vavagiakis, M. Vissers, and S. Walker. Sensitivity of the Prime-Cam Instrument on the CCAT-Prime Telescope. *Journal of Low Temperature Physics*, 199(3):1089–1097, May 2020.

[18] S. K. Choi, C. J. Duell, J. Austermann, N. F. Cothard, J. Gao, R. G. Freundt, C. Groppi, T. Herter, J. Hubmayr, Z. B. Huber, B. Keller, Y. Li, P. Mauskopf, M. D. Niemack, T. Nikola, K. Rossi, A. Sinclair, G. J. Stacey, E. M. Vavagiakis, M. Vissers, C. Tucker, E. Weeks, and J. Wheeler. CCAT-Prime: Characterization of the First 280 GHz MKID Array for Prime-Cam. *Journal of Low Temperature Physics*, 209(5):849–856, December 2022.

[19] Steve K. Choi, Matthew Hasselfield, Shuay-Pwu Patty Ho, Brian Koopman, Marius Lungu, Maximilian H. Abitbol, Graeme E. Addison, Peter A. R. Ade, Simone Aiola, David Alonso, Mandana Amiri, Stefania Amodeo, Elio Angile, Jason E. Austermann, Taylor Baildon, Nick Battaglia, James A. Beall, Rachel Bean, Daniel T. Becker, J. Richard Bond, Sarah Marie Bruno, Erminia Calabrese, Victoria Calafut, Luis E. Campusano, Felipe Carrero, Grace E. Chesmore, Hsiao-mei Cho, Susan E. Clark, Nicholas F. Cothard, Devin Crichton, Kevin T. Crowley, Omar Darwish, Rahul Datta, Edward V. Denison, Mark J. Devlin, Cody J. Duell, Shannon M. Duff, Adriaan J. Duivenvoorden, Jo Dunkley, Rolando Dünner, Thomas Essinger-Hileman, Max Fankhanel, Simone Ferraro, Anna E. Fox, Brittany Fuzia, Patricio A. Gallardo, Vera Gluscevic, Joseph E. Golec, Emily Grace, Megan Gralla, Yilun Guan, Kirsten Hall, Mark Halpern, Dongwon Han, Peter Hargrave, Shawn Henderson, Brandon Hensley, J. Colin Hill, Gene C. Hilton, Matt Hilton, Adam D. Hincks, Renée Hložek, Johannes Hubmayr, Kevin M. Huffenberger, John P. Hughes, Leopoldo Infante, Kent Irwin, Rebecca Jackson, Jeff Klein, Kenda Knowles, Arthur Kosowsky, Vincent Lakey, Dale Li, Yaqiong Li, Zack Li, Martine Lokken, Thibaut Louis, Amanda MacInnis, Mathew Madhavacheril, Felipe Maldonado, Maya Mallaby-Kay, Dan-

ica Marsden, Loïc Maurin, Jeff McMahon, Felipe Menanteau, Kavilan Moodley, Tim Morton, Sigurd Naess, Toshiya Namikawa, Federico Nati, Laura Newburgh, John P. Nibarger, Andrina Nicola, Michael D. Niemack, Michael R. Nolta, John Orlowski-Sherer, Lyman A. Page, Christine G. Pappas, Bruce Partridge, Phumlani Phakathi, Heather Prince, Roberto Puddu, Frank J. Qu, Jesus Rivera, Naomi Robertson, Felipe Rojas, Maria Salatino, Emmanuel Schaan, Alessandro Schillaci, Benjamin L. Schmitt, Neelima Sehgal, Blake D. Sherwin, Carlos Sierra, Jon Sievers, Cristobal Sifon, Precious Sikhosana, Sara Simon, David N. Spergel, Suzanne T. Staggs, Jason Stevens, Emilie Storer, Dhaneshwar D. Sunder, Eric R. Switzer, Ben Thorne, Robert Thornton, Hy Trac, Jesse Treu, Carole Tucker, Leila R. Vale, Alexander Van Engelen, Jeff Van Lanen, Eve M. Vavagiakis, Kasey Wagoner, Yuhan Wang, Jonathan T. Ward, Edward J. Wollack, Zhilei Xu, Fernando Zago, and Ningfeng Zhu. The Atacama Cosmology Telescope: a measurement of the Cosmic Microwave Background power spectra at 98 and 150 GHz. *Journal of Cosmology and Astroparticle Physics*, 2020(12):045, December 2020.

[20] COAX Co., Ltd. Cryogenic cables. http://www.coax.co.jp/en/cryogenic. Accessed: 2022-09-07.

[21] CCAT-Prime Collaboration, Manuel Aravena, Jason E. Austermann, Kaustuv Basu, Nicholas Battaglia, Benjamin Beringue, Frank Bertoldi, Frank Bigiel, J. Richard Bond, Patrick C. Breysse, Colton Broughton, Ricardo Bustos, Scott C. Chapman, Maude Charmetant, Steve K. Choi, Dongwoo T. Chung, Susan E. Clark, Nicholas F. Cothard, Abigail T. Crites, Ankur Dev, Kaela Douglas, Cody J. Duell, Rolando Dünner, Haruki Ebina, Jens Erler, Michel Fich, Laura M. Fissel, Simon Foreman, R. G. Freundt,

Patricio A. Gallardo, Jiansong Gao, Pablo García, Riccardo Giovanelli, Joseph E. Golec, Christopher E. Groppi, Martha P. Haynes, Douglas Henke, Brandon Hensley, Terry Herter, Ronan Higgins, Renée Hložek, Anthony Huber, Zachary Huber, Johannes Hubmayr, Rebecca Jackson, Douglas Johnstone, Christos Karoumpis, Laura C. Keating, Eiichiro Komatsu, Yaqiong Li, Benjamin Magnelli, Brenda C. Matthews, Philip D. Mauskopf, Jeffrey J. McMahon, P. Daniel Meerburg, Joel Meyers, Vyoma Muralidhara, Norman W. Murray, Michael D. Niemack, Thomas Nikola, Yoko Okada, Roberto Puddu, Dominik A. Riechers, Erik Rosolowsky, Kayla Rossi, Kaja Rotermund, Anirban Roy, Sarah I. Sadavoy, Reinhold Schaaf, Peter Schilke, Douglas Scott, Robert Simon, Adrian K. Sinclair, Gregory R. Sivakoff, Gordon J. Stacey, Amelia M. Stutz, Juergen Stutzki, Mehrnoosh Tahani, Karun Thanjavur, Ralf A. Timmermann, Joel N. Ullom, Alexander van Engelen, Eve M. Vavagiakis, Michael R. Vissers, Jordan D. Wheeler, Simon D. M. White, Yijie Zhu, and Bugao Zou. CCAT-prime Collaboration: Science Goals and Forecasts with Prime-Cam on the Fred Young Submillimeter Telescope. *The Astrophysical Journal Supplement Series*, 264(1):7, December 2022. Publisher: The American Astronomical Society.

[22] N. F. Cothard, S. K. Choi, C. J. Duell, T. Herter, J. Hubmayr, J. McMahon, M. D. Niemack, T. Nikola, C. Sierra, G. J. Stacey, E. M. Vavagiakis, E. J. Wollack, and B. Zou. The Design of the CCAT-prime Epoch of Reionization Spectrometer Instrument. *Journal of Low Temperature Physics*, 199(3):898–907, May 2020.

[23] K. P. Coughlin, J. J. McMahon, K. T. Crowley, B. J. Koopman, K. H. Miller, S. M. Simon, and E. J. Wollack. Pushing the Limits of Broadband and

High-Frequency Metamaterial Silicon Antireflection Coatings. *Journal of Low Temperature Physics*, 193(5):876–885, December 2018.

[24] CryoCoax. Cryogenic Cable and Cable Assembly Specifications. https://cryocoax.com/cryogenic-cable-and-cable-assemblies/. Accessed: 2022-09-07.

[25] R. Datta, C. D. Munson, M. D. Niemack, J. J. McMahon, J. Britton, E. J. Wollack, J. Beall, M. J. Devlin, J. Fowler, P. Gallardo, J. Hubmayr, K. Irwin, L. Newburgh, J. P. Nibarger, L. Page, M. A. Quijada, B. L. Schmitt, S. T. Staggs, R. Thornton, and L. Zhang. Large-aperture wide-bandwidth antireflection-coated silicon lenses for millimeter wavelengths. *Applied Optics*, 52(36):8747–8758, December 2013. Publisher: Optica Publishing Group.

[26] Peter K. Day, Henry G. LeDuc, Benjamin A. Mazin, Anastasios Vayonakis, and Jonas Zmuidzinas. A broadband superconducting detector suitable for use in large arrays. *Nature*, 425(6960):817–821, October 2003. Number: 6960 Publisher: Nature Publishing Group.

[27] P. J. de Visser. *Quasiparticle dynamics in aluminium superconducting microwave resonators*. PhD thesis, Delft University of Technology, 2014.

[28] P. J. de Visser, J. J. A. Baselmans, J. Bueno, N. Llombart, and T. M. Klapwijk. Fluctuations in the electron system of a superconductor exposed to a photon flux. *Nature Communications*, 5(1):3130, February 2014. Publisher: Nature Publishing Group.

[29] P. J. de Visser, D. J. Goldie, P. Diener, S. Withington, J. J. A. Baselmans, and T. M. Klapwijk. Evidence of a Nonequilibrium Distribution of Quasipar-

ticles in the Microwave Response of a Superconducting Aluminum Resonator. *Physical Review Letters*, 112(4):047004, January 2014. Publisher: American Physical Society.

[30] P. J. de Visser, S. J. C. Yates, T. Guruswamy, D. J. Goldie, S. Withington, A. Neto, N. Llombart, A. M. Baryshev, T. M. Klapwijk, and J. J. A. Baselmans. The non-equilibrium response of a superconductor to pair-breaking radiation measured over a broad frequency band. *Applied Physics Letters*, 106(25):252602, June 2015.

[31] S. R. Dicker, P. A. Gallardo, J. E. Gudmundsson, P. D. Mauskopf, A. Ali, P. C. Ashton, G. Coppi, M. J. Devlin, N. Galitzki, S. P. Ho, C. A. Hill, J. Hubmayr, B. Keating, A. T. Lee, M. Limon, F. Matsuda, J. McMahon, M. D. Niemack, J. L. Orlowski-Scherer, L. Piccirillo, M. Salatino, S. M. Simon, S. T. Staggs, R. Thornton, J. N. Ullom, E. M. Vavagiakis, E. J. Wollack, Z. Xu, and N. Zhu. Cold optical design for the Large Aperture Simons Observatory telescope, December 2019. arXiv:1808.05058 [astro-ph].

[32] B. Dober, J. A. Austermann, J. A. Beall, D. Becker, G. Che, H. M. Cho, M. Devlin, S. M. Duff, N. Galitzki, J. Gao, C. Groppi, G. C. Hilton, J. Hubmayr, K. D. Irwin, C. M. McKenney, D. Li, N. Lourie, P. Mauskopf, M. R. Vissers, and Y. Wang. Optical Demonstration of THz, Dual-Polarization Sensitive Microwave Kinetic Inductance Detectors. *Journal of Low Temperature Physics*, 184(1):173–179, July 2016.

[33] Bradley J. Dober, Peter A. R. Ade, Peter Ashton, Francesco E. Angilè, James A. Beall, Dan Becker, Kristi J. Bradford, George Che, Hsiao-Mei Cho, Mark J. Devlin, Laura M. Fissel, Yasuo Fukui, Nicholas Galitzki, Jiansong Gao, Christopher E. Groppi, Seth Hillbrand, Gene C. Hilton,

Johannes Hubmayr, Kent D. Irwin, Jeffrey Klein, Jeff Van Lanen, Dale Li, Zhi-Yun Li, Nathan P. Lourie, Hamdi Mani, Peter G. Martin, Philip Mauskopf, Fumitaka Nakamura, Giles Novak, David P. Pappas, Enzo Pascale, Fabio P. Santos, Giorgio Savini, Douglas Scott, Sara Stanchfield, Joel N. Ullom, Matthew Underhill, Michael R. Vissers, and Derek Ward-Thompson. The next-generation BLASTPol experiment. In *Millimeter, Submillimeter, and Far-Infrared Detectors and Instrumentation for Astronomy VII*, volume 9153, pages 137–148. SPIE, July 2014.

[34] Bradley Jerald Dober. *The Next Generation Balloon-Borne Large Aperture Submillimeter Telescope (blast-Tng)*. PhD thesis, University of Pennsylvania, January 2016. Issue: 1688.

[35] Scott Dodelson. *Modern cosmology*. Academic press, San Diego (Calif.), 2003.

[36] Simon Doyle. *Lumped element Kinetic Inductance Detectors*. phd, Cardiff University, 2008. ISBN: 9781303213311.

[37] D. J. Fixsen. The Temperature of the Cosmic Microwave Background. *The Astrophysical Journal*, 707:916–920, December 2009. Publisher: IOP ADS Bibcode: 2009ApJ...707..916F.

[38] D. Flanigan, H. McCarrick, G. Jones, B. R. Johnson, M. H. Abitbol, P. Ade, D. Araujo, K. Bradford, R. Cantor, G. Che, P. Day, S. Doyle, C. B. Kjellstrand, H. Leduc, M. Limon, V. Luu, P. Mauskopf, A. Miller, T. Mroczkowski, C. Tucker, and J. Zmuidzinas. Photon noise from chaotic and coherent millimeter-wave sources measured with horn-coupled, aluminum lumped-element kinetic inductance detectors. *Applied Physics Letters*, 108(8):083504, February 2016.

[39] Nicholas Galitzki, Peter Ade, Francesco E. Angilè, Peter Ashton, Jason Austermann, Tashalee Billings, George Che, Hsiao-Mei Cho, Kristina Davis, Mark Devlin, Simon Dicker, Bradley J. Dober, Laura M. Fissel, Yasuo Fukui, Jiansong Gao, Samuel Gordon, Christopher E. Groppi, Seth Hillbrand, Gene C. Hilton, Johannes Hubmayr, Kent D. Irwin, Jeffrey Klein, Dale Li, Zhi-Yun Li, Nathan P. Lourie, Ian Lowe, Hamdi Mani, Peter G. Martin, Philip Mauskopf, Christopher McKenney, Federico Nati, Giles Novak, Enzo Pascale, Giampaolo Pisano, Fabio P. Santos, Douglas Scott, Adrian Sinclair, Juan D. Soler, Carole Tucker, Matthew Underhill, Michael Vissers, and Paul Williams. Instrumental performance and results from testing of the BLAST-TNG receiver, submillimeter optics, and MKID detector arrays. In *Millimeter, Submillimeter, and Far-Infrared Detectors and Instrumentation for Astronomy VIII*, volume 9914, pages 108–118. SPIE, July 2016.

[40] G. Gamow. Expanding Universe and the Origin of Elements. *Physical Review*, 70(7-8):572–573, October 1946. Publisher: American Physical Society.

[41] J. Gao, J. Zmuidzinas, A. Vayonakis, P. Day, B. Mazin, and H. Leduc. Equivalence of the Effects on the Complex Conductivity of Superconductor due to Temperature Change and External Pair Breaking. *Journal of Low Temperature Physics*, 151(1):557–563, April 2008.

[42] Jiansong Gao. *The Physics of Superconducting Microwave Resonators*. phd, California Institute of Technology, 2008.

[43] Jiansong Gao, Miguel Daal, John M. Martinis, Anastasios Vayonakis, Jonas Zmuidzinas, Bernard Sadoulet, Benjamin A. Mazin, Peter K. Day,

and Henry G. Leduc. A semiempirical model for two-level system noise in superconducting microresonators. *Applied Physics Letters*, 92(21):212504, May 2008.

[44] Jiansong Gao, Miguel Daal, Anastasios Vayonakis, Shwetank Kumar, Jonas Zmuidzinas, Bernard Sadoulet, Benjamin A. Mazin, Peter K. Day, and Henry G. Leduc. Experimental evidence for a surface distribution of two-level systems in superconducting lithographed microwave resonators. *Applied Physics Letters*, 92(15):152505, April 2008.

[45] Jiansong Gao, Jonas Zmuidzinas, Benjamin A. Mazin, Henry G. LeDuc, and Peter K. Day. Noise properties of superconducting coplanar waveguide microwave resonators. *Applied Physics Letters*, 90(10):102507, March 2007.

[46] R. E. Glover and M. Tinkham. Conductivity of Superconducting Films for Photon Energies between 0.3 and $40k{T}_{c}$. *Physical Review*, 108(2):243–256, October 1957. Publisher: American Physical Society.

[47] D. J. Goldie and S. Withington. Non-equilibrium superconductivity in quantum-sensing superconducting resonators. *Superconductor Science and Technology*, 26(1):015004, November 2012. Publisher: IOP Publishing.

[48] Joseph E. Golec, Jeffrey J. McMahon, Aamir M. Ali, Grace E. Chesmore, Leah Cooperrider, Simon Dicker, Nicholas Galitzki, Kathleen Harrington, Rebecca Jackson, Benjamin Westbrook, Edward J. Wollack, Zhilei Xu, and Ningfeng Zhu. Design and fabrication of metamaterial anti-reflection coatings for the Simons Observatory. In *Advances in Optical and Mechanical Technologies for Telescopes and Instrumentation IV*, volume 11451, pages 1115–1122. SPIE, December 2020.

[49] Yilun Guan, Susan E. Clark, Brandon S. Hensley, Patricio A. Gallardo, Sigurd Naess, Cody J. Duell, Simone Aiola, Zachary Atkins, Erminia Calabrese, Steve K. Choi, Nicholas F. Cothard, Mark Devlin, Adriaan J. Duivenvoorden, Jo Dunkley, Rolando Dünner, Simone Ferraro, Matthew Hasselfield, John P. Hughes, Brian J. Koopman, Arthur B. Kosowsky, Mathew S. Madhavacheril, Jeff McMahon, Federico Nati, Michael D. Niemack, Lyman A. Page, Maria Salatino, Emmanuel Schaan, Neelima Sehgal, Cristóbal Sifón, Suzanne Staggs, Eve M. Vavagiakis, Edward J. Wollack, and Zhilei Xu. The Atacama Cosmology Telescope: Microwave Intensity and Polarization Maps of the Galactic Center. *The Astrophysical Journal*, 920(1):6, October 2021. Publisher: The American Astronomical Society.

[50] Jon E. Gudmundsson, Patricio A. Gallardo, Roberto Puddu, Simon R. Dicker, Alexandre E. Adler, Aamir M. Ali, Andrew Bazarko, Grace E. Chesmore, Gabriele Coppi, Nicholas F. Cothard, Nadia Dachlythra, Mark Devlin, Rolando Dünner, Giulio Fabbian, Nicholas Galitzki, Joseph E. Golec, Shuay-Pwu Patty Ho, Peter C. Hargrave, Anna M. Kofman, Adrian T. Lee, Michele Limon, Frederick T. Matsuda, Philip D. Mauskopf, Kavilan Moodley, Federico Nati, Michael D. Niemack, John Orlowski-Scherer, Lyman A. Page, Bruce Partridge, Giuseppe Puglisi, Christian L. Reichardt, Carlos E. Sierra, Sara M. Simon, Grant P. Teply, Carole Tucker, Edward J. Wollack, Zhilei Xu, and Ningfeng Zhu. The Simons Observatory: modeling optical systematics in the Large Aperture Telescope. *Applied Optics*, 60(4):823–837, February 2021. Publisher: Optica Publishing Group.

[51] S. Guns, A. Foster, C. Daley, A. Rahlin, N. Whitehorn, P. A. R. Ade,

Z. Ahmed, E. Anderes, A. J. Anderson, M. Archipley, J. S. Avva, K. Aylor, L. Balkenhol, P. S. Barry, R. Basu Thakur, K. Benabed, A. N. Bender, B. A. Benson, F. Bianchini, L. E. Bleem, F. R. Bouchet, L. Bryant, K. Byrum, J. E. Carlstrom, F. W. Carter, T. W. Cecil, C. L. Chang, P. Chaubal, G. Chen, H. M. Cho, T. L. Chou, J. F. Cliche, T. M. Crawford, A. Cukierman, T. de Haan, E. V. Denison, K. Dibert, J. Ding, M. A. Dobbs, D. Dutcher, W. Everett, C. Feng, K. R. Ferguson, J. Fu, S. Galli, A. E. Gambrel, R. W. Gardner, N. Goeckner-Wald, R. Gualtieri, N. Gupta, R. Guyser, N. W. Halverson, A. H. Harke-Hosemann, N. L. Harrington, J. W. Henning, G. C. Hilton, E. Hivon, G. P. Holder, W. L. Holzapfel, J. C. Hood, D. Howe, N. Huang, K. D. Irwin, O. B. Jeong, M. Jonas, A. Jones, T. S. Khaire, L. Knox, A. M. Kofman, M. Korman, D. L. Kubik, S. Kuhlmann, C. L. Kuo, A. T. Lee, E. M. Leitch, A. E. Lowitz, C. Lu, D. P. Marrone, S. S. Meyer, D. Michalik, M. Millea, J. Montgomery, A. Nadolski, T. Natoli, H. Nguyen, G. I. Noble, V. Novosad, Y. Omori, S. Padin, Z. Pan, P. Paschos, J. Pearson, K. A. Phadke, C. M. Posada, K. Prabhu, W. Quan, C. L. Reichardt, D. Riebel, B. Riedel, M. Rouble, J. E. Ruhl, J. T. Sayre, E. Schiappucci, E. Shirokoff, G. Smecher, J. A. Sobrin, A. A. Stark, J. Stephen, K. T. Story, A. Suzuki, K. L. Thompson, B. Thorne, C. Tucker, C. Umilta, L. R. Vale, J. D. Vieira, G. Wang, W. L. K. Wu, V. Yefremenko, K. W. Yoon, M. R. Young, and L. Zhang. Detection of Galactic and Extragalactic Millimeter-wavelength Transient Sources with SPT-3G. *The Astrophysical Journal*, 916:98, August 2021. Publisher: IOP ADS Bibcode: 2021ApJ...916...98G.

[52] T. Guruswamy, D. J. Goldie, and S. Withington. Quasiparticle generation efficiency in superconducting thin films. *Superconductor Science and Technology*, 27(5):055012, March 2014. Publisher: IOP Publishing.

[53] Erin Healy, Daniel Dutcher, Zachary Atkins, Jason Austermann, Steve K. Choi, Cody J. Duell, Shannon Duff, Nicholas Galitzki, Zachary B. Huber, Johannes Hubmayr, Bradley R. Johnson, Heather McCarrick, Michael D. Niemack, Rita Sonka, Suzanne T. Staggs, Eve Vavagiakis, Yuhan Wang, Zhilei Xu, and Kaiwen Zheng. The Simons Observatory 220 and 280 GHz Focal-Plane Module: Design and Initial Characterization. *Journal of Low Temperature Physics*, 209:815–823, December 2022. Publisher: Springer ADS Bibcode: 2022JLTP..209..815H.

[54] S. W. Henderson, R. Allison, J. Austermann, T. Baildon, N. Battaglia, J. A. Beall, D. Becker, F. De Bernardis, J. R. Bond, E. Calabrese, S. K. Choi, K. P. Coughlin, K. T. Crowley, R. Datta, M. J. Devlin, S. M. Duff, J. Dunkley, R. Dünner, A. van Engelen, P. A. Gallardo, E. Grace, M. Hasselfield, F. Hills, G. C. Hilton, A. D. Hincks, R. Hlo$\hat{z}$ek, S. P. Ho, J. Hubmayr, K. Huffenberger, J. P. Hughes, K. D. Irwin, B. J. Koopman, A. B. Kosowsky, D. Li, J. McMahon, C. Munson, F. Nati, L. Newburgh, M. D. Niemack, P. Niraula, L. A. Page, C. G. Pappas, M. Salatino, A. Schillaci, B. L. Schmitt, N. Sehgal, B. D. Sherwin, J. L. Sievers, S. M. Simon, D. N. Spergel, S. T. Staggs, J. R. Stevens, R. Thornton, J. Van Lanen, E. M. Vavagiakis, J. T. Ward, and E. J. Wollack. Advanced ACTPol Cryogenic Detector Arrays and Readout. *Journal of Low Temperature Physics*, 184:772–779, August 2016. Publisher: Springer ADS Bibcode: 2016JLTP..184..772H.

[55] Shawn W. Henderson, Jason R. Stevens, Mandana Amiri, Jason Austermann, James A. Beall, Saptarshi Chaudhuri, Hsiao-Mei Cho, Steve K. Choi, Nicholas F. Cothard, Kevin T. Crowley, Shannon M. Duff, Colin P. Fitzgerald, Patricio A. Gallardo, Mark Halpern, Matthew Hasselfield, Gene Hilton, Shuay-Pwu Patty Ho, Johannes Hubmayr, Kent D. Ir-

win, Brian J. Koopman, Dale Li, Yaqiong Li, Jeff McMahon, Federico Nati, Michael Niemack, Carl D. Reintsema, Maria Salatino, Alessandro Schillaci, Benjamin L. Schmitt, Sara M. Simon, Suzanne T. Staggs, Eve M. Vavagiakis, and Jonathan T. Ward. Readout of two-kilopixel transition-edge sensor arrays for Advanced ACTPol. In *Millimeter, Submillimeter, and Far-Infrared Detectors and Instrumentation for Astronomy VIII*, volume 9914, pages 346–362. SPIE, July 2016.

[56] J. W. Henning, P. Ade, K. A. Aird, J. E. Austermann, J. A. Beall, D. Becker, B. A. Benson, L. E. Bleem, J. Britton, J. E. Carlstrom, C. L. Chang, H.-M. Cho, T. M. Crawford, A. T. Crites, A. Datesman, T. de Haan, M. A. Dobbs, W. Everett, A. Ewall-Wice, E. M. George, N. W. Halverson, N. Harrington, G. C. Hilton, W. L. Holzapfel, J. Hubmayr, K. D. Irwin, M. Karfunkle, R. Keisler, J. Kennedy, A. T. Lee, E. Leitch, D. Li, M. Lueker, D. P. Marrone, J. J. McMahon, J. Mehl, S. S. Meyer, J. Montgomery, T. E. Montroy, J. Nagy, T. Natoli, J. P. Nibarger, M. D. Niemack, V. Novosad, S. Padin, C. Pryke, C. L. Reichardt, J. E. Ruhl, B. R. Saliwanchik, J. T. Sayre, K. K. Schaffer, E. Shirokoff, K. Story, C. Tucker, K. Vanderlinde, J. D. Vieira, G. Wang, R. Williamson, V. Yefremenko, K. W. Yoon, and E. Young. Feedhorn-coupled TES polarimeter camera modules at 150 GHz for CMB polarization measurements with SPTpol. In *Millimeter, Submillimeter, and Far-Infrared Detectors and Instrumentation for Astronomy VI*, volume 8452, pages 986–1000. SPIE, October 2012.

[57] E. P. Hubble. Cepheids in Spiral Nebulae. *Popular Astronomy*, 33:252–255, January 1925. ADS Bibcode: 1925PA.....33..252H.

[58] Edwin Hubble. A relation between distance and radial velocity among

extra-galactic nebulae. *Proceedings of the National Academy of Sciences*, 15(3):168–173, March 1929. Publisher: Proceedings of the National Academy of Sciences.

[59] J. Hubmayr, J. Beall, D. Becker, H.-M. Cho, M. Devlin, B. Dober, C. Groppi, G. C. Hilton, K. D. Irwin, D. Li, P. Mauskopf, D. P. Pappas, J. Van Lanen, M. R. Vissers, Y. Wang, L. F. Wei, and J. Gao. Photon-noise limited sensitivity in titanium nitride kinetic inductance detectors. *Applied Physics Letters*, 106(7):073505, February 2015.

[60] R. M. J. Janssen, A. Endo, P. J. de Visser, T. M. Klapwijk, and J. J. A. Baselmans. Equivalence of optical and electrical noise equivalent power of hybrid NbTiN-Al microwave kinetic inductance detectors. *Applied Physics Letters*, 105(19):193504, November 2014.

[61] M. S. Khalil, M. J. A. Stoutimore, F. C. Wellstood, and K. D. Osborn. An analysis method for asymmetric resonator transmission applied to superconducting devices. *Journal of Applied Physics*, 111(5):054510, March 2012. arXiv: 1108.3117.

[62] S. Krinner, S. Storz, P. Kurpiers, P. Magnard, J. Heinsoo, R. Keller, J. Lütolf, C. Eichler, and A. Wallraff. Engineering cryogenic setups for 100-qubit scale superconducting circuit systems. *EPJ Quantum Technology*, 6(1):1–29, December 2019. Number: 1 Publisher: SpringerOpen.

[63] Shwetank Kumar, Jiansong Gao, Jonas Zmuidzinas, Benjamin A. Mazin, Henry G. LeDuc, and Peter K. Day. Temperature dependence of the frequency and noise of superconducting coplanar waveguide resonators. *Applied Physics Letters*, 92(12):123503, March 2008.

[64] Antony Lewis. Rayleigh scattering: blue sky thinking for future CMB observations. *Journal of Cosmology and Astroparticle Physics*, 2013(08):053, August 2013.

[65] Yaqiong Li, Emily Biermann, Sigurd Naess, Simone Aiola, Rui An, Nicholas Battaglia, Tanay Bhandarkar, Erminia Calabrese, Steve K. Choi, Kevin T. Crowley, Mark Devlin, Cody J. Duell, Shannon M. Duff, Jo Dunkley, Rolando Dünner, Patricio A. Gallardo, Yilun Guan, Carlos Hervías-Caimapo, Adam D. Hincks, Johannes Hubmayr, Kevin M. Huffenberger, John P. Hughes, Arthur Kosowsky, Thibaut Louis, Maya Mallaby-Kay, Jeff McMahon, Federico Nati, Michael D. Niemack, John Orlowski-Scherer, Lyman Page, Maria Salatino, Cristóbal Sifón, Suzanne T. Staggs, Cristian Vargas, Eve M. Vavagiakis, Yuhan Wang, and Edward J. Wollack. The Atacama Cosmology Telescope: Systematic Transient Search of 3 Day Maps. *The Astrophysical Journal*, 956(1):36, October 2023. Publisher: The American Astronomical Society.

[66] X. Liu, W. Guo, Y. Wang, M. Dai, L. F. Wei, B. Dober, C. M. McKenney, G. C. Hilton, J. Hubmayr, J. E. Austermann, J. N. Ullom, J. Gao, and M. R. Vissers. Superconducting micro-resonator arrays with ideal frequency spacing. *Applied Physics Letters*, 111(25):252601, December 2017.

[67] P. D. Mauskopf. Transition Edge Sensors and Kinetic Inductance Detectors in Astronomical Instruments. *Publications of the Astronomical Society of the Pacific*, 130(990):082001, June 2018. Publisher: The Astronomical Society of the Pacific.

[68] P. D. Mauskopf, S. Doyle, P. Barry, S. Rowe, A. Bidead, P. A. R. Ade, C. Tucker, E. Castillo, A. Monfardini, J. Goupy, and M. Calvo. Photon-

Noise Limited Performance in Aluminum LEKIDs. *Journal of Low Temperature Physics*, 176(3):545–552, August 2014.

[69] B. A. Mazin, S. R. Meeker, M. J. Strader, P. Szypryt, D. Marsden, J. C. van Eyken, G. E. Duggan, A. B. Walter, G. Ulbricht, M. Johnson, B. Bumble, K. O'Brien, and C. Stoughton. ARCONS: A 2024 Pixel Optical through Near-IR Cryogenic Imaging Spectrophotometer. *Publications of the Astronomical Society of the Pacific*, 125(933):1348, November 2013. Publisher: IOP Publishing.

[70] J. McMahon, J. W. Appel, J. E. Austermann, J. A. Beall, D. Becker, B. A. Benson, L. E. Bleem, J. Britton, C. L. Chang, J. E. Carlstrom, H. M. Cho, A. T. Crites, T. Essinger-Hileman, W. Everett, N. W. Halverson, J. W. Henning, G. C. Hilton, K. D. Irwin, J. Mehl, S. S. Meyer, S. Mossley, M. D. Niemack, L. P. Parker, S. M. Simon, S. T. Staggs, C. Visnjic, E. Wollack, K. U.-Yen, K. W. Yoon, and Y. Zhao. Planar Orthomode Transducers for Feedhorn-coupled TES Polarimeters. *AIP Conference Proceedings*, 1185(1):490–493, December 2009.

[71] A. Monfardini, A. Benoit, A. Bideaud, L. Swenson, A. Cruciani, P. Camus, C. Hoffmann, F. X. Désert, S. Doyle, P. Ade, P. Mauskopf, C. Tucker, M. Roesch, S. Leclercq, K. F. Schuster, A. Endo, A. Baryshev, J. J. A. Baselmans, L. Ferrari, S. J. C. Yates, O. Bourrion, J. Macias-Perez, C. Vescovi, M. Calvo, and C. Giordano. A DUAL-BAND MILLIMETER-WAVE KINETIC INDUCTANCE CAMERA FOR THE IRAM 30 m TELESCOPE. *The Astrophysical Journal Supplement Series*, 194(2):24, May 2011. Publisher: The American Astronomical Society.

[72] Jenna E. Moore, Tanay Bhandarkar, Brooke DiGia, Cody Duell, Nicholas

Galitzki, Justin Mathewson, John Orlowski-Scherer, Max Silva-Feaver, Yuhan Wang, Caleb Wheeler, Zhilei Xu, and Philip Mauskopf. Development and performance of universal readout harness for the Simons Observatory. In *Millimeter, Submillimeter, and Far-Infrared Detectors and Instrumentation for Astronomy XI*, volume 12190, pages 912–924. SPIE, August 2022.

[73] Sigurd Naess, Simone Aiola, Nick Battaglia, Richard J. Bond, Erminia Calabrese, Steve K. Choi, Nicholas F. Cothard, Mark Halpern, J. Colin Hill, Brian J. Koopman, Mark Devlin, Jeff McMahon, Simon Dicker, Adriaan J. Duivenvoorden, Jo Dunkley, Valentina Fanfani, Simone Ferraro, Patricio A. Gallardo, Yilun Guan, Dongwon Han, Matthew Hasselfield, Adam D. Hincks, Kevin Huffenberger, Arthur B. Kosowsky, Thibaut Louis, Amanda Macinnis, Mathew S. Madhavacheril, Federico Nati, Michael D. Niemack, Lyman Page, Maria Salatino, Emmanuel Schaan, John Orlowski-Scherer, Alessandro Schillaci, Benjamin Schmitt, Neelima Sehgal, Cristóbal Sifón, Suzanne Staggs, Alexander Van Engelen, and Edward J. Wollack. The Atacama Cosmology Telescope: A Search for Planet 9. *The Astrophysical Journal*, 923:224, December 2021. Publisher: IOP ADS Bibcode: 2021ApJ...923..224N.

[74] National Institute for Standards and Technology. NIST cryogenic material properties database. https://trc.nist.gov/cryogenics/materials/materialproperties.htm. Accessed: 2022-09-07.

[75] Marko Neric. Terahertz Astronomy Cryogenic IF Design Calibration and Measurement. Technical report, Arizona State University, 2023.

[76] Michael D. Niemack. Designs for a large-aperture telescope to map the

CMB 10× faster. *Applied Optics*, 55(7):1688–1696, March 2016. Publisher: Optica Publishing Group.

[77] Omid Noroozian. *Superconducting Microwave Resonator Arrays for Submillimeter/Far-infrared Imaging*. phd, California Institute of Technology, 2012.

[78] Omid Noroozian, Jiansong Gao, Jonas Zmuidzinas, Henry G. LeDuc, and Benjamin A. Mazin. Two-level system noise reduction for Microwave Kinetic Inductance Detectors. *AIP Conference Proceedings*, 1185(1):148–151, December 2009.

[79] C. S. Owen and D. J. Scalapino. Superconducting State under the Influence of External Dynamic Pair Breaking. *Physical Review Letters*, 28(24):1559–1561, June 1972. Publisher: American Physical Society.

[80] A. Paiella, E. S. Battistelli, M. G. Castellano, I. Colantoni, F. Columbro, A. Coppolecchia, G. D'Alessandro, P. de Bernardis, S. Gordon, L. Lamagna, H. Mani, S. Masi, P. Mauskopf, G. Pettinari, F. Piacentini, and G. Presta. Kinetic Inductance Detectors and readout electronics for the OLIMPO experiment. *Journal of Physics: Conference Series*, 1182(1):012005, February 2019. Publisher: IOP Publishing.

[81] David P. Pappas, Michael R. Vissers, David S. Wisbey, Jeffrey S. Kline, and Jiansong Gao. Two Level System Loss in Superconducting Microwave Resonators. *IEEE Transactions on Applied Superconductivity*, 21(3):871–874, June 2011. Conference Name: IEEE Transactions on Applied Superconductivity.

[82] Stephen C. Parshley, Jörg Kronshage, James Blair, Terry Herter, Mike

Nolta, Gordon J. Stacey, Andrew Bazarko, Frank Bertoldi, Ricardo Bustos, Donald B. Campbell, Scott Chapman, Nicolas Cothard, Mark Devlin, Jens Erler, Michel Fich, Patricio A. Gallardo, Riccardo Giovanelli, Urs Graf, Scott Gramke, Martha P. Haynes, Richard Hills, Michele Limon, Jeffrey G. Mangum, Jeff McMahon, Michael D. Niemack, Thomas Nikola, Markus Omlor, Dominik A. Riechers, Karl Steeger, Jürgen Stutzki, and Eve M. Vavagiakis. CCAT-prime: a novel telescope for sub-millimeter astronomy. In *Ground-based and Airborne Telescopes VII*, volume 10700, pages 1744–1758. SPIE, July 2018.

[83] A. A. Penzias and R. W. Wilson. A Measurement of Excess Antenna Temperature at 4080 Mc/s. *The Astrophysical Journal*, 142:419–421, July 1965. Publisher: IOP ADS Bibcode: 1965ApJ...142..419P.

[84] S. Perlmutter, G. Aldering, G. Goldhaber, R. A. Knop, P. Nugent, P. G. Castro, S. Deustua, S. Fabbro, A. Goobar, D. E. Groom, I. M. Hook, A. G. Kim, M. Y. Kim, J. C. Lee, N. J. Nunes, R. Pain, C. R. Pennypacker, R. Quimby, C. Lidman, R. S. Ellis, M. Irwin, R. G. McMahon, P. Ruiz-Lapuente, N. Walton, B. Schaefer, B. J. Boyle, A. V. Filippenko, T. Matheson, A. S. Fruchter, N. Panagia, H. J. M. Newberg, W. J. Couch, and The Supernova Cosmology Project. Measurements of Ω and Λ from 42 High-Redshift Supernovae. *The Astrophysical Journal*, 517:565–586, June 1999. Publisher: IOP ADS Bibcode: 1999ApJ...517..565P.

[85] Planck Collaboration, N. Aghanim, Y. Akrami, F. Arroja, M. Ashdown, J. Aumont, C. Baccigalupi, M. Ballardini, A. J. Banday, R. B. Barreiro, N. Bartolo, S. Basak, R. Battye, K. Benabed, J. P. Bernard, M. Bersanelli, P. Bielewicz, J. J. Bock, J. R. Bond, J. Borrill, F. R. Bouchet, F. Boulanger,

M. Bucher, C. Burigana, R. C. Butler, E. Calabrese, J. F. Cardoso, J. Carron, B. Casaponsa, A. Challinor, H. C. Chiang, L. P. L. Colombo, C. Combet, D. Contreras, B. P. Crill, F. Cuttaia, P. de Bernardis, G. de Zotti, J. Delabrouille, J. M. Delouis, F. X. Désert, E. Di Valentino, C. Dickinson, J. M. Diego, S. Donzelli, O. Doré, M. Douspis, A. Ducout, X. Dupac, G. Efstathiou, F. Elsner, T. A. Enßlin, H. K. Eriksen, E. Falgarone, Y. Fantaye, J. Fergusson, R. Fernandez-Cobos, F. Finelli, F. Forastieri, M. Frailis, E. Franceschi, A. Frolov, S. Galeotta, S. Galli, K. Ganga, R. T. Génova-Santos, M. Gerbino, T. Ghosh, J. González-Nuevo, K. M. Górski, S. Gratton, A. Gruppuso, J. E. Gudmundsson, J. Hamann, W. Handley, F. K. Hansen, G. Helou, D. Herranz, S. R. Hildebrandt, E. Hivon, Z. Huang, A. H. Jaffe, W. C. Jones, A. Karakci, E. Keihänen, R. Keskitalo, K. Kiiveri, J. Kim, T. S. Kisner, L. Knox, N. Krachmalnicoff, M. Kunz, H. Kurki-Suonio, G. Lagache, J. M. Lamarre, M. Langer, A. Lasenby, M. Lattanzi, C. R. Lawrence, M. Le Jeune, J. P. Leahy, J. Lesgourgues, F. Levrier, A. Lewis, M. Liguori, P. B. Lilje, M. Lilley, V. Lindholm, M. López-Caniego, P. M. Lubin, Y. Z. Ma, J. F. Macías-Pérez, G. Maggio, D. Maino, N. Mandolesi, A. Mangilli, A. Marcos-Caballero, M. Maris, P. G. Martin, M. Martinelli, E. Martínez-González, S. Matarrese, N. Mauri, J. D. McEwen, P. D. Meerburg, P. R. Meinhold, A. Melchiorri, A. Mennella, M. Migliaccio, M. Millea, S. Mitra, M. A. Miville-Deschênes, D. Molinari, A. Moneti, L. Montier, G. Morgante, A. Moss, S. Mottet, M. Münchmeyer, P. Natoli, H. U. Nørgaard-Nielsen, C. A. Oxborrow, L. Pagano, D. Paoletti, B. Partridge, G. Patanchon, T. J. Pearson, M. Peel, H. V. Peiris, F. Perrotta, V. Pettorino, F. Piacentini, L. Polastri, G. Polenta, J. L. Puget, J. P. Rachen, M. Reinecke, M. Remazeilles, C. Renault, A. Renzi, G. Rocha,

C. Rosset, G. Roudier, J. A. Rubiño-Martín, B. Ruiz-Granados, L. Salvati, M. Sandri, M. Savelainen, D. Scott, E. P. S. Shellard, M. Shiraishi, C. Sirignano, G. Sirri, L. D. Spencer, R. Sunyaev, A. S. Suur-Uski, J. A. Tauber, D. Tavagnacco, M. Tenti, L. Terenzi, L. Toffolatti, M. Tomasi, T. Trombetti, J. Valiviita, B. Van Tent, L. Vibert, P. Vielva, F. Villa, N. Vittorio, B. D. Wandelt, I. K. Wehus, M. White, S. D. M. White, A. Zacchei, and A. Zonca. Planck 2018 results. I. Overview and the cosmological legacy of Planck. *Astronomy and Astrophysics*, 641:A1, September 2020. ADS Bibcode: 2020A&A...641A...1P.

[86] Planck Collaboration, Y. Akrami, M. Ashdown, J. Aumont, C. Baccigalupi, M. Ballardini, A. J. Banday, R. B. Barreiro, N. Bartolo, S. Basak, K. Benabed, J. P. Bernard, M. Bersanelli, P. Bielewicz, J. R. Bond, J. Borrill, F. R. Bouchet, F. Boulanger, A. Bracco, M. Bucher, C. Burigana, E. Calabrese, J. F. Cardoso, J. Carron, H. C. Chiang, C. Combet, B. P. Crill, P. de Bernardis, G. de Zotti, J. Delabrouille, J. M. Delouis, E. Di Valentino, C. Dickinson, J. M. Diego, A. Ducout, X. Dupac, G. Efstathiou, F. Elsner, T. A. Enßlin, E. Falgarone, Y. Fantaye, K. Ferrière, F. Finelli, F. Forastieri, M. Frailis, A. A. Fraisse, E. Franceschi, A. Frolov, S. Galeotta, S. Galli, K. Ganga, R. T. Génova-Santos, T. Ghosh, J. González-Nuevo, K. M. Górski, A. Gruppuso, J. E. Gudmundsson, V. Guillet, W. Handley, F. K. Hansen, D. Herranz, Z. Huang, A. H. Jaffe, W. C. Jones, E. Keihänen, R. Keskitalo, K. Kiiveri, J. Kim, N. Krachmalnicoff, M. Kunz, H. Kurki-Suonio, J. M. Lamarre, A. Lasenby, M. Le Jeune, F. Levrier, M. Liguori, P. B. Lilje, V. Lindholm, M. López-Caniego, P. M. Lubin, Y. Z. Ma, J. F. Macías-Pérez, G. Maggio, D. Maino, N. Mandolesi, A. Mangilli, P. G. Martin, E. Martínez-González, S. Matarrese, J. D. McEwen, P. R. Meinhold, A. Melchiorri, M. Migliac-

cio, M. A. Miville-Deschênes, D. Molinari, A. Moneti, L. Montier, G. Morgante, P. Natoli, L. Pagano, D. Paoletti, V. Pettorino, F. Piacentini, G. Polenta, J. L. Puget, J. P. Rachen, M. Reinecke, M. Remazeilles, A. Renzi, G. Rocha, C. Rosset, G. Roudier, J. A. Rubiño-Martín, B. Ruiz-Granados, L. Salvati, M. Sandri, M. Savelainen, D. Scott, J. D. Soler, L. D. Spencer, J. A. Tauber, D. Tavagnacco, L. Toffolatti, M. Tomasi, T. Trombetti, J. Valiviita, F. Vansyngel, B. Van Tent, P. Vielva, F. Villa, N. Vittorio, I. K. Wehus, A. Zacchei, and A. Zonca. Planck 2018 results. XI. Polarized dust foregrounds. *Astronomy and Astrophysics*, 641:A11, September 2020. ADS Bibcode: 2020A&A...641A..11P.

[87] David M. Pozar. *Microwave engineering*. Wiley, Hoboken, NJ, 4th ed edition, 2012. OCLC: ocn714728044.

[88] Scott W. Randall, Maxim Markevitch, Douglas Clowe, Anthony H. Gonzalez, and Marusa Bradač. Constraints on the Self-Interaction Cross Section of Dark Matter from Numerical Simulations of the Merging Galaxy Cluster 1E 0657-56. *The Astrophysical Journal*, 679:1173–1180, June 2008. Publisher: IOP ADS Bibcode: 2008ApJ...679.1173R.

[89] Adam G. Riess, Alexei V. Filippenko, Peter Challis, Alejandro Clocchiatti, Alan Diercks, Peter M. Garnavich, Ron L. Gilliland, Craig J. Hogan, Saurabh Jha, Robert P. Kirshner, B. Leibundgut, M. M. Phillips, David Reiss, Brian P. Schmidt, Robert A. Schommer, R. Chris Smith, J. Spyromilio, Christopher Stubbs, Nicholas B. Suntzeff, and John Tonry. Observational Evidence from Supernovae for an Accelerating Universe and a Cosmological Constant. *The Astronomical Journal*, 116:1009–1038, September 1998. Publisher: IOP ADS Bibcode: 1998AJ....116.1009R.

[90] W. Rindler. Visual horizons in world models. *Monthly Notices of the Royal Astronomical Society*, 116:662, January 1956. Publisher: OUP ADS Bibcode: 1956MNRAS.116..662R.

[91] Vera C. Rubin and W. Kent Ford, Jr. Rotation of the Andromeda Nebula from a Spectroscopic Survey of Emission Regions. *The Astrophysical Journal*, 159:379, February 1970. Publisher: IOP ADS Bibcode: 1970ApJ...159..379R.

[92] Mayuri Sathyanarayana Rao, Maximiliano Silva-Feaver, Aamir Ali, Kam Arnold, Peter Ashton, Bradley J. Dober, Cody J. Duell, Shannon M. Duff, Nicholas Galitzki, Erin Healy, Shawn Henderson, Shuay-Pwu Patty Ho, Jonathan Hoh, Anna M. Kofman, Akito Kusaka, Adrian T. Lee, Aashrita Mangu, Justin Mathewson, Philip Mauskopf, Heather McCarrick, Jenna Moore, Michael D. Niemack, Christopher Raum, Maria Salatino, Trevor Sasse, Joseph Seibert, Sara M. Simon, Suzanne Staggs, Jason R. Stevens, Grant Teply, Robert Thornton, Joel Ullom, Eve M. Vavagiakis, Benjamin Westbrook, Zhilei Xu, and Ningfeng Zhu. Simons Observatory Microwave SQUID Multiplexing Readout: Cryogenic RF Amplifier and Coaxial Chain Design. *Journal of Low Temperature Physics*, 199(3):807–816, May 2020.

[93] A. V. Semenov, I. A. Devyatov, P. J. de Visser, and T. M. Klapwijk. Coherent Excited States in Superconductors due to a Microwave Field. *Physical Review Letters*, 117(4):047002, July 2016. Publisher: American Physical Society.

[94] Seth Robert Siegel. *A Multiwavelength Study of the Intracluster Medium and*

the Characterization of the Multiwavelength Sub/millimeter Inductance Camera. phd, California Institute of Technology, 2016.

[95] Sara M. Simon, Joseph E. Golec, Aamir Ali, Jason Austermann, James A. Beall, Sarah Marie M. Bruno, Steve K. Choi, Kevin T. Crowley, Simon Dicker, Bradley Dober, Shannon M. Duff, Erin Healy, Charles A. Hill, Shuay-Pwu Patty Ho, Johannes Hubmayr, Yaqiong Li, Marius Lungu, Jeff McMahon, John Orlowski-Scherer, Maria Salatino, Suzanne Staggs, Edward J. Wollack, Zhilei Xu, and Ningfeng Zhu. Feedhorn development and scalability for Simons Observatory and beyond. In *Millimeter, Submillimeter, and Far-Infrared Detectors and Instrumentation for Astronomy IX*, volume 10708, pages 1145–1156. SPIE, July 2018.

[96] Adrian K. Sinclair, James R. Burgoyne, Yaqiong Li, Cody Duell, Scott C. Chapman, Anthony I. Huber, and Ruixuan Xie. Breaking the 10 mW/pixel Limit for Kinetic Inductance Detector Readout Electronics, May 2023. Publication Title: arXiv e-prints ADS Bibcode: 2023arXiv230500928S.

[97] Adrian K. Sinclair, Ryan C. Stephenson, Cody A. Roberson, Eric L. Weeks, James Burgoyne, Anthony I. Huber, Philip M. Mauskopf, Scott C. Chapman, Jason E. Austermann, Steve K. Choi, Cody J. Duell, Michel Fich, Christopher E. Groppi, Zachary Huber, Michael D. Niemack, Thomas Nikola, Kayla M. Rossi, Adhitya Sriram, Gordon J. Stacey, Erik Szakiel, Joel Tsuchitori, Eve M. Vavagiakis, and Jordan D. Wheeler. CCAT-prime: RFSoC based readout for frequency multiplexed kinetic inductance detectors. In *Millimeter, Submillimeter, and Far-Infrared Detectors and Instru-*

mentation for Astronomy XI, volume 12190, pages 444–463. SPIE, August 2022.

[98] V. M. Slipher. The radial velocity of the Andromeda Nebula. *Lowell Observatory Bulletin*, 2:56–57, January 1913. ADS Bibcode: 1913LowOB...2...56S.

[99] V. M. Slipher. Spectrographic Observations of Nebulae. *Popular Astronomy*, 23:21–24, January 1915. ADS Bibcode: 1915PA.....23...21S.

[100] L. J. Swenson, P. K. Day, B. H. Eom, H. G. Leduc, N. Llombart, C. M. McKenney, O. Noroozian, and J. Zmuidzinas. Operation of a titanium nitride superconducting microresonator detector in the nonlinear regime. *Journal of Applied Physics*, 113(10):104501, March 2013.

[101] Loren J. Swenson, Peter K. Day, Charles D. Dowell, Byeong H. Eom, Matthew I. Hollister, Robert Jarnot, Attila Kovács, Henry G. Leduc, Christopher M. McKenney, Ryan Monroe, Tony Mroczkowski, Hien T. Nguyen, and Jonas Zmuidzinas. MAKO: a pathfinder instrument for on-sky demonstration of low-cost 350 micron imaging arrays. In *Millimeter, Submillimeter, and Far-Infrared Detectors and Instrumentation for Astronomy VI*, volume 8452, pages 190–199. SPIE, September 2012.

[102] C. N. Thomas, S. Withington, and D. J. Goldie. Electrothermal model of kinetic inductance detectors. *Superconductor Science and Technology*, 28(4):045012, February 2015. Publisher: IOP Publishing.

[103] C. N. Thomas, S. Withington, Z. Sun, T. Skyrme, and D. J. Goldie. Nonlinear effects in superconducting thin film microwave resonators. *New Journal of Physics*, 22(7):073028, July 2020. Publisher: IOP Publishing.

[104] Michael Tinkham. *Introduction to superconductivity*. Dover books on physics. Dover Publ, Mineola, NY, 2 ed edition, 2015.

[105] Carole E. Tucker and Peter A. R. Ade. Thermal filtering for large aperture cryogenic detector arrays. In *Millimeter and Submillimeter Detectors and Instrumentation for Astronomy III*, volume 6275, pages 239–247. SPIE, June 2006.

[106] E. M. Vavagiakis, Z. Ahmed, A. Ali, K. Basu, N. Battaglia, F. Bertoldi, R. Bond, R. Bustos, S. C. Chapman, D. Chung, G. Coppi, N. F. Cothard, S. Dicker, C. J. Duell, S. M. Duff, J. Erler, M. Fich, N. Galitzki, P. A. Gallardo, S. W. Henderson, T. L. Herter, G. Hilton, J. Hubmayr, K. D. Irwin, B. J. Koopman, J. McMahon, N. Murray, M. D. Niemack, T. Nikola, M. Nolta, J. Orlowski-Scherer, S. C. Parshley, D. A. Riechers, K. Rossi, D. Scott, C. Sierra, M. Silva-Feaver, S. M. Simon, G. J. Stacey, J. R. Stevens, J. N. Ullom, M. R. Vissers, S. Walker, E. J. Wollack, Z. Xu, and N. Zhu. Prime-Cam: a first-light instrument for the CCAT-prime telescope. In *Millimeter, Submillimeter, and Far-Infrared Detectors and Instrumentation for Astronomy IX*, volume 10708, pages 375–390. SPIE, July 2018.

[107] Eve M. Vavagiakis, Cody J. Duell, Jason Austermann, James Beall, Tanay Bhandarkar, Scott C. Chapman, Steve K. Choi, Gabriele Coppi, Simon Dicker, Mark Devlin, Rodrigo G. Freundt, Jiansong Gao, Christopher Groppi, Terry L. Herter, Zachary B. Huber, Johannes Hubmayr, Doug Johnstone, Ben Keller, Anna M. Kofman, Yaqiong Li, Philip Mauskopf, Jeff McMahon, Jenna Moore, Colin C. Murphy, Michael D. Niemack, Thomas Nikola, John Orlowski-Scherer, Kayla M. Rossi, Adrian K. Sinclair, Gordon J. Stacey, Joel Ullom, Michael Vissers, Jordan Wheeler, Zhilei Xu,

Ningfeng Zhu, and Bugao Zou. CCAT-prime: design of the Mod-Cam receiver and 280 GHz MKID instrument module. In *Millimeter, Submillimeter, and Far-Infrared Detectors and Instrumentation for Astronomy XI*, volume 12190, pages 61–76. SPIE, August 2022.

[108] Amit Vishwas, Stephen C. Parshley, George E. Gull, German Cortes-Medellin, Kayla M. Rossi, Terry L. Herter, Donald B. Campbell, Mitchell C. Burnett, Spencer M. Ammermon, Nathaniel Ashcraft, Erich Nygaard, Karl F. Warnick, Brian D. Jeffs, Hamdi Mani, Christopher E. Groppi, and Phil Perillat. ALPACA: a fully cryogenic L-band phased array feed for radio astronomy. In *Millimeter, Submillimeter, and Far-Infrared Detectors and Instrumentation for Astronomy XI*, volume PC12190, page PC121900G. SPIE, August 2022.

[109] Steven Weinberg. *Cosmology*. Oxford university press, New York, 2008.

[110] Jordan Wheeler, Jason Austermann, Michael Vissers, James Beall, Jiansong Gao, Jozsef Imrek, Edwin Heilweil, Douglas Bennett, Johnathan Gard, Jeff van Lanen, Johannes Hubmayr, and Joel Ullom. Broadband kinetic inductance detectors for far-IR observations. In *Millimeter, Submillimeter, and Far-Infrared Detectors and Instrumentation for Astronomy XI*, volume 12190, pages 92–111. SPIE, August 2022.

[111] S. D. M. White, G. Efstathiou, and C. S. Frenk. The amplitude of mass fluctuations in the universe. *Monthly Notices of the Royal Astronomical Society*, 262:1023–1028, June 1993. Publisher: OUP ADS Bibcode: 1993MNRAS.262.1023W.

[112] Simon D. M. White, Julio F. Navarro, August E. Evrard, and Carlos S. Frenk. The baryon content of galaxy clusters: a challenge to cosmological

orthodoxy. *Nature*, 366(6454):429–433, December 1993. Publisher: Nature Publishing Group.

[113] N. Whitehorn, T. Natoli, P. A. R. Ade, J. E. Austermann, J. A. Beall, A. N. Bender, B. A. Benson, L. E. Bleem, J. E. Carlstrom, C. L. Chang, H. C. Chiang, H. M. Cho, R. Citron, T. M. Crawford, A. T. Crites, T. de Haan, M. A. Dobbs, W. Everett, J. Gallicchio, E. M. George, A. Gilbert, N. W. Halverson, N. Harrington, J. W. Henning, G. C. Hilton, G. P. Holder, W. L. Holzapfel, S. Hoover, Z. Hou, J. D. Hrubes, N. Huang, J. Hubmayr, K. D. Irwin, R. Keisler, L. Knox, A. T. Lee, E. M. Leitch, D. Li, J. J. McMahon, S. S. Meyer, L. Mocanu, J. P. Nibarger, V. Novosad, S. Padin, C. Pryke, C. L. Reichardt, J. E. Ruhl, B. R. Saliwanchik, J. T. Sayre, K. K. Schaffer, G. Smecher, A. A. Stark, K. T. Story, C. Tucker, K. Vanderlinde, J. D. Vieira, G. Wang, and V. Yefremenko. Millimeter Transient Point Sources in the SPTpol 100 Square Degree Survey. *The Astrophysical Journal*, 830:143, October 2016. Publisher: IOP ADS Bibcode: 2016ApJ...830..143W.

[114] Grant W. Wilson, Sophia Abi-Saad, Peter Ade, Itziar Aretxaga, Jason Austermann, Yvonne Ban, Joseph Bardin, James Beall, Marc Berthoud, Sean Bryan, John Bussan, Edgar Castillo, Miguel Chavez, Reid Contente, N. S. DeNigris, Bradley Dober, Miranda Eiben, Daniel Ferrusca, Laura Fissel, Jiansong Gao, Joseph E. Golec, Robert Golina, Arturo Gomez, Sam Gordon, Robert Gutermuth, Gene Hilton, Mohsen Hosseini, Johannes Hubmayr, David Hughes, Stephen Kuczarski, Dennis Lee, Emily Lunde, Zhiyuan Ma, Hamdi Mani, Philip Mauskopf, Michael McCrackan, Christopher McKenney, Jeffrey McMahon, Giles Novak, Giampaolo Pisano, Alexandra Pope, Amy Ralston, Ivan Rodriguez, David Sánchez-Argüelles, F. Peter Schloerb, Sara Simon, Adrian Sinclair, Kamal

Souccar, Ana Torres Campos, Carole Tucker, Joel Ullom, Eric Van Camp, Jeff Van Lanen, Miguel Velazquez, Michael Vissers, Eric Weeks, and Min S. Yun. The TolTEC camera: an overview of the instrument and in-lab testing results. In *Millimeter, Submillimeter, and Far-Infrared Detectors and Instrumentation for Astronomy X*, volume 11453, page 1145302. SPIE, December 2020.

[115] Zhilei Xu, Grace E. Chesmore, Shunsuke Adachi, Aamir M. Ali, Andrew Bazarko, Gabriele Coppi, Mark Devlin, Tom Devlin, Simon R. Dicker, Patricio A. Gallardo, Joseph E. Golec, Jon E. Gudmundsson, Kathleen Harrington, Makoto Hattori, Anna Kofman, Kenji Kiuchi, Akito Kusaka, Michele Limon, Frederick Matsuda, Jeff McMahon, Federico Nati, Michael D. Niemack, Aritoki Suzuki, Grant P. Teply, Robert J. Thornton, Edward J. Wollack, Mario Zannoni, and Ningfeng Zhu. The Simons Observatory: metamaterial microwave absorber and its cryogenic applications. *Applied Optics*, 60(4):864–874, February 2021. Publisher: Optica Publishing Group.

[116] Qingjuan Yu, David N. Spergel, and Jeremiah P. Ostriker. Rayleigh Scattering and Microwave Background Fluctuations. *The Astrophysical Journal*, 558(1):23, September 2001. Publisher: IOP Publishing.

[117] Ningfeng Zhu, Tanay Bhandarkar, Gabriele Coppi, Anna M. Kofman, John L. Orlowski-Scherer, Zhilei Xu, Shunsuke Adachi, Peter Ade, Simone Aiola, Jason Austermann, Andrew O. Bazarko, James A. Beall, Sanah Bhimani, J. Richard Bond, Grace E. Chesmore, Steve K. Choi, Jake Connors, Nicholas F. Cothard, Mark Devlin, Simon Dicker, Bradley Dober, Cody J. Duell, Shannon M. Duff, Rolando Dünner, Giulio Fabbian, Nicholas Gal-

itzki, Patricio A. Gallardo, Joseph E. Golec, Saianeesh K. Haridas, Kathleen Harrington, Erin Healy, Shuay-Pwu Patty Ho, Zachary B. Huber, Johannes Hubmayr, Jeffrey Iuliano, Bradley R. Johnson, Brian Keating, Kenji Kiuchi, Brian J. Koopman, Jack Lashner, Adrian T. Lee, Yaqiong Li, Michele Limon, Michael Link, Tammy J. Lucas, Heather McCarrick, Jenna Moore, Federico Nati, Laura B. Newburgh, Michael D. Niemack, Elena Pierpaoli, Michael J. Randall, Karen Perez Sarmiento, Lauren J. Saunders, Joseph Seibert, Carlos Sierra, Rita Sonka, Jacob Spisak, Shreya Sutariya, Osamu Tajima, Grant P. Teply, Robert J. Thornton, Tran Tsan, Carole Tucker, Joel Ullom, Eve M. Vavagiakis, Michael R. Vissers, Samantha Walker, Benjamin Westbrook, Edward J. Wollack, and Mario Zannoni. The Simons Observatory Large Aperture Telescope Receiver. *The Astrophysical Journal Supplement Series*, 256(1):23, September 2021. Publisher: The American Astronomical Society.

[118] Yijie Zhu, Benjamin Beringue, Steve K. Choi, Nicholas Battaglia, P. Daniel Meerburg, and Joel Meyers. Estimating the impact of foregrounds on the future detection of Rayleigh scattering. *Journal of Cosmology and Astroparticle Physics*, 2022(09):048, September 2022. Publisher: IOP Publishing.

[119] Jonas Zmuidzinas. Superconducting Microresonators: Physics and Applications. *Annual Review of Condensed Matter Physics*, 3(1):169–214, 2012.